PATH INTEGRAL MONTE CARLO SIMULATIONS OF HOT DENSE HYDROGEN

BY

BURKHARD MILITZER

Diplom, Humboldt Universität, Berlin, 1996

THESIS

Submitted in partial fulfillment of the requirements
for the degree of Doctor of Philosophy in Physics
in the Graduate College of the
University of Illinois at Urbana-Champaign, 2000

Urbana, Illinois

PATH INTEGRAL MONTE CARLO SIMULATIONS OF HOT DENSE HYDROGEN

Burkhard Militzer, Ph.D.
Department of Physics
University of Illinois at Urbana-Champaign, 2000
David M. Ceperley, Advisor

Path integral Monte Carlo (PIMC) simulations are a powerful computational method to study interacting quantum systems at finite temperature. In this work, PIMC has been applied to study the equilibrium properties of hot, dense hydrogen in the temperature and density range of $5000 \leq T \leq 10^6\,\mathrm{K}$ and $10^{-3} \leq \rho \leq 2.7\,\mathrm{gcm}^{-3}$. We determine the equation of state (EOS) and the high temperature phase diagram. Under these conditions, hydrogen is a dense fluid that exhibits a molecular, an atomic and a plasma regime at low density. A high density, it is predicted to go into a metallic state. The determination of these properties has direct application to the understanding of brown dwarfs and Jovian planets.

The restricted PIMC method relies on a nodal surface, taken from a trial density matrix, in order to deal with Fermi statistics. This method has been applied extensively using free particle nodes. We develop a variational technique that allows us to obtain a variational many-body density matrix (VDM). In a first application, we derive a VDM that describes the principle physical effects in high temperature hydrogen such as ionization and dissociation.

In the PIMC simulation, we employ the VDM in order to replace the free particle nodes and study the effect on the derived thermodynamic properties. The modifications are particularly significant at low temperature and high density where PIMC using free particle nodes have suggested a first order plasma phase transition. We critically review these findings and show improved results from simulations with VDM nodes.

Recent laser shock wave experiments are of particular relevance to this research because they represent the first direct EOS measurements in the megabar regime. We estimate the shock Hugoniot from the calculated EOS and compare with the experimental findings. We study finite size effects and the dependence on the time step and on the type of nodes.

Furthermore, we extend the restricted PIMC method to open paths in order to determine off-diagonal density matrix elements and apply this method to the momentum distribution of the electron gas and to the natural orbitals in hydrogen.

Acknowledgments

First of all, I would like to thank my advisor, Prof. David M. Ceperley, for his guidance, stimulating discussions and support. He has made my graduate experience at the University of Illinois at Urbana-Champaign an excellent one. I also learned a great deal about exactness in numerical simulations.

I am particularly thankful to benefit from all the previous work that has been done to develop the PIMC method. This also includes Roy Pollock who was my advisor for two summers when I worked as a student at Lawrence Livermore National Laboratory. We developed on the variational density matrix together but I would also like to mention his bike-riding and vine-making skills.

Furthermore, I got a lot of support from Bill Magro who had worked on dense hydrogen before me and shared all his experience, taught me many computational skills and spent nights with me to parallelize the fermionic part of the path integral code.

I am very grateful to Prof. Richard M. Martin and Dr. Lubos Mitas for support and many helpful discussions. I would also like to thank all my fellow graduate students in the group, in particular John Shumway, Mark Dewing, Tommaso Torelli, and Fengua Zong. The numerous discussions helped me tremendously in my research and pointed out a lot of things I did not understand.

I also got a lot of support from Gregory Bauer who helped me with many things I needed as a German in America. Furthermore, I remember many useful discussions with him and the other post-docs Carmen Gordillo, Tadashi Ogitsu, and Fabrice Douchin.

I also wish to thank Prof. Bernard Bernu in Paris who was a kind host during my visits and an good collaborator interested in all PIMC details.

I would also like to thank for the support I got from the people at the National Center for Supercomputing Applications (NCSA). In particular, I would like to mention Rachael Brady, who provided me with her fancy visualization program so that I could modify it to show my path integral simulations in the CAVE virtual reality system at NCSA, for which I almost got more attention than for the numbers I calculated. Jeff Carpenter and Holly Korup are listed because they produced the video about our research on hot, dense hydrogen.

Furthermore, I would like to acknowledge the work by Nan Zhong and Guochun Shi who wrote the library that dumps the data of my simulation code.

Foremost, I am thankful to my girl-friend Nicole for her loving support and understanding for my work demands. It also should be mentioned that her proof-reading skills had a significant impact on this work. Last but not least, I thank my parents who have taught me many skills, were always there for me and gave me a lot of support even during my years in America.

I am grateful for the support by the Department of Physics at the University of Illinois and by the U.S. Department of Energy through the University of California under Subcontract number B341494.

Contents

List of Tables

List of Figures

Notations

BRW	Brownian random walk,
DE	Direct estimator,
EOS	Equation of state,
FP	Free particle,
MC	Monte Carlo,
PIMC	Path integral Monte Carlo,
PPT	Plasma phase transition,
RPA	Random Phase Approximation,
TE	Thermodynamic estimator,
VDM	Variational density matrix,
a	Wigner-Seitz radius,
a_0	Electron Bohr radius,
$A(s \to s')$	Acceptance probability for MC step $s \to s'$,
β	$1/k_B T$,
D	Spatial dimension, here 3,
d	Amplitude parameter in Gaussian density matrix,
E	Internal energy per atom,
E_i	Internal energy of state i,

E_F	Fermi energy,
F	Free energy,
$g_{ij}(r)$	Pair distribution function of species i and j,
λ	$\hbar^2/2m$,
Λ	Thermal de Broglie wave length $\sqrt{4\pi\lambda\beta}$,
$\mathcal{K}$	Kinetic energy operator,
K	Kinetic energy function,
$\mathbf{k}$	D dimensional reciprocal lattice vector,
k_B	Boltzmann factor,
M	Number of time slices,
$\mathbf{m}$	Position vector in Gaussian density matrix,
n	Number of particles per unit volume, for hydrogen atoms per unit volume,
$\mathbf{n}$	Integer vector in D dimensions,
N	Number of particles,
n_{A}	Order in expansion formula 2.38 used to calculate the pair action,
n_{E}	Order in corresponding expansion formula 2.38 for the energy,
$n(k)$	Momentum distribution,
$n(r)$	One particle reduced density matrix,
$\mathcal{O}$	Operator in quantum mechanics,
p	Pressure,
$P(s \to s')$	Probability for MC step $s \to s'$,
$\mathcal{P}$	Permutation of identical particles,
Q	Electronic charge of one ion,

$\pi(s)$	Probability of state s,
$\|\Psi\rangle$	Hilbert vector,
$\mathbf{r}$	D dimensional coordinate vector,
$\mathbf{R}$	Set of coordinates of N particles in D dimensions,
r_s	density parameter a/a_0,
ρ	Density matrix,
ϱ	Mass density $mN/\hat{V}$,
S	Action in path integral,
s	State in configuration space,
T	Temperature,
T_F	Fermi temperature E_F/k_B,
$T(s \to s')$	Sampling distribution for MC step $s \to s'$,
t	Imaginary time,
τ	Time step in path integrals,
θ	Degeneracy parameter T/T_F,
w	Width parameter in Gaussian density matrix,
$\mathcal{V}$	Potential energy operator,
V	Potential energy,
$\hat{V}$	Volume of the simulation cell L^D,
Z	Canonical partition function.

Chapter 1

Introduction

Hydrogen is the most abundant element in the universe. Its properties are crucial for the evolution of stars and the characteristics of the Jovian planets (Jupiter, Saturn, Uranus, and Neptune). Despite the simple composition, its phase diagram is surprisingly complex and has been the topic of numerous experimental and theoretical approaches. Many of them were devoted to the high-temperature phase diagram, which is the subject of this work. At high temperature ($T > 5000\,\mathrm{K}$), hydrogen is a dense, hot fluid that undergoes considerable structural changes. At low density ($\rho \leq 0.3\,\mathrm{gcm}^{-3}$), one finds a plasma of free electrons and protons, an atomic and a molecular regime, while at high density hydrogen is expected to go into a metallic state. This transition has first been predicted by the pioneering work of Wigner and Huntington (1935) for $T = 0$. Several attempts have been made to observe this transition experimentally. Diamond-anvil measurements (Silvera and Pravica, 1998; Mao and Hemley, 1994) have reached pressure up to 100 GPa at room temperature and shock wave experiments (Da Silva *et al.*, 1997; Collins *et al.*, 1998) achieved up to 390 GPa at much higher temperature ($T \lesssim 10^5\,\mathrm{K}$). To date, no conclusive observation of metallic hydrogen has been made. However, in the gas gun shock wave experiments by Weir *et al.* (1996) reaching 140 GPa at $T < 5000\,\mathrm{K}$, a drop an increase in the conductivity over 4 orders of magnitude has been found, which is an indication that a metallic or nearly metallic state has been reached.

The simplicity of hydrogen also provides an uncluttered problem for theoretical consideration and computational methods. The main challenge lies in the complex interplay of different physical effects. Any theoretical approach must deal with strong coupling, degeneracy effects as well as with bound states. In this work, we apply path integral Monte Carlo simulations (PIMC) (Ceperley, 1995), a first principles simulation technique that describes all the mentioned effects. The main purpose of this work is to provide accurate numerical results for the equilibrium properties of hot, dense hydrogen. This topic has be studied extensively using various form of free energy models (see section 1.4). They inevitably require a number of uncontrolled approximations including fit parameters but have the advantage of low numerical requirements and that additional physical observables can be estimated that are not available in PIMC. With our PIMC simulation, we will provide an accurate equation of state table. One purpose would be that free energy model can be fit to it.

Furthermore, we use our equation of state to calculate the deuterium hugoniot, which can be directly compared to the above mentioned shock wave experiments. Since they provide this first direct measurements in this regime, the comparison is of particular significance to this work and will be discussed in detail in section 4.6.

1.1 The High-Temperature Phase Diagram

At the beginning, we will introduce the standard set of parameters used to describe plasmas and fluids. The degeneracy parameter θ is defined as the ratio of the temperature to Fermi temperature,

$$\theta = T/T_F \qquad \text{with} \qquad E_F \equiv k_B T_F \tag{1.1}$$

where the Fermi temperature is taken from an ideal quantum gas of electrons in two spin states in $D=3$ dimensions,

$$E_F = \lambda\,(3\pi^2 n)^{2/3}, \tag{1.2}$$

where $n = N/\hat{V}$ is the density of N atoms in the volume denoted by $\hat{V}$. Fermionic effects become important at sufficiently low temperature when $\theta \lesssim 1$. The density is often discussed in terms of the parameter

$$r_s = \frac{a}{a_0} \quad , \quad \frac{4}{3}\pi a^3 = n^{-1} \quad , \quad a_0 = \hbar^2/m_e e^2 \quad , \tag{1.3}$$

where a_0 denotes the electron Bohr radius and a the Wigner-Seitz radius. The coupling parameter Γ describes the ratio of potential energy and kinetic energy,

$$\Gamma = \frac{e^2}{4\pi\epsilon_0}\,\frac{1}{a k_B T} \quad . \tag{1.4}$$

Small values of Γ such as $\Gamma \lesssim 0.1$ describe a weakly coupled plasma, in which the Coulomb interaction can be treated as a correction to the dominating kinetic effects. In this limit, the Debye screening model in appendix C gives a reliable description.

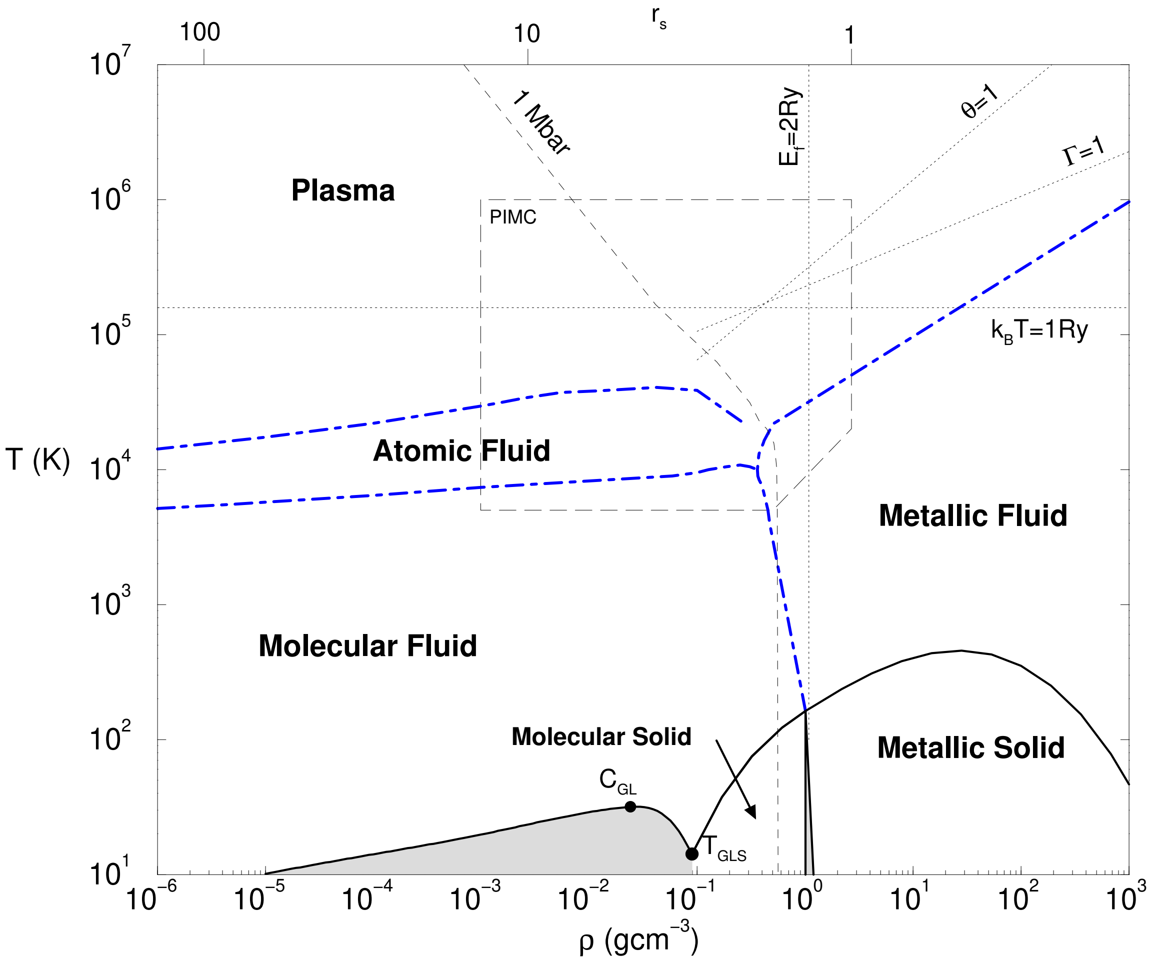

Figure 1.1: Hydrogen phase diagram as function of temperature vs. mass density. The solid lines show phase boundaries belonging to discontinuous transitions while dash-dotted lines represent continuous transitions that were estimated from PIMC simulations. Controversial is the nature of the transition from the molecular to the metallic fluid. The PIMC simulations by Magro *et al.* (1996) have suggested a first order plasma phase transition. At zero temperature, a first order transition from the molecular to the metallic solid has been predicted by Ceperley and Alder (1987). The gas-liquid coexistence region (shaded area) with the critical point C_{GL} and gas-liquid-solid triple point T_{GPL} were taken from Kitamura and Ichimaru (1998).

The hydrogen phase diagram Fig. 1.1 was designed to show the various regimes of hydrogen and discuss the principle physical effects. It should be noted that several regions are not yet well understood e.g. how the high temperature results at 5000 K connect up to the room temperature regime. We used our estimates from PIMC simulations and extrapolated into different directions. In our approach, we do not consider relativistic effects, which become important when the thermal energy or the Fermi energy become of the order of the rest mass energy of the electron, which corresponds to a temperatures of $4 \times 10^9\,\mathrm{K}$ and a density of $1.5 \times 10^3\,\mathrm{gcm}^{-3}$.

In the low density and low temperature region of the phase diagram, hydrogen is composed of neutral species. Molecules dominate at low temperature ($T < 10^4\,\mathrm{K}$), which dissociate into atoms with increasing temperature. If the temperature is increased further atoms become gradually ionized and a plasma of unbound electrons and protons is generated. Above the temperature corresponding to the binding energy of 1 Ry (157 887 K) the probability for the occupation of bound states goes to zero.

Similarly in the limit of very high density, bound states cannot exist because the degeneracy effects dominate. There, delocalized states have a smaller energy than an antisymmetric combination of bound orbitals. This regime is expect to prevail when the Fermi energies become of the order 1 Ry. However, it should noted this represents a extremely simplified calculation and that the precise value probably lies significantly over 1Ry. In the high-density limit, the electrons also form a rigid background and hydrogen behaves like a one-component plasma of ions with neutralizing background. In the phase diagram, we label this state as metallic fluid because the electrons behave like a degenerate Fermi gas and the estimated conductivity is high. The degeneracy also distinguishes this regime from the plasma state. We observed a continuous transition between the two regimes.

In the phase diagram, the region of PIMC simulations from this work combined with earlier ones by Pierleoni *et al.* (1994) and Magro *et al.* (1996) has been indicated. The region is of particular interest because there hydrogen is characterized by strong coupling, a substantial degree of degeneracy, but also by the formation of atom and molecules. It is very difficult to design a chemical model (see section 1.4) that includes all of the mentioned effects in a reliable approximation. In particular the interaction of neutral species with charged particles has been proven to be rather complicated. The advantage of the PIMC technique is that it is a quantum-statistical method, which includes all the mentioned effects just by considering protons and electrons interacting via the Coulomb potential. The method is exact except for requiring a nodal surface in order to deal with the fermion sign problem. In this work, we will derive a variational density matrix (VDM) that allows us to replace free particle nodes by a density matrix that includes interactions and bound states. It was found that the type of nodes begin to have a noticeable effect on the derived thermodynamic quantities for $\theta \lesssim 0.15$.

Furthermore, there are also some practical limitations that put a limit on the applicability of the PIMC method in its current implementation, which originate from the available computational resources. For example, it has been proven to be difficult to go below temperatures of 5000 K because this would require paths with more 200 time slices in order to describe the formation of molecules accurately. Also the fermion nodes can reduce the efficiency for very high values of the degeneracy. Currently we are able to study hydrogen for $\theta \gtrsim 0.034$. For very low density, the MC efficiency is reduced because particles rarely collide. This is also the case for PIMC but this limit has not been reached for $r_s = 14$. The reason why we have not performed simulations at higher temperature or lower density is that analytical models are expected to work very well in the regime of weak coupling.

The phase diagram also shows a region where the four discussed regimes: molecular, atomic, metallic fluid and plasma meet approximately. The region continues to be controversial. Many models have predicted a first-order *plasma phase transition* (PPT) with critical point and coexistence region of two fluids characterized by different degrees of ionization and densities. This existence of a PPT was first mentioned in a phase diagram by Landau and Zeldovich (1943). First calculations have been made by Norman and Starostin (1968) and Ebeling and Sändig (1973). Since then the research community has been divided. A number of different free energy models such as those by (Saumon and Chabrier, 1992; Kitamura and Ichimaru, 1998; Beule *et al.*, 1999) predict a PPT. The exact location of the critical point and the coexistence region differ considerably. Other models show continuous transitions (Ross, 1998).

Also in the PIMC work by Magro *et al.* (1996), a first order phase transition between the molecular to a metallic phase was predicted. These predictions will be critically reviewed in this work. It will be discussed what effect the free particle nodes and the time step have on the nature of the transition.

The gas-liquid coexistence regime with the critical point and gas-liquid-solid triple point were taken from the work by Kitamura and Ichimaru (1998). The first order phase transition from molecular to metallic hydrogen was calculated by Ceperley and Alder (1987). From the work by Ceperley and Alder (1980) it is known that the Wigner crystal of electrons melts at $r_s = 100$. Similarly any solid structure of protons must become unstable if the proton parameter $r_s^{[\mathrm{p}]} = r_s m_\mathrm{p}/m_\mathrm{e}$ reaches 100. That is the reason why the melting line of the metallic solid must decrease with temperature in the limit of high density.

Furthermore, it should noted that there exist different molecular phases in solid hydrogen at about 1 Mbar ($r_s \approx 1.5$), which have been studied intensely using diamond anvil cell experiments (Silvera and Pravica, 1998; Mao and Hemley, 1994) as well as with various simulation methods (Kitamura *et al.*, 2000; Cui *et al.*, 1997; Surh *et al.*, 1997). The phases are labelled I, II and III and correspond to different orderings of the molecules in the crystal. Phase I is characterized by free rotation of the molecules represented by an angular momentum state $J = 0$. In Phase III, the rotational degree of freedom are frozen in and one refers to it as a state of classical orientational ordering. Phase II is believed to be distinguished by the ordering angular momentum states.

1.2 Astrophysical Relevance

Giant planets and brown dwarfs consist of more than 90% hydrogen. The same hydrogen content is found in main sequence stars in the initial phase when they formed by the collapse of hydrogen clouds. Then nuclear reactions reduce the fraction of hydrogen in the process of stellar evolution. The high content of hydrogen is the reason why the high temperature equation of state is relevant for the static properties of these objects and why they enter into models that determine their evolution (Burrows *et al.*, 1997). In these model, one assumes a well mixed state that corresponds to an isentropic change of state from core to surface.

In Fig. 1.2, curves from models for the interior of Jupiter and different stars are shown. The gaseous envelope of Jupiter is dominated by molecules. Further inside, pressure and density are sufficiently high that one can expect to find metallic hydrogen. If there existed a PPT, there would be a critical radius, at which the density is discontinuous. The two phases would have different properties such as the solubility of helium. As a consequence, helium would primarily be concentrated in one of the two phases.

The other curves in Fig. 1.2 represent stars with 0.3, 1, and 15 solar masses ($M_\odot$). The low mass star of $0.3 M_\odot$ exhibits a complex change of properties. Near its core, one finds a moderately degenerate plasma ($\theta = 1$). With increasing radius, the temperature decreases, which increases the coupling and promotes recombination processes. Eventually, all free electrons will be bound in atoms, which leads to a non-degenerate atomic fluid. Near the surface, the temperature will be low enough so that molecules can form, which at some point will become the predominant species.

The sun is hotter and less dense. Near the core, it is weakly coupled and moderately degenerate. The coupling parameter stays approximately constant ($\Gamma \approx 0.1$). Near the surface, the temperature is reduced to about $10^4\,\mathrm{K}$, recombination takes place and atoms are formed.

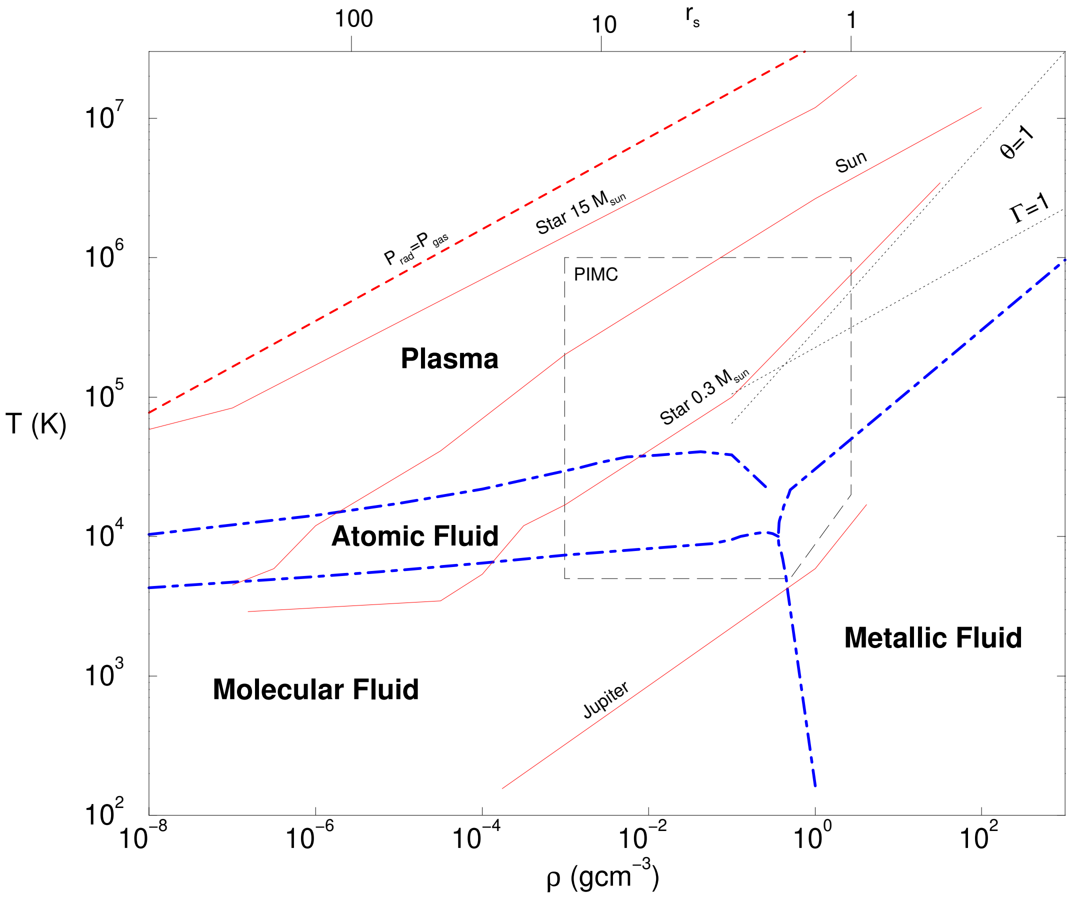

Figure 1.2: Hydrogen phase diagram as displayed in Fig. 1.1 showing the equation of state for different stars and giant planets (Saumon *et al.*, 1995). The dashed line indicates where the radiation pressure equals the gas pressure. The solid lines correspond to Jupiter and stars having 0.3, 1, and 15 times the mass of the sun.

For a more massive star of 15 $M_\odot$, the modeling is simpler because it remains in a weakly coupled and hardly degenerate regime. However, the radiation leads to a significant contribution to the pressure. Brown dwarfs occupy the region between the curves of Jupiter and the $0.3M_\odot$ star.

1.3 Experimental Applications

Figure 1.3 shows different areas of laboratory application of various types of plasmas, which are spread over a large temperature and density interval. For this work, the laser shock wave experiments by Da Silva *et al.* (1997) and Collins *et al.* (1998) are most relevant since they were the first direct measurements of the hydrogen equation of state in the megabar regime. A detailed comparison will be performed in section 4.6. Earlier gas gun experiments by Nellis *et al.* (1983), Holmes *et al.* (1995), and Weir

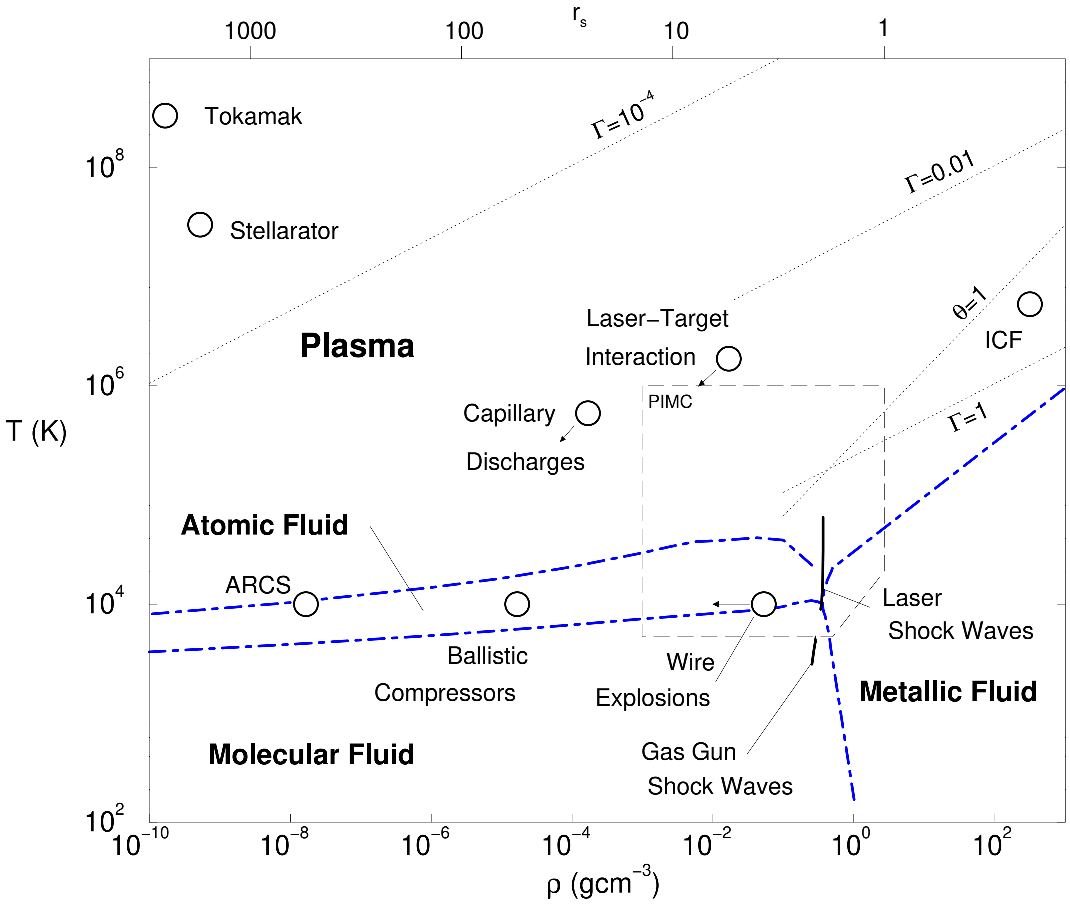

Figure 1.3: Plasma phase diagram as displayed in Fig. 1.1 showing different areas of application of plasmas as suggested by Ebeling *et al.* (1996)

et al. (1996) did not reach temperatures over 5000 K and therefore the comparison is only based on an extrapolation our data. The wire explosion experiments in Fig. 1.3 are only applicable to materials a wire can be made of.

1.4 Free Energy Models

There are two conceptually different approaches to describe hydrogen and related materials. One method is based on the *physical picture* where one treats the fundamental particles, in this case electrons and proton, individually and compound particles such as atoms and molecules are formed if the fundamental particle are bound together. In PIMC, this approach is used, which has the advantage that one can build a simulation from first principles that allows one to describe regimes where one has a mixture of different species without any additional assumptions. However, it should be noted that the computational requirements are orders of magnitude higher than in the chemical models described in the following.

In the *chemical picture*, one assumes different chemical species. For hydrogen one usually considers molecules (H_2), atoms (H), free protons (p), and electrons (e). Other species such as H_2^+, H_2^- or H^- are neglected, because their binding energies are very small compared to the thermal energy. For the chemical species under consideration, one constructs a free energy function with the particle numbers $N_{\mathrm{H_2}}$, N_{H}, N_{p}, and N_{e} as parameters.

$$
\begin{aligned}
F(\hat{V},T,N_{\mathrm{H_2}},N_{\mathrm{H}},N_{\mathrm{p}},N_{\mathrm{e}}) &= F_0^{\mathrm{id}}(\hat{V},T,N_{\mathrm{H_2}},N_{\mathrm{H}}) + F_{\pm}^{\mathrm{id}}(\hat{V},T,N_{\mathrm{p}},N_{\mathrm{e}}) \\
&+ F_0^{\mathrm{int}}(\hat{V},T,N_{\mathrm{H_2}},N_{\mathrm{H}}) + F_{\pm}^{\mathrm{int}}(\hat{V},T,N_{\mathrm{p}},N_{\mathrm{e}}) \\
&+ F^{\mathrm{int}}(\hat{V},T,N_{\mathrm{H_2}},N_{\mathrm{H}},N_{\mathrm{p}},N_{\mathrm{e}}) \quad , \qquad (1.5)
\end{aligned}
$$

where the superscripts *id* and *int* denote the ideal contribution from non-interacting particles and the part caused by the interactions. The interaction terms are derived from known analytical expressions or from computer simulations. The subscripts 0 and $\pm$ refer to neutral and charged. Introduce the total particle number,

$$
N = 2N_{\mathrm{H_2}} + N_{\mathrm{H}} + N_{\mathrm{p}} \qquad \text{with} \qquad N_{\mathrm{p}} = N_{\mathrm{e}} \quad , \qquad (1.6)
$$

one can define the number concentration $x_i = N_i/N$. The free energy is maximized with respect to the chemical composition under fixed external conditions, here temperature and volume. This lead to the condition for chemical equilibrium of dissociation $H_2 \rightleftharpoons 2H$ and ionization $H \rightleftharpoons p + e$:

$$
\left.\frac{\partial \tilde{F}}{\partial x_{\mathrm{H_2}}}\right|_{x_{\mathrm{H}},\hat{V},T,N} = \left.\frac{\partial \tilde{F}}{\partial x_{\mathrm{H}}}\right|_{x_{\mathrm{H_2}},\hat{V},T,N} = 0 \qquad (1.7)
$$

with $\tilde{F}(\hat{V},T,N,x_{\mathrm{H_2}},x_{\mathrm{H}}) = F(\hat{V},T,Nx_{\mathrm{H_2}},Nx_{\mathrm{H}},N_{\mathrm{p}} = N[1-2x_{\mathrm{H_2}}-x_{\mathrm{H}}],N_{\mathrm{e}} = N_{\mathrm{p}})$. In terms of the chemical potentials,

$$
\mu_i = \left.\frac{\partial F}{\partial N_i}\right|_{\hat{V},T,N_{j\neq i}} \qquad (1.8)
$$

chemical equilibrium is obtained from,

$$
\mu_{\mathrm{H_2}} = 2\mu_{\mathrm{H}} \quad , \quad \mu_{\mathrm{H}} = \mu_{\mathrm{p}} + \mu_{\mathrm{e}} \quad . \qquad (1.9)
$$

Chemical models are known to work very well in regimes of weak interaction between the different species. This is usually called the Saha limit because the ideal Saha equation (Fowler and Guggenheim, 1965), which neglects interaction between particles, gives a reasonable approximation. The free energy models currently used to predict properties of hydrogen employ elaborate schemes to determine the interaction terms. Not all of them were constructed to describe the whole high temperature phase diagram as done by Saumon and Chabrier (1992). Ebeling and Richert (1985b) studied the plasma and the atomic regime, while models by Beule *et al.* (1999) and Bunker *et al.* (1997) were designed to the describe the dissociation transition. The Ross (1998) model was primarily developed to study the molecular-metallic transition. One difficulty common to free energy models is how to treat the interaction of charged and neutral particles. Often, this is done by introducing hard-sphere radii and additional corrections. These kinds of approximation lead to rather different predictions from various chemical models. The differences are especially pronounced in the regime of the molecular-metallic transition because of the high density and the presence of neutral and charged species. If the derivative of the free energy function is a continuous function in this region, then no PPT is predicted. If on the other hand the different components in F lead to a discontinuous first derivative, a PPT is inevitably predicted.

One purpose of our PIMC calculation is to provide data so that free energy models can be fitted to it. Those can then be used to derive additional information, which can not be obtained directly from PIMC simulations.

1.5 Computational Methods

In this section, we will give a brief overview of different computational methods used to study hot, dense hydrogen. The first simulations used quasi-classical methods based on effective potential (Hansen, 1973). In recent years a variety of simulation techniques have been developed from first principles, which include density-functional-theory molecular dynamics (Hohl *et al.*, 1993; Kohanoff and Hansen, 1995; Galli *et al.*, 2000; Lenosky *et al.*, 2000) and tight-binding molecular dynamics (Kwon *et al.*, 1994; Collins *et al.*, 1995; Lenosky *et al.*, 1997a,b). The density function theory and the tight-binding approach are used to describe the electron-electron and the electron-proton interactions, while classical dynamics is used for the protons. The PIMC equation of state will be compared with results from these methods. Also wave packet molecular dynamics has been applied to dense hydrogen (Klakow *et al.*, 1994a,b; Ebeling and Militzer, 1997; Nagel *et al.*, 1998). It employs a Hartree-Fock type ansatz for the wave function and time-dependent variational principle to describe its evolution.

Furthermore there is PIMC, which represent an exact quantum-statistical method to determine equilibrium properties, which relies on an approximation for the nodal surfaces in order to deal with the fermion sign problem. It treats protons and electrons quantum-mechanically. A general description of the path-integral formalism can be found in (Feynman, 1972; Schulman, 1981; Kleinert, 1990).

The path integral technique as a numerical method in the form used in this work has been developed in series of works including (Pollock and Ceperley, 1984, 1987). It has been applied to the variety of different bosonic systems including the study of the lambda phase transition in ^{4}He (Ceperley, 1995), hard-sphere bosons (Grüter *et al.*, 1997), the melting transition of molecular hydrogen surfaces (Wagner and Ceperley, 1996), and conditions of superfluidity of molecular hydrogen (Gordillo and Ceperley, 1997). Also a number of fermionic systems have been studied: the crystallization of the one-component plasma Jones and Ceperley (1996), electronic forces on molecules (Zong and Ceperley, 1998) and the electron hole plasma (Shumway and Ceperley, 1999).

First simulations of dense hydrogen have been by Pierleoni *et al.* (1994) and Magro *et al.* (1996). Densities corresponding to $1.0 \lesssim r_s \lesssim 2.2$ have been studied using free particle nodes. In this work, we extend the investigation into the non-degenerate regime up to $r_s = 14$. Then we perform a time step analysis and study finite size effects. Furthermore, a variational density matrix method is developed, which is used to replace the free particle nodes. Using this improved nodal surface we reexamine the PPT predicted by Magro *et al.* (1996). Furthermore, we extended the restricted PIMC method to open paths and calculate the momentum distribution as well as natural orbitals.

1.6 Units

Throughout this work, atomic units of energy and length,

$$\begin{aligned} 1\,\mathrm{Ha} &= 4.359748 \cdot 10^{-18}\,\mathrm{J} \\ 1\,a_0 &= 0.529177 \cdot 10^{-10}\mathrm{m} \quad , \end{aligned}$$

will be used except where explicitly indicated otherwise. Temperatures are given in Kelvin and it is useful to know, $1\,\mathrm{eV}/k_B = 11604.4\,\mathrm{K}$ and $1\,\mathrm{Ha}/k_B = 315\,773\,\mathrm{K}$. It should also be noted that we dropped a factor k_B for simplicity when the time step is specified e.g. $\tau^{-1} = 10^6\,\mathrm{K}$.

1.7 Thesis Overview

Chapter 2 starts with a review of the path integral Monte Carlo method that will be used throughout this work. Chapter 3 introduces a new variational principle in order to derive a variational density matrix that will be employed for a variational calculation of hydrogen and used to construct the nodal surfaces in PIMC. In chapter 4, we present thermodynamic properties including energy, pressure, and pair-correlation functions from PIMC simulation of hydrogen and deuterium. We discuss the high temperature phase diagram including the regime of the hypothetical plasma phase transition. Additionally, a hugoniot function will be derived and compared with recent laser shock wave experiments. Chapter 5 presents the calculation of off-diagonal density matrix elements, which requires the sampling of open paths. After a description on how this method can be applied to fermionic systems, the momentum distribution for the electron gas and for the electrons in hydrogen is discussed, which is followed by an introduction to natural orbitals. Chapter 6 presents the conclusion.

Chapter 2

Path Integral Monte Carlo Method

In this chapter, we will give a review of the PIMC technique (Ceperley, 1995) and discuss all the necessary components required to build fermionic PIMC simulations. Starting from the thermal density, the path integral formalism will be introduced, a pair action method will be derived and the role of permuting paths in bosonic and fermionic systems will be explained. Then, the origin of the fermion sign problem will be discussed as well as the suggested solution based on the nodal surfaces of a trial density matrix (Ceperley, 1991, 1996). Furthermore, a new time step analysis will be presented that studies the effect of the nodal action. Finally the distribution of permutation cycles from recent hydrogen simulations will be shown.

2.1 The Thermal Density Matrix

A quantum mechanical system in a pure state can be described by single wave function $|\Psi\rangle$, which can be expressed in terms of eigenvalues E_i and eigenfunctions $|\Psi_i\rangle$ of the Hamiltonian $\mathcal{H}$. The corresponding density matrix operator is given by,

$$\rho = |\Psi\rangle \langle\Psi| \quad . \tag{2.1}$$

The density matrix provides a convenient way to extend the study to finite temperature. Following the principles of statistical mechanics, one puts the system in contact with a heat bath and assigns classical probabilities p_i to the quantum mechanical states $|\Psi_i\rangle$, which leads to a thermal density matrix,

$$\rho = \sum_i p_i \; |\Psi_i\rangle \langle\Psi_i| \quad . \tag{2.2}$$

In the canonical ensemble at temperature T, the probabilities are proportional to the Boltzmann factor $p_i \propto \exp(-\beta E_i)$, where $k_B T = 1/\beta$. The density matrix now reads,

$$\rho = \sum_i e^{-\beta E_i} \, |\Psi_i\rangle \langle \Psi_i| = e^{-\beta \mathcal{H}} \quad . \tag{2.3}$$

The expectation of any operator $\mathcal{O}$ is given by,

$$\langle \mathcal{O} \rangle = \frac{\mathrm{Tr}\,[\mathcal{O}\rho]}{\mathrm{Tr}\,\rho} = \frac{1}{Z} \sum_i e^{-\beta E_i} \, \langle \Psi_i | \, \mathcal{O} \, | \Psi_i \rangle \tag{2.4}$$

and the canonical partition function is $Z = \sum_i e^{-\beta E_i}$. For sake of numerical simulations, it is convenient to change to a position-space representation. Introducing the set of coordinates for a system of N particles in D dimensions $\mathbf{R} = \{\mathbf{r}_1 \ldots \mathbf{r}_N\}$, the density matrix becomes,

$$\rho(\mathbf{R}, \mathbf{R}'; \beta) = \langle \mathbf{R} | \, e^{-\beta \mathcal{H}} \, | \mathbf{R}' \rangle = \sum_i e^{-\beta E_i} \, \Psi_i^*(\mathbf{R}) \, \Psi_i(\mathbf{R}') \quad . \tag{2.5}$$

For any hermitian Hamiltonian $\mathcal{H}$ the density matrix is symmetric in its two arguments,

$$\rho(\mathbf{R}, \mathbf{R}'; \beta) = \rho(\mathbf{R}', \mathbf{R}; \beta) \quad . \tag{2.6}$$

The expectation value is given by,

$$\langle \mathcal{O} \rangle = \frac{1}{Z} \int \mathbf{dR} \, \mathbf{dR}' \; \rho(\mathbf{R}, \mathbf{R}'; \beta) \; \langle \mathbf{R}' | \, \mathcal{O} \, | \mathbf{R} \rangle \tag{2.7}$$

$$Z = \int \mathbf{dR} \; \rho(\mathbf{R}, \mathbf{R}; \beta) \quad . \tag{2.8}$$

For a free particle in a periodically repeated box of size L and volume $\hat{\mathcal{V}} = L^D$, the density matrix can derived from the exact eigenfunctions of the Hamiltonian given by plane waves,

$$\Psi_{\mathbf{n}}(\mathbf{r}) = \frac{1}{\sqrt{\hat{\mathcal{V}}}} \, e^{-i\,\mathbf{k_n r}} \tag{2.9}$$

with k-vector $\mathbf{k_n} = 2\pi\mathbf{n}/L$, where $\mathbf{n}$ is a D-dimensional integer vector. Hence,

$$\rho(\mathbf{r}, \mathbf{r}'; \beta) = \frac{1}{\hat{\mathcal{V}}} \sum_{\mathbf{n}} \exp\{-\beta\lambda \mathbf{k}_{\mathbf{n}}^2 + i\,\mathbf{k_n}(\mathbf{r} - \mathbf{r}')\} \tag{2.10}$$

$$= (4\pi\lambda\beta)^{-D/2} \sum_{\mathbf{n}} \exp\left\{ -\frac{(\mathbf{r} - \mathbf{r}' - \mathbf{nL})^2}{4\lambda\beta} \right\} \tag{2.11}$$

$$\approx (4\pi\lambda\beta)^{-D/2} \exp\left\{ -\frac{(\mathbf{r} - \mathbf{r}')^2}{4\lambda\beta} \right\} \quad \text{if} \quad \lambda\beta \ll L^2 \quad , \tag{2.12}$$

where $\lambda = \hbar^2/2m$ for a particle of mass m. Alternatively, this solution can be derived from the Bloch equation,

$$\frac{\partial \rho}{\partial \beta} = \mathcal{H}\rho \quad , \tag{2.13}$$

which is a diffusion equation in imaginary time β. The initial condition is provided by the known high temperature limit,

$$\rho(\mathbf{R}, \mathbf{R}'; 0) = \delta(\mathbf{R} - \mathbf{R}') \quad . \tag{2.14}$$

For free particles, the Bloch equation simply reads,

$$\frac{\partial \rho}{\partial \beta} = -\lambda \Delta \rho \quad . \tag{2.15}$$

The Δ operator can be applied either to the first or to the second argument in $\rho(\mathbf{r}, \mathbf{r}'; \beta)$. In any case, this equation describes the diffusion of paths in imaginary time. The exact solution is given by Eq. 2.11. The diffusion constant λ is determined by the mass of the particle. It is large for light particles leading to a fast diffusion in imaginary time, and small for heavy and therefore classical particles. The width of the density matrix is given by $\sqrt{4\lambda\beta}$, which is related to the frequently used thermal de Broglie wave length defined as,

$$\Lambda = \frac{h}{\sqrt{2\pi m k_B T}} \equiv \sqrt{4\pi\lambda\beta} \quad . \tag{2.16}$$

If this length reaches the order of the inter-particle spacing, many body quantum effects become important. This relation is usually discussed in terms of the degeneracy parameter,

$$n\Lambda^D \quad , \tag{2.17}$$

which relates the volume per particle $\hat{V}/N \equiv n^{-1}$ to the volume occupied by an individual path Λ^D. This parameter defines a temperature scale for the emergence of quantum statistical effects such as Bose condensation in Bosonic systems and the formation of a Fermi surface in Fermion systems. The latter process will be discussed in detail in sections 2.6 and 5.3.

2.2 Imaginary Time Path Integrals

The underlying principle for the introduction of path integrals in imaginary time is the product property of the density matrix stating that the low temperature density matrix can be expressed as a product of high temperature matrices. In operator notation this reads,

$$e^{-\beta\mathcal{H}} = \left(e^{-\tau\mathcal{H}}\right)^M , \tag{2.18}$$

where the *time step* is $\tau = \beta/M$. In position space this becomes a convolution, in which one has to integrate over all intermediate time slices,

$$\rho(\mathbf{R},\mathbf{R}';\beta) = \int\ldots\int \mathbf{dR}_1\,\mathbf{dR}_2\,\ldots\,\mathbf{dR}_{M-1}\,\rho(\mathbf{R},\mathbf{R}_1;\tau)\,\rho(\mathbf{R}_1,\mathbf{R}_2;\tau)\ldots\rho(\mathbf{R}_{M-1},\mathbf{R}';\tau). \tag{2.19}$$

This is called a path integral in imaginary time. The expression is exact for any $M \geq 1$. In the limit $M \to \infty$, it becomes a continuous paths beginning at $\mathbf{R}$ and ending at $\mathbf{R}'$.

The reason for using a path integral is in the limit of high temperature, the density matrix can be calculated. Usually the Hamiltonian can be split in a kinetic and in a potential part, $\mathcal{H} = \mathcal{K} + \mathcal{V}$ and the density matrix can expressed using the following operator identity (Raedt and Raedt, 1983),

$$e^{-\tau(\mathcal{K}+\mathcal{V})} = e^{-\tau\mathcal{K}}e^{-\tau\mathcal{V}}e^{-\tau^2 C_2}e^{-\tau^3 C_3} + O(\tau^4) \quad , \tag{2.20}$$

where

$$C_2 = [A,B]/2 \quad , \tag{2.21}$$

and

$$C_3 = [[B,A], A+2B]/6 \qquad . \tag{2.22}$$

In the limit of $\tau \to 0$, one can neglect the commutators, which are of higher order in τ. This is known as the *primitive approximation*,

$$e^{-\tau(\mathcal{K}+\mathcal{V})} \approx e^{-\tau\mathcal{K}}e^{-\tau\mathcal{V}} \quad . \tag{2.23}$$

It states that in the limit of $M \to \infty$, the density matrix can be written as product of a potential and kinetic density matrix. This has been shown by Trotter (1959),

$$e^{-\beta(\mathcal{K}+\mathcal{V})} = \lim_{M\to\infty}\left(e^{-\frac{\beta}{M}\mathcal{K}}\,e^{-\frac{\beta}{M}\mathcal{V}}\right)^M . \tag{2.24}$$

The density matrix for a system of N particles in the primitive approximation is given by,

$$\begin{aligned}\rho(\mathbf{R}_0,\mathbf{R}_M,\beta) \;&=\; \int\ldots\int \mathbf{dR}_1\,\mathbf{dR}_2\,\ldots\,\mathbf{dR}_{M-1}\,(4\pi\lambda\tau)^{DNM/2} \\ &\times \exp\left\{-\sum_{i=1}^{M}\left[\frac{(\mathbf{R}_{i-1}-\mathbf{R}_i)^2}{4\lambda\tau} + \frac{\tau}{2}\left(V(\mathbf{R}_{i-1})+V(\mathbf{R}_i)\right)\right]\right\}. \end{aligned} \tag{2.25}$$

In the path integral formalism this is written as,

$$\rho(\mathbf{R},\mathbf{R}';\beta) = \int\limits_{\mathbf{R}\to\mathbf{R}'} \mathbf{dR}_t \;\; e^{-S[\mathbf{R}_t]} \quad , \tag{2.26}$$

where $S[\mathbf{R}_t]$ is the *action* of the path. Alternatively, one separates the kinetic and potential parts,

$$\begin{aligned}\rho(\mathbf{R}_0,\mathbf{R}_M,\beta) \;\; = \;\; & \int \ldots \int \mathbf{dR}_1\,\mathbf{dR}_2\,\ldots\,\mathbf{dR}_{M-1} \\ & \langle \mathbf{R}_0 |\, e^{-\tau\mathcal{K}}\, |\mathbf{R}_1\rangle \ldots \langle \mathbf{R}_{M-1} |\, e^{-\tau\mathcal{K}}\, |\mathbf{R}_M\rangle \exp\left\{ -\tau \sum_{i=1}^{M} V(\mathbf{R}_i) \right\} \; .\end{aligned}$$

The free particle terms act like a weight over all Brownian random walks (BRW) in imaginary time β starting at $\mathbf{R}_0$ and ending at $\mathbf{R}_M$. In the limit of $M \to \infty$, this leads to the Feynman-Kac relation

$$\rho(\mathbf{R},\mathbf{R}',\beta) = \rho_0(\mathbf{R},\mathbf{R}',\beta) \;\left\langle e^{-\int_0^\beta dt\; V(\mathbf{R}(t))} \right\rangle_{\mathrm{BRW}} \quad . \tag{2.27}$$

In the *semi-classical approximation*, one considers only the classical path,

$$\mathbf{R}_{\mathrm{sc}}(t) = \left(1 - \frac{t}{\beta}\right)\mathbf{R} + \frac{t}{\beta}\,\mathbf{R}' \quad , \tag{2.28}$$

instead of integrating over all BRW. The resulting semi-classical density matrix reads,

$$\rho_{\mathrm{sc}}(\mathbf{R},\mathbf{R}',\beta) = \rho_0(\mathbf{R},\mathbf{R}',\beta)\; e^{-\int_0^\beta dt\; V(\mathbf{R}_{\mathrm{sc}}(t))} \quad . \tag{2.29}$$

Already, the primitive approximation is a sufficient basis for a path integral Monte Carlo simulation. However, the required number of time slices to reach accurate results would be enormous. The following sections, we discuss methods to derive a more accurate high temperature density matrix in order to reduce the number of slices to a computationally feasible level. A pair action will be derived, which contains the exact solution of the two particle problem. This means only one time slice is required for a simulation of two particles at any temperature. However, in many particle systems, a path integral is needed because of many-particle effects and the fermion nodes, which will be discussed in section 2.6.

2.3 Pair Density Matrix

For the systems under study, the interactions consist of pairwise additive potentials, $V(\mathbf{R}) = \sum_{i<j} V_{ij}(\mathbf{r}_i - \mathbf{r}_j)$. The full density matrix given by the Feynman-Kac relation,

$$\left\langle e^{-\int_0^\tau dt\; V(\mathbf{R}(t))} \right\rangle_{\mathrm{BRW}} = \left\langle \prod_{i<j} e^{-\int_0^\tau dt\; V_{ij}(\mathbf{r}_{ij}(t))} \right\rangle_{\mathrm{BRW}} \quad , \tag{2.30}$$

which, in the limit of sufficiently small τ, can by approximated by a product of pair density matrices

$$\left\langle e^{-\int_0^\tau dt\, V(\mathbf{R}(t))} \right\rangle_{\mathrm{BRW}_\mathbf{R}} \approx \prod_{i<j} \left\langle e^{-\int_0^\tau dt\, V_{ij}(\mathbf{r}_{ij}(t))} \right\rangle_{\mathrm{BRW}_{\mathbf{r}_{ij}}} \quad . \tag{2.31}$$

This is known as the *pair approximation.* It means that the correlation of two particles becomes independent of other particles within a sufficiently small time interval. The derivation of the pair density matrix will be discussed in the remaining part of this section.

Electrons and protons interact via the Coulomb potential. For the two particle problem, the eigenfunctions of the Hamiltonian can be expressed in terms of special functions and the pair density matrix can be calculated by performing the sum over all states (Pollock, 1988). However, the states are only known analytically in an infinite volume. For the purpose of a simulation in a periodic cell, the Coulomb potential is broken up into a short range part in real space and a long range part in k-space using an optimized Ewald break-up (Ewald, 1917) developed by (Natoli and Ceperley, 1995). For both parts separately, a pair action will be derived as discussed in the following sections. It should be noted that the break up of the potential is an approximation, which is made in order to calculate the pair density matrix corresponding to a long-range pair potential in a periodic system. Ideally, one would calculate the full action and then perform an Ewald break-up.

2.3.1 Short Range Action

The exact pair density matrix for any interaction potential in infinite volume can be calculated by the matrix squaring technique by Storer (1968). This method is applied to the short-range part generated by the Ewald break-up of the Coulomb potential. Since the potential is short range the periodicity is irrelevant. First, one factorizes the density matrix into a center-of-mass term and a term depending on the relative coordinates. The latter term is equivalent to the density matrix for a particle with the reduced mass $\mu^{-1} = m_1^{-1} + m_2^{-1}$ in an external potential. The one expands the pair density matrix in partial waves. In $D = 3$ dimensions, it reads,

$$\rho(\mathbf{r}, \mathbf{r}'; \tau) = \frac{1}{4\pi r r'} \sum_{l=0}^{\infty} (2l+1)\; \rho_l(r, r'; \tau)\; \mathrm{P}_l(\cos\theta) \quad , \tag{2.32}$$

where θ is the angle between $\mathbf{r}$ and $\mathbf{r}'$ and P_l denotes the lth Legendre polynomial. For spherically symmetric interaction potentials, different partial wave components

ρ_l do not mix and can be derived from independent matrix squaring procedures. The six dimensional pair density matrix is reduced to a sum of two dimensional objects. Each component ρ_l satisfies a 1 dimensional Bloch equation with an additional term,

$$-\frac{\partial \rho_l(r,r';\beta)}{\partial \beta} = \left[-\lambda \frac{d^2}{dr^2} + v(r) + \frac{\lambda}{r^2}\, l(l+1)\right] \rho_l(r,r';\beta) \tag{2.33}$$

and also fulfills the convolution equation,

$$\rho_l(r,r';\beta) = \int_0^\infty dr''\; \rho_l(r,r'';\beta/2)\; \rho_l(r'',r';\beta/2) \quad . \tag{2.34}$$

This is a one dimensional integral for a given pair of r and r', which can be calculated numerically. In order to derive the pair density matrix for a time step $\tau^{-1} = 10^6\,\mathrm{K}$, one typically performs of the order of $m = 12$ matrix squarings starting at the inverse temperature $\tau_0^{-1} = 2^m \times 10^6\,\mathrm{K}$. The partial waves are initialized using semi-classical expression analogous to Eq. 2.29, for details see Ceperley (1995) and Magro (1996). The resulting pair density matrix can be verified by using the Feynman-Kac formula Eq. 2.27 in a separate MC simulation (Pollock and Ceperley, 1984).

The pair density matrix is between two particles at initial position $(\mathbf{r}_i, \mathbf{r}_j)$ and final position $(\mathbf{r}'_i, \mathbf{r}'_j)$ needs to be evaluated very frequently in a PIMC simulation. Using the fact that initial and final position cannot be too far apart, one can expand the action in a power series. It is convenient to use the three distance

$$\begin{aligned} q &= \frac{1}{2}(|\mathbf{r}| + |\mathbf{r}'|) && (2.35)\\ s &= |\mathbf{r} - \mathbf{r}'| && (2.36)\\ z &= |\mathbf{r}| - |\mathbf{r}'|, && (2.37) \end{aligned}$$

where $\mathbf{r} = \mathbf{r}_i - \mathbf{r}_j$ and $\mathbf{r}' = \mathbf{r}'_i - \mathbf{r}'_j$. The variables s and z are of the order of $\sqrt{\lambda\tau}$. The action can then be expanded as,

$$u(\mathbf{r},\mathbf{r}';\tau) = \frac{1}{2}\left[u_0(r;\tau) + u_0(r';\tau)\right] + \sum_{k=1}^{n_\mathrm{A}} \sum_{j=0}^{k} u_{kj}(q;\tau)\, z^{2j}\, s^{2(k-j)} \quad . \tag{2.38}$$

where n_A denotes the order of the expansion. In zeroth order, only the first term, the end-point action, is considered. The following terms are *off-diagonal* contributions, which are important because they allow to reduce the number of time slices in a PIMC simulation. The same expansion formula is used for the contributions to the energy given by β derivative of the action. n_E denotes the order in this expansion.

2.3.2 Long Range Action

The long range part of the potential leads to long range action. As a first step, it can be calculated from the primitive approximations as used in (Shumway, 1999). Alternatively, one can use the random phase approximation (RPA) (Pines and Nozieres, 1989) to obtain an improved long range action (for details see (Magro, 1996)), which is constructed in such a way that the *local energy* is minimized,

$$E_L = \frac{1}{\rho}\left(\frac{\partial \rho}{\partial \beta} + \mathcal{H}\rho\right) \quad . \tag{2.39}$$

E_L vanishes for a solution of the Bloch equation 2.13. One assumes a given short range density matrix ρ_s, which solves the Bloch equation for the Hamiltonian $\mathcal{H}_s = -\lambda\nabla^2 + V_s$. For the full Hamiltonian $\mathcal{H} = \mathcal{H}_s + V_l$ with the additional potential V_l, one derives a long range density matrix ρ_l such that the density matrix $\rho_l\rho_s$ leads to $E_L = 0$. One writes the long range potential V_l and action e^{-U_l} in the form,

$$V_l(\mathbf{R}) = \sum_{\mathbf{k}}\sum_{\alpha\beta} v_k^{\alpha\beta} \sum_{\substack{i\in \mathrm{T}(\alpha)\\ j\in \mathrm{T}(\beta)}} e^{i\mathbf{k}(\mathbf{r}_i-\mathbf{r}_j)} \tag{2.40}$$

$$= \sum_{\mathbf{k}} v_k^{\alpha\beta}\, \rho_{\mathbf{k}}^{\alpha}\, \rho_{-\mathbf{k}}^{\beta} \quad , \tag{2.41}$$

$$U_l(\mathbf{R}) = \sum_{\mathbf{k}} u_k^{\alpha\beta}\, \rho_{\mathbf{k}}^{\alpha}\, \rho_{-\mathbf{k}}^{\beta} \quad , \tag{2.42}$$

$$\rho_{\mathbf{k}}^{\alpha} = \sum_{j\in \mathrm{T}(\alpha)} e^{i\mathbf{k}\mathbf{r}_j} \quad , \tag{2.43}$$

where $v_k^{\alpha\beta}$ is the Fourier transform of the potential between particle of type α and β denoted by $\mathrm{T}(\alpha)$ and $\mathrm{T}(\beta)$. Setting $E_L = 0$, leads to three body terms, which are approximated by the RPA. The resulting first order differential equations, which are integrated numerically in imaginary time from 0 to β with the initial condition $u_k = 0$. The calculated coefficients u_k^{ij} then enter PIMC simulations as long range action in form of Eq. 2.42.

2.4 Path Integrals for Fermions and Bosons

According to the spin-statistics theorem, fermion systems are described by totally antisymmetric wave functions and bosonic systems by symmetric ones. In other words, the wave functions must be antisymmetric/symmetric under the exchange of two identical particles,

$$\Psi_{\mathrm{B/F}}(\mathbf{R}) = (\pm 1)^{\mathcal{P}}\; \Psi_{\mathrm{B/F}}(\mathcal{P}\mathbf{R}) \quad , \tag{2.44}$$

where $\mathcal{P}$ stands for any of the $N!$ permutations of the particle label in the many-body coordinate R. In systems with additional internal degrees of freedom such as spin, the permutation is applied to those as well. The + sign corresponds bosonic systems (B) and the − sign to fermionic systems (F). This symmetry property can be realized by applying an antisymmetrization/symmetrization operator to a wave function for distinguishable particles $\Psi_D(\mathbf{R})$,

$$\Psi_{\mathrm{B/F}}(\mathbf{R}) = \frac{1}{N!} \sum_{\mathcal{P}} (\pm 1)^{\mathcal{P}} \; \Psi_{\mathrm{D}}(\mathcal{P}\mathbf{R}) \quad . \tag{2.45}$$

The density matrix for a fermion/bosonic system is constructed from these states and can be written as,

$$\rho_{\mathrm{B/F}}(\mathbf{R},\mathbf{R}';\beta) = \frac{1}{N!} \sum_{\mathcal{P}} (\pm 1)^{\mathcal{P}} \; \rho_{\mathrm{D}}(\mathbf{R},\mathcal{P}\mathbf{R}';\beta) \quad . \tag{2.46}$$

One can (anti)symmetrize with respect to the first or second argument or both. All three ways are equivalent and lead to the same physical observables. The (anti)symmetry enters into the path integral formalism as a sum over all $N!$ permutations. In addition to the integral over all configurations of paths, one has to sum over possible permutations of final set of coordinates $\mathbf{R}'$. Eq. 2.19 then reads,

$$\begin{aligned}
\rho_{\mathrm{B/F}}(\mathbf{R},\mathbf{R}';\beta) &= \frac{1}{N!} \sum_{\mathcal{P}} (\pm 1)^{\mathcal{P}} \int \!\ldots\! \int \mathbf{dR}_1 \, \mathbf{dR}_2 \, \ldots \, \mathbf{dR}_{M-1} \\
&\qquad \rho_{\mathrm{D}}(\mathbf{R},\mathbf{R}_1;\tau)\, \rho_{\mathrm{D}}(\mathbf{R}_1,\mathbf{R}_2;\tau) \ldots \rho_{\mathrm{D}}(\mathbf{R}_{M-1},\mathcal{P}\mathbf{R}';\tau) & (2.47) \\
&= \frac{1}{N!} \sum_{\mathcal{P}} (\pm 1)^{\mathcal{P}} \int\limits_{\mathbf{R}\to\mathcal{P}\mathbf{R}'} \mathbf{dR}_t \;\; e^{-S[\mathbf{R}_t]} \quad . & (2.48)
\end{aligned}$$

The $\beta \to 0$ limit from Eq. 2.14 now becomes,

$$\rho_{\mathrm{B/F}}(\mathbf{R},\mathbf{R}';0) = \frac{1}{N!} \sum_{\mathcal{P}} (\pm 1)^{\mathcal{P}} \; \delta(\mathbf{R} - \mathcal{P}\mathbf{R}') \quad . \tag{2.49}$$

In most applications, one uses the path integrals to calculate averages from Eq. 2.7. There one needs the trace of the density matrix, which means one sums up all *closed* paths (for sampling with open paths see chapter 5). For distinguishable particles, they start at any $\mathbf{R}$ and return to it. For fermions and bosons one also sums over paths that return to a permuted set of coordinates given by $\mathcal{P}\mathbf{R}$. Those contributions become relevant if the degeneracy parameter (Eq. 2.17) is the order of 1 or greater.

The path integral technique has been applied extensively to bosonic systems in particular to liquid ^{4}He (Ceperley, 1995; Grüter *et al.*, 1997). It is an *exact* method because all permutations carry the same sign and one does not have to deal with cancellation effects of positive and negative contributions as in fermionic systems. Those will be discussed in section 2.6. We call a method exact (see (Ceperley, 1996)), if it only contains approximations, which can be controlled by an adjustable parameter, and therefore converges to the exact numerical results with increasing accuracy.

2.5 Monte Carlo Sampling

2.5.1 Metropolis Monte Carlo

Most path integral calculations work with a Metropolis rejection algorithm (Metropolis *et al.*, 1953), in which a Markov process is constructed in order to generate a random walk through state space, $\{s_0, s_1, s_2, \ldots\}$. A transition rule $P(s \to s')$ depending on the initial state s and the final state s' is exploited to step from s_i to s_{i+1}, which is chosen in such a way that the distribution of $\{s_n\}$ converges to a given distribution $\pi(s)$. If the transition rule is ergodic and fulfills the *detailed balance*

$$\pi(s)\, P(s \to s') = \pi(s')\, P(s' \to s), \tag{2.50}$$

then the probability distribution converges to an equilibrium state satisfying,

$$\sum_s \pi(s)\, P(s \to s') = \pi(s') \quad . \tag{2.51}$$

The transition probability $P(s \to s')$ can be split into two parts, the sampling distribution $T(s \to s')$ that determines how the next trial state s' is selected in state s and the acceptance probability $A(s \to s')$ for the particular step,

$$P(s \to s') = T(s \to s')\, A(s \to s') \quad . \tag{2.52}$$

The detailed balance can be satisfied by choosing $A(s \to s')$ to be,

$$A(s \to s') = \min\left\{ 1\,,\, \frac{T(s' \to s)\,\pi(s')}{T(s \to s')\,\pi(s)} \right\} \quad . \tag{2.53}$$

One starts the MC process at any arbitrary state s. Most likely this state has only a very small probability because in thermodynamic system, $\pi(s)$ is a sharply peaked function that usually spans many orders of magnitude. Therefore, it would be over-represented in averages calculated from,

$$\langle \mathcal{O} \rangle = \frac{1}{m} \sum_{i=1}^{m} \mathcal{O}(s_i) \quad . \tag{2.54}$$

In the averages, one notices a transient behavior that eventually reaches a regime, where it fluctuates around a steady mean. From approximately that point on, one starts to collect statistics. For *uncorrelated* measurements, the estimator for the standard deviation σ and the error bars ϵ can be determined from

$$\sigma_{\mathcal{O}}^2 = \frac{1}{m-1}\sum_{i=1}^{m}(\mathcal{O}_i - \langle\mathcal{O}\rangle)^2 \quad , \tag{2.55}$$

$$\epsilon_{\mathcal{O}} = \frac{\sigma_{\mathcal{O}}}{\sqrt{m}} \quad . \tag{2.56}$$

However, in most MC simulations the events are correlated because one only moves a small fraction of the particles at a time. The *correlation time* κ can be shown to be estimated by

$$\kappa_{\mathcal{O}} = 1 + \frac{2}{\sigma_{\mathcal{O}}^2(m-1)}\sum_{k=1}^{m-1}\sum_{i=1}^{m}\left(\mathcal{O}_i - \langle\mathcal{O}\rangle\right)\left(\mathcal{O}_{i+k} - \langle\mathcal{O}\rangle\right) \quad . \tag{2.57}$$

The true statistical error considering correlations is given by

$$\epsilon_{\mathcal{O}}\sqrt{\kappa_{\mathcal{O}}} \quad . \tag{2.58}$$

Alternatively, it can be obtained from a *blocking analysis*. There, one averages over 2^m events $\mathcal{O}_i$ before calculating the error bar from Eq. 2.56. This error will grow as a function of m and eventually converge when the interval 2^m is long enough that the averages can be considered to be statistically independent. It should be noted that there can be different reasons for correlations in MC simulations that can occur on different time scales. In certain cases, it becomes difficult to estimate the correlation time from Eq. 2.55 because of long correlations that can only be determine accurately from very long series of simulations data.

The aim of an efficient MC procedure is to decrease the error bars as rapidly as possible for given computer time. The efficiency is defined by,

$$\frac{1}{\kappa_{\mathcal{O}}\sigma_{\mathcal{O}}^2 T_s} \quad , \tag{2.59}$$

where T_s is the computer time per step.

For certain applications, the sampling distribution $\pi(s)$ leads to error bars for a subset of observables that are too large. A typical example in classical MC is the pair correlation function $g(r)$ at small distances. In those cases, *importance sampling* can be applied. One employs an importance function $f(s)$ to generate a Markov chain according to modified distribution

$$\tilde{\pi}(s) = \pi(s)f(s) \tag{2.60}$$

rather than to $\pi(s)$. In the end, one divides it out and calculates averages from

$$\langle \mathcal{O} \rangle = \sum_{i=1}^{m} \frac{\mathcal{O}(s_i)}{f(s_i)} \Bigg/ \sum_{i=1}^{m} \frac{1}{f(s_i)} \quad . \tag{2.61}$$

This method will be applied to the sampling with open paths in chapter 5. It works well as long as the modifications to the sampling distribution are not too disruptive. Otherwise, the variance $\sigma_{\mathcal{O}}$ grows or even becomes infinite. A sufficient condition for the applicability is that $\langle \mathcal{O}^2 \rangle$ stays finite.

2.5.2 Single Slice Moves

In classical MC, the particles are represented by points in D dimensional space, which are moved in every MC step. Most simply, one can choose the displacement of particles according to a uniform distribution. In PIMC, particles are represented by path and the equivalent moves would shift the entire polymer to a new position without changing its internal structure. We call this *displacement moves* and use them for the protons because their paths stay very localized. They are more efficient than single or multi-slice moves discussed in the following.

In a single slice move, one selects a particle and a time slice i and samples a new configuration $\mathbf{r}'_i$ while keeping $\mathbf{r}_{i-1}$ and $\mathbf{r}_{i+1}$ fixed. From now on, the subscript denotes the time slice. The optimal choice for the sampling distribution of $\mathbf{r}_i$ is given by the *heat bath* rule, which will be described in section 2.5.4. It states that the new coordinate should by chosen according to its equilibrium distribution,

$$T(\mathbf{r}_i \to \mathbf{r}'_i) \equiv T(\mathbf{r}'_i) = \frac{\rho(\mathbf{r}_{i-1}, \mathbf{r}'_i; \tau)\, \rho(\mathbf{r}'_i, \mathbf{r}_{i+1}; \tau)}{\int \mathbf{dr}\, \rho(\mathbf{r}_{i-1}, \mathbf{r}; \tau)\, \rho(\mathbf{r}, \mathbf{r}_{i+1}; \tau)} = \frac{\rho(\mathbf{r}_{i-1}, \mathbf{r}'_i; \tau)\, \rho(\mathbf{r}'_i, \mathbf{r}_{i+1}; \tau)}{\rho(\mathbf{r}_{i-1}, \mathbf{r}'_{i+1}; 2\tau)} \, . \tag{2.62}$$

Unlike lattice MC methods, the normalization is difficult to compute, which is why one uses the distribution of non-interacting particles, which is a Gaussian centered around the midpoint $\mathbf{r}_{\mathrm{m}} = (\mathbf{r}_{i-1} + \mathbf{r}_{i+1})/2$,

$$T(\mathbf{r}_i) = (2\pi\lambda\tau)^{-D/2} \exp\left\{ -\frac{(\mathbf{r}_i - \mathbf{r}_{\mathrm{m}})^2}{2\lambda\tau} \right\} \quad . \tag{2.63}$$

We call this implementation *free particle sampling.* For non-interacting particles, this leads to an acceptance ratio of 100% but interactions reduce this ratio. For very dense systems, like liquid ^{4}He, which interacts approximately via a hard-sphere potential, it can become close to zero. For all hydrogen applications, the free particle sampling worked very well.

2.5.3 Multilevel Moves

One notices that the average displacement in a single slice move is of order $\sqrt{\tau\lambda}$, which means that the diffusion through phase space goes to zero for small time steps. This is clearly an unwanted effect in particular because one would like to have an algorithm that is almost independent of the time step. This can be done by introducing *multi-slice moves*. Instead of moving one bead one cuts out and regrows a whole section of the path containing $2^k - 1$ slices. The number k is called the *level* of the move. Different methods have been suggested to regrow the path such as *Lévy flights* (Lévy, 1939) or the *bisection* method. The latter method will be described here using free particle sampling. The distribution in Eq. 2.63 for any level k reads,

$$T_k(\mathbf{r}) = (2^k \lambda\tau\pi)^{-D/2} \exp\left\{ -\frac{(\mathbf{r}-\mathbf{r}_\mathrm{m})^2}{2^k\lambda\tau} \right\} \quad . \tag{2.64}$$

First, one samples the bead $\mathbf{r}_i$ at slice $i + 2^{k-1}$ from a Gaussian distribution T_k centered at the midpoint of $\mathbf{r}_i$ and $\mathbf{r}_{i+2^k}$. As a second step with $k \to k-1$, one samples the slices corresponding to the next lower level $i+2^{k-1}$ and $i+3*2^{k-1}$ using the new T_k and then keeps filling in the new coordinates until level $k=1$ is reached and a complete set of trial coordinates has been created. Finally, one performs one Metropolis step on the entire move.

The efficiency of this method can be improved by a *multilevel Metropolis method*. It rejects certain unlikely paths at an earlier level instead of waiting until the end and then using a single metropolis step. One starts at the highest level k, samples beads according to T_k, and accepts with

$$A(s_k \to s_k') = \min\left\{ 1\,,\, \frac{T_k(s_k' \to s_k)\,\pi_k(s_k')}{T_k(s_k \to s_k')\,\pi_k(s_k)} \right\} \quad . \tag{2.65}$$

Note that the sampling distribution T_k as well as the probability function π_k are derived from the density matrix corresponding to the time step $2^k\tau$. If the move is rejected one starts again from the beginning. Otherwise, one continues at the next lower level $k \to k-1$ and samples all the midpoints according to the new T_k and uses a modified acceptance probability,

$$A(s_k \to s_k') = \min\left\{ 1\,,\, \frac{T_k(s_k' \to s_k)\,\pi_k(s_k')\,\pi_{k+1}(s_k)}{T_k(s_k \to s_k')\,\pi_k(s_k)\,\pi_{k+1}(s_k')} \right\} \quad . \tag{2.66}$$

The bisection is continued until the final level has been accepted. Only in this case, the particle coordinates are updated. This method has the advantage that unlikely moves are rejected early. The algorithm as a whole satisfies detailed balance because it is fulfilled on each level,

$$\frac{\pi_k(s_k)}{\pi_{k+1}(s_{k+1})}\, T_k(s_k \rightarrow s_k')\, A_k(s_k \rightarrow s_k') = \frac{\pi_k(s_k')}{\pi_{k+1}(s_{k+1}')}\, T_k(s_k' \rightarrow s_k)\, A_k(s_k' \rightarrow s_k)\ . \tag{2.67}$$

The total transition probability for the move being accepted at all levels is given by the following product,

$$\mathcal{P}(s \rightarrow s') = \prod_{k=1}^{k_{\max}} T_k(s_k \rightarrow s_k')\, A_k(s_k \rightarrow s_k') \quad . \tag{2.68}$$

It is worth noting that one can use an approximate form of π_k for all levels except for the lowest. These kinds of approximation modify only the acceptance ratios but not the MC averages. Therefore, it can be advantageous to use a simplified action, which can be computed faster. We often used the approximation $u_k \approx 2^{k-1}u_1$, which means that we can re-use the diagonal part of the pair action from the previous levels. Furthermore, the long-range as well as the off-diagonal contributions to the action are only calculated at the lowest level.

2.5.4 Permutation Sampling

Fermi and Bose statistics require to sum over all permutations in addition to the integration in real space. Both can be combined into one MC process that samples configurations in the space of coordinates and permutations.

In Eq. 2.47, one sums paths beginning at $\mathbf{R}$ and going to $\mathcal{P}\mathbf{R}'$. One can also think of two sets of coordinates $\mathbf{R}$ and $\mathbf{R}'$, for which one integrates over all possible ways to link the individual particles. In this picture, the permutation of the paths can be carried out at any time slice because the permutation operator permutes with the Hamiltonian. This is what is done in the actual MC simulation. One selects a time slice denoted by $t_{\mathcal{P}}$, at which one switches from the unpermuted to the permuted coordinates. $t_{\mathcal{P}}$ can be shifted to any slice along the paths. In a permutation move, one introduces a new permutation and simultaneously regrows the paths between the fixed points $\mathbf{R}_i$ and $\mathbf{R}_j$ with $j = i + 2^k$. The equilibrium distribution of the permutation is given by,

$$\pi(\mathcal{P}) = \frac{\rho(\mathbf{R}_i, \mathcal{P}\mathbf{R}_j; 2^k\tau)}{\sum_{P'} \rho(\mathbf{R}_i, \mathcal{P}'\mathbf{R}_j; 2^k\tau)} \quad . \tag{2.69}$$

Since there are $N!$ permutations, it is advisable to put an upper limit on the step size in permutation space. Typically, one only considers changes in current permutations that involve the cyclic exchange of up to 3 or 4 particles. Since the normalization is known in Eq. 2.69 one can use the *heat bath* transition rule, in which a permutation $\mathcal{P}'$ is sampled from the neighborhood $\mathcal{N}(\mathcal{P})$ of the current permutation $\mathcal{P}$ using their equilibrium distribution,

$$T_{\mathrm{hb}}(\mathcal{P} \rightarrow \mathcal{P}') = \frac{\pi(\mathcal{P})}{C(\mathcal{P})} \quad , \tag{2.70}$$

where the normalization is given by the sum over all neighboring states,

$$C(\mathcal{P}) = \sum_{\mathcal{P}' \in \mathcal{N}(\mathcal{P})} \pi(\mathcal{P}') \quad . \tag{2.71}$$

The acceptance probability follows from Eq. 2.53,

$$A_{\mathrm{hb}}(\mathcal{P} \rightarrow \mathcal{P}') = \min\left\{ 1 \, , \, \frac{C(\mathcal{P})}{C(\mathcal{P}')} \right\} \quad . \tag{2.72}$$

If the neighborhoods of $\mathcal{P}$ and $\mathcal{P}'$ are equal, all moves will be accepted. In the MC simulation, one uses the free particle density matrix to construct a permutation table containing all permutations in the neighborhood. Then $\mathcal{P}'$ is selected and accepted with the probability in Eq. 2.72, which does not exactly equal one unless the permutation table exhausts the whole space.

2.6 Fermion Nodes

2.6.1 Fermion Sign Problem

In simulations of fermionic systems, one has to deal with an extra complication emerging from the cancellation of positive and negative contributions to the averages calculated from,

$$\langle \mathcal{O} \rangle = \frac{\sum_{\mathcal{P}} (-1)^{\mathcal{P}} \int \mathbf{dRdR}' \, \langle \mathbf{R} | \, \mathcal{O} \, | \mathcal{P}\mathbf{R}' \rangle \, \rho(\mathcal{P}\mathbf{R}', \mathbf{R}; \beta)}{\sum_{\mathcal{P}} (-1)^{\mathcal{P}} \int \mathbf{dR} \, \rho(\mathbf{R}, \mathcal{P}\mathbf{R}; \beta)} \quad . \tag{2.73}$$

Even permutations have positive signs and odd ones have negative signs. The magnitude of the contributions from non-identity permutations depends on the degeneracy of the systems, which can be discussed in terms of the parameter $n\Lambda^D$ or equivalently as the ratio of temperature to Fermi temperature $\theta = T/T_F$. Here, we compare to the Fermi energy $E_F = k_B T_F$ of an ideal quantum gas in 3 dimensions,

$$E_F = \lambda \, (6\pi^2 n)^{2/3}, \tag{2.74}$$

where n is the density of particles in this particular spin state, which leads to

$$\theta^{-3} = \frac{9\pi}{16} \, (n\Lambda^3)^2 \quad . \tag{2.75}$$

If the temperature is of the order of the T_F non-identity permutations or lower are important. Those also lead to a significant fraction of negative contributions to the enumerator as well as to the denominator in Eq. 2.73. The consequence are large fluctuations in the computed averages. This is known as the *fermion sign problem.* While Eq. 2.73 always leads to the exact answer it becomes numerically increasingly difficult to compute the averages at the point where the interesting fermionic effects start to occur. It was shown by Ceperley (1996) that the efficiency of the straightforward implementation scales like $e^{-2\beta N f}$, where f is the free energy difference per particle of a corresponding fermionic and bosonic system while N is the number of particles.

2.6.2 Restricted Path Integrals

In the work by Ceperley (1991, 1996), it has been shown that one can evaluate the path integral by restricting the path to only specific positive contributions. One introduces a reference point $\mathbf{R}^*$ on the path that specifies the nodes of the density matrix, $\rho_F(\mathbf{R}, \mathbf{R}^*, t) = 0$. A *node-avoiding* path for $0 < t \leq \beta$ neither touches nor crosses a node: $\rho_F(\mathbf{R}(t), \mathbf{R}^*, t) \neq 0$. By restricting the integral to node-avoiding paths,

$$\rho_F(\mathbf{R}^*, \mathbf{R}_\beta; \beta) = \int \mathbf{dR}_0 \, \rho_F(\mathbf{R}_0, \mathbf{R}^*; 0) \oint\limits_{\mathbf{R}_0 \to \mathbf{R}_\beta \in \Upsilon(\mathbf{R}^*)} \mathbf{dR}_t \;\; e^{-S[\mathbf{R}_t]} \tag{2.76}$$

$$= \frac{1}{N!} \sum_{\mathcal{P}} (-1)^{\mathcal{P}} \oint\limits_{\mathcal{P}\mathbf{R}^* \to \mathbf{R}_\beta \in \Upsilon(\mathbf{R}^*)} \mathbf{dR}_t \;\; e^{-S[\mathbf{R}_t]} \quad , \tag{2.77}$$

where $\Upsilon(\mathbf{R}^*)$ denotes the nodal restriction with respect to the reference point $\mathbf{R}^*$. The nodal restriction remains the same if any permutation $\mathcal{P}$ is applied to the reference point, which leads to $\Upsilon(\mathbf{R}^*) \equiv \Upsilon(\mathcal{P}\mathbf{R}^*)$ because $\rho_F(\mathbf{R}, \mathbf{R}^*; \beta) = 0$ implies $\rho_F(\mathbf{R}, \mathcal{P}\mathbf{R}^*; \beta) = 0$. Eq. 2.77 can now be written in the following alternative form,

$$\rho_F(\mathbf{R}^*, \mathbf{R}_\beta; \beta) = \frac{1}{N!} \sum_{\mathcal{P}} (-1)^{\mathcal{P}} \oint\limits_{\mathcal{P}\mathbf{R}^* \to \mathbf{R}_\beta \in \Upsilon(\mathcal{P}\mathbf{R}^*)} \mathbf{dR}_t \;\; e^{-S[\mathbf{R}_t]} \tag{2.78}$$

$$= \frac{1}{N!} \sum_{\mathcal{P}} (-1)^{\mathcal{P}} \oint\limits_{\mathbf{R}^* \to \mathcal{P}\mathbf{R}_\beta \in \Upsilon(\mathbf{R}^*)} \mathbf{dR}_t \;\; e^{-S[\mathbf{R}_t]} \quad , \tag{2.79}$$

where we have applied the permutation $\mathcal{P}^{-1}$ to the entire path and changed the summation index using that the sign of $\mathcal{P}$ and $\mathcal{P}^{-1}$ are equal.

In the case of *diagonal* density matrix elements, Eq. 2.79 can be simplified because odd permutations inevitably cross a node since $\rho_F(\mathbf{R}^*, \mathbf{R}^*; 0) = -\rho_F(\mathbf{R}^*, \mathcal{P}_{\text{odd}}\mathbf{R}^*; 0)$. Eq. 2.79 then reads,

$$\rho_F(\mathbf{R}, \mathbf{R}; \beta) = \frac{1}{N!} \sum_{\substack{\mathcal{P} \\ \text{even}}} \oint_{\mathbf{R} \to \mathcal{P}\mathbf{R} \in \Upsilon(\mathbf{R}^* \equiv \mathbf{R})} \mathbf{dR}_t \; e^{-S[\mathbf{R}_t]} \quad . \tag{2.80}$$

For *off-diagonal* density matrix elements however, odd permutations need to be considered and lead to negative contributions, which will be discussed in chapter 5.

Since all contributions to the diagonal density matrix elements are positive the restricted PIMC technique represents, in principle, a solution to the sign problem. The method is exact if the exact fermionic density matrix is used in the restriction. The proof given by Ceperley (1996) consists of three steps.

(i) The initial condition for the Bloch equation 2.13 are given by,

$$\rho_F(\mathbf{R}, \mathbf{R}^*; 0) = \frac{1}{N!} \sum_{\mathcal{P}} (-1)^{\mathcal{P}} \; \delta(\mathbf{R} - \mathcal{P}\mathbf{R}^*) \tag{2.81}$$

and $\rho(\mathbf{R}^*, \mathbf{R}^*; 0) \geq 0$. $\mathbf{R}^*$ and therefore the initial conditions are kept fixed for the following arguments. The solution of the Bloch equation is uniquely determined by the boundary conditions, which means $\rho_F(\mathbf{R}, \mathbf{R}'; \beta)$ can be derived from the values on a certain boundary $\Upsilon(\mathbf{R}; \beta')$ for all $\beta' < \beta$.

(ii) The nodes of $\rho_F(\mathbf{R}, \mathbf{R}^*; \beta)$ carve the space-time into a finite number ($\leq N!$) of nodal cells, that are sets of points in the space-time connected by node-avoiding paths. From (i), it follows that the solution inside each nodal cell can be constructed from the initial condition and the zero boundary condition on the surface, which is determined by the nodes.

(iii) Enforcing zero boundary conditions at the nodes can be done by introducing a infinite repulsive potential on the nodes, which prevents any paths from crossing and therefore guarantees that the density matrix vanishes at the cell boundaries.

2.6.3 Trial Density Matrix

The exact density matrix is only known in a few cases. In practice, applications have approximated the fermionic trial density matrix $\rho_T(\mathbf{R}, \mathbf{R}'; \beta)$, most commonly by a Slater determinant of single particle density matrices,

$$\rho_T(\mathbf{R}, \mathbf{R}'; \beta) = \begin{vmatrix} \rho_1(\mathbf{r}_1, \mathbf{r}'_1; \beta) & \dots & \rho_1(\mathbf{r}_N, \mathbf{r}'_1; \beta) \\ \dots & \dots & \dots \\ \rho_1(\mathbf{r}_1, \mathbf{r}'_N; \beta) & \dots & \rho_1(\mathbf{r}_N, \mathbf{r}'_N; \beta) \end{vmatrix} \quad . \tag{2.82}$$

More generally, we now discuss systems of spin $\frac{1}{2}$ fermions, for which the Hamiltonian is spin-independent because we do not consider magnetic fields nor relativistic effects including spin-orbit interactions. There, the spin component in $\hat{z}$ direction S_z can be quantized leading to a good quantum number m, which describes the magnetization of the systems. For ensembles with fixed magnetization m, the density matrix can be written as a product of two determinants,

$$\rho_T(\mathbf{R},\mathbf{R}';\beta) = \left\|\rho_1(\mathbf{r}_i,\mathbf{r}'_j)\right\|_{i,j\in\uparrow} \left\|\rho_1(\mathbf{r}_i,\mathbf{r}'_j)\right\|_{i,j\in\downarrow} \quad . \tag{2.83}$$

If one applies an operator that antisymmetrizes completely and then projects out states of magnetization m one finds only configurations that can again be written as such a product of two determinants but with relabelled particles. From now on, we only consider spin unpolarized systems ($m = 0, N_\uparrow = N_\downarrow$). Enforcing the nodes means that each determinant stays positive all along the paths because configurations where both determinants flip signs simultaneously have zero measure.

Extensions of this type of nodes are necessary to describe a pairing mechanism that permits the formation of Cooper pairs in super conductors and electron-hole pairs in semi-conductors, which then can Bose condense (Bouchard *et al.*, 1988). Simulations with pairing nodes have been done at zero temperature by Gilgien (1997) and Zhu *et al.* (1996) and at finite temperature by Shumway and Ceperley (1999).

The above trial density matrix has been extensively applied using the free particle (FP) nodes (Ceperley, 1996) including applications to dense hydrogen (Pierleoni *et al.*, 1994; Magro *et al.*, 1996; Militzer *et al.*, 1999). In this case, the density matrix of a single FP in a periodically repeated box given by Eq. 2.11 is used in Eq. 2.83. It can be shown that for high temperatures, the interacting nodal surface approaches the FP nodal surface. In addition, in the limit of low density, exchange effects are negligible, the nodal constraint has a small effect on the paths and therefore, its precise shape is not important. The FP nodes also become exact in the limit of high density when kinetic effects dominate over the interaction potential. However, for high densities and high degeneracy, interactions could have a significant effect on the fermionic density matrix. To gain some quantitative estimate of the possible effect of the nodal restriction on the thermodynamic properties, it is necessary to try an alternative. In addition to FP nodes, a variational density matrix (VDM) is derived in chapter 3 that already includes interactions and atomic and molecular bound states. The effects on the thermodynamic properties from using those as nodes will be discussed in section 4.3.

2.6.4 The Reference Point

The FP nodes as well as the VDM nodes represent approximations to the exact fermion nodes that become increasingly accurate for high temperatures. There is a simple trick that uses two reference points instead of one and allows to enforce the nodes by taking the sign of the trial density matrix from $\rho(\mathbf{R},\mathbf{R}^*;\beta)$ rather than from $\rho(\mathbf{R},\mathbf{R}^*;2\beta)$.

The density matrix $\rho(\mathbf{R}_\beta,\mathbf{R}'_\beta;2\beta)$ can be expressed in terms of the convolution equation,

$$\rho_F(\mathbf{R}_\beta,\mathbf{R}'_\beta;2\beta) = \int \mathbf{dR}^* \; \rho_F(\mathbf{R}_\beta,\mathbf{R}^*;\beta)\; \rho_F(\mathbf{R}'_\beta,\mathbf{R}^*;\beta) \quad , \tag{2.84}$$

which can be interpreted as an integral over all pairs of paths, one going from $\mathbf{R}^*$ to $\mathbf{R}_\beta$ and a second one from $\mathbf{R}^*$ to $\mathbf{R}'_\beta$. Both fermion density matrices can evaluated using a restricted path integral with the same reference point $\mathbf{R}^*$. This requires the time argument to be zero at $\mathbf{R}^*$ and to increase in both directions up to β at $\mathbf{R}_\beta$ and $\mathbf{R}'_\beta$. Using the explicit form of ρ_F in Eq. 2.77 the above equation becomes,

$$\begin{aligned}
\rho(\mathbf{R}_\beta,\mathbf{R}'_\beta;2\beta) &= \frac{1}{N!^2}\int \mathbf{dR}^* \sum_{\mathcal{P}\mathcal{P}'} (-1)^{\mathcal{P}+\mathcal{P}'} \oint\limits_{\mathcal{P}\mathbf{R}^*\to\mathbf{R}_\beta\in\Upsilon(\mathbf{R}^*)} \mathbf{dR}_t \; e^{-S[\mathbf{R}_t]} \oint\limits_{\mathcal{P}'\mathbf{R}^*\to\mathbf{R}'_\beta\in\Upsilon(\mathbf{R}^*)} \mathbf{dR}_t \; e^{-S[\mathbf{R}_t]} && (2.85)\\
&= \frac{1}{N!^2}\sum_{\mathcal{P}\mathcal{P}'} (-1)^{\mathcal{P}+\mathcal{P}'} \int \mathbf{dR}^* \oint\limits_{\mathbf{R}^*\to\mathcal{P}\mathbf{R}_\beta\in\Upsilon(\mathbf{R}^*)} \mathbf{dR}_t \; e^{-S[\mathbf{R}_t]} \oint\limits_{\mathbf{R}^*\to\mathcal{P}'\mathbf{R}'_\beta\in\Upsilon(\mathbf{R}^*)} \mathbf{dR}_t \; e^{-S[\mathbf{R}_t]} && (2.86)\\
&= \frac{1}{N!}\sum_{\mathcal{P}} (-1)^{\mathcal{P}} \int \mathbf{dR}^* \oint\limits_{\mathbf{R}^*\to\mathbf{R}_\beta\in\Upsilon(\mathbf{R}^*)} \mathbf{dR}_t \; e^{-S[\mathbf{R}_t]} \oint\limits_{\mathbf{R}^*\to\mathcal{P}\mathbf{R}'_\beta\in\Upsilon(\mathbf{R}^*)} \mathbf{dR}_t \; e^{-S[\mathbf{R}_t]} \quad , && (2.87)
\end{aligned}$$

where we have employed the equivalence of Eq. 2.77 and 2.79 and also the fact that the double sum over permutations be converted into a single one because the following path integral can be treated as two independent factors. This expression can be interpreted as a single path integral of the form $\rho_F(\mathbf{R}_\beta,\mathbf{R}'_\beta;2\beta)$. The paths start at $\mathbf{R}_\beta$, goes through the reference $\mathbf{R}^*$ at the middle of the path, and ends at $\mathcal{P}\mathbf{R}'_\beta$. The time argument to check the nodes gets chosen according to,

$$t_{\rm ref} = \begin{cases} t & \text{for} \quad 0 \le t \le \beta/2 \\ \beta - t & \text{for} \quad \beta/2 \le t \le \beta \quad , \end{cases} \tag{2.88}$$

which means one only needs to evaluate the trial density matrix up to $\beta/2$. This time doubling procedure cannot be applied further without reintroducing the sign problem.

2.6.5 Example: Nodes for Two Particles

The following example describes the restricted path integral method and illustrates why it leads to the exact solution in the case that the nodes are exactly known. It represents a simplified version of the illustration by Ceperley (1996) that uses the example of the hydrogen molecule. Here, we talk about the simplest possible problem that has a node: two free identical particles. For those, the exact nodes are given by,

$$\rho(\mathbf{r}_1, \mathbf{r}_2, \mathbf{r}_1^*, \mathbf{r}_2^*; \beta) \equiv \begin{vmatrix} \rho_1(\mathbf{r}_1, \mathbf{r}_1^*; \beta) & \rho_1(\mathbf{r}_1, \mathbf{r}_2^*; \beta) \\ \rho_1(\mathbf{r}_2, \mathbf{r}_1^*; \beta) & \rho_1(\mathbf{r}_2, \mathbf{r}_2^*; \beta) \end{vmatrix} = 0 \quad , \tag{2.89}$$

where ρ_1 is given by the free particle density matrix Eq. 2.12. The solution of this equation is given by,

$$(\mathbf{r}_1 - \mathbf{r}_2) \cdot (\mathbf{r}_1^* - \mathbf{r}_2^*) = 0 \quad . \tag{2.90}$$

Introducing the relative coordinate $\mathbf{r} = \mathbf{r}_1 - \mathbf{r}_2$, the node is a plane at the origin $\mathbf{r} = 0$ perpendicular to the vector given by reference point separation $\mathbf{r}^* = \mathbf{r}_1^* - \mathbf{r}_2^*$.

In this example, we discuss closed paths that end in the reference point $\mathbf{r}(\beta) = \mathbf{r}^*$. In the case of a permutation, the path must start at $-\mathbf{r}^*$, otherwise at $\mathbf{r}^*$. One can distinguish three types of paths as shown in Fig. 2.1,

A The path does not cross the node, therefore it starts and ends at $\mathbf{r}^*$.

B It crosses the node an even number of times > 0, therefore also starts and ends at $\mathbf{r}^*$.

C It goes an odd number of times across the node and therefore must start at $-\mathbf{r}^*$.

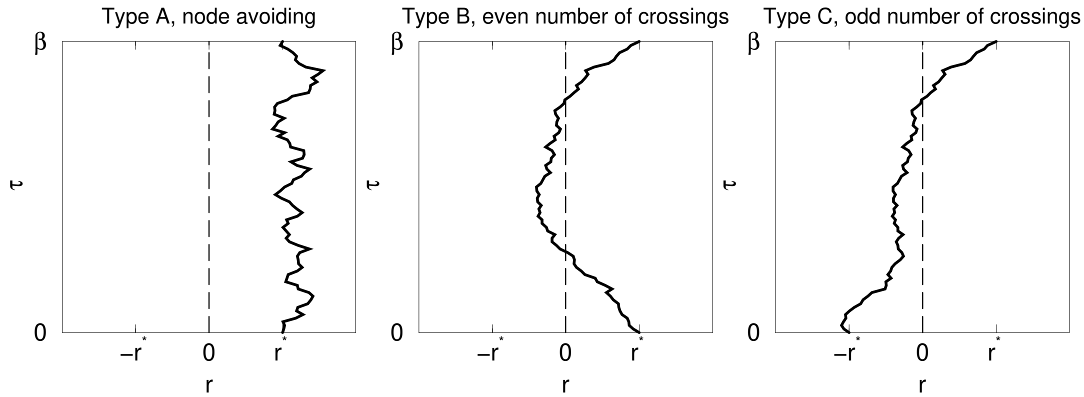

Figure 2.1: Illustration of the nodal constraint for paths going to $\mathbf{r}(\beta) = \mathbf{r}^*$. Type A paths are node-avoiding, Type B cross the nodes an even number of times, and Type C permutes, therefore must start at $\mathbf{r}(0) = -\mathbf{r}^*$ and cross the node an odd number of times.

The various kinds of paths have different physical interpretations. In a system of distinguishable particles, no permutations can occur and no nodes exist. Therefore only paths of type A and B contribute. For bosons, one sums over all permutations, nodes are irrelevant and no negative signs come in. For fermions, one has the choice of the *direct fermion method* or the *restricted path method.* Both methods are equivalent if the exact nodes are used. In case of the direct method, one considers all permutations with positive and negative signs and does not restrict the path. One sums up contributions from all types including those from type C with a negative sign. For restricted path integrals, one enforces the node, which rules out any permutations in two particle systems. Therefore, there are no negative contributions. Furthermore, the nodal constraint also prevents paths of type B from occurring and one is left with paths of type A, that stay within the half space given by the nodal plane. Essentially, one employs the cancellation of B and C in this method. Both cancel exactly because the flux of the paths is given by the gradient of the density matrix, which is the same on both sides of the node since the derivative is a continuous function. Summarizing, it reads,

- Distinguishable particles: A+B
- Bosons: A+B+C
- Fermions without nodes: A+B−C
- Fermions with nodes: Only A.

The magnitude of the different contributions can also be understood studying the exact solution to the problem stated in Eq. 2.46. For this system of two fermions, it reads,

$$\rho(\mathbf{r},\mathbf{r}^*;\beta) = \rho_{\mathrm{D}}(\mathbf{r},\mathbf{r}^*;\beta) - \rho_{\mathrm{D}}(-\mathbf{r},\mathbf{r}^*;\beta) \quad . \tag{2.91}$$

Setting $\mathbf{r} = \mathbf{r}^*$, the positive first term is greater in magnitude than the second because it is a diagonal density matrix element. It represents paths of type A and B, while the second term is smaller in magnitude and describes paths of type C. This equation also shows how a node emerges at $\mathbf{r} = 0$. The second term can be regarded a result from an image charge with opposite sign on the other side of the node similarly to the method of image charges in electrostatics. Both contributions are solutions to the Bloch equation that added together lead to a zero at the node. The determining parameter for the importance of the image charge is the distance to the node. This will be used in the derivation of the nodal action in the following section.

2.6.6 Nodal Action

In restricted PIMC simulation, one enforces the node by checking the sign of the determinant at each time slice. If it turns out to be negative for a proposed configuration, the move is rejected. The nodes act like an infinite potential barrier. In this method, it is implicitly assumed that the paths do not wander too far between the slices and in particular do not cross a node. This puts an additional lower bound on the number of slices used in a simulation in order to enforce the nodes accurately. By inserting additional slices, one finds that the some paths are rejected on the finer scale, which could not have been detected earlier because they crossed and recrossed the node within the slice. This error can be corrected for by introducing the *nodal action* U_N.

One assumes a flat node between two slices like in the example discussed in the previous section, which is a reasonable approximation for small τ. The difference in action between a system containing a node compared to one without it can be expressed as,

$$e^{-U_N^i} = e^{-(U^i_{\text{rest.}} - U^i_{\text{free}})} = \frac{\rho(\mathbf{r}_{i-1}, \mathbf{r}_i, \tau) - \rho(\mathbf{r}_{i-1}, \mathbf{r}_i - 2\mathbf{d}_i, \tau)}{\rho(\mathbf{r}_{i-1}, \mathbf{r}_i, \tau)} \quad , \tag{2.92}$$

where $\mathbf{d}_i$ is the distance to the nearest node at the time slice i. The image charge is placed at $\mathbf{r}_i - 2\mathbf{d}_i$. Using the free particle density matrix, the nodal action can be written in terms of the distances to the node at the two slices,

$$e^{-U_N^i} = 1 - \exp\left[\, - d_i \, d_{i-1} \, / \, \lambda\tau \,\right] \quad . \tag{2.93}$$

The distance is difficult to calculate but it can be estimated using Newton-Raphson procedure,

$$d_i = \frac{\rho_T(\mathbf{R}_i, \mathbf{R}^*; \beta)}{|\nabla_{\mathbf{R}}\, \rho_T(\mathbf{R}_i, \mathbf{R}^*; \beta)|} \quad . \tag{2.94}$$

If ρ_T is given in matrix form $\rho_{ij} = \rho_1(\mathbf{r}_i, \mathbf{r}^*_j; \beta)$, its derivatives (denoted by $'$) can be calculated efficiently from the *cofactor* matrix (its transposed inverse) ρ^{-1}_{ji},

$$||\rho_{ij}||' = ||\rho_{ij}||^2 \sum_{ij} \rho'_{ij}\, \rho^{-1}_{ji} \quad . \tag{2.95}$$

The distance to the node then reads,

$$d^{-2} = \sum_i \left(\sum_j \left(\nabla_{\mathbf{r}_i} \rho_{ij}\right)^2 \rho^{-1}_{ji} \right)^2 \quad . \tag{2.96}$$

The additional term in the action U_N also leads to a contribution to the internal energy, which can be derived from

$$E_N = -\frac{dU_N}{d\tau} = -\frac{1}{1 - e^{-x}} \frac{dx}{d\tau} \quad , \tag{2.97}$$

$$x \equiv \frac{d_{i-1}\, d_i}{\lambda\tau} \quad . \tag{2.98}$$

The time derivative of x can be approximated by,

$$-\frac{dx}{d\tau} = \frac{x}{\tau} - \frac{x}{d_i}\frac{dd_i}{d\tau} - \frac{x}{d_{i-1}}\frac{dd_{i-1}}{d\tau} \tag{2.99}$$

$$\approx \frac{x}{\tau} \quad . \tag{2.100}$$

This approximation omits the change in the distance to the node with imaginary time. It has the advantage that one does not have to compute the derivatives of the distance to the nearest node d_i, which would require extra numerical work.

The effect of the nodal action U_N is shown in Fig. 2.2, where two simulations, one

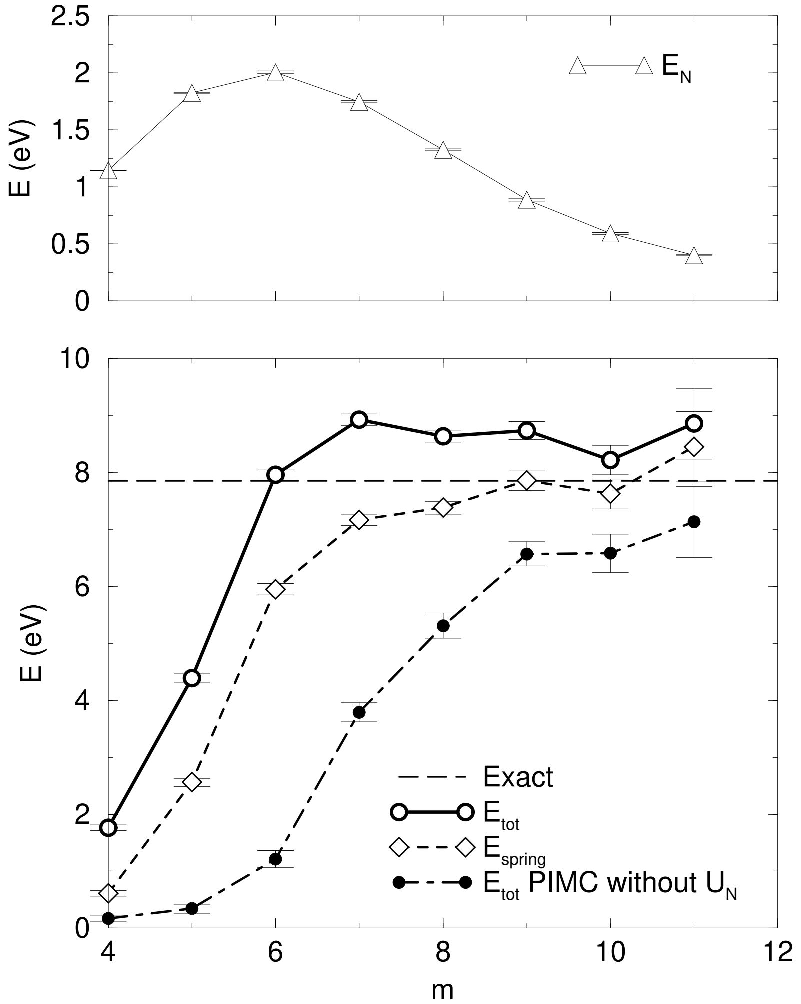

Figure 2.2: Comparison of the internal energy per electron from two simulations, one with nodal action ($\circ$) and one without ($\bullet$), for 16 free particles at $r_s = 2.52$ and $T = 15\,625\,\mathrm{K}$ for different number of time slices 2^m leading to a time step $\tau^{-1} = 2^{m-6}10^6\,\mathrm{K}$. $\triangle$ shows the nodal energy and $\diamond$ denotes the spring kinetic energy given by $E_{tot} - E_N$. The long dashed line shows the exact energy for this finite system. All simulations were 3.2×10^6 steps of level $k = m - 3$ long.

with it and without it, are compared as a function of time step. In these simulations, $N = 16$ spin-polarized free electrons were studied at $T = 15\,625\,\mathrm{K}$ and $r_s = 2.520$. The conditions were chosen in correspondence with hydrogen simulations discussed in chapter 4 where 32 protons and 32 electrons in two spin states are studied at a typical density corresponding to $r_s = 2.0$. The Fermi temperature for an infinite system (Eq. 2.74) under these conditions is $145\,381\,\mathrm{K}$. For a system with $N = 16$, it becomes $29\,747\,\mathrm{K}$. The difference is that large because the only 3 k-shells are occupied while in Eq. 2.74 sum of k-shells were approximated by an integral. The number of states per k-shell starting from $k = 0$ are 1, 6, 12, 8, 6, 24, ...

All hydrogen simulations discussed later are performed with $\tau^{-1} = 10^6\,\mathrm{K}$ (64 slices, $m = 6$) or smaller time steps. The required time step can be estimated from the corresponding degeneracy parameter,

$$n\Lambda_\tau^D \equiv n\,(4\pi\lambda\tau)^{D/2} \quad , \tag{2.101}$$

which relates the average distance the path travels between the slices,

$$\Delta r \equiv \sqrt{\langle(\mathbf{r}_{i+1} - \mathbf{r}_i)^2\rangle} = \sqrt{2D\pi\lambda\tau} \tag{2.102}$$

to the inter-particle spacing. For the above example with $\tau^{-1} = 10^6\,\mathrm{K}$, one finds $n\Lambda_\tau^3 = 0.041$ and $\Delta r = 1.725$, which must be compared to the inter-particle spacing given by $r_s = 2.520$. For the example of $N = 16$ particles at this degeneracy, Fig. 2.2 predicts that choosing the time step such that $\Delta r / r_s \lesssim 0.7$ ($n\Lambda_\tau^3 \lesssim 0.04$) leads to energies reasonably close to the exact value. To go up to 2048 slices ($m = 11$) is only possible for a system of free particles this small. The figure shows clearly that in simulations with the nodal action term, the internal energy converges faster to the exact value of 7.844 eV, the reason being that configurations of paths where the nodal constraints are likely to be violated between the slices are rejected because of the U_N term. However, the graph also shows that the nodal energy is overestimated leading to an internal energy 10% too large. Possible explanations for this discrepancy include the approximations in the way the distance to the node is estimated, the implicit assumption that the nodes are planar within the time interval τ and the omission of two terms in Eq. 2.99. However, in the limit of small τ all those approximations do not matter and one should find the above mentioned exact value, which was calculated by a separate MC method in k-space. The nodal constraint there is realized by restricting each k-point to only one particle. However, the method relies on the exactly known eigenstates of the Hamiltonian.

2.6.7 Improvements in the Nodal Action

In the previous section, it has been shown how a nodal action can be used to predict the probability that paths cross the nodes between two time slices. The procedure has the advantage that it allows to employ a large time step, which can be crucial for simulation at low temperature with a high computational demand. However, there exists still an upper bound on the time step because the assumption of a planar nodal surface between two slices breaks down. The effects on the thermodynamic variables calculated from a simulation with too large a time step are especially drastic in attractive systems like hydrogen. There, the nodes realize the Pauli exclusion principle, which make matter stable. If it is not guaranteed the system will inevitably collapse at some point in time during a simulation as shown by Theilhaber and Alder (1991).

An example of node violations is shown in Fig. 2.3. All determinants at a time slice have a positive sign and the predicted distance to the nodes has a reasonable value greater than 0. However, if one interpolates the coordinates linearly between two slices and then calculates the determinant and the distance to the node one finds some points where the path crosses the node. This could not happen if the nodes were planar. This analysis shows the break down of the nodal action procedure described in the previous section for too large time steps. In a simulation of hydrogen, one finds that the pressure becomes unphysically low and even negative. Simultaneously, the system partially collapses.

Fig. 2.3 also reveals ways to improve the nodal action. One possibility is to study the classical path that connects the two slices $\mathbf{R}_i$ and $\mathbf{R}_{i+1}$ in order to predict violations of the nodal surfaces. We propose to use the function,

$$f(\mathbf{R}(t);t) = \frac{\rho(\mathbf{R}(t),\mathbf{R}^*;t)}{\rho(\mathbf{R}^*,\mathbf{R}^*;t)} \tag{2.103}$$

and to determine its value and its gradient at the two slices. Those are fit a third order polynomial and it will be checked if it goes through zero. The reason for dividing by the term $\rho(\mathbf{R}^*,\mathbf{R}^*;t)$ is that the magnitude of the density matrix changes considerably even with a small time interval. Checking for node violations on the classical path gives rise to an additional restriction for a proposed configuration. In order to derive a nodal action one needs to study an ensemble of the paths. Due to the lack of analytical solutions of the diffusion equation for this problem we suggest to use a set of randomly sampled semi-classical paths,

$$\mathbf{R}(t) = (1-x)\,\mathbf{R}_i + x\,\mathbf{R}_{i+1} + \sum_k Q_k\, e^{-2\pi i x k} \qquad \text{with} \qquad x = \frac{t}{\tau} - i \quad , \tag{2.104}$$

where Q_k are DN dimensional normal-mode vectors that have a Gaussian distribution. The simplest way is to use only the first mode and to determine the width of the Gaussian from the free particle density matrix. Practically, one would sample a number Q_k, constructed the corresponding semi-classical paths, perform the fit of f to the polynomial along each paths and check if the node would be crossed. The fraction of node avoiding paths would then be used in a metropolis rejection step. This analysis does predict some of the node violations that could not be detected with previous method. However, a detailed analysis if it actually improves the efficiency compare to a simulation with a smaller time step remains to be done.

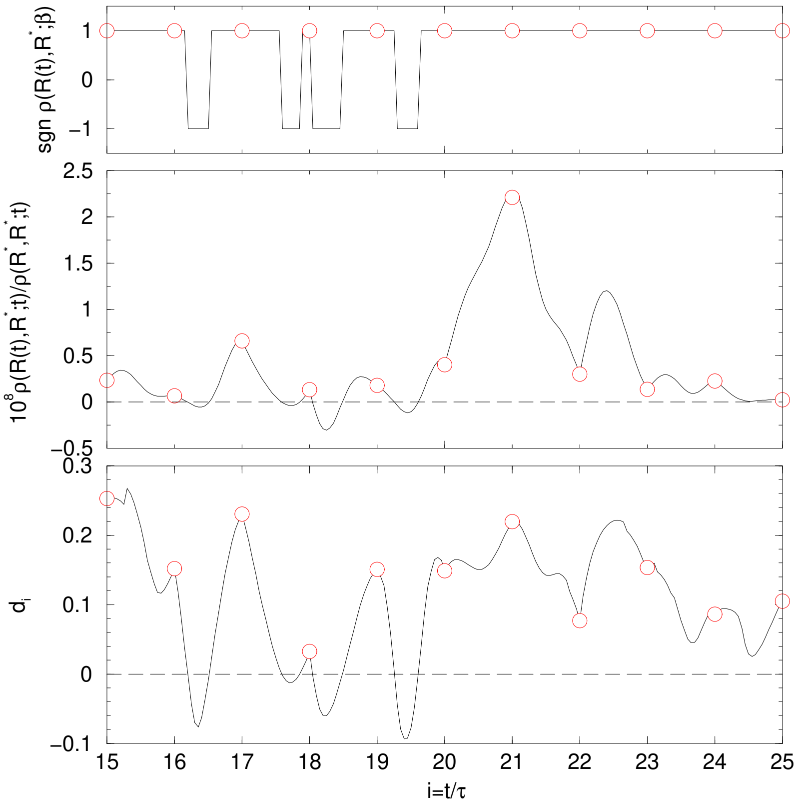

Figure 2.3: Demonstration of violations of the nodal surfaces for one configuration of a hydrogen simulation with too large a time step. The $\circ$ correspond to the time slice, at which the sign of the trial density matrix is checked. The solid lines display same properties on a classical path connecting the slices. The middle graphs shows the trial density matrix $\rho(\mathbf{R}(t), \mathbf{R}^*; t)$ divided by $\rho(\mathbf{R}^*, \mathbf{R}^*; t)$ vs. imaginary time t. The upper graph exhibits sign of ρ and in the lower graph, the distance to the node from Eq. 2.94. The sign of this distance indicates, which side of the node the paths is on. The classical paths exhibits four node crossings the could not be predict using the nodal action from Eq. 2.93. This fact as well the middle graph demonstrates the nodes are not sufficiently planar in the time interval τ.

2.6.8 Distribution of Permutation Cycles

The distribution of permutation cycles has significant effects on the thermodynamics properties of the studied system since they represent the fermionic character. Here, we will discuss how it changes with increasing degeneracy.

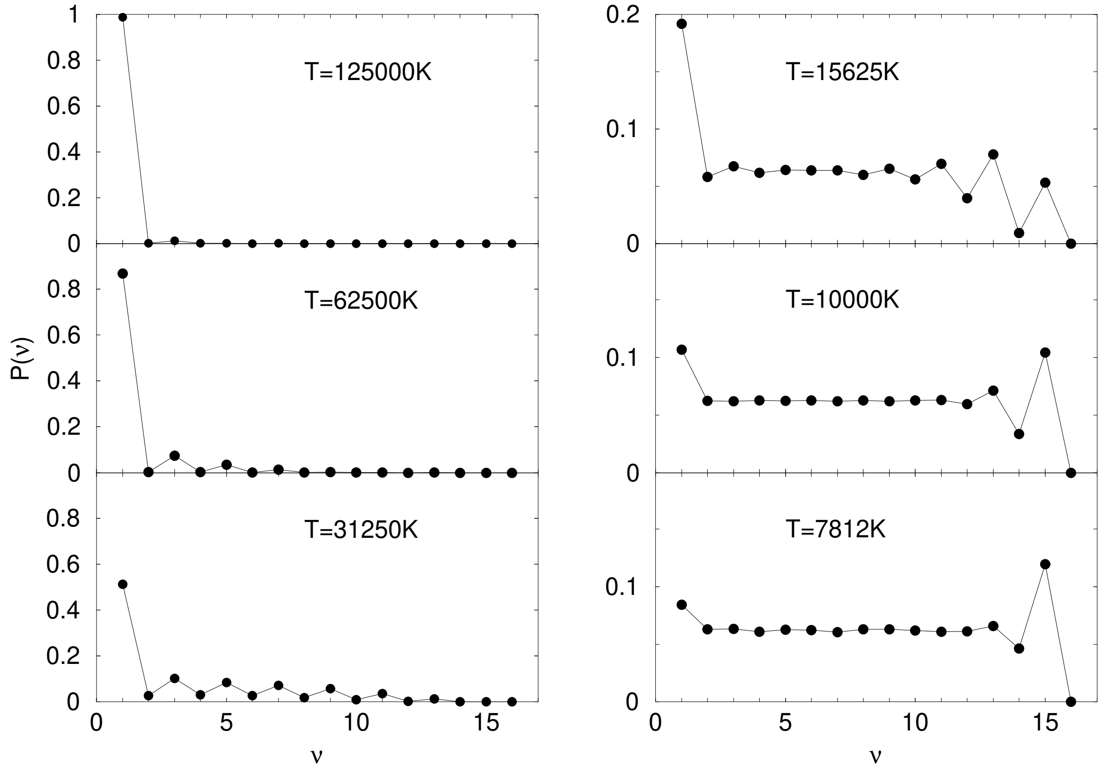

Figure 2.4: Comparison of the cycle length distributions (probability of an electron being involved in a permutation cycle of the length ν) in a PIMC simulation of hydrogen with 32 protons and 16 electrons of each spin state at $r_s = 1.86$ for different temperatures T using free particle nodes. Decreasing T leads to an increased degeneracy and more uniform cycle distribution.

In Fig. 2.4, the probability distribution P_ν of permutation cycles of different length ν from PIMC simulations are shown. The normalization is given $\sum_\nu P_\nu = 1$. We found that the fraction of 1-cycles P_1 is a good candidate to discuss the degree degeneracy. Beginning at 1 in a non-degenerate system, it decreases with increasing degeneracy. Simultaneously, states with higher cycle lengths are populated. At first, odd cycles have a higher probability, while one finds an almost uniform distribution at high degeneracy. The reason is that the nodal surfaces prohibit even permutations, which means an even number of even cycles must occur simultaneously and more importantly within the distance of the order of the thermal de Broglie wave length. It can be shown from the determinant that isolated even cycles would violate the nodes.

This is also the reason why systems with even numbers of particles cannot form one long chain ($P_{16} = 0$ in Fig. 2.4). At high degeneracy where the thermal de Broglie wave length is larger than the inter-particle spacing, the nodal constraint does not discriminate between even and odd cycles.

This observed cycle distribution with fermion nodes is very different from what one expects from direct fermion methods, where one considers the signs explicitly and does not use nodal surfaces, e.g. the cycle distribution of a system of non-interacting fermions can be calculated in the grand canonical ensemble (Feynman, 1972). One has to differentiate between odd and even cycle lengths leading to positive and negative contributions to the partition function. Incorporating the sign into P_ν, it reads

$$P_\nu = (-1)^\nu \, \frac{1}{n} \, \frac{e^{\nu\mu\beta}}{(4\pi\lambda\beta\nu)^{3/2}} \,, \tag{2.105}$$

where the chemical potential μ for given β and density n is determined by the normalization $\sum_{\nu=1}^{\infty} P_\nu = 1$. P_ν is the rapidly decaying function of ν, which has little in common with observed cycle distributions from restricted path integrals.

2.6.9 Sampling Procedure

The sampling procedure used in the MC simulations consists of several steps, which will be briefly described here,

1. Select the time slices to be modified $(i \ldots i+2^k)$ either at random or by making random steps with an upper limit.

2. Build a permutation table containing up to 3 particle permutations using the probability similar to Eq. 2.69

$$T(\mathcal{P} \to \mathcal{P}') \propto \frac{\rho(\mathbf{R}_i, \mathcal{P}'\mathbf{R}_j; 2^k\tau)}{\rho(\mathbf{R}_i, \mathcal{P}\mathbf{R}_j; 2^k\tau)} \quad . \tag{2.106}$$

   This can be considered the zeroth step in the multilevel sampling procedure. Dividing out the current permutation term has the advantage that it lead to 100% acceptance for free particles in the following first slice sampling step. In the case of fermions and close paths, permutations of a even number of particles do not enter the table since they will inevitably lead to a violation of the nodes.

3. Determine the new midpoints given by $(\mathbf{R}_i + \mathcal{P}'\mathbf{R}_{i+2^k})/2$, sample the new coordinates from Eq. 2.64 and accept with probability,

$$A(s_k \to s_k') = \min\left\{ 1 \,,\, T(\mathcal{P} \to \mathcal{P}') \, \frac{T_k(s_k' \to s_k)\, \pi_k(s_k')}{T_k(s_k \to s_k')\, \pi_k(s_k)} \right\} \quad . \tag{2.107}$$

We use only the diagonal part of the pair action at this level. Note that for high levels where $\sqrt{2^k \lambda \tau}$ is of the order of the box size, corrections to T_k need to be considered because points in the tail of the Gaussian fall out of the box and are mapped back in by the periodic boundary conditions. This leads to additional terms in the probability of sampling a particular point. If this move of rejected here or at any later stage continue at step 2 or 1.

4. Continue the bisection method based on Eq. 2.66 down to level 1. Consider the long-range as well as the off-diagonal pair action only at the last level.

5. Perform a Metropolis rejection step on the permutations by calculating the probability for the reverse move,

$$A(\mathcal{P} \to \mathcal{P}') = \min \left\{ 1 \, , \, \frac{C(\mathcal{P})}{C(\mathcal{P}')} \, \frac{1}{T(\mathcal{P} \to \mathcal{P}')} \right\} \quad . \tag{2.108}$$

   The factor $\left[T(\mathcal{P} \to \mathcal{P}')\right]^{-1}$ cancels with the extra term in Eq. 2.107.

6. Check the nodal surfaces in each slice, verify that $\rho_T(\mathbf{R}_t, \mathbf{R}^*; t) > 0$.

7. Make a Metropolis rejection step based on the difference in the nodal action,

$$A(\mathbf{R} \to \mathbf{R}') = \min \left\{ 1 \, , \, \frac{e^{-U_N(\mathbf{R}')}}{e^{-U_N(\mathbf{R})}} \right\} \quad . \tag{2.109}$$

8. Upon final acceptance, update all coordinates. Continue at step 1 or 2.

Some averages are calculated at every step, others less frequently e.g. only when one moves to a new section of the paths. In the MC simulation, some displacement moves are intertwined with the multilevel sampling moves described above. This completes the description for a simulation with closed paths. The modifications required for open paths are discussed in chapter 5.

Chapter 3

Variational Density Matrix Technique

3.1 Analogy to Zero Temperature Methods

Considerable effort has been devoted to systems where finite temperature ions (treated either classically or quantum mechanically by path integral methods) are coupled to degenerate electrons on the Born-Oppenheimer surface. In contrast, the theory for similar systems with non-degenerate electrons (T a significant fraction of T_F) is relatively underdeveloped except at the extreme high T limit where Thomas-Fermi and similar theories apply. In this chapter, we present a variational approach for systems with non-degenerate electrons analogous to the methods used for ground state many body computations.

Although an oversimplification, we may usefully view the ground state computations as consisting of three levels of increasing accuracy (Hammond *et al.*, 1994).

1. At the first level, the ground state wave function consists of determinants, for both spin species, of single particle orbitals often taken from local density functional theory

$$\psi_{GS}(\mathbf{R}) = \begin{vmatrix} \phi_1(\mathbf{r}_1) & \dots & \phi_N(\mathbf{r}_1) \\ \dots & \dots & \dots \\ \phi_1(\mathbf{r}_N) & \dots & \phi_N(\mathbf{r}_N) \end{vmatrix} \quad . \tag{3.1}$$

   The majority of ground state condensed matter calculations stop at this level.

2. If desired, additional correlations may be included by multiplying the above wave function by a Jastrow factor, $\prod_{i,j} f(r_{ij})$, where f will also depend on the type of pair (electron-electron, electron-ion). Computing expectations exactly (within statistical uncertainty), with this type of wave function now requires Monte Carlo methods.

3. Finally diffusion Monte Carlo (Ceperley and Mitas, 1996; Foulkes *et al.*, 1999) methods using the nodes of this wave function to avoid the Fermion problem may be used to calculate the exact correlations consistent with the nodal structure.

The finite temperature theory proceeds similarly. Rather than the ground state wave function a thermal density matrix Eq. 2.5 is needed to compute the thermal averages of operators as shown in Eq. 2.7.

1. At the first level, this many body density matrix may be approximated by determinants of one-body density matrices, for both spin types, as well as the ions
$$\rho(\mathbf{R},\mathbf{R}';\beta) = \begin{vmatrix} \rho_1(\mathbf{r}_1,\mathbf{r}'_1;\beta) & \dots & \rho_1(\mathbf{r}_N,\mathbf{r}'_1;\beta) \\ \dots & \dots & \dots \\ \rho_1(\mathbf{r}_1,\mathbf{r}'_N;\beta) & \dots & \rho_1(\mathbf{r}_N,\mathbf{r}'_N;\beta) \end{vmatrix} . \tag{3.2}$$

2. The Jastrow factor can be extended to finite temperatures and the above density matrix multiplied by $\prod_{i,j} f(r_{ij}, r'_{ij};\beta)$. In particular, the high temperature density matrix used in path integral computations has this form.

3. Finally, the nodal structure from this variational density matrix (VDM) will be used in restricted path integral Monte Carlo simulations as described in chapter 4. This method has been extensively applied using the free particle nodes (Pierleoni *et al.*, 1994; Magro *et al.*, 1996). One aim of the approach is to provide more realistic nodal structures as input to PIMC.

This chapter considers the first level in this approach. The next section is devoted to a general variational principle which will be used to determine the many body density matrix. The principle is then applied to the problem of a single particle in an external potential and compared to exact results for the hydrogen atom density matrix. After a discussion of some general properties, many body applications are considered starting with a hydrogen molecule and then proceeding to warm, dense hydrogen. It is shown that the method and the ansatz considered can describe dense hydrogen in the molecular, the dissociated and the plasma regime. Structural and thermodynamic properties for this system over a range of temperatures (T$= 5\,000$ to $250\,000\,K$) and densities (electron sphere radius $r_s = 1.75$ to 4.0) are presented.

3.2 Variational Principle for the Many Body Density Matrix

The Gibbs-Delbruck variational principle for the free energy based on a trial density matrix

$$F \leq \mathrm{Tr}[\tilde{\rho}\mathcal{H}] + kT\ \mathrm{Tr}[\tilde{\rho}\ln\tilde{\rho}] \tag{3.3}$$

where

$$\tilde{\rho} = \rho/\mathrm{Tr}[\rho] \tag{3.4}$$

is well known and convenient for discrete systems (e.g. Hubbard models) but the logarithmic entropy term makes it difficult to apply to continuous systems. Here, we propose a simpler variational principle patterned after the Dirac-Frenkel-McLachlan variational principle used in the time dependent quantum problem (McLachlan, 1964). Consider the quantity

$$I\left(\frac{\partial\rho}{\partial\beta}\right) = \mathrm{Tr}\left(\frac{\partial\rho}{\partial\beta} + \mathcal{H}\rho\right)^2 \tag{3.5}$$

as a functional of

$$\Theta \equiv \frac{\partial\rho}{\partial\beta} \tag{3.6}$$

$$I\left(\Theta\right) = \mathrm{Tr}\left(\Theta + \mathcal{H}\rho\right)^2 \tag{3.7}$$

with ρ fixed. $I\left(\Theta\right) = 0$ when Θ satisfies the Bloch equation, $\Theta = -\mathcal{H}\rho$, and is otherwise positive. Varying I with Θ gives the minimum condition

$$\mathrm{Tr}\ \left[\delta\Theta\left(\Theta + \mathcal{H}\rho\right)\right] = 0 \quad . \tag{3.8}$$

This may be written in a real space basis as

$$\int\int \delta\Theta(\mathbf{R}', \mathbf{R}; \beta)\left[\Theta(\mathbf{R}, \mathbf{R}'; \beta) + \mathcal{H}\rho(\mathbf{R}, \mathbf{R}'; \beta)\right]\mathbf{dRdR}' = 0 \tag{3.9}$$

or, using the symmetry of the density matrix in $\mathbf{R}$ and $\mathbf{R}'$,

$$\int\int \delta\Theta(\mathbf{R}, \mathbf{R}'; \beta)\left[\Theta(\mathbf{R}, \mathbf{R}'; \beta) + \mathcal{H}\rho(\mathbf{R}, \mathbf{R}'; \beta)\right]\mathbf{dRdR}' = 0 \quad . \tag{3.10}$$

Finally, we may consider a variation at some arbitrary, fixed $\mathbf{R}'$ to get

$$\int \delta\Theta(\mathbf{R}, \mathbf{R}'; \beta)\left[\Theta(\mathbf{R}, \mathbf{R}'; \beta) + \mathcal{H}\rho(\mathbf{R}, \mathbf{R}'; \beta)\right]\mathbf{dR} = 0\ \ \forall\mathbf{R}'. \tag{3.11}$$

It should be noted that in going from Eq. 3.9 to Eq. 3.10 a density matrix symmetric in $\mathbf{R}$ and $\mathbf{R}'$ is assumed, which is a property of the exact density matrix. If the variational ansatz does not manifestly have this invariance Eq. 3.11 minimizes the quantity,

$$\int \left[\Theta(\mathbf{R},\mathbf{R}';\beta) + \mathcal{H}\rho(\mathbf{R},\mathbf{R}';\beta)\right]^2 \mathbf{dR} = 0 \quad . \tag{3.12}$$

This represents the actual variational principle that will be used throughout this work. By construction, it leads to an approximate solution of the Bloch equation, which we propose to derive by parameterizing the density matrix with a set of parameters q_i depending on imaginary time β and $\mathbf{R}'$,

$$\rho(\mathbf{R},\mathbf{R}';\beta) = \rho(\mathbf{R},q_1,\ldots,q_m) \quad \text{where} \quad q_i = q_i(\mathbf{R}';\beta), \quad i = 1,\ldots,m \tag{3.13}$$

so

$$\Theta(\mathbf{R},\mathbf{R}';\beta) = \sum_{i=1}^{m} \frac{\partial q_i(\mathbf{R}';\beta)}{\partial \beta}\frac{\partial \rho(\mathbf{R},q)}{\partial q_i} = \sum_{i=1}^{m} \dot{q}_i \,\frac{\partial \rho}{\partial q_i} \,. \tag{3.14}$$

In the imaginary time derivative Θ, only variations in $\dot{q}$ and not q are considered since ρ is fixed so,

$$\delta\Theta(\mathbf{R},\mathbf{R}';\beta) = \sum_{i=1}^{m} \delta\dot{q}_i(\mathbf{R}';\beta)\,\frac{\partial \rho(\mathbf{R},q)}{\partial q_i} \quad . \tag{3.15}$$

Using this in equation 3.11 gives for each variational parameter, since these are independent,

$$\int \frac{\partial \rho}{\partial q_j}\left(\Theta + \mathcal{H}\rho\right) \mathbf{dR} = 0 \ \ . \tag{3.16}$$

This is the imaginary-time equivalent to the approach of Singer and Smith (1986) for an approximate solution of the time dependent Schödinger equation using wave packets (see section 3.3). Introducing the notation

$$p_i \equiv \frac{\partial(\ln\rho)}{\partial q_i} \tag{3.17}$$

and using Eq. 3.14, the fundamental set of first order differential equations for the dynamics of the variation parameters in imaginary time follows from Eq.. 3.16 as,

$$\int p_j\,\rho\mathcal{H}\rho\;\mathbf{dR} \;+ \sum_{i=1}^{m} \dot{q}_i \int p_j\,p_i\,\rho^2\;\mathbf{dR} \;=\; 0 \tag{3.18}$$

or in matrix form

$$\frac{1}{2}\frac{\partial H}{\partial \vec{q}} + \overleftrightarrow{\mathcal{N}}\;\dot{\vec{q}} = 0 \tag{3.19}$$

where

$$H \equiv \int \rho\mathcal{H}\rho\;\mathbf{dR} \tag{3.20}$$

and the norm matrix

$$\mathcal{N}_{ij} \equiv \int p_i \, p_j \, \rho^2 \, \mathbf{dR} = \lim_{q' \to q} \frac{\partial^2 N}{\partial q_i \partial q_j'} \tag{3.21}$$

with

$$N \equiv \int \rho(\mathbf{R}, \vec{q}\,; \beta) \; \rho(\mathbf{R}, \vec{q}\,'\,; \beta) \; \mathbf{dR} \;\; . \tag{3.22}$$

The initial conditions follow from the free particle limit of the density matrix at high temperature, $\beta \to 0$,

$$\rho(\mathbf{R}, \mathbf{R}'; \beta) \to \exp\left[-(\mathbf{R} - \mathbf{R}')^2 / 4\lambda\beta \right] / (4\pi\lambda\beta)^{3N/2} \quad \text{where} \quad \lambda = 1/2m \quad . \tag{3.23}$$

Various ansatz forms for ρ may now be used with this approach. After considering the analogy to real time wave packet molecular dynamics, the principle is first applied to the problem of a particle in an external field.

3.3 Analogy to Real-Time Wave Packet Molecular Dynamics

Wave packet molecular dynamics (WPMD) was first used by Heller (1975) and later applied to scattering processes in nuclear physics (Feldmeier, 1990) and plasma physics (Klakow *et al.*, 1994b; Ebeling and Militzer, 1997). An ansatz for the wave function $\psi(q_\nu)$ is made and the equation of motions for the parameters q_ν in real time can be derived from the principle of stationary action (Feldmeier, 1990),

$$\delta \int dt \, L = 0 \quad , \quad L\left(q_\nu(t), \dot{q}_\nu(t)\right) = \left\langle \psi \left| i\partial_t - \mathcal{H} \right| \psi \right\rangle \tag{3.24}$$

This leads to a set of first order equations, which provides an approximate solution of the Schrödinger equation. However, this principle cannot be directly applied to the Bloch equation because there is no imaginary part in the density matrix. For this reason, we followed in our derivation in section 3.2 the principle by McLachlan (1964), which minimizes the quantity

$$\int \left| \mathcal{H}\psi - i\Theta \right|^2 dt, \quad \Theta = \frac{\partial \psi}{\partial t} \; . \tag{3.25}$$

This method was employed by Singer and Smith (1986) to obtain the dynamical equations in real time.

The VDM approach and WPMD method share the zero temperate limit, which is given by the Rayleigh-Ritz principle (see section 3.5.1). At high temperature, the width of wave packets in WPMD grows without limits, which is a known problem of this method (Militzer, 1996; Knaup *et al.*, 1999). In the VDM approach, the correct high temperature limit of free particles is included. The average width shown in Fig. 3.11 can be used to verify the attempts to correct the dynamics of the real time wave packets by Knaup *et al.* (1999).

3.4 Example: Particle in an External Field

As a first example, we apply this method to the problem of one particle in an external potential

$$\mathcal{H} = -\lambda \nabla^2 + V(r) \quad . \tag{3.26}$$

The one-particle density matrix will be approximated as a Gaussian with mean $\mathbf{m}$, width w and amplitude factor D,

$$\rho_1(\mathbf{r}, \mathbf{r}', \beta) = (\pi w)^{-3/2} \exp\left\{ -\frac{1}{w}(\mathbf{r}-\mathbf{m})^2 + D \right\} \tag{3.27}$$

as variational parameters. The initial conditions at $\beta \longrightarrow 0$ are $w = 4\lambda\beta$, $\mathbf{m} = \mathbf{r}'$ and $D = 0$ in order to regain the correct free particle limit, Eq. 3.23. For this ansatz H, defined in Eq. 3.20 as

$$H \equiv \int \rho \mathcal{H} \rho \, \mathbf{dr} = \left(\frac{3\lambda}{w} + V^{[0]} \right) \frac{e^{2D}}{(2\pi w)^{3/2}} \tag{3.28}$$

where

$$V^{[n]} \equiv \left(\frac{2}{\pi w} \right)^{3/2} \int (\mathbf{r}-\mathbf{m})^n V(r) e^{-2(\mathbf{r}-\mathbf{m})^2/w} \mathbf{dr} \tag{3.29}$$

and

$$N \equiv \int \rho \rho' \mathbf{dr} = [\pi(w+w')]^{-3/2} \exp\left\{ -(\mathbf{m}-\mathbf{m}')^2/(w+w') \right\} \exp(D+D') \quad . \tag{3.30}$$

From Eq. 3.19, the equations for the variational parameters are,

$$\dot{w} = 4\lambda + 2wV^{[0]} - \frac{8}{3}V^{[2]} \tag{3.31}$$

$$\dot{\mathbf{m}} = -2\mathbf{V}^{[1]} \tag{3.32}$$

$$\dot{D} = \frac{1}{2}V^{[0]} - \frac{2}{w}V^{[2]} \quad . \tag{3.33}$$

In absence of a potential, the exact free particle density matrix is recovered. The harmonic oscillator case is also correct since the Gaussian approximation is exact there. For a hydrogen atom, $\lambda = 1/2$, $V(r) = -1/r$ and

$$
\begin{aligned}
V^{[0]} &= -\frac{1}{m}\mathrm{erf}\left(m\sqrt{2/w}\right) && (3.34)\\
\mathbf{V}^{[1]} &= \frac{\mathbf{m}}{m^3}\frac{w}{4}\left[\mathrm{erf}\left(m\sqrt{2/w}\right) - \sqrt{\frac{8}{\pi w}}e^{-2m^2/w}\right] && (3.35)\\
V^{[2]} &= \sqrt{\frac{w}{2\pi}}e^{-2m^2/w} + \frac{3w}{4}V^{[0]} \quad . && (3.36)
\end{aligned}
$$

At low temperature, the density matrix as a function of $\mathbf{r}$ goes to the ground state wave function as discussed in more detail in the next section. One expects this to be a fixed point of the dynamics of the parameters $\mathbf{m}$ and w determined by $\dot{\mathbf{m}} = 0$ and $\dot{w} = 0$ while $\dot{D} = -E_0$. The $\beta \to \infty$ fixed point: $\mathbf{m} = 0$, $w = 9\pi/8$, $\dot{D} = 4/3\pi$ corresponds to the well known Rayleigh-Ritz variational result for a Gaussian trial wave function

$$\Psi_0(\mathbf{r}) = \left(\frac{4}{3\pi}\right)^{3/2} \exp(-8r^2/9\pi) \; . \qquad (3.37)$$

In ground state variational studies, addition of two more Gaussians brings the ground state energy to within 0.6% of the exact value and similar improvement would be obtained here.

Results at finite β require a numerical solution, which is illustrated in the figure below comparing the Gaussian variational density matrix with the exact (Pollock, 1988) and the free particle density matrix at several temperatures for the initial condition $\mathbf{r}' = 1$. At high temperatures ($\beta = 0.05$ and $\beta = 0.25$) the Gaussian approximation correctly reproduces the limiting free particle density matrix. At lower temperatures, the cusp in the exact density matrix due to the Coulombic singularity at the proton becomes evident and the peak shifts to the origin somewhat faster than the Gaussian variational approximation. As β increases the exact result grows faster than the variational since the correct energy, -0.5, is lower than $-4/3\pi$ but the Gaussian variational approximation remains rather accurate for $r > 1$. The free particle density matrix remains centered at $\mathbf{r} = 1$ and beyond $\beta = 0.5$ ($T = 54.4$ eV) bears little resemblance to the correct result.

3.5 Variational Density Matrix Properties

3.5.1 Zero Temperature Limit

In the preceding section, it was shown that for the hydrogen atom the Gaussian variational density matrix, as a function of $\mathbf{R}$ converges at low temperature to the

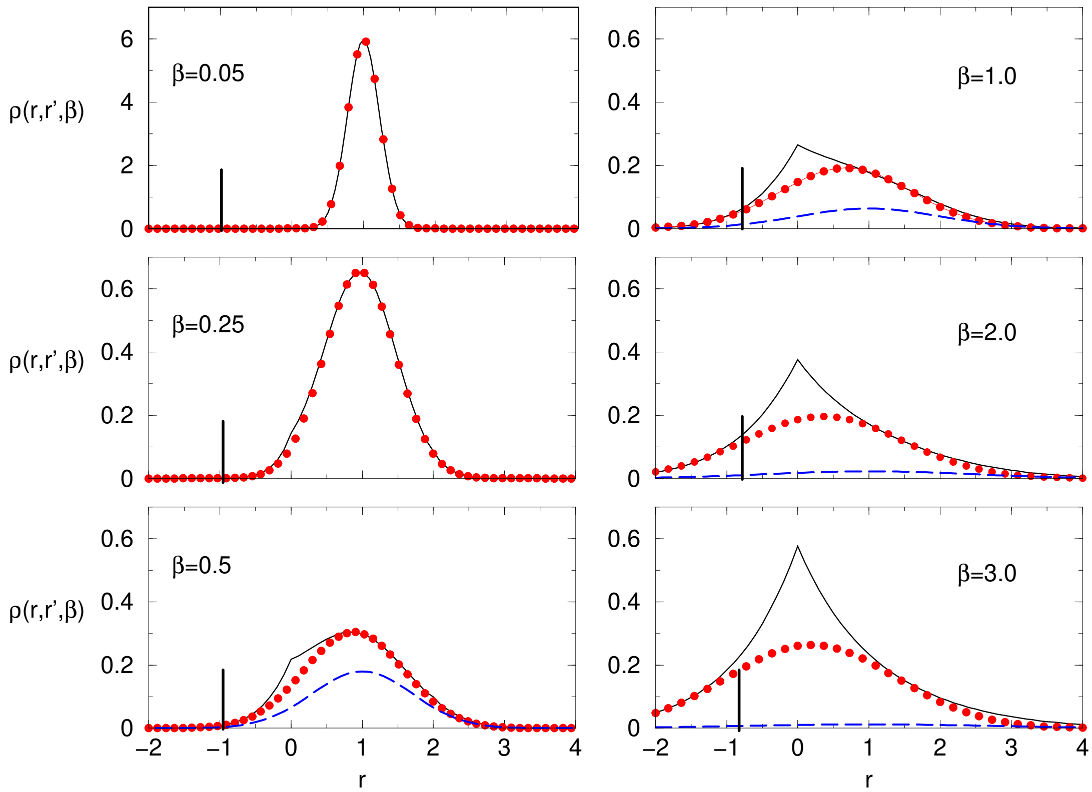

Figure 3.1: Comparison of the Gaussian variational approximation (circles) with the exact density matrix $\rho(\mathbf{r}, \mathbf{r}'; \beta)$ (solid line) for a hydrogen atom. The free particle density matrix (dashed line) is also shown. The plotted r is along the line from the proton at the origin (marked by the vertical bar) through the initial electron position $\mathbf{r}' = 1$.

Gaussian ground state wave function given by the Rayleigh-Ritz variational principle. It is generally true that the Rayleigh-Ritz ground state corresponds to the zero temperature limit of the VDM as we now show.

The Rayleigh-Ritz principle states that for any real parameterized wave function $\Psi(\mathbf{R}, q_1, \ldots, q_m)$ the variational energy

$$E(\{q\}) = \frac{\int \psi(\mathbf{R}) \mathcal{H} \psi(\mathbf{R}) \; \mathbf{dR}}{\int \psi(\mathbf{R})^2 \; \mathbf{dR}} \tag{3.38}$$

is greater than or equal to the true ground state energy even at the minimum determined by

$$\frac{\partial}{\partial q_k} \, E(\{q\}) = 0 \;\; \forall k \; . \tag{3.39}$$

For the VDM ansatz, an amplitude parameter D is assumed such that

$$\rho(\mathbf{R}, \mathbf{R}'; \beta) = e^{D(\mathbf{R}'; \beta)} \tilde{\rho}(\mathbf{R}, \{q(\mathbf{R}'; \beta)\}) \; . \tag{3.40}$$

As in the one particle example, it is expected that at low temperature, $\beta \to \infty$, the other $\dot{q}_k \to 0$ while $\dot{D} \to$ constant. From this assumption, Eq. 3.19 implies that as $\beta \to \infty$

$$\frac{\partial H}{\partial q_k} + \dot{D}\frac{\partial N}{\partial q_k} = 0 \tag{3.41}$$

for all variational parameters, where we have defined $H \equiv \int \rho \mathcal{H} \rho \, \mathbf{dR}$ and $N \equiv \int \rho^2 \, \mathbf{dR}$. Since $\partial H/\partial D = 2H$ and $\partial N/\partial D = 2N$, Eq. 3.41 for $q_k \equiv D$ implies $\dot{D} = -H/N \equiv -E_0$. So Eq. 3.41 may be rewritten as

$$\frac{\partial}{\partial q_k}\left(\frac{H}{N}\right) = 0 \tag{3.42}$$

at the $\beta \to \infty$ fixed point. With the correspondence

$$\rho(\mathbf{R}, \{q(\mathbf{R}', \beta)\}) \to e^{D(\mathbf{R}';\beta)}\psi(\mathbf{R}, \{q\}) \quad , \tag{3.43}$$

this is equivalent to Eq. 3.39 and thus the Rayleigh-Ritz ground state corresponds to a zero temperature fixed point in the dynamics of the parameters.

D is a function of $\mathbf{R}'$ and β, which is calculated by integrating from $\beta = 0$ with Eq. 3.23 as initial conditions. The zero temperature limit of $\dot{D}$ is a constant, $-E_0$, which means in the low temperature limit D can written as

$$D(\mathbf{R}'; \beta) = -\beta E_0 + f(\mathbf{R}') \quad . \tag{3.44}$$

The function $f(\mathbf{R}')$ can be rewritten as,

$$f(\mathbf{R}') = \ln\{\psi_0(\mathbf{R}')\,[\,1 + \delta(\mathbf{R}')\,]\} \quad , \tag{3.45}$$

where the function $\delta(\mathbf{R}')$ is introduced to describe the variational error in the solution of the Bloch equation. It is identical to zero if the variational ansatz includes the exact solution. It leads to loss of symmetry in $\mathbf{R}$ and $\mathbf{R}'$, which will discussed in the next section. Eq. 3.43 now reads,

$$\rho(\mathbf{R}, \mathbf{R}', \beta \to \infty) = e^{-\beta E_0}\psi_0(\mathbf{R})\psi_0(\mathbf{R}')\,[1 + \delta(\mathbf{R}')] \quad . \tag{3.46}$$

For certain potentials, several fixed points of the dynamics can exist. From Eq. 3.46, it follows that only the lowest energy state contributes to physical observables calculated from Eq. 2.4. This completes the argument that the zero temperature limit of the VDM corresponds to the Rayleigh-Ritz ground state.

In the case of an anti-symmetrized ansatz for the density matrix, it can be shown that the fixed point of the dynamics in imaginary time corresponds to the Rayleigh-Ritz ground state for an anti-symmetrized wave function.

3.5.2 Loss of Symmetry

The exact density matrix is symmetric under $\mathbf{R} \leftrightarrow \mathbf{R}'$. Since we have singled out $\mathbf{R}'$ as the initial point for the imaginary time dynamics, it is not clear that the approximation given in Eq. 3.27 automatically satisfies this condition. For the free particle limit and the harmonic oscillator, where the Gaussian is the exact solution, it obviously does but in general it does not.

As a specific example, we consider again the ground state limit of the hydrogen atom in the Gaussian approximation. Using the ground state values for the variational parameters, $\mathbf{m} = 0$ and $w = 9\pi/\beta$, Eq. 3.27 becomes,

$$\lim_{\beta\to\infty} \rho(\mathbf{r}, \mathbf{r}'; \beta) = e^{D(r';\beta)} \, (8/9\pi^2)^{3/2} e^{-8r^2/9\pi} \; . \tag{3.47}$$

For this to be symmetric under $\mathbf{r} \leftrightarrow \mathbf{r}'$, we must have

$$\lim_{\beta\to\infty} D(r'; \beta) = -8r'^2/9\pi + c(\beta) \tag{3.48}$$

and from the result for $\dot{D}$, $\lim_{\beta\to\infty} c(\beta) = 4\beta/3\pi + c_1$.

Figure 3.2 compares the $D(r, \beta)$ from the Gaussian VDM with Eq. 3.48 using $c(\beta) = 4\beta/3\pi + 3/2 \ln 2$.

There are several consequences of this small violation of $\mathbf{R} \leftrightarrow \mathbf{R}'$ symmetry. As shown generally in the section above, in the $\beta \to \infty$ limit $-\dot{D}$ is the Rayleigh-Ritz variational ground state energy for a Gaussian wave function, which for the hydrogen atom is $E_0 = -4/3\pi = -0.4244$. Because of the loss of symmetry this is not the same as the energy given by the estimator

$$\langle E \rangle = \langle \mathcal{H} \rangle \equiv \frac{\mathrm{Tr}[\mathcal{H}\rho]}{\mathrm{Tr}[\rho]} \tag{3.49}$$

in the $\beta \to \infty$ limit, which for the hydrogen atom gives the more accurate result $\langle E \rangle = -0.4709$. This will be seen again below for the hydrogen molecule where Eq. 3.49 also gives more accurate ground state energies. Other consequences are less pleasant. Although the energy is more accurate the virial theorem, $\langle K \rangle = -\langle U \rangle / 2$, between the kinetic and potential energy is violated by about 3% (while both are more accurate than the usual ground state variational Gaussian result). This has consequences for calculating the equation of state particularly at low density. Slightly more complicated, explicitly symmetric forms for the VDM could be used but in this paper we will continue to explore the basic Gaussian approximation.

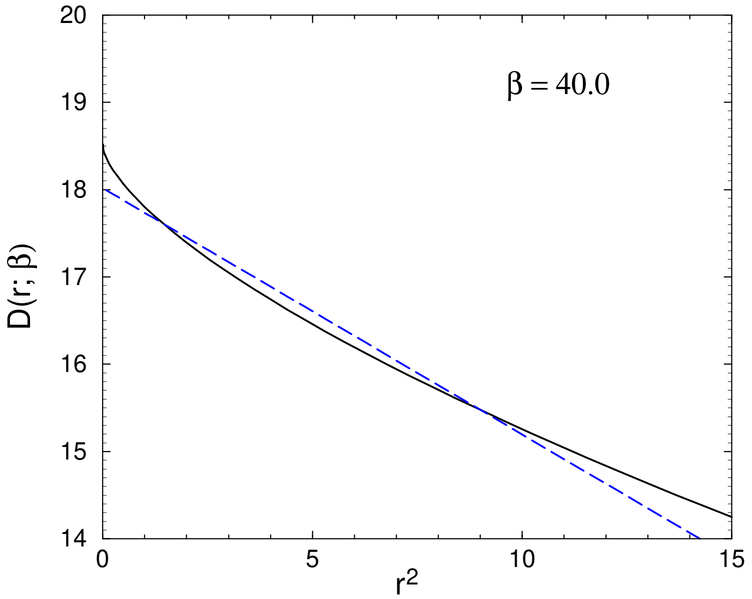

Figure 3.2: $D(r, \beta)$ from the Gaussian approximation in the ground state limit (solid line) of the hydrogen atom. Deviations of this function from linearity indicate a breakdown of symmetry in the Gaussian approximation for $\rho(\mathbf{r}, \mathbf{r}'; \beta)$. The dashed line is $-8r^2/9\pi + 4\beta/3\pi + 3/2 \ln 2$ expected from the Rayleigh-Ritz ground state Eq. 3.37.

3.5.3 Thermodynamic Estimators

Since the VDM, except in the simplest cases, is not exact various estimators for the same quantity will differ. For example the variational principle introduced in section II consists essentially in globally minimizing the squared difference between $\partial\rho/\partial\beta$ and $\mathcal{H}\rho$, either of which can be used in estimating the energy. As mentioned above the energy estimator Eq. 3.49 and its kinetic and potential energy pieces do not automatically satisfy the virial theorem for Coulomb systems at low density. As an alternative to Eq. 3.49, one can use the thermodynamic estimators,

$$\begin{aligned} \langle E \rangle &= -\left\langle \frac{\partial}{\partial\beta} \ln \rho \right\rangle, && (3.50) \\ \langle K \rangle &= -\frac{\lambda}{\beta} \left\langle \frac{\partial}{\partial\lambda} \ln \rho \right\rangle, && (3.51) \\ \langle V \rangle &= -\frac{e^2}{\beta} \left\langle \frac{\partial}{\partial e^2} \ln \rho \right\rangle && (3.52) \end{aligned}$$

for the total, kinetic and potential energy where $\langle \ldots \rangle$ denote thermal averages calculate from Eq. 2.4. These estimators satisfy

$$\langle E \rangle = \langle K \rangle + \langle V \rangle \tag{3.53}$$

by the following argument. Any function $f = f(\beta\lambda, \beta e^2)$ satisfies

$$\beta\frac{\partial f}{\partial\beta} = \lambda\frac{\partial f}{\partial\lambda} + e^2\frac{\partial f}{\partial e^2} \quad . \tag{3.54}$$

From Eq. 3.19 it follows that all parameters $q_i = q_i(\mathbf{R}'; \beta, \lambda, e^2)$ have this property and therefore so does the variational density matrix.

In the zero temperature limit, the thermodynamic estimators satisfy the virial theorem, which is also satisfied by any exact and any variational Rayleigh-Ritz ground state. From the zero temperature limit of the VDM given by Eq. 3.46 and the $1/\beta$ factor in Eqs. 3.51 and 3.52, it is seen that the symmetry error $\delta(\mathbf{R}')$ is unimportant in this limit. It should be noted that calculating the derivatives for $\langle K\rangle$ and $\langle V\rangle$ increases the numerical work. The pressure is estimated from

$$3\,\langle P\rangle\,\hat{V} = 2\,\langle K\rangle + \langle V\rangle \ , \tag{3.55}$$

where $\hat{V}$ is the volume of the simulation cell.

3.6 Variational Many-Particle Density Matrix

We represent the many-particle density matrix by a determinant of one-particle density matrices (Eq. 3.79). It can written as,

$$\begin{aligned} \rho(\mathbf{R}, \mathbf{R}', \beta) &= \sum_{\mathcal{P}} \epsilon_{\mathcal{P}} \prod_k \rho_1(\mathbf{r}_k, \mathbf{r}'_{\mathcal{P}_k}, \beta) & (3.56)\\ &= \sum_{\mathcal{P}} \epsilon_{\mathcal{P}} e^D \prod_k \left(\pi w_{\mathcal{P}_k}\right)^{-3/2} \exp\left\{-\frac{1}{w_{\mathcal{P}_k}}(\mathbf{r}_k - \mathbf{m}_{\mathcal{P}_k})^2\right\} \ , & (3.57)\end{aligned}$$

where a factor $1/N!$ was dropped. The permutation sum is over all permutations of identical particles (e.g. same spin (S_z) electrons) and the permutation signature $\epsilon_{\mathcal{P}} = \pm 1$. The initial conditions for Eq. 3.19 are $w_k = 0$, $\mathbf{m}_k = \mathbf{r}'_k$, and $D = 0$. For this ansatz the generator of the norm matrix, Eq. 3.22 is,

$$N = \exp(D + D') \sum_{\mathcal{P}} \epsilon_{\mathcal{P}} \prod_k [\pi(w_k + w'_{\mathcal{P}_k})]^{-3/2} \exp\left\{-(\mathbf{m}_k - \mathbf{m}'_{\mathcal{P}_k})^2/(w_k + w'_{\mathcal{P}_k})\right\} \ . \tag{3.58}$$

For a periodic system the above equation is also summed over all periodic simulation cell vectors, $\mathbf{L}$, with $\mathbf{m}_k - \mathbf{m}_{\mathcal{P}_k} \rightarrow \mathbf{m}_k - \mathbf{m}_{\mathcal{P}_k} + \mathbf{L}$. If only the identity permutation is considered the norm matrix is easily inverted so that Eq. 3.19 gives

$$\dot{w}_k = -2w_k H_D - \frac{8}{3}w_k^2 H_{w_k} \tag{3.59}$$

$$\dot{\mathbf{m}}_k = -w_k H_{\mathbf{m}_k} \tag{3.60}$$

$$\dot{D} = -\left(\frac{3}{2}n+1\right) H_D - 2\sum_{i=1}^{n} w_i H_{w_i} \quad , \tag{3.61}$$

$$\text{where} \qquad H_{q_k} = \frac{1}{2}\frac{\partial H}{\partial q_k} \; . \tag{3.62}$$

For systems of electrons and ions the full expression for H_{q_k} and the norm matrix are derived in App. A.

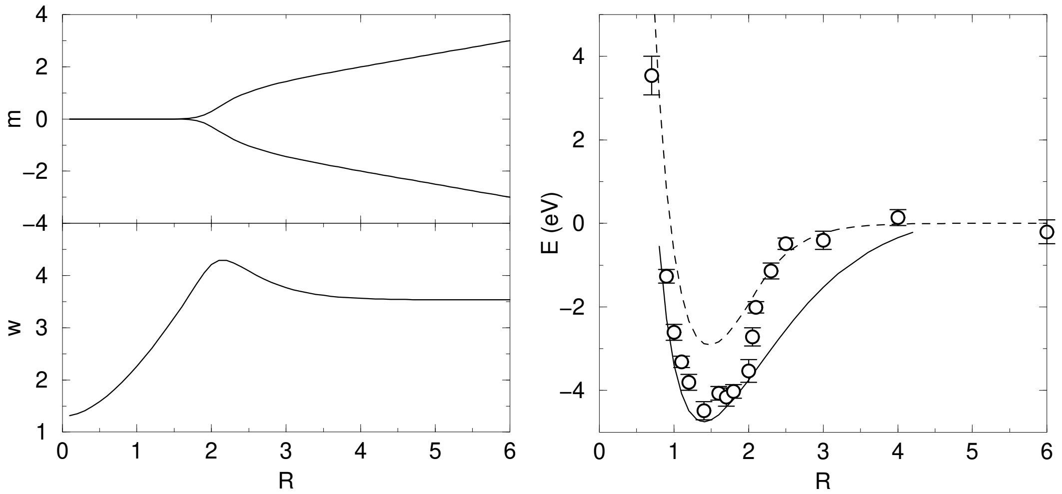

Figure 3.3: Gaussian approximation for the ground state of a hydrogen molecule for bond length R. The top left panel shows the Gaussian mean parameter $\mathbf{m}$ for the two electrons. These stay in the center of the bond ($\mathbf{m} = 0$) until about $R = 2$ and then attach themselves to the separating protons ($\pm\ R/2$). The width parameter, displayed in the lower left panel, makes the transition from the optimal value for a helium atom, $R = 0$, to the hydrogen atom result $w = 9\pi/8$ at large R. The right panel shows the dissociation energy for the singlet state computed from Eq. 3.49 (open circles with error bars) and the thermodynamic estimator ($-dD/d\beta$) (dashed line) compared to the exact results of Kolos and Roothan (solid line).

Application to an isolated hydrogen molecule at low temperature is shown in Figure 3.3. This is for the singlet state (anti-parallel electron spins). The triplet state is considered later after a discussion of how to treat permutation terms in the parameter equations. The bond length at minimum energy is 1.47, compared with the experimental value of 1.40. The direct energy estimator Eq. 3.49 gives a dissociation energy of 4.50 eV at the minimum compared to the experimental value of 4.75 eV. Beyond $R = 2$, the energy rises quickly toward the value given by the Rayleigh-Ritz estimator $-dD/d\beta$.

3.7 Antisymmetry in the Parameter Equations

The determinantal form for the VDM, Eq. 3.56, is correctly antisymmetric under exchange of identical particles. Since ion exchange effects are negligible at the temperatures considered here these are ignored.

The determinantal form leads to $N!$ terms in the equations of motion for the variational parameters presented in appendix A. It was originally hoped that exchange effects could be ignored in these equations while retaining the full determinantal form for the VDM but this leads to an instability in fermionic systems, e.g. it results in an unphysical strong attraction between two hydrogen molecules.

A practical means of treating all exchange terms, in particular terms involving the potential energy, in the variational parameter equations was not found. Instead it was necessary to use an approximation similar to that used in the real time computations (Klakow *et al.*, 1994b; Knaup *et al.*, 1999): only pair exchanges in the kinetic energy terms were retained. This will be illustrated for the hydrogen molecule after first giving the explicit form for this correction. It is stressed that, unlike the real time computations, once the variational parameters are determined the full determinantal form is then used in calculating the various averages.

For two particles with parallel spin, the correction term to the kinetic energy is given by,

$$\begin{aligned} \Delta K &= \frac{N_I}{N_{AS}} \int \mathbf{dR}\, \rho_{AS}\, \hat{K}\, \rho_{AS} \quad - \quad \int \mathbf{dR}\, \rho_I\, \hat{K}\, \rho_I && (3.63) \\ \rho_{AS} &= \rho_1(\mathbf{r}_1)\rho_2(\mathbf{r}_2) - \rho_2(\mathbf{r}_1)\rho_1(\mathbf{r}_2) \quad , \quad \rho_I = \rho_1(\mathbf{r}_1)\rho_2(\mathbf{r}_2) && (3.64) \\ N_{AS} &= \int \mathbf{dR}\, \rho_{AS}^2 \quad , \quad N_I = \int \mathbf{dR}\, \rho_I^2 && (3.65) \end{aligned}$$

For the Gaussian ansatz in Eq. 3.56 it becomes,

$$\begin{aligned} \Delta K &= -\frac{4\lambda N_I}{w N_Q} \left[3\left(1 - \tilde{w}^2\right) - Q^2 \right] \quad , && (3.66) \\ w &= w_1 + w_2 \quad , \quad \tilde{w} = \frac{w}{2\sqrt{w_1 w_2}} \quad , && (3.67) \\ Q^2 &= \frac{2}{w}\left(\mathbf{m}_1 - \mathbf{m}_2\right)^2 \quad , \quad N_Q = \tilde{w}^3 e^{Q^2} - 1 \quad . && (3.68) \end{aligned}$$

The corrections to the norm matrix $\mathcal{N}$ are neglected in order to keep its analytically invertible form. The corrections to H_{q_k} in Eq. 3.62 are given by

$$\Delta K_{q_k} = \frac{1}{2N_I} \frac{\partial}{\partial q_k} \Delta K \tag{3.69}$$

The correction to dynamics of the parameters follow from Eq. 3.59 to 3.61,

$$\Delta\dot{w}_1 = -2\,w_1\left(\Delta K_D + \frac{4}{3}w_1\,\Delta K_{w_1}\right) \tag{3.70}$$

$$\Delta\dot{\mathbf{m}}_1 = -w_1\,\Delta K_{\mathbf{m}_1} \tag{3.71}$$

$$\Delta\dot{D} = -2\left(\Delta K_D + w_1\,\Delta K_{w_1} + w_2\,\Delta K_{w_2}\right) \quad . \tag{3.72}$$

These equations lead to an effective repulsion between the Gaussians for two electrons with parallel spin if there is significant overlap. As a example of this effect the variational parameters for the singlet and triplet states of the hydrogen molecule are compared in Fig. 3.4. For the triplet state parameters, the solution including full exchange effects (long dashed line) are compared with those obtained in the kinetic pair exchange approximation (dot-dashed line). The approximation now prevents the Gaussian means for the same spin electrons from collapsing to the bond center at lower temperature and is numerically close to the solution for full exchange.

Even at the lowest temperature considered here in the dense hydrogen simulations (5000 K) exchange effects between same spin electrons are negligible beyond a few angstroms, i.e. one or perhaps two nearest neighbors. Fig. 3.4 for the triplet state thus overestimates the effect likely in dense hydrogen. The main effect of including exchange in the parameter equations is probably to prevent the instability mentioned above.

Fig. 3.5 shows an energy comparison for the triplet ground state of the hydrogen molecule. First, we compare the Gaussian approximation using only the kinetic exchange term in the parameter equations. For the direct estimator, Eq. 3.49, one finds fairly good agreement with the accurate quantum chemistry result (Kolos and Roothan, 1969). The thermodynamic estimator gives a somewhat more repulsive triplet interaction for $R > 2$. Considering also the Coulomb exchange terms in the Gaussian approximation leads to the dot-dashed line for the thermodynamic estimator. We conclude that leaving out the Coulomb exchange terms in the parameter equations for efficiency reasons is a reasonable approximation in many-particle simulations.

3.8 Results from Many-Particle Simulations

In this section, we report results from VDM Monte Carlo simulation with 32 pairs of protons and electrons in the temperature and density range of $5\,000\,\mathrm{K} \leq T \leq 250\,000\,\mathrm{K}$ and $1.75 \leq r_s \leq 4.0$. Particle configurations are generated by sequencing

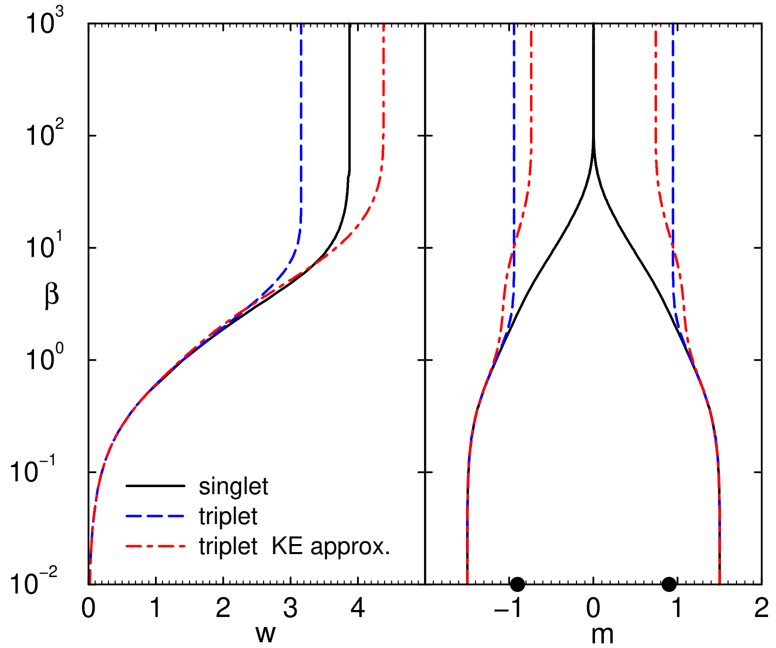

Figure 3.4: Effect of antisymmetry on the density matrix parameters, width and mean, for a hydrogen molecule. The protons (large black dots along x axis) are separated by 1.8 and the initial electron positions $r_e(\beta = 0) = \pm 1.5$ along the molecular axis. The solid line for the singlet state (electron spins anti-parallel) shows both electrons centered in the molecular bond at low temperatures (large β). In the triplet state (parallel electron spins), the electrons are centered close to the protons (long dashed line). The approximation that includes only kinetic exchanges (dot-dashed line) gives a similar result for the mean, with the electrons centered slightly inside the protons but overestimates the Gaussian width (left panel). At high temperature ($\beta \leq 4$), exchange is unimportant and the parameters are nearly the same for all cases.

over all particles, giving the particle a uniform displacement, computing the new density matrix from Eqs. 3.19 and 3.13, and accepting or rejecting the new configuration by the Metropolis algorithm. This is completely analogous to the usual Monte Carlo ground state variational calculations except for the additional work of determining the variational parameters based on the proposed configuration.

Although the Gaussian ansatz VDM will be seen to provide a reasonable model for hydrogen over the full density and temperature regime, the main purpose in presenting these results is to serve as a base for documenting future improvements from better VDMs and the application to PIMC.

The proton-proton pair correlation functions are shown in Fig. 3.6. For temperatures below 20 000 K, a peak emerges near 1.4 that demonstrates clearly the formation of molecules. The comparison with PIMC simulations (Magro *et al.*, 1996; Militzer and Ceperley, 2000) at low density shows that the peak positions agree well but PIMC

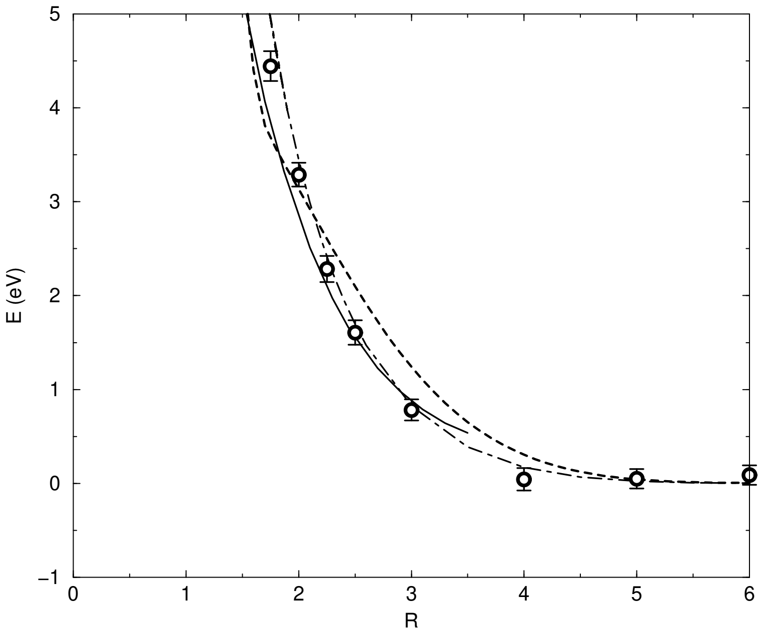

Figure 3.5: Energy of repulsion for the triplet ground state of the hydrogen molecule for bond length R. The thermodynamic (dashed line) and the direct estimator, Eq. 3.49, (circles with error bars) for the Gaussian approximation using the kinetic exchange term in the parameter equations are compared with the Kolos and Roothan results (solid line). The thermodynamic estimator for the Gaussian approximation with all exchange terms is shown by the dot-dashed line.

predicts a significantly bigger height indicating a larger number of molecules. This could be explained by the missing correlations in the VDM ansatz.

At a density of $r_s = 2.0$, proton-proton pair correlation functions from PIMC and VDM are almost identical. If the peak is sufficiently separated from the remaining curve, the area under the peak multiplied by the density gives an estimate for the molecular fraction. By comparing the estimate for different densities at 5 000K, one finds that the molecular fraction is diminished when the density is lowered below that corresponding to $r_s = 2.0$. This effect is well-known and is a result of the increased entropy of dissociated molecules, which leads to complete dissociation and ionization in the low density limit at non-zero temperatures.

Considerable differences between the proton-proton pair correlation functions are found at $r_s = 1.75$ below $T = 20\,000\,K$ where VDM shows a fair number of molecules while PIMC predicts a metallic fluid where all bonds are broken as a result of pressure dissociation (Magro *et al.*, 1996; Militzer *et al.*, 1999). This effect has to be verified by PIMC simulations with VDM nodes because free particle nodes could enhance the transition to a metallic state. Proton-proton pair correlation functions from additional VDM simulations for $r_s = 1.5, 1.25, \text{and} 1.0$ are shown in figure 3.7. The

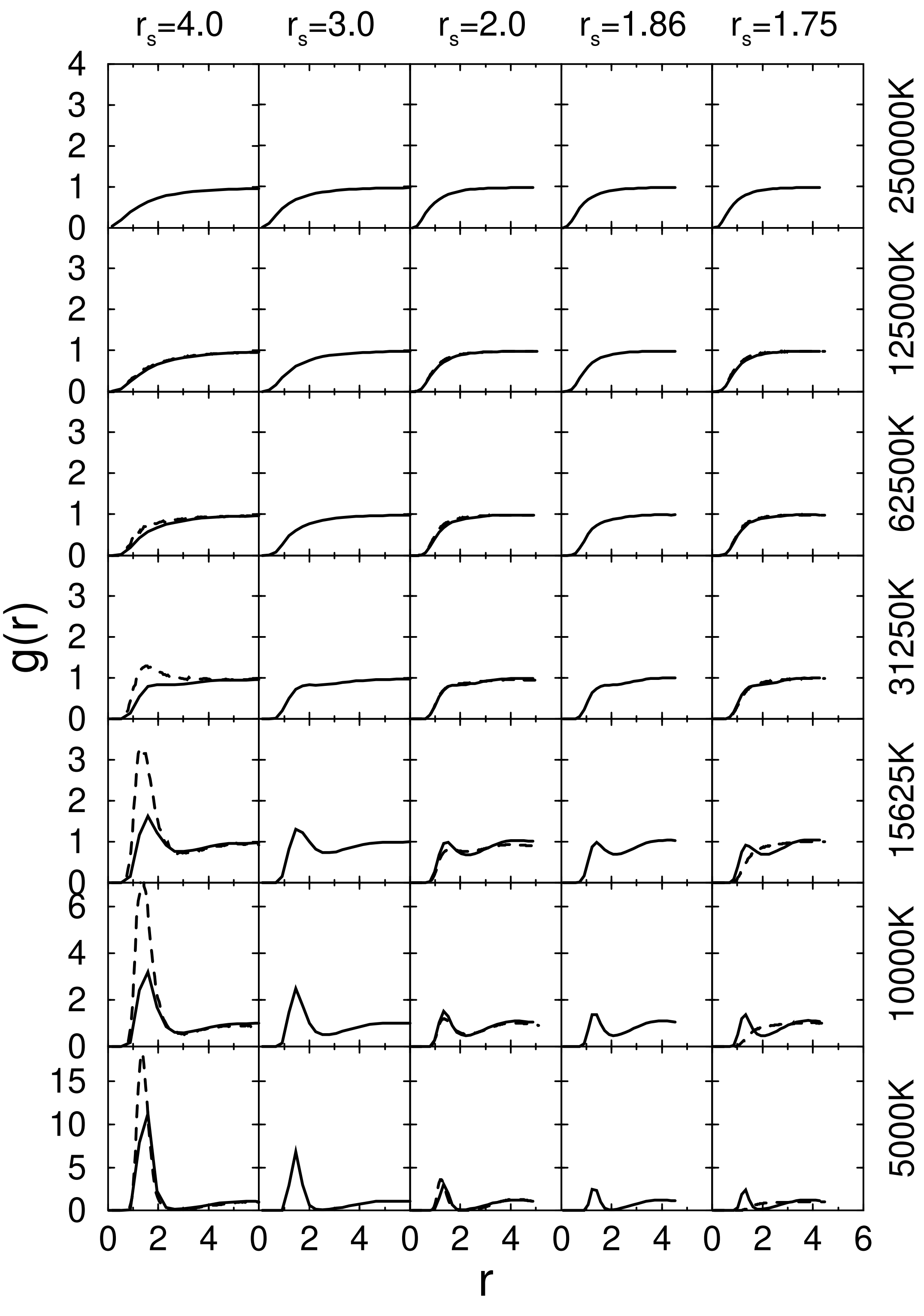

Figure 3.6: Proton-proton pair correlation function from VDM (solid line) and PIMC (dashed lines at r_s=1.75, 2.0, and 4.0 for $T \leq 125\,000\,\text{K}$).

VDM method exhibits a smooth transition from a molecular to a atomic structure, in which the molecular binding is gradually reduced with increasing density.

The position of the peak of the proton-proton pair correlation functions shifts from 1.45 at the lowest density, corresponding to $r_s = 4.0$, to 1.3 at $r_s = 1.75$. The same trend has been found in the PIMC simulations (Magro *et al.*, 1996) but the opposite was reported in (Galli *et al.*, 2000; Rescigno, 1999).

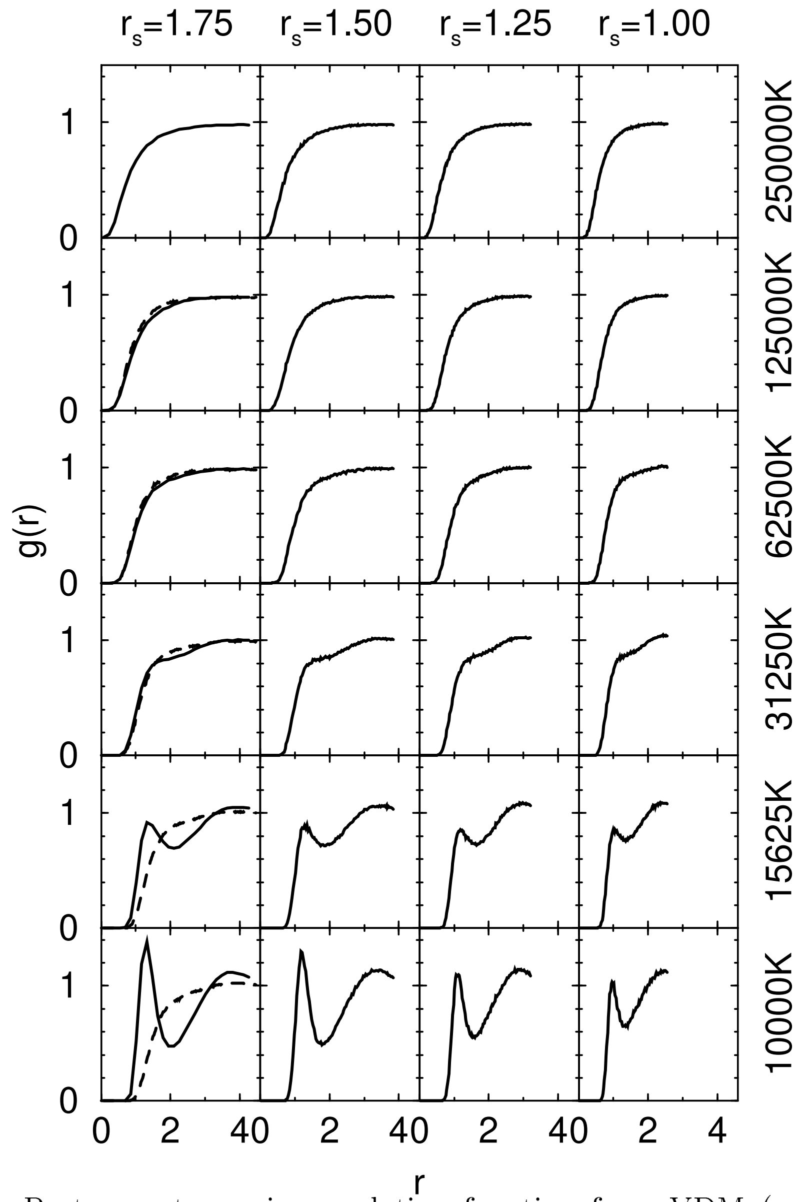

Figure 3.7: Proton-proton pair correlation function from VDM (solid line) and PIMC (dashed lines at r_s=1.75 for $T \leq 125\,000$ K).

In the proton-electron pair correlation functions shown in Fig. 3.8, one finds a strong attraction present even at high temperatures such as 250 000 K. At low temperatures, the electrons are bound in atoms and molecules. This pair correlation

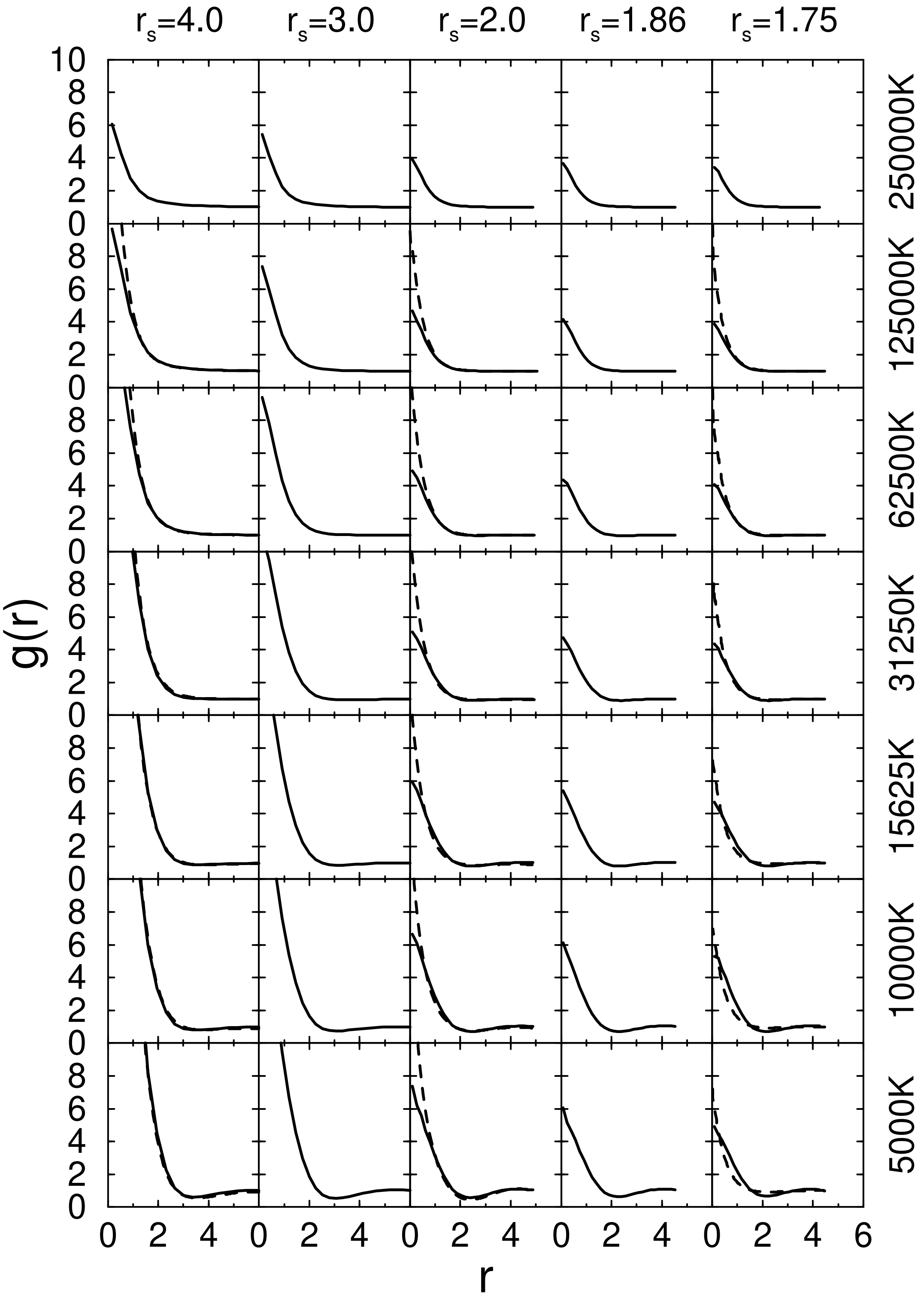

Figure 3.8: Proton-electron pair correlation functions from VDM (solid line) and PIMC (dashed lines at r_s=1.75, 2.0, and 4.0 for $T \leq 125\,000\,\mathrm{K}$).

function does not show a clear distinction between the two cases. From studying the height of the peak at the origin multiplied by the density, one can make comparisons of the number of bound electrons at low temperature. Similar to the molecular fraction, one finds a reduction of bound electrons with decreasing density below that corresponding to $r_s = 2.0$. The comparison with PIMC shows that VDM underestimates the height of the peak. This is probably a result of the Gaussian ansatz, which does not satisfy the cusp condition at the proton.

Fig. 3.9 shows the effect of the Pauli exclusion principle leading to a strong repulsion for electrons in the same spin state. This effect is not present in the interaction of electrons with anti-parallel spin displayed in Fig. 3.10. There one observes the effect of the Coulomb repulsion at high temperature. At low temperature, one finds a peak at the origin as a result of the formation of molecules, in which two electrons of opposite spin are localized along the bond. The differences from the PIMC graphs can be interpreted as a consequence of the different molecular fractions observed in Fig. 3.6.

The average squared width w of the Gaussian is shown in Fig. 3.11 as a function temperature and density. At high temperature and low density, one finds only small deviations from the free particle limit. These become more significant with increasing density and decreasing temperature. At low temperature, the attraction to the protons dominates, which leads to a decreasing average width. Finally bound states form and the width approaches a finite limit. At low densities, this is close to the ground state squared width of the isolated molecule, 3.138. It should be noted that in the limit of very high density, one expects the Gaussians orbitals to be almost as delocalized as the free particle solution because the Coulomb interaction is then a correction to the dominating kinetic terms. This limit does not seem to be represented correctly in this VDM ansatz. The current VDM orbital are too localized in the limit of high density. We interpret this as an effect of the insufficiently accurate treatment of the exchange terms described in section 3.7. In particular, one would need to include corrections to the norm matrix, which where left out because of the drastic increase in the numerical requirements.

In Fig. 3.12, we compare the internal energy from the thermodynamic estimator in Eq. 3.50 and the direct estimator in Eq. 3.49. Both agree fairly well at low density. Differences build up with increasing density and decreasing temperature. Comparing with PIMC simulations, one finds that the VDM energies are generally too high. The magnitude of this discrepancy shows the same density and temperature dependence as the difference between the two VDM estimators. The difference from the PIMC

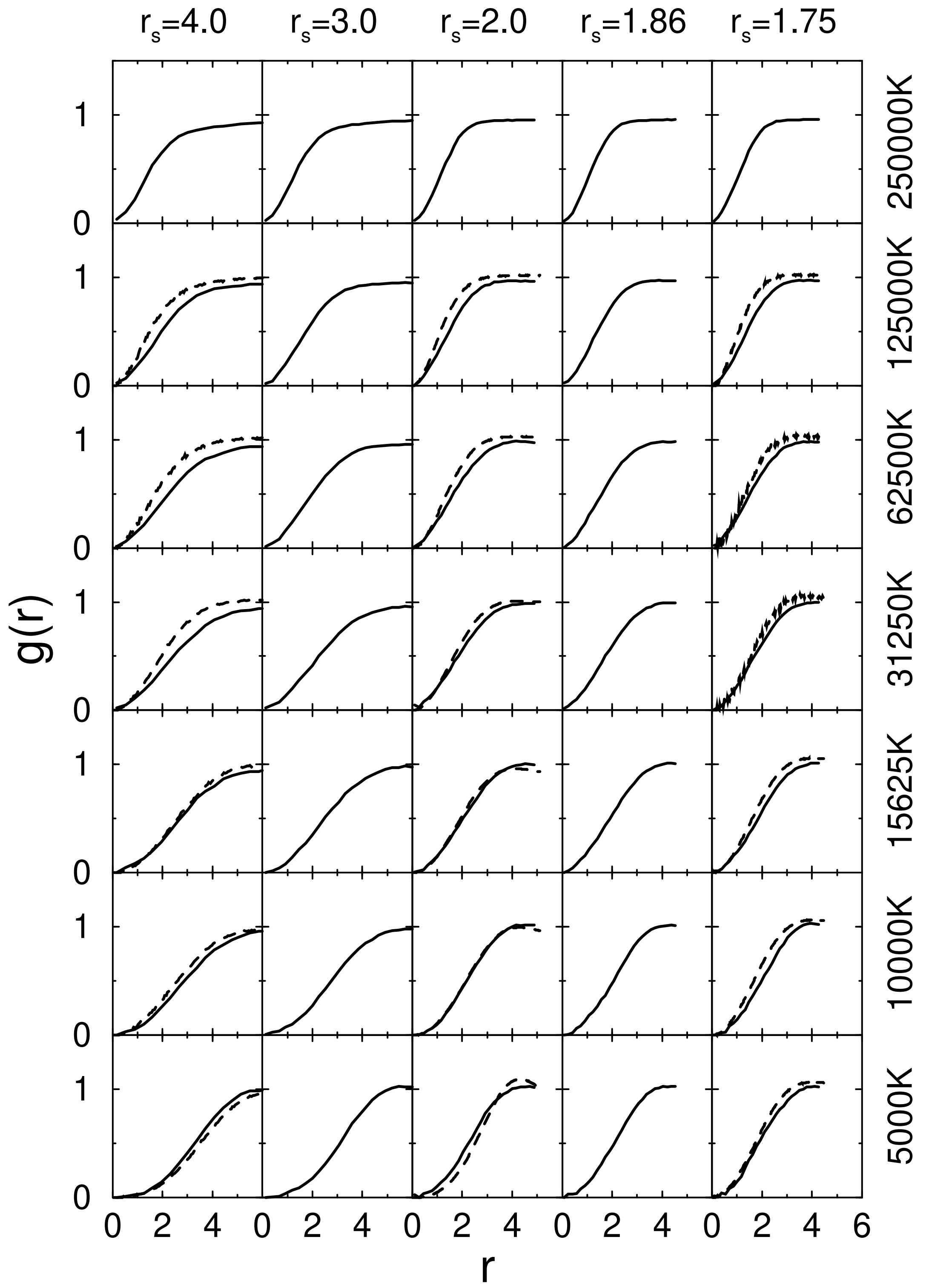

Figure 3.9: Electron-electron pair correlation function for electrons with parallel spin from VDM (solid line) and PIMC (dashed lines at r_s=1.75, 2.0, and 4.0 for $T \leq 125\,000\,\mathrm{K}$).

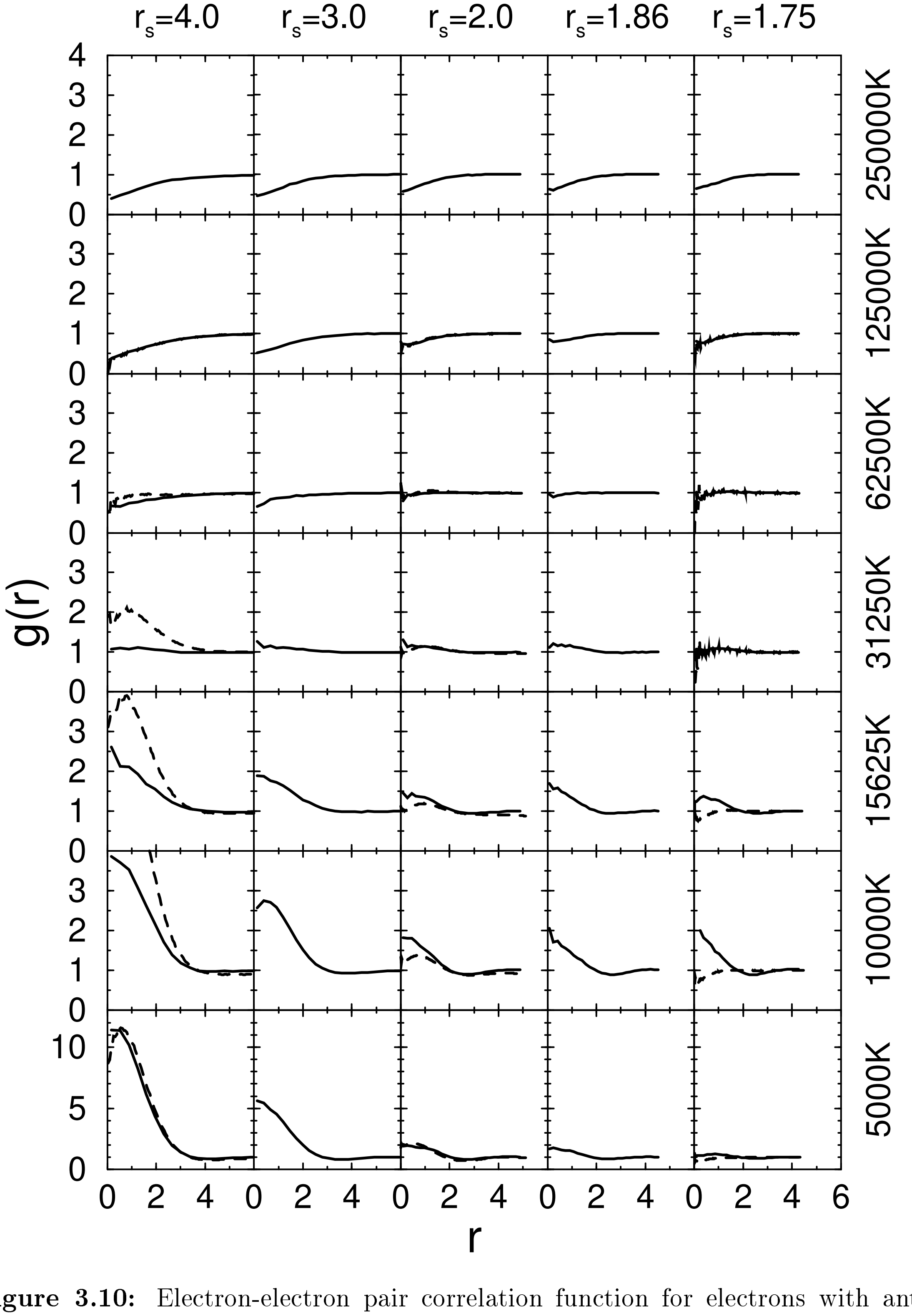

Figure 3.10: Electron-electron pair correlation function for electrons with anti-parallel spin from VDM (solid line) and PIMC (dashed lines at r_s=1.75, 2.0, and 4.0 for $T \leq 125\,000\,\mathrm{K}$). Note the change in scale in the last row.

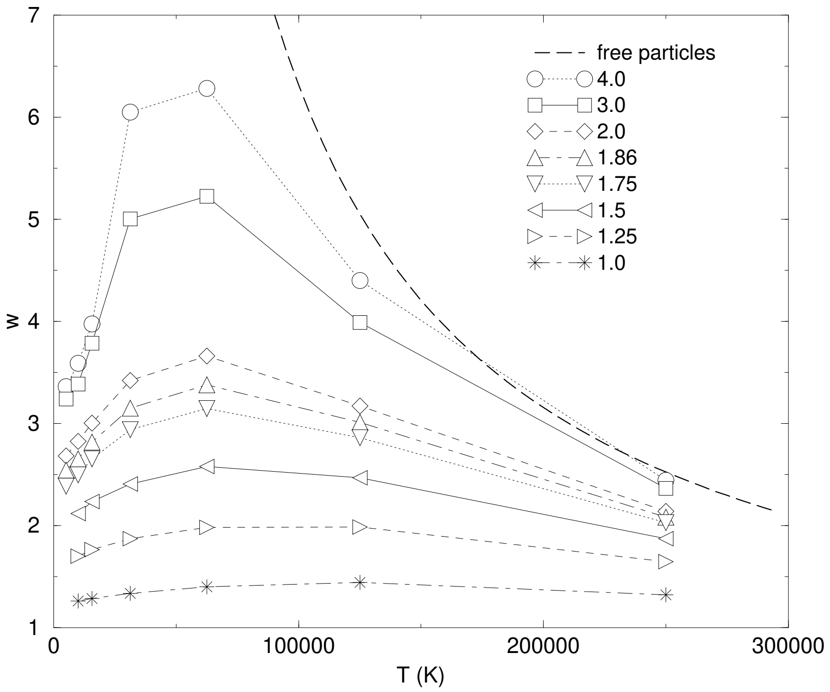

Figure 3.11: Average squared width of the Gaussian single particle density matrices as a function of temperature for different densities

results could be explained by the missing correlation effects in the VDM method.

At high temperature, the thermodynamic estimator always gives lower energies than the direct estimator. Below $T = 25\,000\,\mathrm{K}$, the ordering is reversed. This is consistent with the results from the isolated atom and molecule. The consequence is that the direct estimator is actually closer to the value expected from PIMC simulations. However, it should be noted that this estimator is not thermodynamically consistent (see section 3.5.2).

In Fig. 3.13, we compare pressure as a function of temperature and density from the two VDM estimators with PIMC results. At low density, the agreement is remarkably good. With increasing density and decreasing temperature, the difference grows. For densities over $r_s = 2.0$ below $10\,000\,\mathrm{K}$, one finds a significant drop in the direct estimator for the pressure. We interpret this effect as a result of the thermodynamic inconsistency.

Fig. 3.14, compares the Hugoniot from laser shock wave experiments (Da Silva *et al.*, 1997; Collins *et al.*, 1998) with VDM and PIMC results. VDM direct estimator (DE, full diamonds, Eq. 3.49) and VDM thermodynamic estimator (TE, full circles, Eq. 3.50-3.52)). The long dashed line indicates the theoretical high pressure limit $\rho = 4\rho_0$ of the fully dissociated non-interacting plasma. In the experiments, a shock wave propagates through a sample of precompressed liquid deuterium characterized

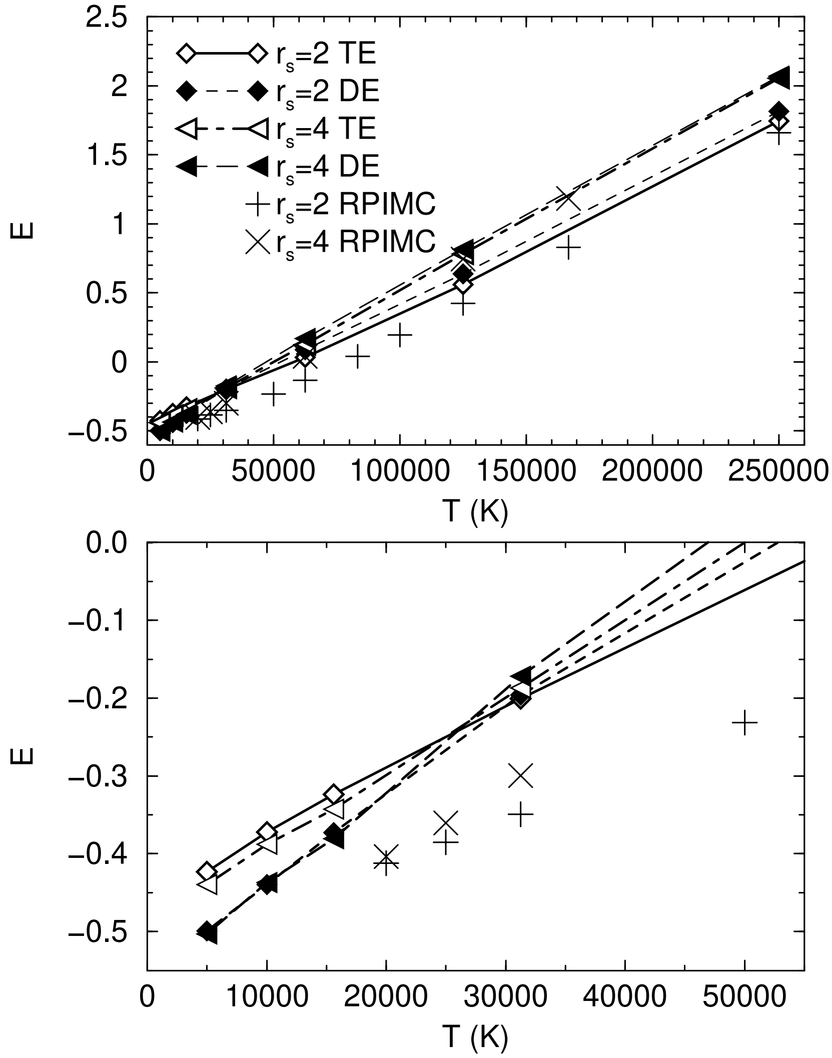

Figure 3.12: Internal energy per atom versus temperature from the VDM using the thermodynamic (TE, Eq. 3.50) and direct estimator (DE, Eq. 3.49) compared with PIMC results.

by its initial state, (E_0, $\hat{V}_0$, p_0). Assuming an ideal shock front, the variables of the shocked material (E, $\hat{V}$, p) satisfy the Hugoniot relation (Zeldovich and Raizer, 1966) (see section 4.6 for details),

$$H = E - E_0 + \frac{1}{2}(\hat{V} - \hat{V}_0)(p + p_0) = 0 \quad . \tag{3.73}$$

The initial conditions in the experiment were $T = 19.6\,\mathrm{K}$ and $\rho = 0.171\,\mathrm{g/cm^3}$. We set $p_0 = 0$ because $p_0 \ll p$. We show two VDM curves based on the thermodynamic and direct estimators. For E_0, we use the corresponding value of the ground state of the isolated hydrogen molecule, $E_0^{TE} = -0.955$ and $E_0^{DE} = -1.124$.

We expect the difference of the two estimators to give a rough estimate of the accuracy of the VDM approach. At high temperature, the difference is relatively small

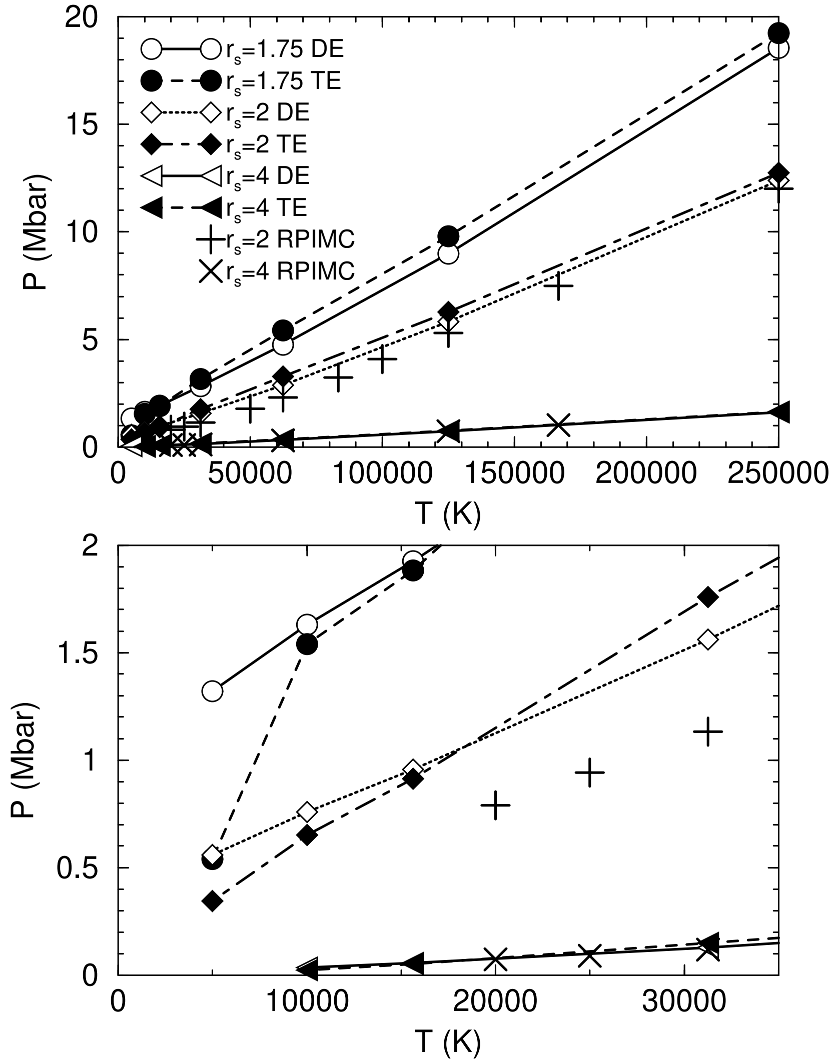

Figure 3.13: Pressure versus temperature in high and low temperature range. VDM pressure is calculated from virial relation using both the direct (DE, Eq. 3.49) and thermodynamic (TE, Eq. 3.51 and 3.52) estimators for kinetic and potential energy.

and agreement with PIMC simulations is reasonable. Both VDM estimators indicate that there is maximal compressibility around 1.5 Mbar. Furthermore, significant deviations are found from the experiments except for may be the lowest pressure point of 0.25Mbar. However, in this regime of high density and relatively low temperature a more careful study seems unavoidable. In section 4.6, we give a more detailed discussion on the Hugoniot that include predictions from other method and results from PIMC simulations using the VDM nodal surface to restrict the paths.

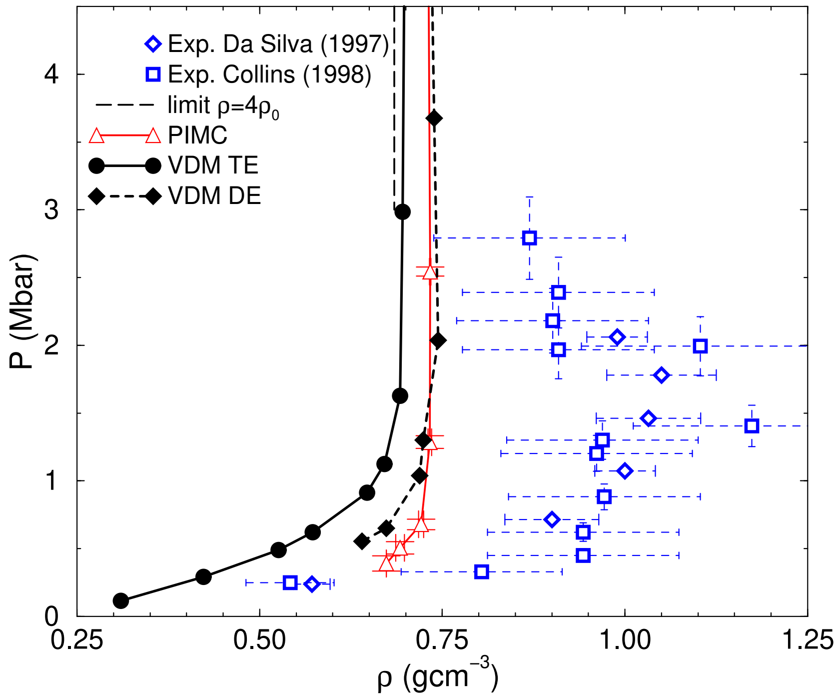

Figure 3.14: Comparison of experimental Hugoniot functions with VDM and PIMC results.

3.9 Extensions of the Gaussian Ansatz

There are several ways the VDM based on the Gaussian ansatz Eq. 3.27 can be improved. First of all, one can write it as a two step path integral,

$$\rho(\mathbf{R}, \mathbf{R}'; \beta) = \int \mathbf{dR}'' \; \rho(\mathbf{R}, \mathbf{R}''; \beta/2) \; \rho(\mathbf{R}'', \mathbf{R}'; \beta/2) \tag{3.74}$$

$$= \int \mathbf{dR}'' \; \rho(\mathbf{R}, \vec{q}(\mathbf{R}''; \beta/2)) \; \rho(\mathbf{R}'', \vec{q}(\mathbf{R}'; \beta/2)) \quad . \tag{3.75}$$

This has the advantage of using a density matrix at higher temperatures corresponding to $\frac{\beta}{2}$, which makes the method more accurate. In a MC simulation sampling Trρ, one would keep two sets of coordinates $\mathbf{R} = \mathbf{R}'$ and $\mathbf{R}''$ as done for path integrals, integrate the parameter equations with the initial conditions at $\mathbf{R}$ and $\mathbf{R}''$ up to $\frac{\beta}{2}$ and evaluate the integrand in Eq. 3.75 rather than calculating $\rho(\mathbf{R}, \mathbf{R}; \beta)$ as done in all simulations discussed previously. The method of matrix squaring cannot be applied further without introducing minus signs, which lead to the fermion sign problem and would also require nodes.

Alternatively, one can try an approximation to the convolution in Eq. 3.74,

$$\rho(\mathbf{R}, \mathbf{R}'; \beta) \approx \int \mathbf{dR}'' \; \rho(\mathbf{R}'', \mathbf{R}; \beta/2) \; \rho(\mathbf{R}'', \mathbf{R}'; \beta/2) \tag{3.76}$$

$$\approx \int \mathbf{dR}'' \; \rho(\mathbf{R}'', \vec{q}(\mathbf{R};\beta/2)) \; \rho(\mathbf{R}'', \vec{q}(\mathbf{R}';\beta/2)) \quad , \tag{3.77}$$

which has the advantage of being symmetric in $\mathbf{R}$ and $\mathbf{R}'$ unlike the ansatz used throughout this work, which was discussed in section 3.5.2. It would also simplify an MC simulation, because one would need only one set of coordinates $\mathbf{R}$, derive one set of variational parameters and could perform convolution analytically,

$$\rho(\mathbf{R}, \mathbf{R}; \beta) \approx \int \mathbf{dR}'' \; [\, \rho(\mathbf{R}'', \vec{q}(\mathbf{R};\beta/2)) \,]^2 \quad . \tag{3.78}$$

Furthermore, the Gaussian ansatz can be improved by including additional variational parameters, e.g. to use a sum of Gaussians. In the zero temperature limit, this would lead to a solution closer to the Hartree Fock result. To go beyond one needs to include additional correlations in the ansatz and derive modified equations for the parameter from Eq. 3.19. Correlations are usually introduced with a Jastrow factor, which can be generalized to finite temperature. The new ansatz then reads,

$$\rho(\mathbf{R}, \mathbf{R}'; \beta) = \begin{vmatrix} \rho_1(\mathbf{r}_1, \mathbf{r}'_1; \beta) & \ldots & \rho_1(\mathbf{r}_N, \mathbf{r}'_1; \beta) \\ \ldots & \ldots & \ldots \\ \rho_1(\mathbf{r}_1, \mathbf{r}'_N; \beta) & \ldots & \rho_1(\mathbf{r}_N, \mathbf{r}'_N; \beta) \end{vmatrix} \quad \exp\left\{ -\frac{1}{2} \sum_{i<j} u(r_{ij}) + u(r'_{ij}) \right\}, \tag{3.79}$$

where u depends on the type of pair (electron-electron, electron-ion). It contains extra parameters, that depend in temperature but we suggest to consider them as fixed in the variational principle. The consequence for the parameter equation is that there are additional terms to the norm matrix and, further, most integrals cannot be expressed analytically.

Alternatively, one can use an unitary correlation operator as suggested by Schnack (1996). The idea is to applied a short range correlation operator to an uncorrelated state in order to generate a correlated state. The fundamental difference to the Jastrow type ansatz above that correlations are introduced by the operator.

Another improvement for many-particle simulations would be to consider all $N!$ terms from the permutations, which would make contributions at very high levels of degeneracy. The scaling of a full exchange method can be reduced to N^4 as suggested by Schnack (1996) for real time wave packet molecular dynamics but the application of this method to the VDM imaginary time remains to be done.

To summarize, one can say that the VDM approach provides a way to systematically improve the many-particle density matrix. Already the simplest ansatz using one Gaussian to describe the single particle density matrices gives a good description of hydrogen in the discussed range of temperature and density. The method includes the correct high temperature behavior and shows the expected formation of atoms and molecules. The thermodynamic variables are in reasonable agreement with PIMC simulations and lead to a good approximation of the Hugoniot function. Further one can use this essentially analytic density matrix to furnish the nodal surface in PIMC simulations, replacing the free particle nodes by a density matrix that already includes the principle physical effects. Results will be discussed in the next chapter.

Chapter 4

Thermodynamic Properties of Dense Hydrogen

In this chapter, the main results from the PIMC simulations of hot, dense hydrogen and deuterium will be discussed. We start with a brief study of the accuracy of the pair density matrix for the isolated hydrogen atom and molecule. Then we show results from many-particle simulations. Special emphasis is put on the comparison of variational and free particle nodes. The development of the VDM in chapter 3 (Militzer and Pollock, 2000a,b) and its application as nodal surface in PIMC simulations is one of the key points of this work. In this context, we discuss the high temperature phase diagram and study the effects of an improved nodal surface. We look at the pair correlation functions as well as the permutation probabilities of the electrons. Both will be used to review the predicted first order plasma phase transition by Magro *et al.* (1996). It will be shown that these results do change drastically if the VDM nodes are used instead of FP nodes. Following this discussion, we show results for densities and temperatures where the precise shape of the nodes is not important, discuss pressure and internal energy, and compare with results from other models and simulation methods. Finally, we give a detailed comparison with the laser shock wave experiments.

4.1 Accuracy of the Pair Density Matrix

The pair density matrices are calculated using the matrix squaring method described in section 2.3.1. They are stored in tables using the expansion formula Eq. 2.38 and then entered into the PIMC simulation program. The accuracy of these tables is crucial for all following results. Using the precomputed pair density matrices allows

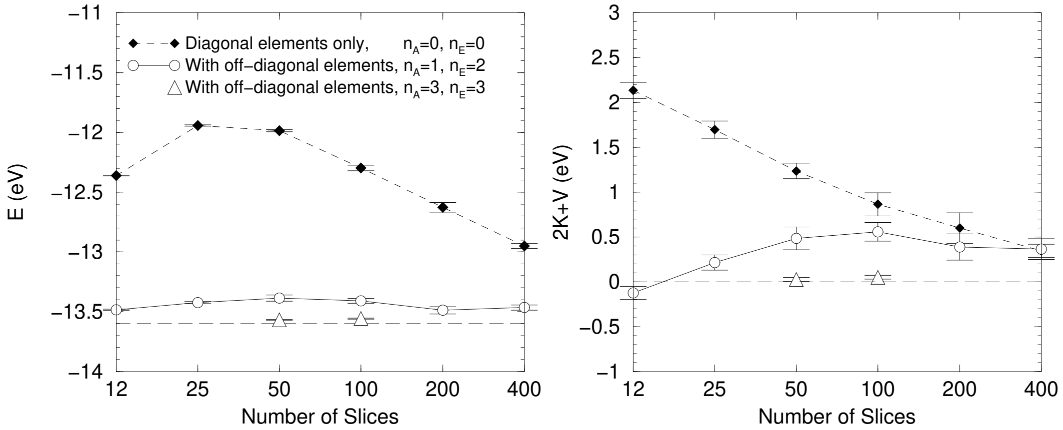

Figure 4.1: Internal energy (left graph) and $2K + V$ (right graph) for an isolated hydrogen atom as a function of the number of time slices at constant temperature of 10 000 K.

one to employ a much larger time step because one starts with a solution of the two-particle problem. Fig. 4.1 shows how accurate this method is. The internal energy of an isolated hydrogen atom at sufficiently temperature ($T = 10\,000\,\mathrm{K}$) in a large box ($L = 26$) is compared with the exact groundstate energy of $-13.6\,\mathrm{eV}$. The temperature was chosen low enough so that excited states can be neglected e.g. the contribution to the energy from the occupation of first excited state is $7 \cdot 10^{-5}\,\mathrm{eV}$ at this temperature. Furthermore, it is tested whether the kinetic energy K and the potential energy V satisfy the virial theorem $2K + V = 0$. If only diagonal action terms are considered in Eq. 2.38 one finds a rather slow convergence as function of the number of time slices (Fig. 4.1). Eventually, the error goes to zero in the Trotter limit, Eq. 2.24, of an infinite number of slices. Using off-diagonal terms in the expansion formula, Eq. 2.38, improves the convergence significantly as shown in Fig. 4.1. One can use different orders to calculate the action n_A and the energy n_E. The resulting accuracy from different orders is shown in Tabs. 4.1 and 4.2. It reveals that using order 2 or higher instead of order 1 in the action decreases the errors by almost one order of magnitude. This is an important observation because most many-particle simulations reported in this work had been performed with $n_\mathrm{A} = 1$ and $n_\mathrm{E} = 2$ (which was found to be sufficient for simulations of Helium particles) before this analysis was done. Because of the resulting inaccuracies, the estimated energies and pressures are slightly too high.

These inaccuracies have also consequences for the isolated hydrogen molecule, which are important to study in order to determine the corrections of results from many particle simulations. The virial theorem for an isolated H_2 molecular with fixed

Table 4.1: Accuracy study of PIMC simulations of the isolated hydrogen atom using different orders in the expansion formula 2.38 for the action and the energy. The calculated $2K + V$ (exact value equals zero) and the deviation of the potential energy V from the exact value of -27.2 eV are listed from simulations at $T = 10\,000$ K using 100 time slices and $\tau^{-1} = 10^6$K.

	$2K + V$ (eV)				$V - V_{\text{exact}}$ (eV)			
energy	action order				action order			
order	0	1	2	3	0	1	2	3
0	0.8 (1)				1.74 (3)			
1		0.47 (2)	-0.18 (3)	-0.071 (25)		-0.176 (08)	0.074 (11)	0.043 (07)
2		0.56 (2)	-0.07 (3)	0.013 (48)		-0.166 (05)	0.063 (09)	0.034 (13)
3		0.61 (4)	-0.06 (3)	0.039 (08)		-0.183 (11)	0.056 (11)	0.031 (03)

Table 4.2: Accuracy study of PIMC simulations using different order in the action and energy expansion as in Tab. 4.1 but with a larger time step of $\tau^{-1} = 0.5 \cdot 10^6$K and 50 time slices.

	$2K + V$ (eV)				$V - V_{\text{exact}}$ (eV)			
energy	action order				action order			
order	0	1	2	3	0	1	2	3
0	1.24 (7)				1.991 (28)			
1		0.46 (4)	-0.12 (5)			-0.074 (12)	0.033 (12)	
2		0.51 (4)	-0.07 (2)			-0.067 (13)	0.044 (07)	
3				0.03 (2)				0.036 (7)

Table 4.3: Accuracy analysis for the isolated hydrogen molecule for different time steps and temperatures using $n_{\text{A}} = 3$ and $n_{\text{E}} = 3$. In this analysis, the nuclei are classical and fixed at the bond length of $R = 1.4008$. $2K+V$ (exact value equals zero) and the deviations from the exact binding potential energy per atom -31.946 eV are listed.

	$2K + V$ (eV)			$V - V_{\text{exact}}$ (eV)		
	τ^{-1} (10^6K)			τ^{-1} (10^6K)		
T(K)	0.5	1	2	0.5	1	2
7812	0.41 (3)	0.16 (3)	-0.06 (8)	-0.422 (10)	-0.112 (8)	0.030 (22)
3906	0.41 (3)	0.19 (3)	0.14 (4)	-0.419 (07)	-0.110 (5)	-0.008 (11)
1953	0.43 (3)	0.16 (2)	0.08 (3)	-0.421 (12)	-0.115 (9)	-0.009 (09)

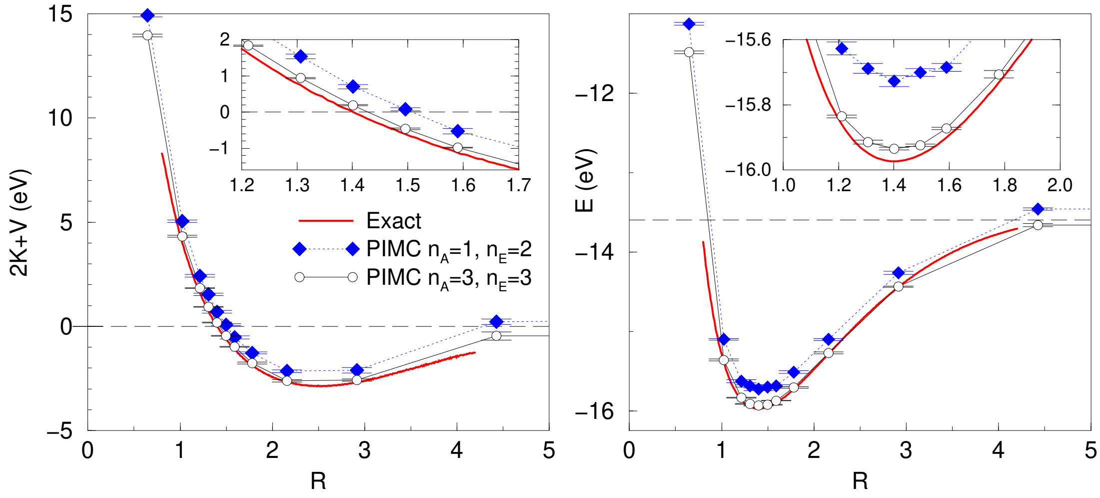

Figure 4.2: Internal energy (right graph) and $2K + V$ (left graph) per atom for an isolated hydrogen molecule as a function of the nuclear separation R. The PIMC results were calculated at T=3906 K using a time step of $\tau^{-1} = 10^6$ K and the orders in the action and energy expansion ($n_{\rm A}$,$n_{\rm E}$) as indicated. The dashed line in the left graph indicates zero of energy and in the right graph, the energy of one isolated atom.

nuclei at separation R reads (Kolos and Wolniewicz, 1964; Steiner, 1976),

$$2K + V = -R\,\frac{dE}{dR} \quad . \tag{4.1}$$

This means one can calculate the kinetic and potential energy from $E(R)$ and its derivative using $E = K + V$. In Fig. 4.2, the exact results by Kolos and Wolniewicz (1964) for E and $2K + V$ are compared with the PIMC calculations. It shows that for PIMC using $\tau^{-1} = 10^6$ K, $n_{\rm A} = 1$, and $n_{\rm E} = 2$, the energy E is too high by 0.25 ± 0.05 eV and $2K+V$ is too large by 0.7 ± 0.1 eV per atom. The latter correction is particularly important because in PIMC simulations of Coulomb systems, we use the virial theorem, Eq. 3.55, to estimate the pressure. The correction to the pressure is equivalent to subtracting the pressure of an ideal H_2 gas at $T = 5400 \pm 800$ K.

The accuracy of PIMC simulations of an isolated molecule is affected by the order in action and energy expansion as well as by the time step because it is a four-particle problem. Tab. 4.3 shows results calculated with $n_{\rm A} = n_{\rm E} = 3$ orders. First, we studied the different temperatures and found no dependence on T, which means that contributions from electronic excited states are negligible. Furthermore, the comparison of different time steps shows a significant dependence. Using a time step $\tau^{-1} = 2 \cdot 10^6$ K allows one to calculate the energy with an accuracy of approximately 0.05 eV and $2K + V$ with an error of about 0.1 eV per atom. Using a smaller time step would bring the results in Fig. 4.2 closer to the exact results.

Most many-particle PIMC simulations discussed in the following sections have been performed using $n_{\rm A}=1$ and $n_{\rm E}=2$ in the action and energy expansion of the pair density matrices. The correction resulting from higher order terms will be estimated based on the following argument. Higher order off-diagonal terms are large for small separations of the two particles. Therefore, we expected the dominant corrections to come from pairs of protons and electron when both particles are close together. Therefore, we suggest to use the integral of the proton-electron pair correlation function up to a cut-off radius,

$$I_{\rm pe} = 4\pi n \int_0^{r_c} dr\; r^2\, g_{\rm pe}(r) \quad , \tag{4.2}$$

in order to estimate the corrections to pressure and energy,

$$\Delta E \;=\; c_1\, I_{\rm pe} \quad , \tag{4.3}$$

$$\Delta p \;=\; c_2\, I_{\rm pe}\, \frac{n}{3} \quad . \tag{4.4}$$

We estimated $r_c = 1.4$ from studying the magnitude of the higher order terms and determined the coefficients c_1 and c_2 from the corrections for the isolated molecule discussed above: $c_1 = -0.24 \pm 0.05\,\mathrm{eV}$ and $c_2 = -0.7 \pm 0.1\,\mathrm{eV}$. In the following discussion of the thermodynamic properties, it will be explicitly stated where this correction has been applied. It turns out that the corrections to the pressure are particularly important at low densities and temperatures, where the pressure becomes of the same order of magnitude as the correction. It should also be noted that the corrections hardly change the hugoniot curve discussed in section 4.6. The effect is significantly smaller than the differences in energy and pressure, which are relevant in this context.

4.2 Phase Diagram

We used PIMC simulations with 32 protons and 32 electrons, a time step $\tau^{-1} = 10^6\,\mathrm{K}$, $n_{\rm A}=1$, and $n_{\rm E}=2$ to generate the phase diagram shown in Fig. 4.3. In the low density and low temperature regime, we find a molecular fluid. In the proton-proton pair correlation functions (see section 4.4, Fig. 4.15), one finds a clear peak at the bond length of 1.4. The integral under the peak is proportional to the number of molecules. This criterion works well for low densities where the peak is well separated from the remaining contributions. Alternatively, one can estimate the number of molecules as well as other compound particles by a *cluster analysis*, in which the individual path configurations from PIMC simulations are analyzed. As described

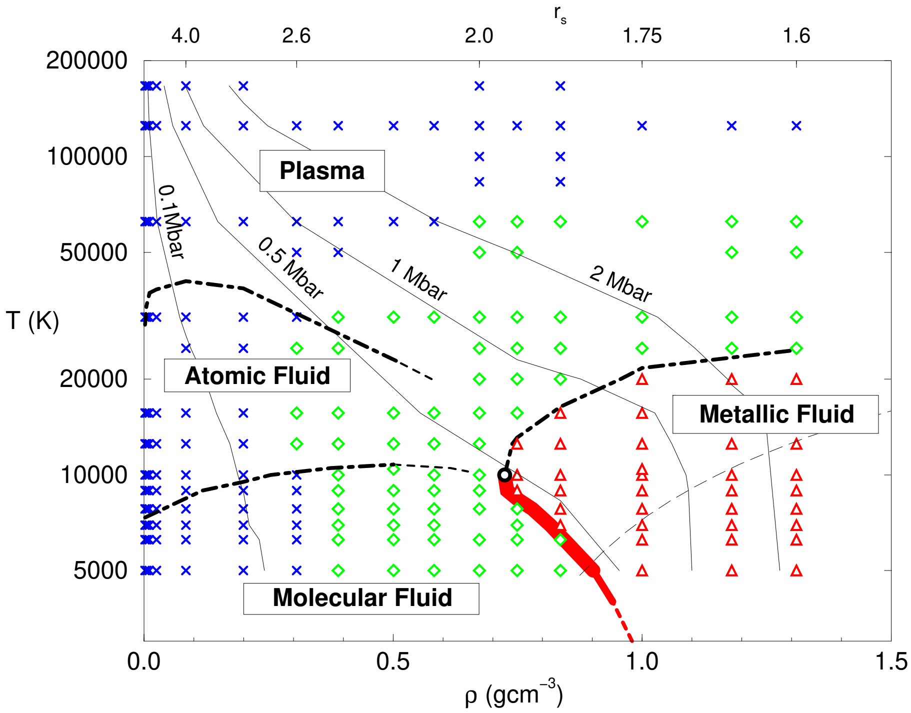

Figure 4.3: The phase diagram of deuterium computed with PIMC simulations using free particle nodes is shown in the temperature-density plane. ($\times, \diamond, \triangle$) indicate the different simulations and distinguish between different degrees of degeneracy of the electrons ($\times$ less than 10% exchanges, $\diamond$ more 10%, and $\triangle$ over 80%). The thin dashed lines indicates the boundary of the metallic regime from simulations with VDM nodes shown below.

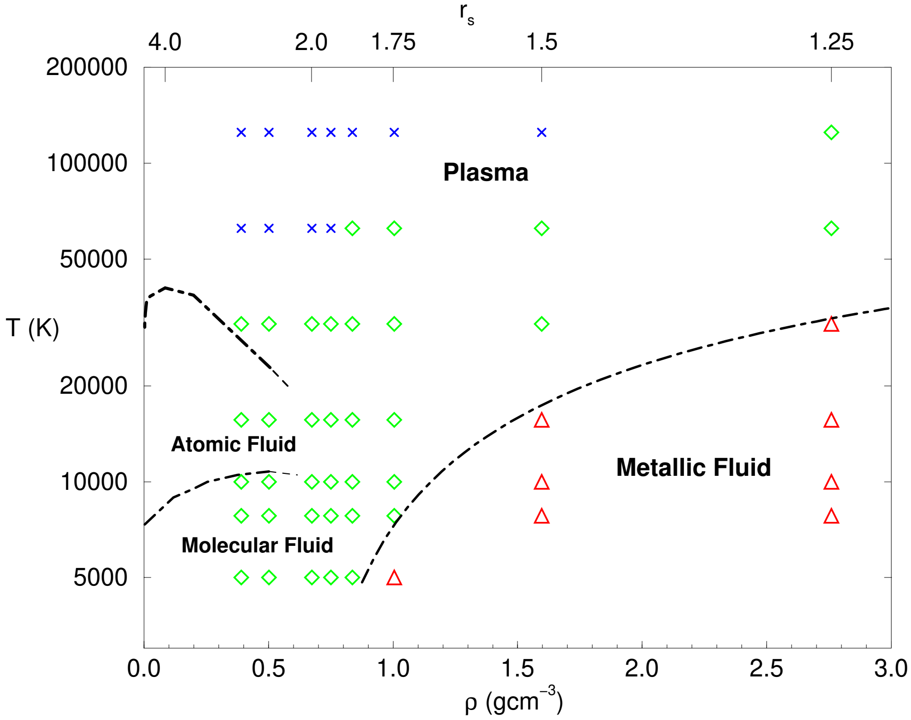

Figure 4.4: Phase diagram of deuterium as in Fig. 4.3 but calculated with PIMC using VDM nodes.

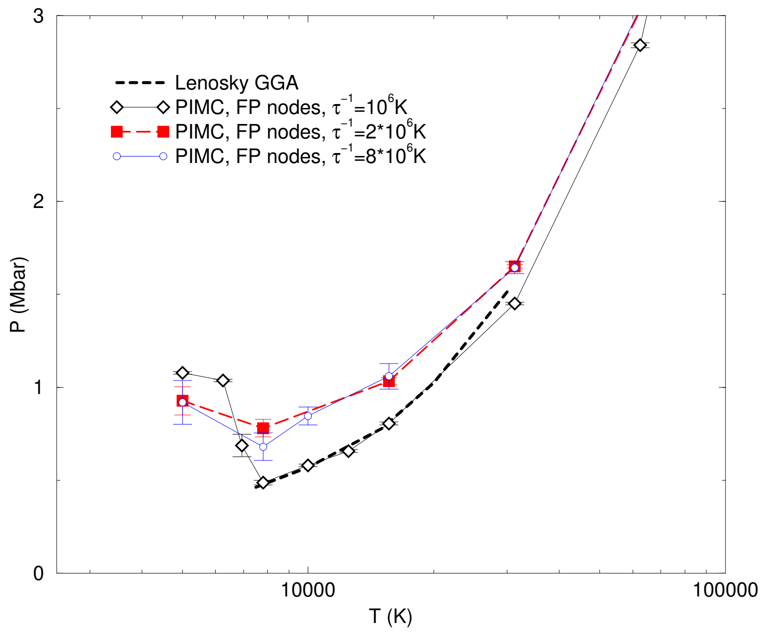

Figure 4.5: Pressure vs. temperature from PIMC simulations of deuterium at $r_s = 2$ with free particle nodes, $n_{\rm A} = 1$, $n_{\rm E} = 2$, and different time steps. The negative slope $\frac{dP}{dT}\big|_{\hat{V}}$ indicates a first order phase transition.

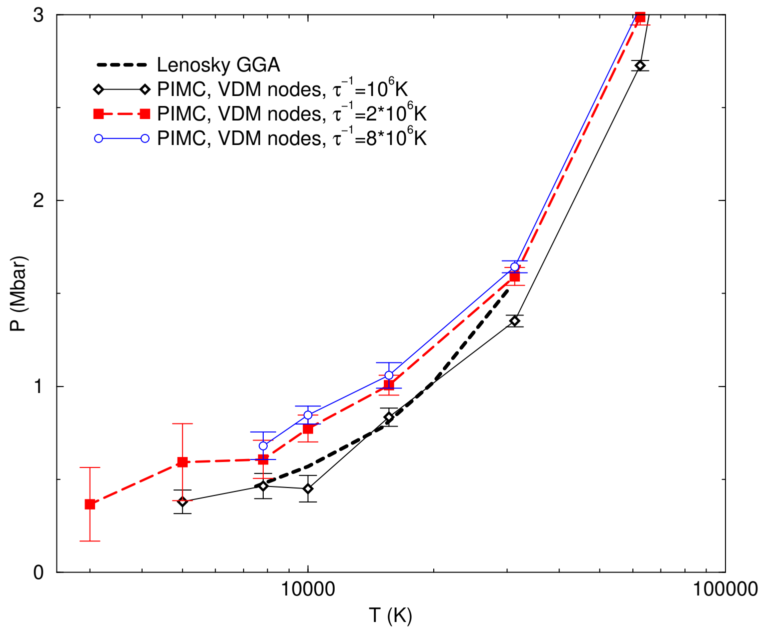

Figure 4.6: Pressure vs. temperature as in Fig. 4.5 but calculated with VDM nodes. Within the error bars, no regions of $\frac{dP}{dT}\big|_{\hat{V}} < 0$ occur.

in (Militzer *et al.*, 1998), we consider two protons as belonging to one cluster if they are less than 1Å apart. An electron belongs to one particular cluster if it is less than 0.75Å away from any proton in the cluster. The two cut-off radii were chosen from the molecular and atomic ground state distribution. This analysis give reasonable estimates for the molecular and atomic fractions at low temperatures. At high temperature, it typically overestimated the number of bound states because in a collision, two particles are close but this is not a bound state. We corrected for this artifact by applying an additional criterion. A particle can only be considered as bound if the difference in action (or energy) to remove it from the cluster is positive. This method leads to the expected corrections at high temperature. The regime boundaries in Fig. 4.3 are hardly affected. Summarizing one can say that PIMC simulations provide good estimates for the number of atoms and molecules at low density but a rigorous quantum-mechanical definition of what a bound state is and how to identify it remains to be given. Several ideas are discussed in the work by Girardeau (1990).

Starting in the molecular regime, one finds that increasing temperature at constant density leads to the gradual process of *thermal dissociation* of molecules, which results into a regime with a majority of atoms. The atoms are then gradually ionized at even higher temperatures leading to a plasma of free protons and electrons. Lowering the density at constant temperature leads to a decrease in the number of molecules, or atoms respectively. We call these processes *entropy dissociation* of molecules and *entropy ionization* of atoms because both processes are driven by the increased entropy of the unbound states due to the larger volume.

If the density is increased at constant temperature, *pressure dissociation* diminishes the molecular fraction. This transition was described by Magro *et al.* (1996). In simulations with the time step $\tau^{-1} = 10^6\,\mathrm{K}$, it was found that the number of molecules drops significantly within a small density interval. Secondly, a region with $\frac{\partial P}{\partial T}\big|_{\hat{V}} < 0$ was found as shown in Fig. 4.5. Both results are consistent with a first order plasma phase transition (PPT). In this case, one expects to find a coexistence region indicated by thick red line in Fig. 4.3, which ends in a critical point.

Since the work by Magro *et al.* (1996), we were able to obtain simulation results with better convergence, smaller time steps, for larger systems and different nodal surfaces. It should be emphasized that the type of nodal surface has a significant effect on the thermodynamic properties in the region of the PPT, which will be discussed in detail in section 4.3. First, we verified that simulations using free particle nodes and smaller time steps ($\tau_B^{-1} = \tau_F^{-1} = 2 \cdot 10^6\,\mathrm{K}$ and $\tau_B^{-1} = 2 \cdot 10^6\,\mathrm{K}$, $\tau_F^{-1} = 8 \cdot 10^6\,\mathrm{K}$) also predict $\frac{\partial P}{\partial T}\big|_{\hat{V}} < 0$ as shown in Fig. 4.5. Using a smaller time step makes the pressure drop less pronounced but it can still be clearly identified.

As a next step, we looked at the number of permuting electrons, which is one of the key properties to understand this transition. We determined the fraction of electrons involved in a permutation as an indication of electronic delocalization. Permuting electrons are required to form a Fermi surface (see chapter 5), which means that a high number of permutations indicates a high degree of degeneracy of the electrons. If, in average, over 80% of the electrons are involved in a permutation we label this state metallic. Permuting electrons form long chains of paths and therefore occupy delocalized states. This delocalization destabilizes the hydrogen molecules. Before all bonds are broken, one finds a molecular fluid with some permuting electrons as visualized in Fig. 4.8. It still shows a significant molecular signature but differs from the molecular fluid at lower density in Fig. 4.7 by the increased fraction of permuting electrons. If the density is increased further, the majority of the electron become delocalized, all bonds are broken, which leads to a metallic fluid of unbound proton and the degenerate electron gas as shown in Fig. 4.9.

Fig. 4.10 shows histograms of the number of permuting electrons. At low density, the permutation probability is small and the peak in the histogram is on the left. The peak position shifts to the right with increasing density indicating the higher fraction of permuting electrons. Eventually, one finds a sharp peak near 1, which corresponds to degenerate electronic states where almost all electrons permute. The histogram also provides information on how this transition occurs in simulations with free particle nodes. Near the critical density, we found that the simulation exhibits a switching behavior between a less degenerate (and presumably more molecular) and highly degenerate (with unbound protons) state. The bimodal distribution can be seen best in the simulation at $r_s = 1.86$ and $T = 6944\,\mathrm{K}$ in Fig. 4.10 and to a lesser extent for $r_s = 1.93$ and $T = 7812\,\mathrm{K}$ as well as for $T = 6944\,\mathrm{K}$. This switching behavior indicates that the transition occurs as a collective effect, which is required for a first order phase transition.

The boundaries of the metallic regime in Fig. 4.3 are determined by two effects. With increasing temperature, the degree of degeneracy of the electrons is reduced and one finds a gradual transition to a less degenerate plasma state. If the temperature is lowered, the attraction to the protons becomes more relevant, which localizes the electrons and decreases the degree of degeneracy as also can be seen in Fig. 4.10.

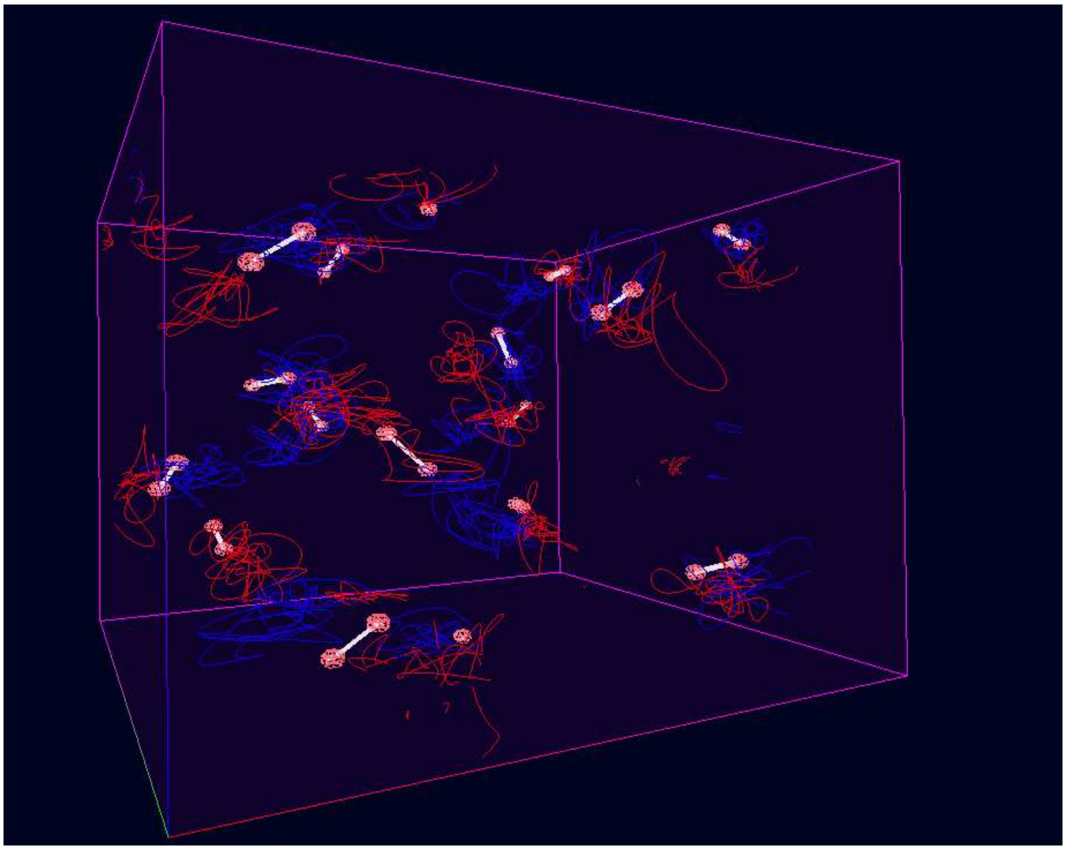

Figure 4.7: Hydrogen in molecular state as it appears in a PIMC simulation at $T = 5\,000\,\mathrm{K}$ and $r_S = 4.0$. The salmon-colored spheres denote the protons. The bonds (white lines) were put in a guide to the eye. The electron paths are shown in red and blue depending on their spin state.

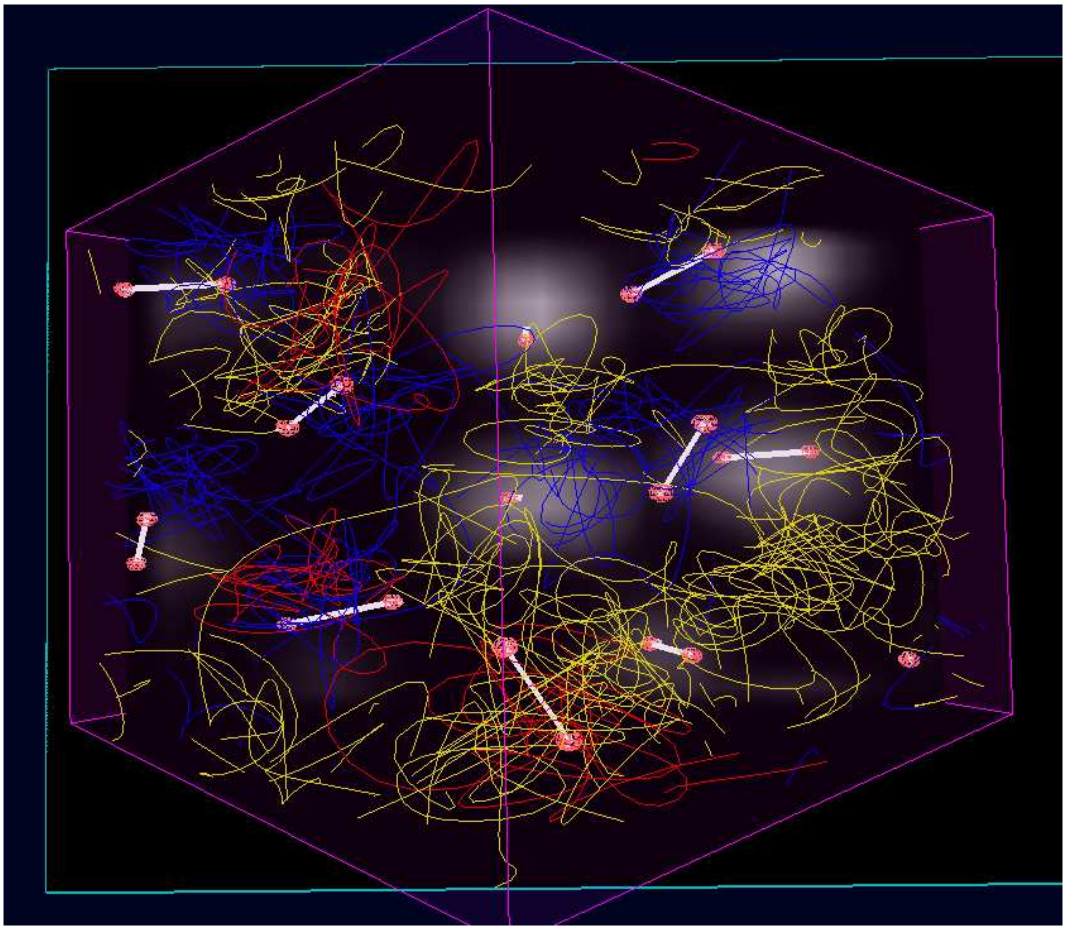

Figure 4.8: Deuterium in molecular state with significantly degenerate electrons as it appears in a PIMC simulation at $T = 5\,000\,\mathrm{K}$ and $r_S = 1.86$ similar to Fig. 4.7. Due to the higher density, the electron paths permute with a higher probability (shown as yellow lines) but are localized enough to form a bond between the two protons in the molecule. The electron density average over many electron configurations is indicated in gray color on the blue rectangles.

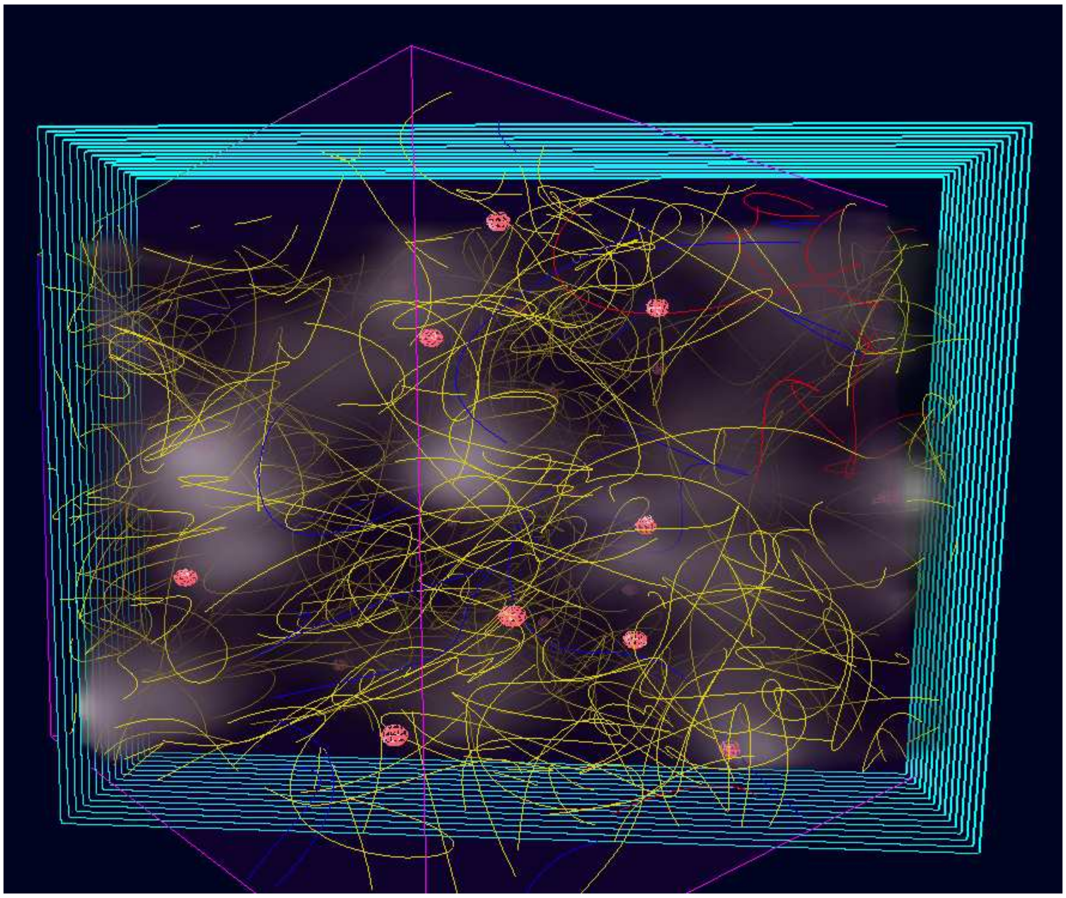

Figure 4.9: Deuterium in metallic state with unbound protons and a gas of degenerate electrons as it appears in a PIMC simulation at $T = 6\,250\,\mathrm{K}$ and $r_s = 1.6$ similar to Fig. 4.8. The electron paths are delocalized and permute frequently.

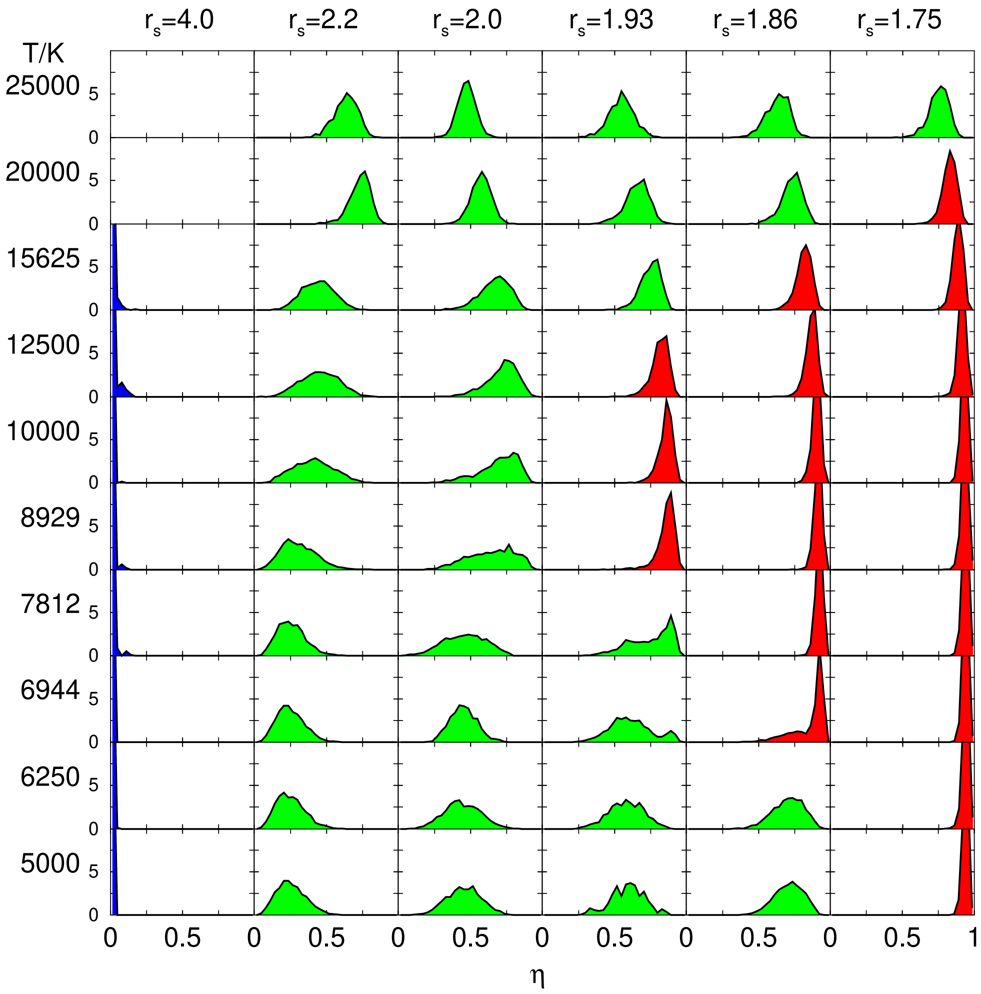

Figure 4.10: Histogram of the fraction of permuting electrons from PIMC simulations with free particle nodes at different temperatures and densities. The colors are chosen as in Fig. 4.3: blue for an average of less than 10% exchanges, green for between 10% and 80%, and red for over 80%.

4.3 Comparison of Variational and Free Particle Nodes

In this section, we are going to compare thermodynamic properties derived from PIMC simulations of deuterium with free particle nodes with those using VDM nodes. The effect of the nodal surfaces is largest in the region of a high degree of electronic degeneracy, found at high density and low temperature. It should be noted for low densities e.g. $r_s \geq 3$, electrons become bound and localized before a significant degree of degeneracy is reached. This can be seen in the phase diagram in Fig. 4.3 and in the histogram of the permutation probabilities in Fig. 4.10. For this reason, we focus in the discussion on the two densities corresponding to $r_s = 2$ and 1.86 where the electronic degeneracy becomes very important for $T \leq 31\,250\,\mathrm{K}$.

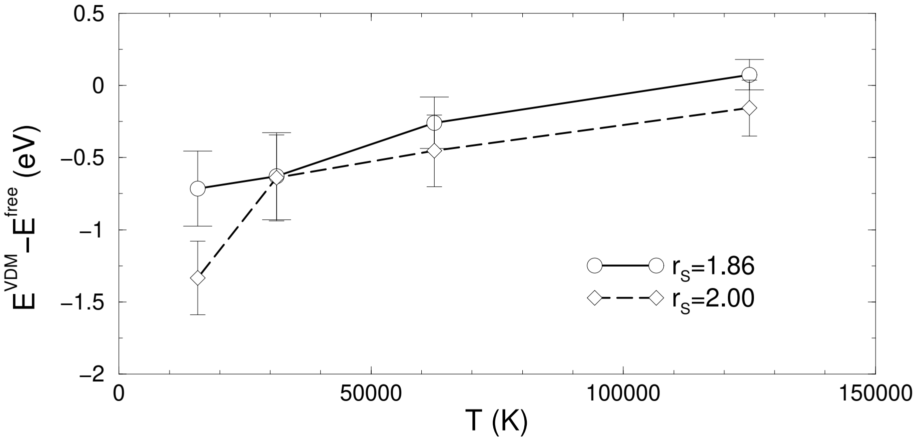

Figure 4.11: Difference in the internal energy per atom from PIMC simulations with VDM and free particle nodes vs. temperature using $N_P = 32$, $\tau^{-1} = 2 \cdot 10^6$K, $n_{\mathrm{A}} = 1$, and $n_{\mathrm{E}} = 2$.

In Fig. 4.11, a comparison of the internal energy from simulations with FP and VDM nodes is shown. Simulations with VDM nodes lead to lower internal energies than those with FP nodes. The differences become smaller with increasing temperature since the both density matrices are exact in this limit. Since the free energy F is the integral of the internal energy over temperature, one can conclude that VDM nodes yield to a smaller F and hence, are the more appropriate nodal surface.

In the following, we will discuss the revised phase diagram shown in Fig. 4.6. First of all, the nodal surfaces are not important for low density e.g. $r_s \gtrsim 3$. Therefore, we copied low density PIMC results from free particle nodes concerning the location of the molecular and atomic regime. Furthermore, we compare the histograms for the permuting probability shown in Fig. 4.12 compared with free particle nodes in Fig. 4.10. Generally, one finds that the permutation probability is reduced for VDM nodes and that the area of metallic regime in the temperature-density plane has shrunk considerably. This can be understood as follows. FP nodes are generated from maximally delocalized orbitals. Therefore, they could favor delocalized state and allow more permutation. VDM nodes include bound states and lead to more localized orbitals, which consequently reduces the fraction of permuting electrons. A comparison of the distribution of the cycle length can be found in Fig. 4.13. However, it should be noted that there is the possibility that the VDM leads to too localized orbitals in the limit of high density, as indicated by the too small width of the Gaussians orbitals shown in Fig. 3.11.

In the next step, we calculated the pressure as a function of temperature for $r_s = 1.86$ using different time steps as in Fig. 4.6. Within the statistical error bars,

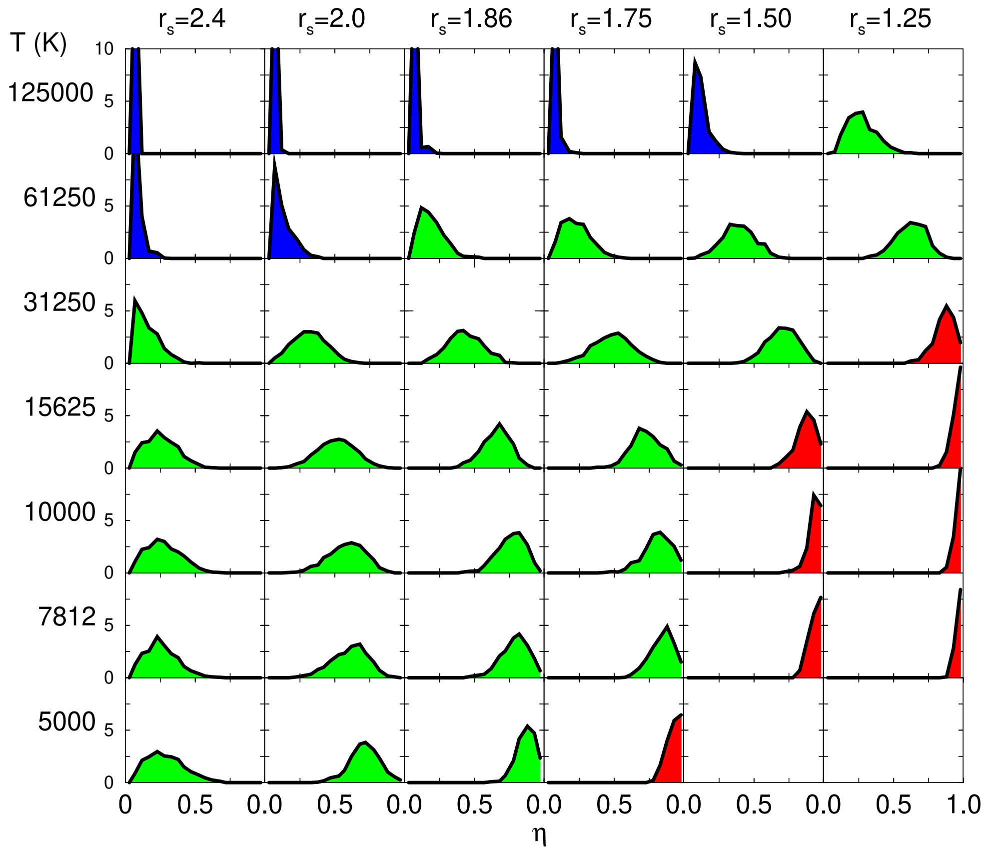

Figure 4.12: Histogram of the permutation probability from PIMC simulations with VDM nodes as in Fig. 4.10 for free particles nodes.

results from PIMC simulations with VDM nodes do not show a region where the pressure drops down with increasing T, $\frac{dP}{dT}\big|_{\hat{V}} < 0$. This shows that the results in regime near the PPT are strongly affected by the type of nodes being used. This also raises some concern on how reliable the PIMC simulations are in this regime. However, one can proceed as is done in QMC at $T = 0$, where one takes those set of nodes which leads to the lowest internal energy. At finite temperature, we used the free energy argument above and concluded that the VDM nodes are more reliable. They do not seem to predict a first order PPT in the particular region of density and temperature shown in Fig. 4.4. However, there is the possibility that the PPT has been shifted to temperatures below 5000 K and that the metallic phase exhibits again a low temperature boundary, which is characterized by a PPT similar to the metallic regime predicted using free particle nodes as shown in Fig. 4.3. On the other hand, one can say that the PPT might have disappeared because we employed VDM nodes that includes a reasonable description of bound states as well as free particle states and therefore, we got rid of the imbalance that the free particle favored the metallic regime.

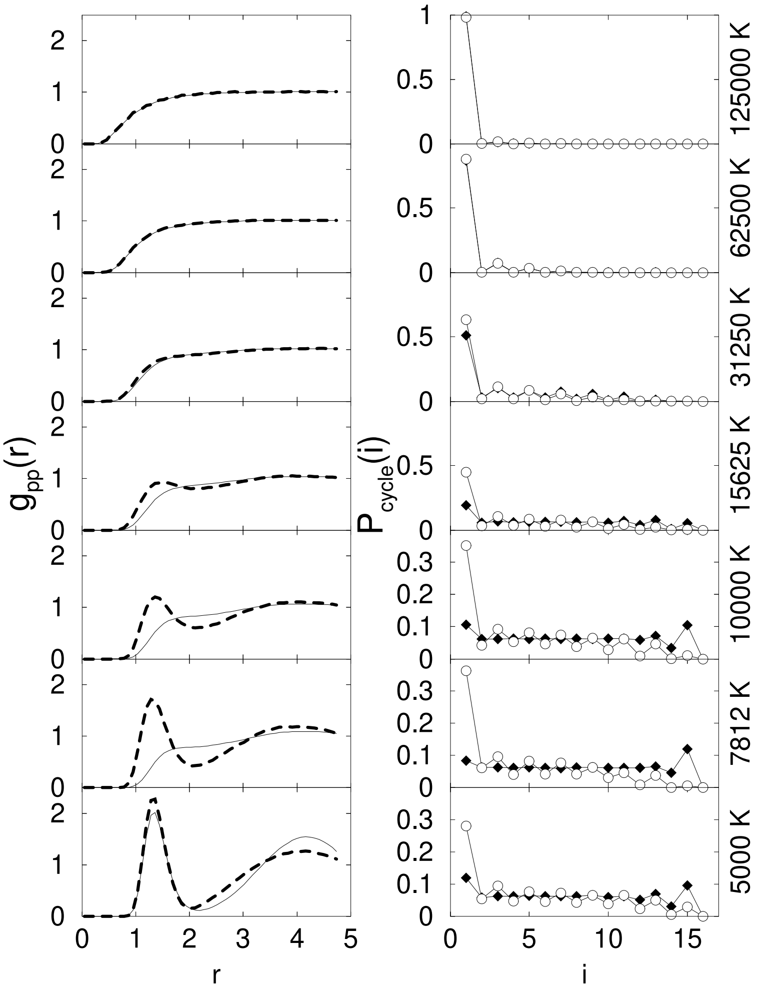

Figure 4.13: The proton-proton pair correlation functions from PIMC simulations with FP nodes (solid lines) and VDM nodes (dashed lines) at $r_s = 1.86$ are shown in the left column for different temperatures, which are indicates on the right. The right graphs show the corresponding electron permutation cycle distributions ($\Diamond$ for FP nodes and $\circ$ for VDM nodes). The VDM nodes show a gradual increase in the number of molecules and a lower permutation probability while FP nodes show a more abrupt change in the molecular fraction and a higher number of permutations, which suggests more delocalized electrons.

The PPT predicted by free particle nodes also predicted a change in the number of molecules. In Fig. 4.13, the proton-proton pair correlation functions as well as the permutation cycle distributions are shown for series of simulations for different temperatures at $r_s = 1.86$. The two functions were chosen in order to characterize the effect of the two different nodal surfaces. At high temperatures such as $T = 125\,000\,\mathrm{K}$, simulations with FP and VDM nodes give identical results because the nodes are equivalent in this limit. At this temperature, hydrogen is composed of strongly interacting gas of free protons and electrons with a moderate degree of electronic degeneracy ($T_F = 168\,090\,\mathrm{K}$). With decreasing temperature, the degeneracy increases, which can be inferred from cycle distributions. At 31 250 K, small deviations between FP and VDM nodes emerge. At half the temperature, the differences have increased further, which consequently lead to a different state with different proton-proton pair correlations. Simulations with VDM nodes predict a significant molecular fraction and a smaller degeneracy, while FP results show no peak in the proton-proton pair correlation function in combination with a larger degeneracy. In the FP case, most of the electrons are delocalized and occupy states similar to a free Fermi gas. VDM nodes predict that the electrons are in more localized states, which leads to the molecular binding.

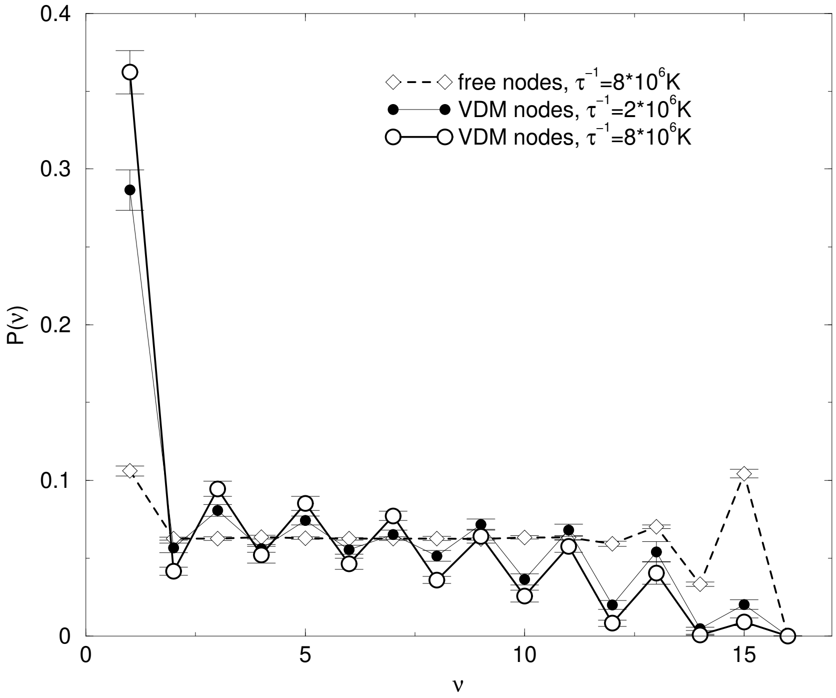

Figure 4.14: Comparison of the cycle length distribution (probability of an electron being involved in a permutation cycle of the length i) in a PIMC simulation of hydrogen with 32 protons and 16 electrons of each spin state at $T = 10\,000\,\mathrm{K}$ and $r_s = 1.86$ ($T_F = 168,090\,\mathrm{K}$).

At 7812 K one finds big differences in the proton-proton pair correlation functions since FP nodes predict a metallic state and VDM nodes a more molecular structure. At 5000 K both are rather similar because according the FP nodes, one has crossed the phase boundary, the pressure has risen and molecules are formed. VDM nodes, on the other hand, predict a smooth transition.

From Fig. 4.14, it can be deduced that the discussed differences in the number of permutations are indeed a consequence of the type of nodes rather than a result of using a too large time step. Going from $\tau^{-1} = 2 \cdot 10^6$K to $8 \cdot 10^6$K reduces the number of permutations slightly because the nodal surfaces are enforced more accurately, which prevents some permutations from occurring. However, the differences to FP results are significantly larger.

4.4 Pair Correlation Functions

In this section, we compare the pair correlation functions for different densities and temperatures from PIMC simulations using free particle and VDM nodes. The pair correlation function is defined as (Allen and Tildesley, 1987),

$$g(r) = \frac{\hat{V}}{N^2} \langle \sum_i \sum_{j \neq i} \delta(\mathbf{r} - \mathbf{r}_{ij}) \rangle \,. \tag{4.5}$$

It goes to 1 in the limit of large r in an infinite system and to $(N-1)/N$ in a system of N particles. The proton-proton pair correlation functions from PIMC simulations with free particle nodes are shown in Figs. 4.15 and 4.16. For $T \lesssim 20\,000\,\text{K}$ a peak at the bond length of 1.4 emerge, which clearly demonstrates the formation of molecules. In the low density region, we find it useful to multiply the pair correlation function by an extra density factor $N/\hat{V}$ so that the area under the peak is proportional to the molecular fraction. For $r_s \gtrsim 2$, the peak height gets smaller with decreasing density as a result of entropy dissociation. Thermal dissociation reduces the number of molecules with increasing temperature. For $r_s \lesssim 2$, pressure dissociation diminishes the peak with increasing density. For PIMC with free particle nodes, this process occurs within a small density interval, in which the system undergoes a transition from a molecular to a metallic regime (see Fig. 4.3).

Fig. 4.17 and 4.18 show the proton-proton pair correlation functions from PIMC simulations with VDM nodes using the standard normalization from Eq. 4.5. We also included simulations at higher densities corresponding to $r_s = 1$. The molecular peak disappears gradually with increasing density, indicating that pressure dissociation leads to a smooth transition to a metallic regime.

The proton-electron radial distribution function $r^2[g_{pe}(r) - 1]$ from different simulations using free particle nodes is shown in Fig. 4.19. For non-interacting particles, this function would be identical to zero. The first peak shows an increased probability of finding a electron near a proton due to the attractive forces. At low temperature, the size of peak can also be interpreted as the occupation of bound electronic states. Also the unbound, scattering states lead to a smaller but non-zero contribution to this

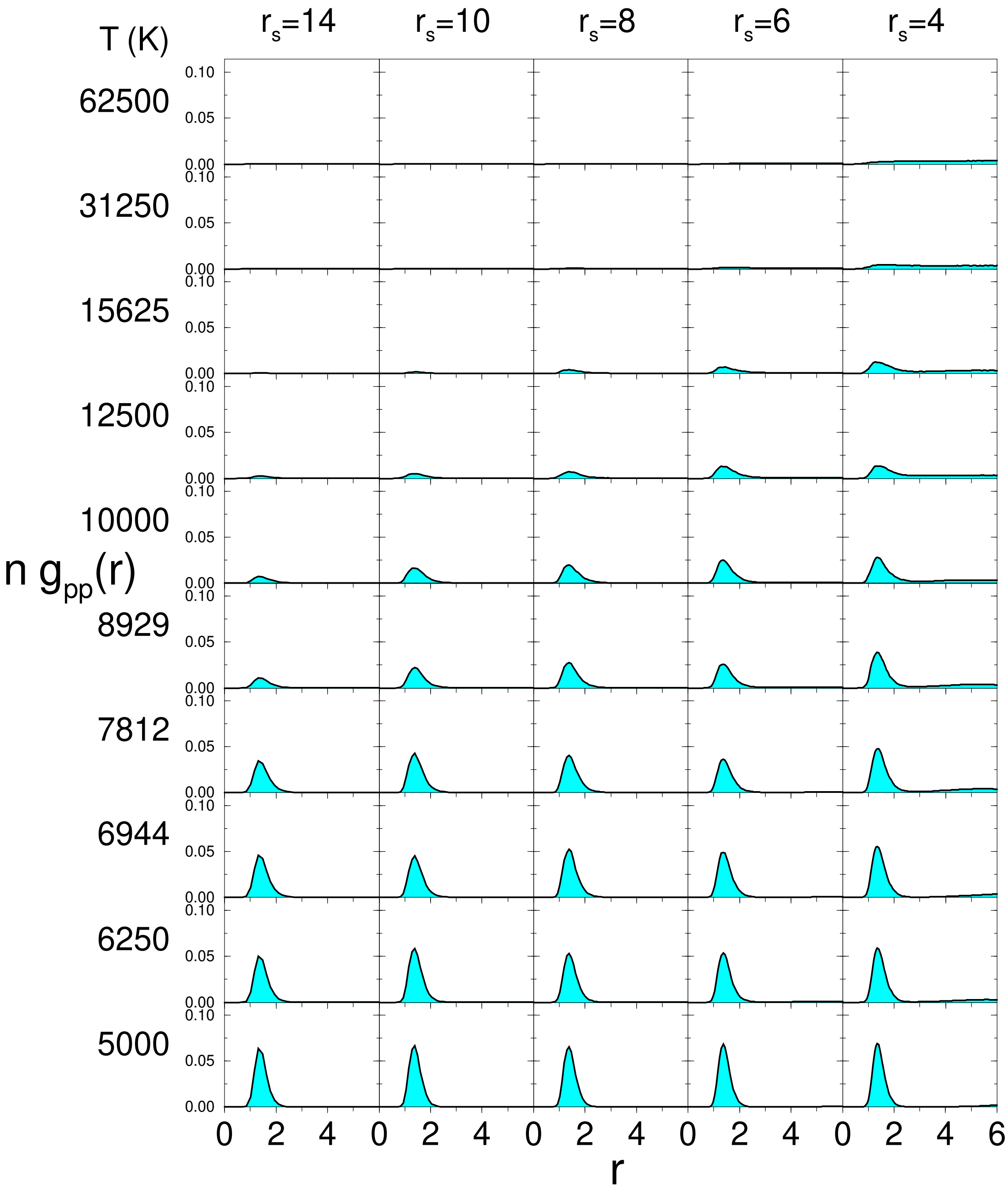

Figure 4.15: Proton-proton pair correlation functions multiplied by the density n from PIMC simulations of hydrogen using free particle nodes. The columns correspond to different r_s values and the rows to different temperatures T.

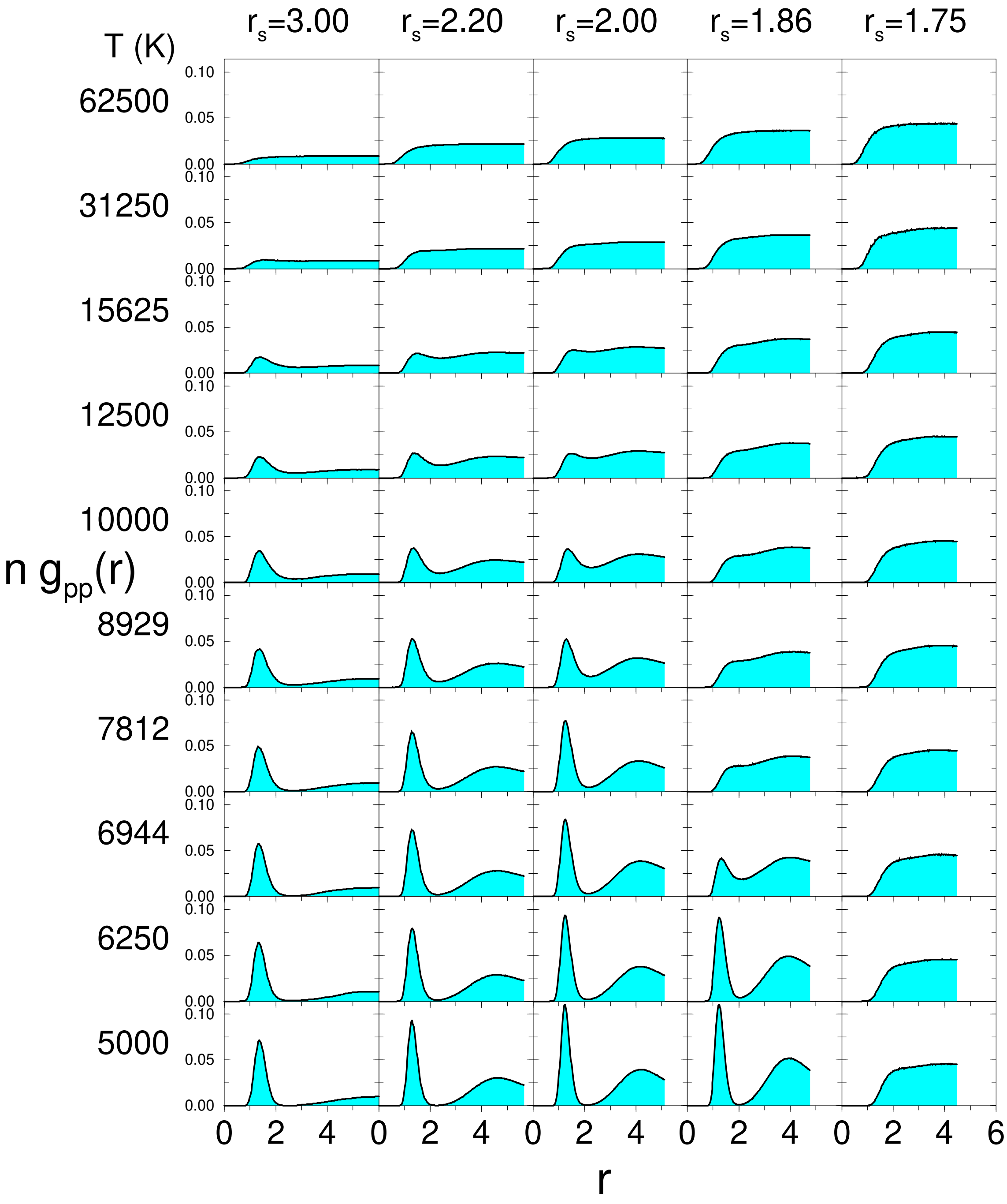

Figure 4.16: Proton-proton pair correlation functions multiplied by the density n as in Fig. 4.15 but for deuterium at higher densities.

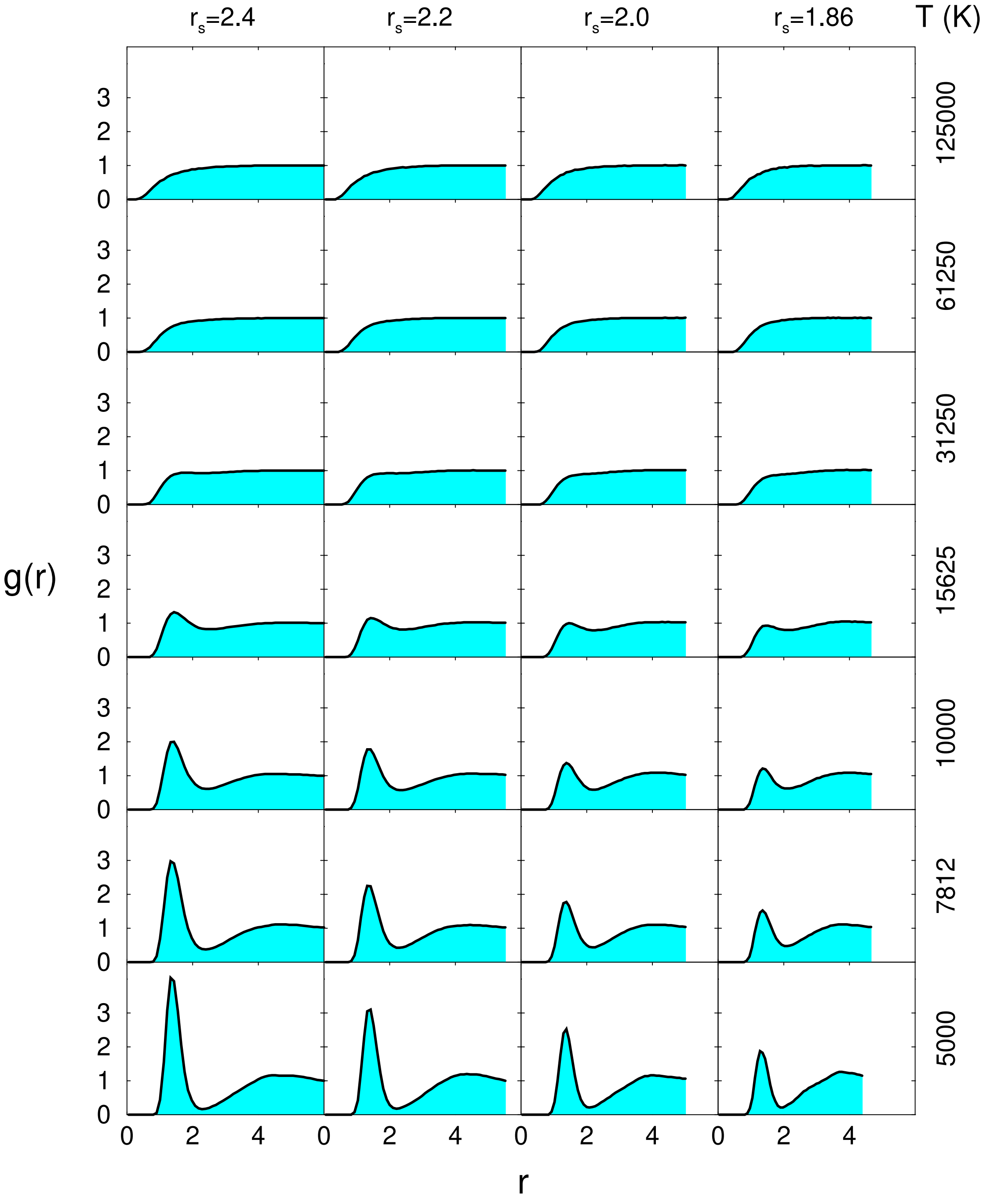

Figure 4.17: Proton-proton pair correlation function from PIMC simulations of deuterium using VDM nodes. The columns correspond to different r_s values and the rows to different temperatures T.

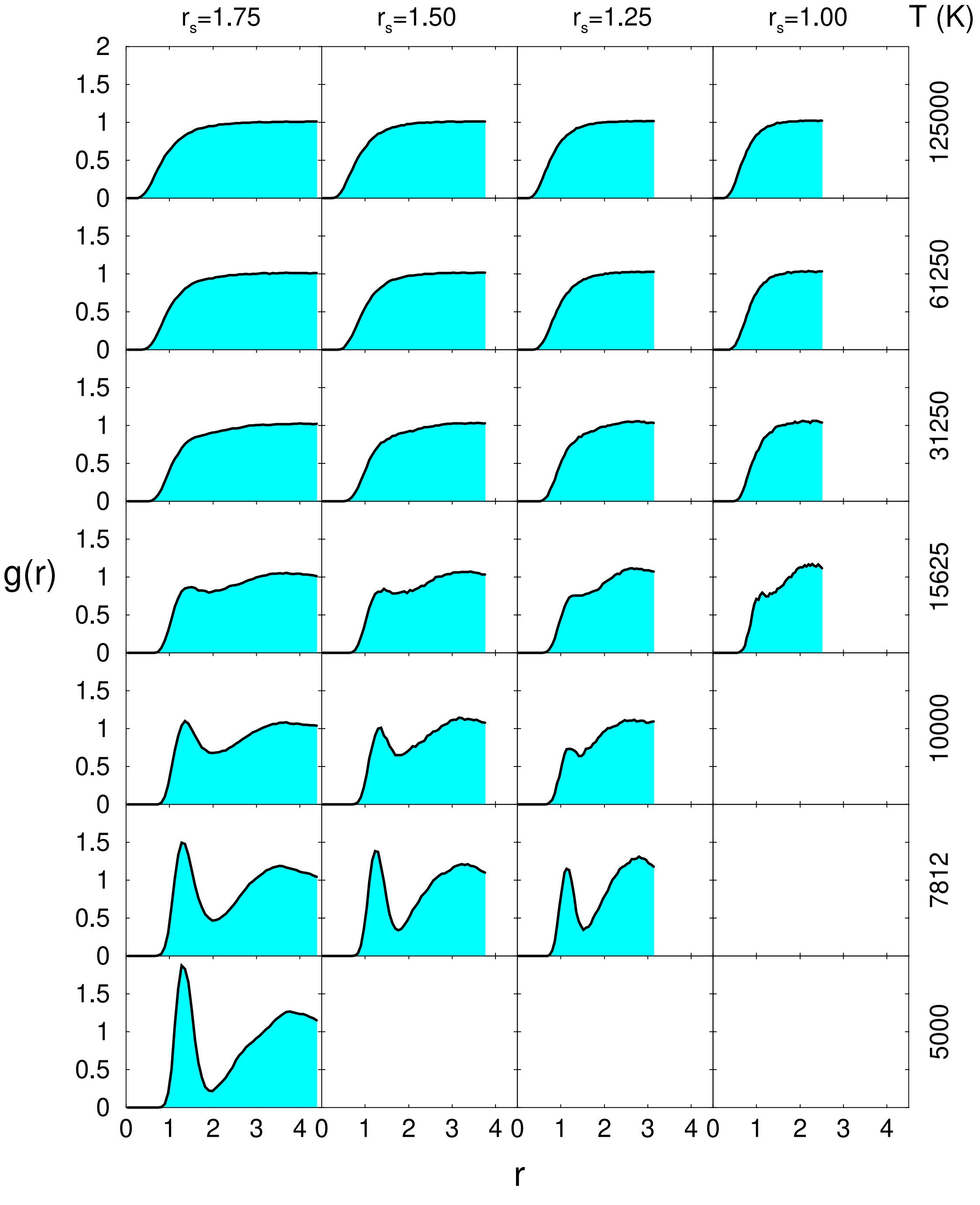

Figure 4.18: Proton-proton pair correlation function as in Fig. 4.17 but for higher densities.

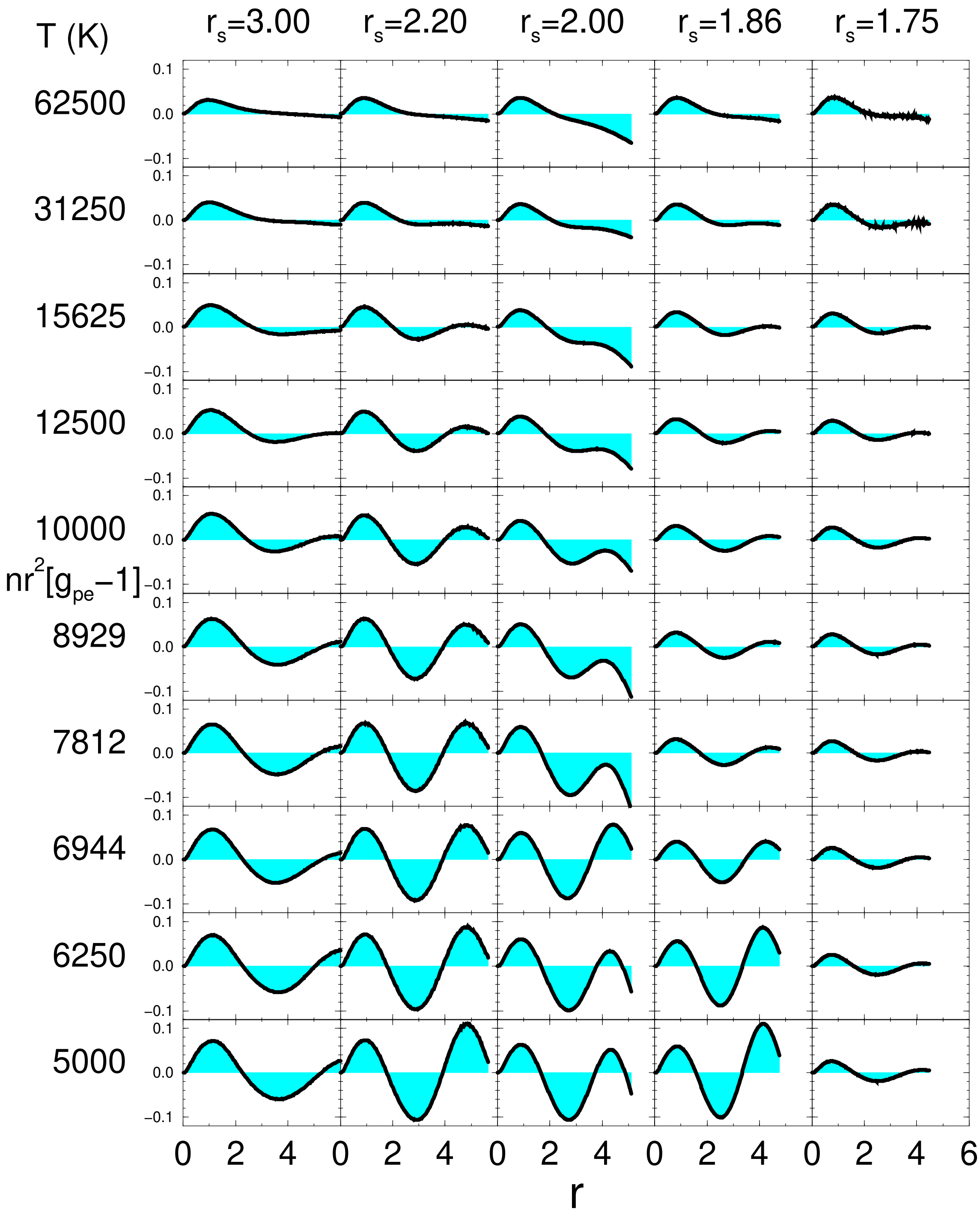

Figure 4.19: Proton-electron radial correlation function multiplied by the density, $n\, r^2\, [g_{pe}(r) - 1]$ from PIMC with free particle nodes. The columns correspond to different r_s values and the rows to different temperatures T.

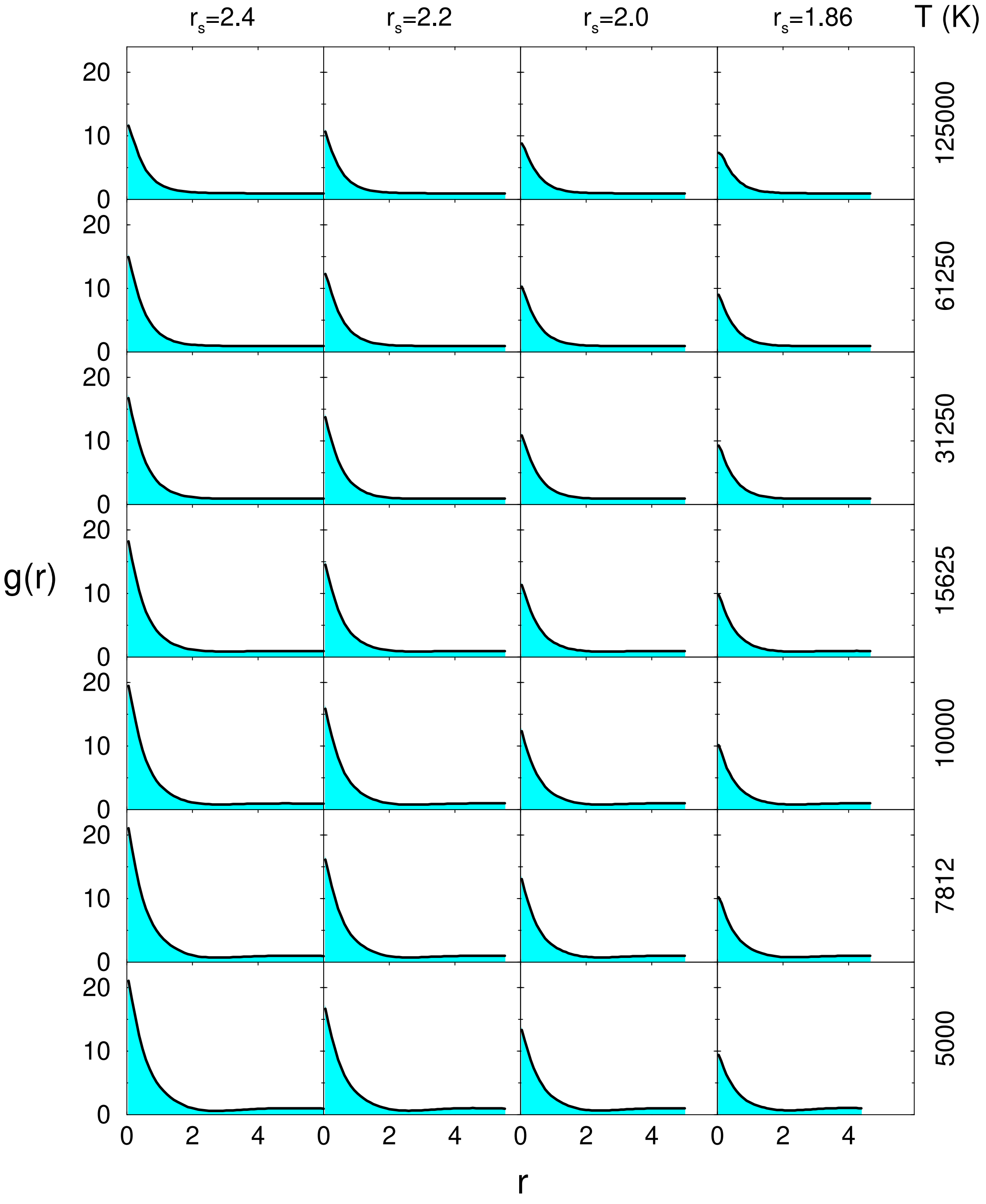

Figure 4.20: Proton-electron pair correlation function from PIMC simulations of deuterium using VDM nodes. The columns correspond to different r_s values and the rows to various temperatures.

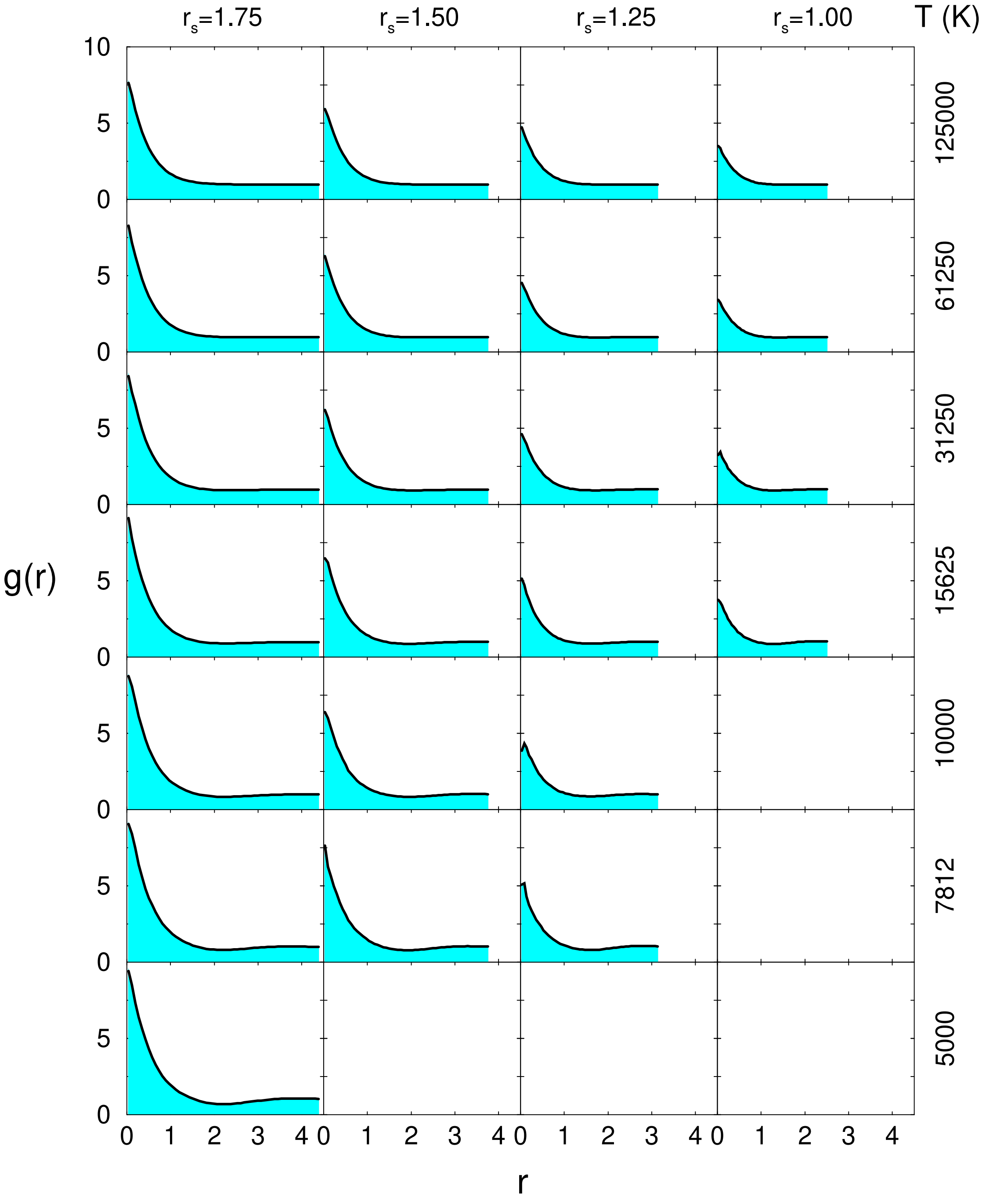

Figure 4.21: Proton-electron pair correlation function as in Fig. 4.20 but for higher densities.

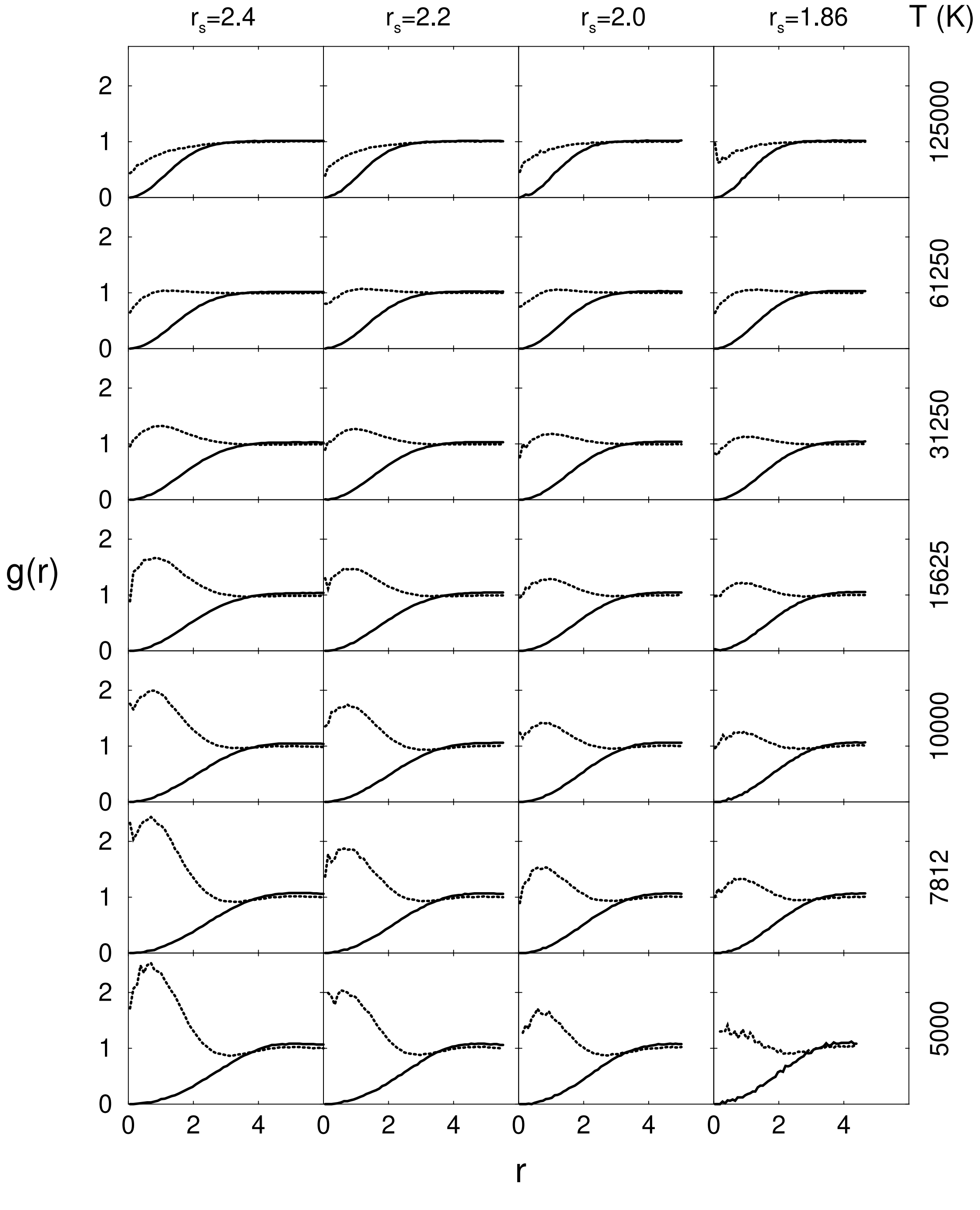

Figure 4.22: Electron-electron pair correlation function from PIMC simulations of deuterium using VDM nodes. Solid lines correspond to pairs with parallel spins and dashed lines to anti-parallel spins. The columns belong to different r_s values and the rows to various temperatures T.

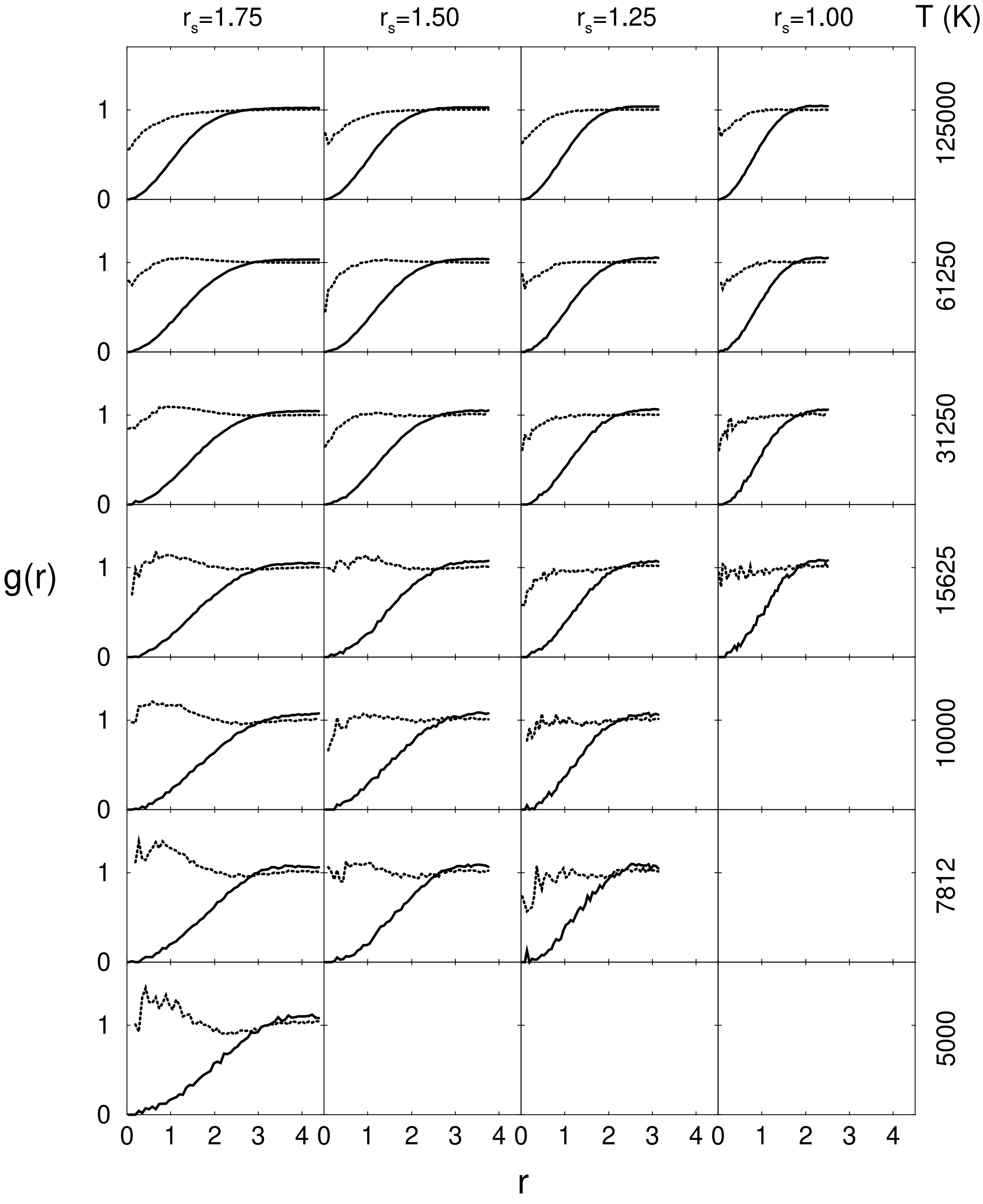

Figure 4.23: Electron-electron pair correlation function as in Fig. 4.22 but for higher densities.

peak. However, one can still deduce that the degree of ionization, inversely related to the peak size, increases with temperature.

Alternatively, one can study the proton-electron pair correlation function as shown in Fig. 4.20 and 4.21 from simulations using VDM nodes, where the same overall behavior is represented in a different form. Fig. 4.22 and 4.23 show the electron-electron pair-correlation functions. The peak for pairs with anti-parallel electron spins indicates the formation of molecules, in which two electrons get very close, in cases where they realize the molecular binding. For same spin electrons, one always finds a strong repulsion due to the Pauli exclusion principle.

4.5 Equation of State

The equation of state (EOS) is central interest in theoretical plasma physics since it is the basic thermodynamic quantity. It is also the key property to test the accuracy of different approaches to hot, dense hydrogen including analytical theories and numerical models. If the predicted EOS seems reasonable, one can have more confidence in all derived properties. The complete EOS data from our PIMC simulations can be found in tables in App. D.

First, we picked the density corresponding to $r_s = 2$ and compared pressure and energy as a function of temperature. We separated the analysis in the high temperature behavior $k_B T \gtrsim 1\,\mathrm{Ry}$ where thermal excitations dominate, and the low temperature regime $k_B T \lesssim 1\,\mathrm{Ry}$ where Coulomb effects and bound states are most relevant.

The pressure and energy in the high temperature regime are shown in Figs. 4.24 and 4.25. In the high temperature limit, kinetic effects are dominant and the hydrogen plasma behaves like a gas of non-interacting protons and electrons. The leading corrections are given by Debye screening effects (see App. C) that scale with the coupling parameter $\Gamma^{3/2}$. For small values of Γ, the (fully ionized) Debye model is a reliable approximation. One finds deviations of less than 20% in pressure and energy for $\Gamma < 0.5$ at $r_s = 2$. For higher values of Γ, quantum effects such as the formation of bound state at low density and degeneracy effects at high density limit the validity. Various extensions to the Debye model have been made, see (Ebeling *et al.*, 1976). However, at sufficiently high Γ, the Debye model overestimates the screening drastically and leads to unphysically low, even negative pressures.

Figs. 4.24 and 4.25 include a comparison with EOS model by Saumon and Chabrier (1992), the Padé approximations in the chemical picture (PACH) by Ebeling and

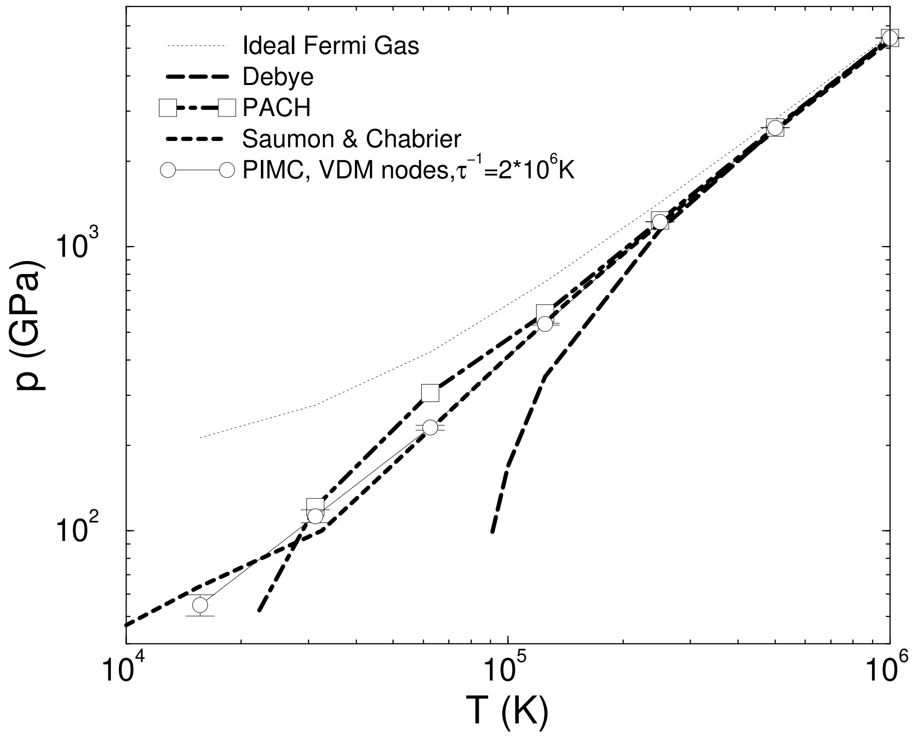

Figure 4.24: Comparison of pressure vs. temperature for $r_s = 2$ from the ideal Fermi gas, the Debye model, the Padé approximations in the chemical picture (PACH) by Ebeling and Richert (1985a), the EOS by Saumon and Chabrier (1992) and from PIMC simulations with VDM nodes, $\tau^{-1} = 2 \cdot 10^6\,\mathrm{K}$, $n_{\mathrm{A}} = 1$, and $n_{\mathrm{E}} = 2$.

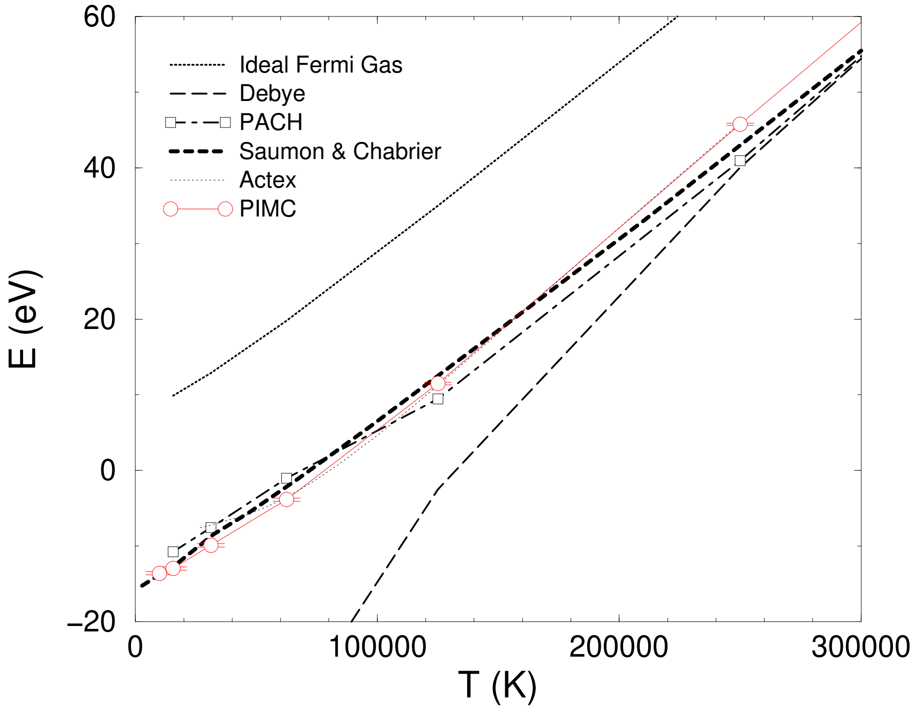

Figure 4.25: Internal energy per atom vs. temperature for $r_s = 2$ from the methods in Fig. 4.24 and the activity expansion (Actex) by Rogers (1990).

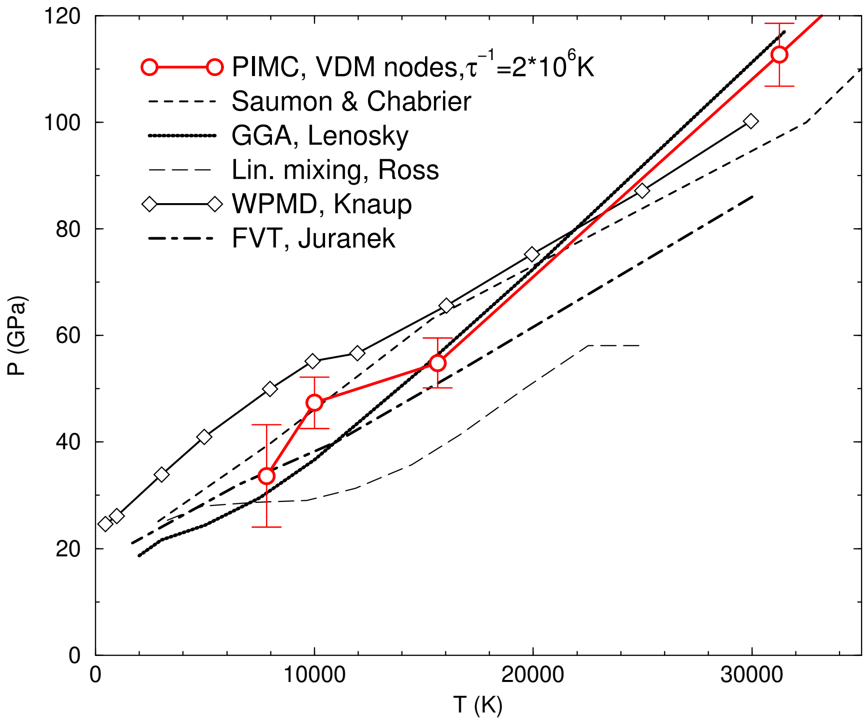

Figure 4.26: Pressure vs. temperature for $r_s = 2$ from the EOS by Saumon and Chabrier (1992), DFT-MD by Lenosky *et al.* (2000), linear mixing model by Ross (1998), wave packet MD by Knaup *et al.* (2000), from the fluid variational theory by Juranek and Redmer (2000) and from PIMC simulations with VDM nodes, $\tau^{-1} = 2 \cdot 10^6\,\mathrm{K}$, $n_\mathrm{A} = 1$, and $n_\mathrm{E} = 2$.

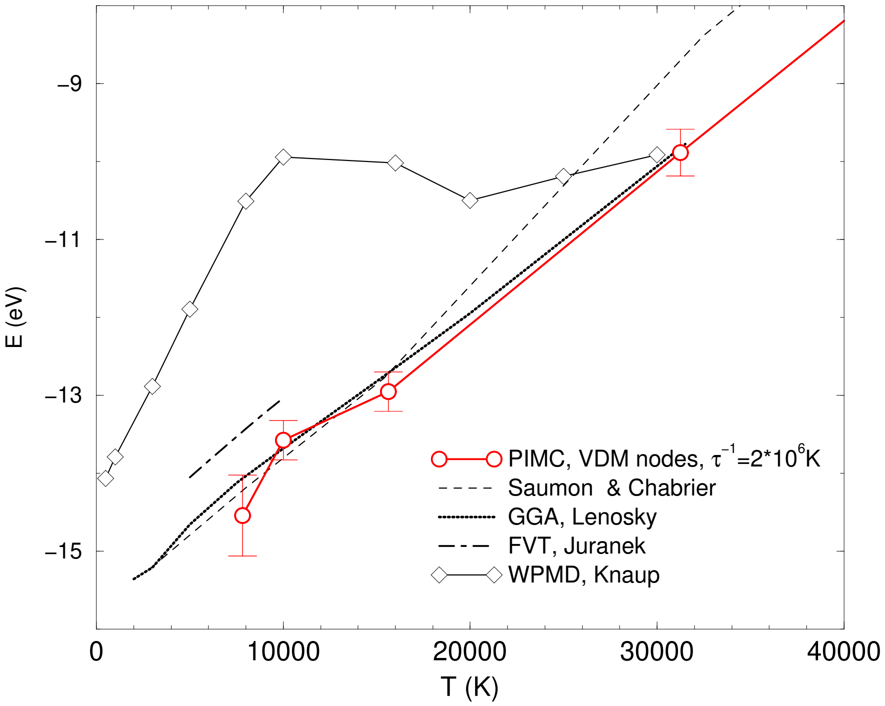

Figure 4.27: Internal energy per atom vs. temperature for $r_s = 2$ from the methods in Fig. 4.26

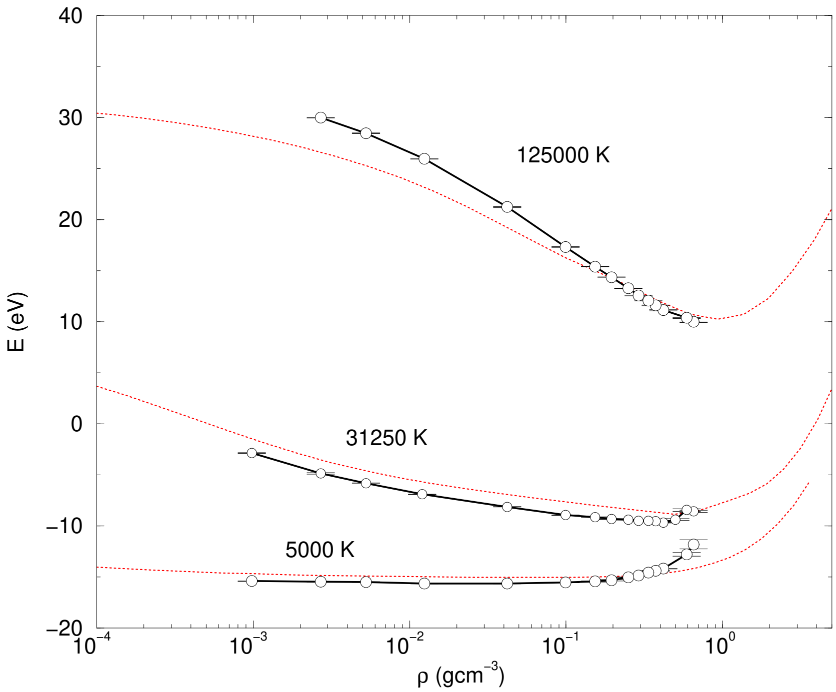

Figure 4.28: Internal energy per atom vs. hydrogen density from PIMC simulation ($\circ$) with $\tau^{-1} = 10^6\,$K, $n_\mathrm{A} = 1$, and $n_\mathrm{E} = 2$ using free particle nodes are compared with the equation of state by Saumon and Chabrier (1992) (dashed lines).

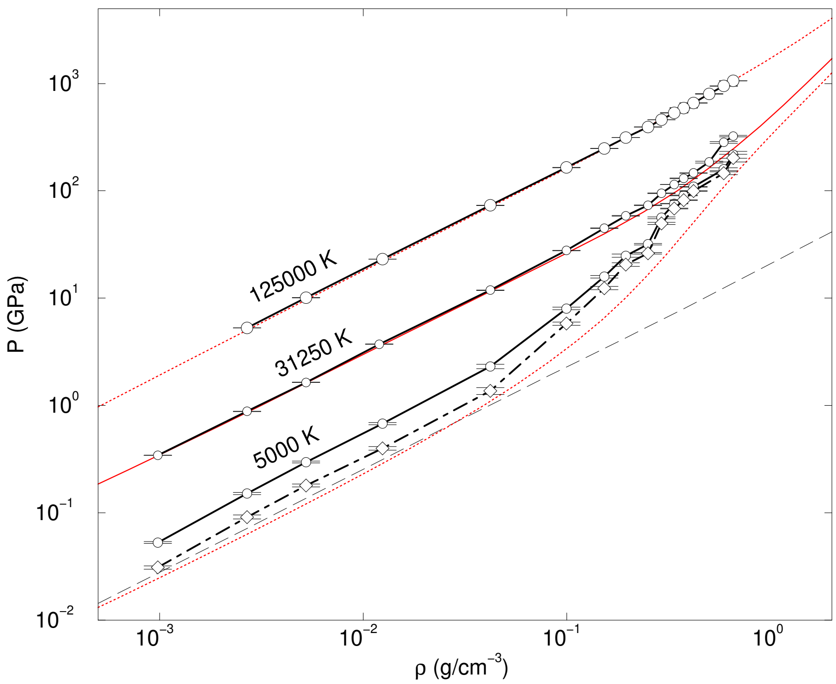

Figure 4.29: Pressure vs. hydrogen density from PIMC simulations ($\circ$) with $\tau^{-1} = 10^6\,$K, $n_\mathrm{A} = 1$, and $n_\mathrm{E} = 2$ using free particle nodes are compared with the equation of state by Saumon and Chabrier (1992) (dash lines). $\Diamond$ show PIMC results with pressure correction $\Delta p = -\frac{n}{3}\ 0.7\,\mathrm{eV}$ discussed section 4.1. The thin dashed line denotes the pressure of an ideal H_2 gas at $T = 5000\,$K.

Richert (1985a), and the activity expansion (Actex) by Rogers (1990). The observed deviations are a result of how interaction and degeneracy effects are treated in those models.

In Figs. 4.26 and 4.27, we compare pressure and energy in the low temperature regime. The EOS properties are determined by a strong coupling combined with a high degeneracy ($T_F = 145\,000\,\mathrm{K}$). The comparison includes EOS by Saumon and Chabrier (1992), the DFT-MD by Lenosky *et al.* (2000), the fluid variational theory by Juranek and Redmer (2000), the wave-packet MD by Knaup *et al.* (2000), the linear mixing model by Ross (1998), and PIMC simulations using free particle nodes and $\tau^{-1} = 2 \cdot 10^6\,\mathrm{K}$. For this density, we found the best agreement of our results with the work by DFT-MD by Lenosky *et al.* (2000).

Finally, we present a comparison of internal energy and pressure as a function of density for different temperatures. Fig. 4.28 shows a reasonably good agreement in the energy between the EOS by Saumon and Chabrier (1992) and our simulation results over a broad range of densities. PIMC energies for low temperatures and densities are consistently lower by the order 1 or 2 eV per atom. For low density and high temperature, relatively large deviations were observed, which is surprising because in this regime, one expects both methods to work very well.

Studying the pressure as function of density in Fig. 4.29, one finds remarkably good agreement for $T = 125\,000$ and $31\,250\,\mathrm{K}$. For 5000 K, the PIMC pressure is far too high because hydrogen under these conditions is a weakly interacting molecular gas with possibly a very small degree of dissociation caused by entropy effects. The PIMC pressure is about twice the expected value, which is a result of the inaccuracies in the pair density matrices discussed in section 4.1. After those corrections have been applied one finds better but not perfect agreement. New calculations with improved density matrices remain to be done.

4.6 Shock Hugoniot

Recent Nova laser shock wave experiments on pre-compressed liquid deuterium (Da Silva *et al.*, 1997; Collins *et al.*, 1998) provided the first direct measurements of the high temperature equation of state of deuterium for pressures up to 330 GPa. It was found that deuterium has a *significantly higher compressibility* than predicted by the semi-empirical equation of state based on plasma many-body theory and lower pressure shock data (see SESAME model by Kerley (1983)). In an earlier series of experiments using the two-stage gas gun (Holmes *et al.*, 1995; Nellis *et al.*, 1983), pressures of up to 23 GPa were reached. The laser experiments are of particular importance to this work because they represent the only experimental data our PIMC simulation results can be directly compared to. The temperatures reached in gas gun experiments did not exceed 4400 K. Therefore a direct comparison with PIMC simulations is currently not feasible.

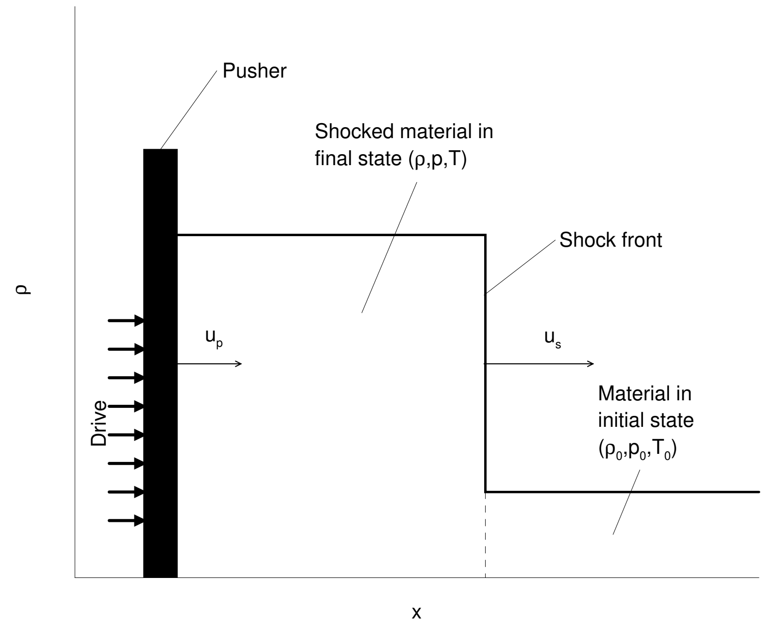

Figure 4.30: Density profile in an idealized shock experiment, in which a driving force moves the pusher at constant velocity u_p. The resulting shock wave travels at velocity u_s.

Shock wave experiments are an established technique (Zeldovich and Raizer, 1966) to determine the equation of state at high pressures and temperature, which has been applied to a wide range of materials including aluminum, iron, and water. In the experiment, a driving force is utilized to propel a pusher at constant velocity u_p into a material at predetermined initial conditions (ϱ_0, p_0, T_0) as shown in Fig. 4.30. The impact generates a planar shock wave, which travels at the constant velocity u_s with $u_s > u_p$. The shock compression drives the material to a point on the principle Hugoniot, which is the locus of all final states characterized by (ϱ, p, T) that can be achieved by a single shock wave passing through. Under the assumption of an *ideal shock* (see below), the conservation laws of mass, momentum, and energy require only the measurement of the velocities of the pusher u_p and the shock front u_s in order to obtain an absolute equation of state data point. Pressure and density of the shock material are related to u_s and u_p by,

$$p - p_0 = \varrho_0 u_s u_p \tag{4.6}$$

$$\frac{\varrho}{\varrho_0} = \frac{u_s}{u_s - u_p} \quad . \tag{4.7}$$

The internal energy in the final state follows from the conservation laws,

$$H = E - E_0 + \frac{1}{2}(\hat{V} - \hat{V}_0)(p + p_0) = 0 \quad , \tag{4.8}$$

which is called the Hugoniot relation. It can also be used to determine the Hugoniot curve analytically from a given equation of state.

By an ideal shock, one means that a planar pusher is driven at constant velocity into the sample. The resulting shock wave is characterized by a planar shock front that travels at constant velocity during the measurement. Furthermore, one assumes that unshocked material remains at known initial conditions and not preheated as for example by x-rays created at the laser target interaction. Under these assumptions, one can determine the equation of state from the measured velocities u_s and u_p using Eqs. 4.6-4.8.

In the recent laser shock experiments, a shock wave is propagating through a sample of pre-compressed liquid deuterium characterized by an initial state, $(E_0, \hat{V}_0, p_0)$

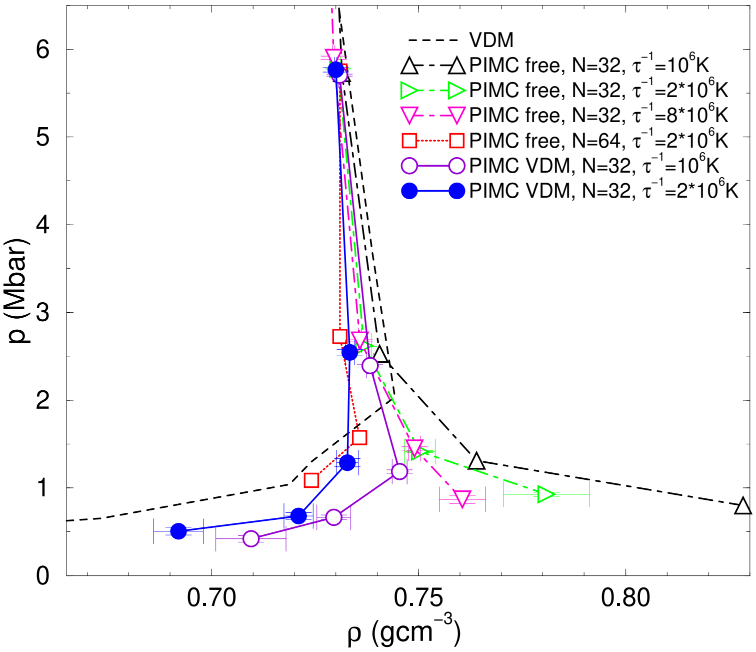

Figure 4.31: Comparison Hugoniot function calculated with PIMC simulations of different accuracy using $n_A = 1$, and $n_E = 2$: FP nodes with N_P=32 ($\triangle$ for $\tau^{-1} = 10^6$K reported by Militzer *et al.* (1998), $\triangleright$ for $\tau^{-1} = 2{\cdot}10^6$K, $\bigtriangledown$ for $\tau_F^{-1} = 8{\cdot}10^6$K and $\tau_B^{-1} = 2 \cdot 10^6$K) and N_P=64 ($\square$ for $\tau^{-1} = 2 \cdot 10^6$K) as well as with VDM nodes and N_P=32 ($\circ$ for $\tau^{-1} = 10^6$K and $\bullet$ for $\tau^{-1} = 2 \cdot 10^6$K). Beginning at high pressures, the points on each Hugoniot correspond to the following temperatures 125 000, 62 500, 31 250, 15 625, and 10 000 K. The dashed line corresponds to a calculation using the VDM alone.

with $T = 19.6\,\mathrm{K}$ and $\varrho_0 = 0.171\,\mathrm{g/cm^3}$. In our calculations, we set E_0 to its exact value of -15.886eV per atom (Kolos and Wolniewicz, 1964) and $p_0 = 0$ because $p \gg p_0$. Using the PIMC simulation results for p and E, we calculate $H(T, \varrho)$ from Eq. 4.8 and then interpolate H linearly at constant T between the two densities corresponding to $r_s = 1.86$ and 2 to obtain a point on the Hugoniot in the (p, ϱ) plane. Results at $r_s = 1.93$ confirm that the function is linear within the statistical errors. The PIMC data for p, E, and the Hugoniot are given in Tab. 4.4.

Table 4.4: Pressure p and internal energy per atom E from PIMC simulations with 32 pairs of electrons and deuterons. For $T \geq 250\,000\,\mathrm{K}$, we list results from simulations with FP nodes and $\tau_F^{-1} = 8 \cdot 10^6\,\mathrm{K}$ and $\tau_B^{-1} = 2 \cdot 10^6\,\mathrm{K}$, otherwise with VDM nodes and $\tau^{-1} = 2 \cdot 10^6\,\mathrm{K}$.

T(K)	p(Mbar)	E(eV)	p(Mbar)	E(eV)	$\varrho^{\mathrm{Hug}}(\mathrm{gcm^{-3}})$	p^{Hug}(Mbar)
	$r_s = 2$	$r_s = 2$	$r_s = 1.86$	$r_s = 1.86$		
1 000 000	53.79 (5)	245.7 (3)	66.85 (8)	245.3 (4)	0.7019 (1)	56.08 (5)
500 000	25.98 (4)	113.2 (2)	32.13 (5)	111.9 (2)	0.7130 (1)	27.48 (4)
250 000	12.12 (3)	45.7 (2)	14.91 (3)	44.3 (2)	0.7242 (1)	12.99 (2)
125 000	5.29 (4)	11.5 (2)	6.66 (2)	11.0 (1)	0.7300 (3)	5.76 (2)
62 500	2.28 (4)	-3.8 (2)	2.99 (4)	-3.8 (2)	0.733 (1)	2.54 (3)
31 250	1.11 (6)	-9.9 (3)	1.58 (7)	-9.7 (3)	0.733 (3)	1.28 (5)
15 625	0.54 (5)	-12.9 (3)	1.01 (5)	-12.0 (2)	0.721 (4)	0.68 (4)
10 000	0.47 (5)	-13.6 (3)	0.80 (8)	-13.2 (4)	0.690 (7)	0.51 (5)

In Fig. 4.31, we compare the effects of different approximations made in the PIMC simulations such as time step τ, number of pairs N_P and the type of nodal restriction. For pressures above 3 Mbar, all these approximations have a very small effect. The reason is that PIMC simulation become increasingly accurate as temperature increases. The first noticeable difference occurs at $p \approx 2.7$Mbar, which corresponds to $T = 62\,500\,\mathrm{K}$. At lower pressures, the differences become more and more pronounced. We have performed simulations with free particle nodes and $N_P = 32$ for three different values of τ. Using a smaller time step makes the simulations computationally more demanding and it shifts the Hugoniot curves to lower densities. These differences come mainly from enforcing the nodal surfaces more accurately, which seems to be more relevant than the simultaneous improvements in the accuracy of the action S, that is the time step is more constrained by the Fermi statistics than it is by the potential energy. We improved the efficiency of the algorithm by using a smaller time step τ_F for evaluating the Fermi action than the time step τ_B used for the potential action. Unless specified otherwise, we used $\tau_F = \tau_B = \tau$. At even lower pressures not shown in Fig. 4.31, all of the Hugoniot curves with FP nodes turn around and go to low densities as expected.

As a next step, we replaced the FP nodes by VDM nodes. Those results show that the form of the nodes has a significant effect for p below 2 Mbar. Using a smaller τ also shifts the curve to slightly lower densities. In the region where atoms and molecules are forming, it is plausible that VDM nodes are more accurate than free nodes because they can describe those states (see chapter 3). We also show a Hugoniot derived on the basis of the VDM alone (dashed line). These results are quite reasonable considering the approximations (Hartree-Fock) made in that calculation. Therefore, we consider the PIMC simulation with the smallest time step using VDM nodes ($\bullet$) to be our most reliable Hugoniot. Going to bigger system sizes $N_P = 64$ and using FP nodes also shows a shift towards lower densities.

Fig. 4.32 compares the Hugoniot from laser shock wave experiments (Da Silva *et al.*, 1997; Collins *et al.*, 1998) with PIMC simulations (VDM nodes, $\tau^{-1} = 2 \cdot 10^6\,\mathrm{K}$) and several theoretical approaches: SESAME model by Kerley (1983) (thin solid line), linear mixing model (dashed line) by Ross (1998), DFT-MD by Lenosky *et al.* (2000) (dash-dotted line), Padé approximation in the chemical picture (PACH) by Ebeling and Richert (1985a) (dotted line), and the work by Saumon and Chabrier (1992) (thin dash-dotted line).

The differences of the various PIMC curves in Fig. 4.31 as well as in Fig. 4.32 are small compared to the deviation from the experimental results by Da Silva *et al.* (1997) and Collins *et al.* (1998). One finds that the corrections from Eq. 4.3 have only a small effect on the Hugoniot. In the experiments, an increased compressibility with a maximum value of 6 ± 1 was found while PIMC predicts 4.3 ± 0.1, only slightly higher than that given by the SESAME model. Only for $p > 2.5$Mbar, does our Hugoniot lie within experimental error bars. In this regime, the deviations in the PIMC and PACH Hugoniot are relatively small, less than $0.05\,\mathrm{gcm}^{-3}$ in density. In the high pressure limit, the Hugoniot goes to the FP limit of 4-fold compression. This trend is also present in the experimental findings. For pressures below 1 Mbar, the PIMC Hugoniot goes back to lower densities and shows the expected tendency towards the experimental values from earlier gas gun work Nellis *et al.* (1983); Holmes *et al.* (1995) and lowest data points from Da Silva *et al.* (1997); Collins *et al.* (1998). This trend can be studied best in the logarithmic graph shown in Fig 4.33, where we also included our lowest available pressure point on the Hugoniot, which was obtained from simulations with 32 pairs of electrons and deuterons and the time step $\tau_F^{-1} = 8 \cdot 10^6\,\mathrm{K}$ and $\tau_B^{-1} = 2 \cdot 10^6\,\mathrm{K}$. Within the statistical error bars, the PIMC

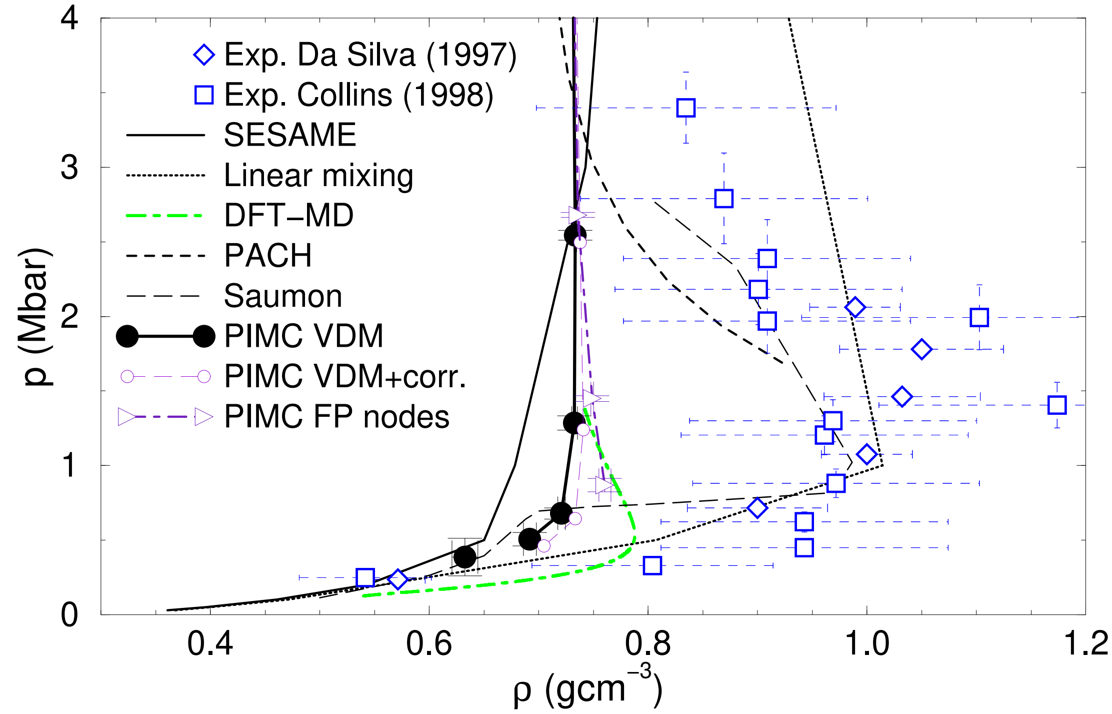

Figure 4.32: Comparison of experimental and several theoretical Hugoniot functions. All three PIMC curves were calculated with $\tau^{-1} = 2 \cdot 10^6\,\mathrm{K}$, $n_\mathrm{A} = 1$, $n_\mathrm{E} = 2$, and 32 pairs of electrons and deuterons. They were obtained with free particle nodes, VDM nodes, and VDM nodes plus the corrections from Eq. 4.3.

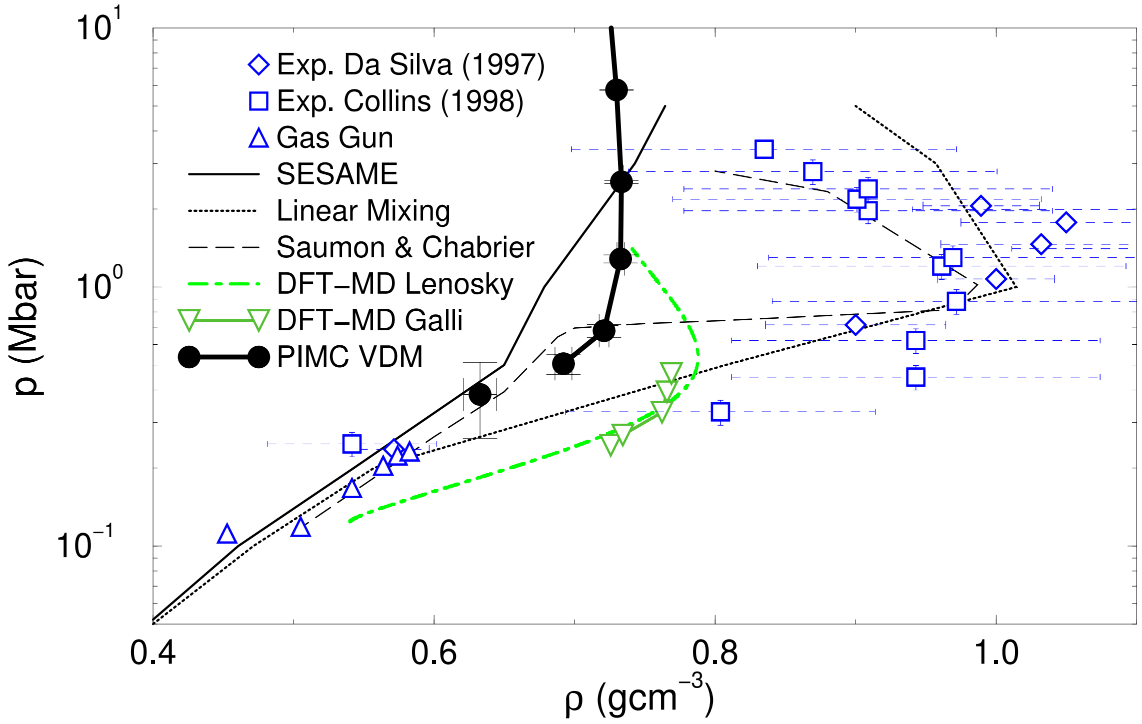

Figure 4.33: Logarithmic Hugoniot graph as in Fig. 4.32. including the gas gun experiments by Holmes *et al.* (1995) and Nellis *et al.* (1983).

Hugoniot curve tends towards the results from gas gun experiments. For these low pressures, one also finds that the differences between PIMC and DFT-MD are also relatively small compared to the deviation from the laser shock data.

Using the PIMC equation of state, one can also determine the shock and pusher velocity on the Hugoniot. From Eqs. 4.6 and 4.7, one finds,

$$m_D u_s^2 = \frac{\varrho}{\varrho - \varrho_0} \frac{p}{\varrho_0} \quad , \tag{4.9}$$

$$m_D u_p^2 = p \left(\frac{1}{\varrho_0} - \frac{1}{\varrho} \right) \quad . \tag{4.10}$$

The results are shown in Fig. 4.34 and compared to the experimental shock and pusher velocities published in (Collins *et al.*, 1998). First of all, one finds the differences between theory and experiment are not as pronounced as in the p-ϱ graph in Fig. 4.32. This fact simply follows from Eq. 4.7 where one divides by the difference of u_s and u_p. It means that one needs a high accuracy in the measurements of both velocities,

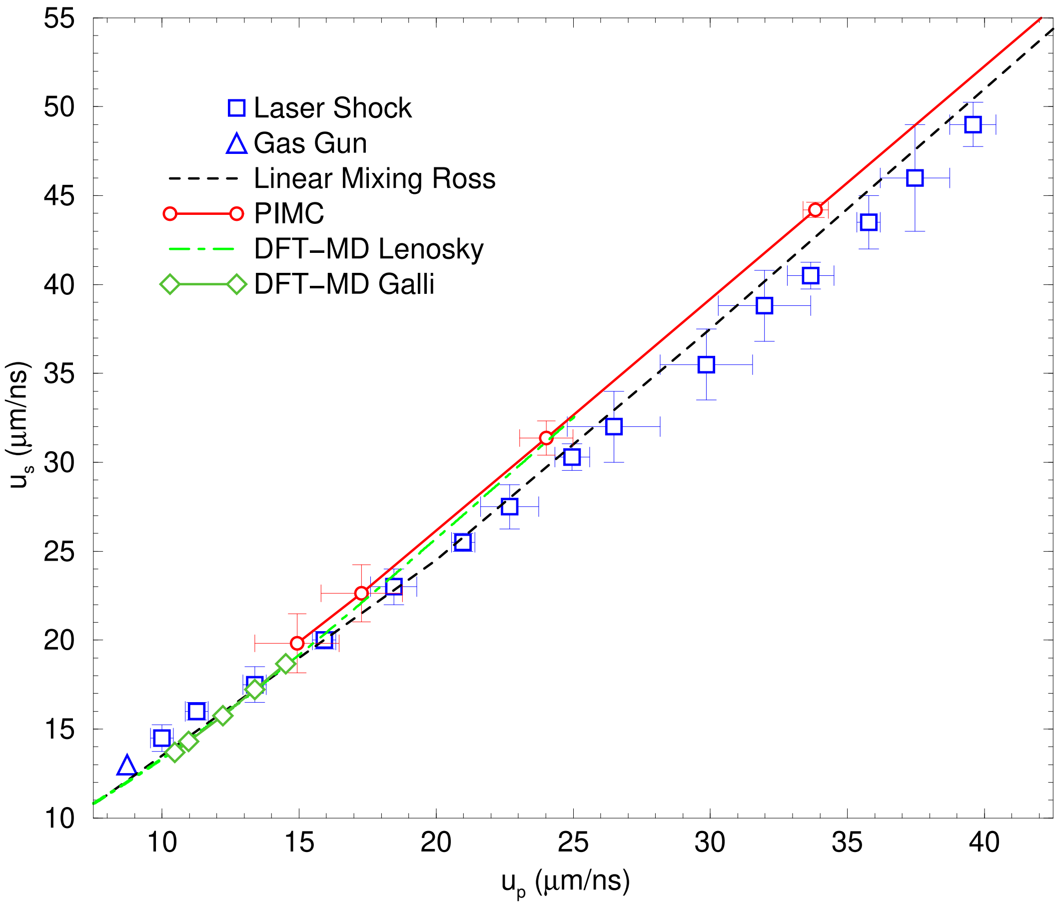

Figure 4.34: Shock velocity vs. pusher velocity as directly measured in the shock wave experiment and the comparison with estimates from PIMC simulation with VDM nodes.

since error bars will increase substantially when the density is determined. However, it is not obvious why the PIMC and DFT-MD results are in within the corners of the experimental u_s-u_p error bars. A simple error propagation of these u_s and u_p error bars leads to much bigger error bars in the density than those reported by Da Silva *et al.* (1997) and Collins *et al.* (1998) and shown in Fig. 4.31. Possibly the experiments allow a more accurate determination of the difference $u_s - u_p$ than of the individual velocities.

Summarizing, one can say that PIMC simulations predict a slightly increased compressibility of 4.3 ± 0.1 compared to the SESAME model but they cannot reproduce the experimental findings of values of about 6 ± 1. Further theoretical and experimental work will be needed to resolve this discrepancy.

Chapter 5

Off-Diagonal Density Matrix Elements

In this chapter, we are going to describe the sampling of off-diagonal matrix elements using the path-integral formalism. Instead of calculating diagonal density matrix elements $\rho(\mathbf{R}, \mathbf{R}' = \mathbf{R}; \beta)$, for which the paths return to their starting point, we now include the possibility of open paths. Opening one path allows one the sampling of the *single-particle reduced density matrix* defined by,

$$\rho^{[1]}(\mathbf{r}_1, \mathbf{r}'_1) = \frac{\hat{V}}{Z} \int d\mathbf{r}_2 \cdots d\mathbf{r}_N \, \rho(\mathbf{r}_1, \mathbf{r}_2, \ldots, \mathbf{r}_N \,, \, \mathbf{r}'_1, \mathbf{r}_2, \ldots, \mathbf{r}_N) \quad , \tag{5.1}$$

which is related to the momentum distribution. A PIMC simulation with two open paths samples the *two-particle reduced density matrix*,

$$\rho^{[2]}(\mathbf{r}_1, \mathbf{r}_2, \mathbf{r}'_1, \mathbf{r}'_2) = \frac{\hat{V}^2}{Z} \int d\mathbf{r}_3 \cdots d\mathbf{r}_N \, \rho(\mathbf{r}_1, \mathbf{r}_2, \mathbf{r}_3, \ldots, \mathbf{r}_N \,, \, \mathbf{r}'_1, \mathbf{r}'_2, \mathbf{r}_3, \ldots, \mathbf{r}_N) \quad , \tag{5.2}$$

which will be used to study *natural orbitals*. In the following two sections, we discuss the modifications to the sampling procedure in order to deal with the open ends.

5.1 Sampling with Open Paths

In this section, the multilevel sampling procedure from sections 2.5.3 and 2.6.9 will be extended to the sampling with open paths for Bosons and distinguishable particles. Fermions will be discussed in section 5.2. A picture of an open path is shown in Fig. 5.1. We chose to put the open ends at time slice $\frac{\beta}{2}$ because we will apply the double reference method from section 2.6.4 to fermionic systems. For distinguishable particles, the open path is a single polymer that interacts with the other particles. The contributions to the action are calculated in the same way as is done for closed paths except for the diagonal pair action in the time slice containing the open ends.

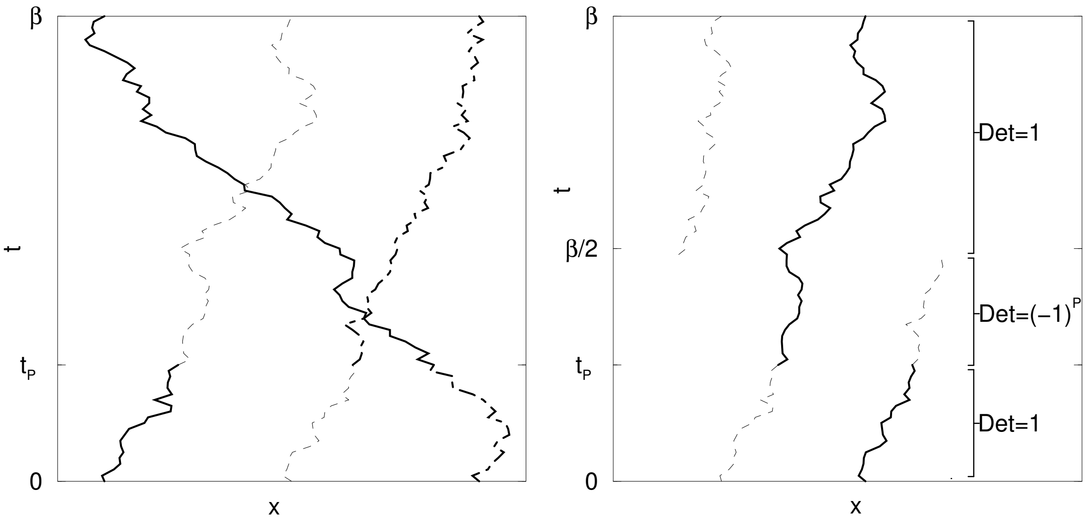

Figure 5.1: Illustration of a permutation of closed and open paths showing imaginary time T vs. one spatial dimension x. In the left graph, a permutation of three closed paths, each with a different lines style, is displayed. t_p denotes the slice where the relabelling of the particle indices takes place. The fermion determinant is always positive. On the right, a two particle permutation involving an open paths with the open end at $\frac{\beta}{2}$ is shown. Slice for which the fermion determinant has to be negative, are indicated.

There, each open end contributes with the weight $\frac{1}{2}$, which can be understood from Eq. 2.25.

Without interactions, the distribution of the open ends is by definition given by the free particle density matrix in Eq. 2.11. This equation will be used in the free particle sampling method for the generation of new path sections that contain the open ends. For closed paths, one samples the new positions from a Gaussian distribution centered at the midpoint between the slice above and below (Eq. 2.63) because of the two spring terms in the free particle action. The open ends are only connected in one direction in imaginary time. Therefore, the free particle sampling distribution for open ends being connected to $\mathbf{r}_{i+1}$ or $\mathbf{r}_{i-1}$ reads,

$$T(\mathbf{r}_i) = (4\pi\lambda\tau)^{-D/2} \exp\left\{ -\frac{(\mathbf{r}_i - \mathbf{r}_{i\pm1})^2}{4\lambda\tau} \right\} \quad . \tag{5.3}$$

For Bosons and Fermions, one also needs to sample the permutation space, which can be done as for closed paths described in section 2.5.4. The open paths can then form long chains consisting of several particles. Those correspond to off-diagonal long-range order. In ^{4}He, they lead to the condensate fraction of atoms with precisely zero momentum as shown by Ceperley (1995).

5.2 Nodal Restriction for Open Paths

The restricted PIMC method leads to some additional questions on how to constrain the open paths, which will be addressed in this section. First of all, one has to decide where to put the open ends with respect to the reference point $\mathbf{R}^*$. Since we are going to use the double reference point method from section 2.6.4, the open ends consequently have to be located in slice $t_O = \frac{\beta}{2}$, which is illustrated in Fig. 5.1. This method has the advantage that the trial density matrix is only needed up $\frac{\beta}{2}$.

The most significant difference between fermionic PIMC simulations with closed and open paths lies in the fact that *for open paths, odd permutations do not necessarily cross the nodes.* They will be included in the sampling and lead to *negative signs.* As pointed out in section 2.6.2, the nodal constraint only prevents negative contributions to diagonal density matrix elements. For open paths, the sign $(-1)^{\mathcal{P}}$ comes into a PIMC simulation as an additional factor when the averages are computed.

The nodes are taken from the trial density matrix in Eq. 2.82. They are enforced by the condition $\rho_T(\mathbf{R}(t), \mathbf{R}^*; t) > 0$ where the reference point is $\mathbf{R}^* \equiv \mathbf{R}(0)$. This is used for closed as well as for open paths. For closed paths, one can simply check if the signs of all the determinants are positive. For open paths, the situation is more complicated because one needs to be able to move the point of permutation $t_{\mathcal{P}}$ described in section 2.5.4 to any time slice. *If $t_{\mathcal{P}}$ is at the slice with the open ends, $t_O = t_{\mathcal{P}}$, all determinants must be positive as in the case of closed paths.* If $t_{\mathcal{P}}$ is moved to a different time slice some rows in the determinants $\rho_{ij} = \rho_1(\mathbf{r}_i, \mathbf{r}_j^*; \beta)$ on the way are switched because a permutation $\mathcal{P}$ is applied to the coordinates $\mathbf{r}_i$. For the slices between $t_{\mathcal{P}}$ and t_O, the determinants must have the sign $(-1)^{\mathcal{P}}$ in order to fulfill the nodal condition. This is illustrated in Fig. 5.1. This reasoning still holds if $t_{\mathcal{P}}$ is moved across the reference point slice because then the columns in ρ_{ij} change as well. These rules have consequences for the ways odd permutations can be introduced into a system. There are two required conditions for such a move in order to have at least the chance not to violate the nodes:

- It is impossible to permute an even number of closed path while keeping all other particle coordinates fixed.
- It is impossible to permute an open and a closed path in a move that does not change the slice with the open ends t_O.

This puts a restriction on the trial permutations entering the permutation table from section 2.5.4 because certain permutations would inevitably be rejected when the nodes are checked.

5.3 Momentum Distribution

In the path integral formalism, the momentum distribution can be derived by projecting out a many particle state with momentum $\mathbf{K}$. The projection operator is given by,

$$\hat{P}_{\mathbf{K}} = |\psi_{\mathbf{K}}\rangle \langle\psi_{\mathbf{K}}| \tag{5.4}$$

$$= \int \mathbf{dRdR'}\; |\mathbf{R}\rangle\; e^{-i\mathbf{K}(\mathbf{R}-\mathbf{R}')}\; \langle\mathbf{R}'| \quad . \tag{5.5}$$

Applying it to the thermal density matrix using Eq. 2.7 leads to

$$\left\langle \hat{P}_{\mathbf{K}} \right\rangle = \frac{1}{Z} \int \mathbf{dRdR'}\; \rho(\mathbf{R},\mathbf{R}';\beta)\; e^{-i\mathbf{K}(\mathbf{R}'-\mathbf{R})} \quad . \tag{5.6}$$

To find the single particle momentum distribution, one averages over the momentum of all particles except the first, which is equivalent to performing the integrals $\mathbf{dk}_2 \ldots \mathbf{dk}_N$. Including an extra normalization factor of $(2\pi)^{-ND}$, this leads to the single particle momentum distribution,

$$n(\mathbf{k}) = (2\pi)^{-3} \int \mathbf{dr}_1 \mathbf{dr}_1'\; e^{-\mathbf{k}(\mathbf{r}_1'-\mathbf{r}_1)}\; \rho^{[1]}(\mathbf{r}_1,\mathbf{r}_1'), \tag{5.7}$$

where $\rho^{[1]}(\mathbf{r}_1,\mathbf{r}_1')$ is the one-particle reduced density matrix defined in Eq. 5.1. The normalizations are given by $\int \mathbf{dr}\, \rho^{[1]}(\mathbf{r},\mathbf{r}) = \hat{\mathcal{V}}$ and $\int \mathbf{dk}\, n(\mathbf{k}) = 1$. For isentropic homogeneous systems, the one-particle reduced density matrix is only a function of $|\mathbf{r}-\mathbf{r}'|$, which allows one to introduce the function $n(|\mathbf{r}-\mathbf{r}'|) \equiv \rho^{[1]}(\mathbf{r},\mathbf{r}')$ with $n(0)=1$. It represents the distribution function of the separation of open ends in a PIMC simulation with one open path.

Classical particles exhibit the Maxwellian momentum distribution. Therefore, the single particle density matrix is a Gaussian,

$$n(\mathbf{k}) = \left(\frac{\lambda\beta}{\pi}\right)^{D/2} \exp\left\{-\beta\lambda\mathbf{k}^2\right\} \tag{5.8}$$

$$n(\mathbf{r}) = (4\pi\lambda\beta)^{-D/2} \exp\left\{-\frac{\mathbf{r}^2}{4\lambda\beta}\right\} \quad . \tag{5.9}$$

For an ideal Fermi gas at $T=0$, the momentum distribution is a Fermi function,

$$n(\mathbf{k}) = \begin{cases} 1/(8\pi^3 n) & \text{for} \quad k \le k_F \quad \text{with} \quad k_F = (6\pi^2 n)^{1/3} \\ 0 & \text{for} \quad k > k_F \end{cases} \tag{5.10}$$

$$n(\mathbf{r}) = 3/x^3\,[\sin x - x\,\cos x] \qquad \text{with} \quad x = rk_F \quad . \tag{5.11}$$

Table 5.1: Minimal number of particles N required to observe the ith zero in the single particle density matrix

i	$x = rk_F$	$N(\frac{L}{2})$	$N(\frac{L}{2}\sqrt{3})$
1	4.493	12.2	2.4
2	7.725	62.3	12.0
3	10.904	175.1	33.7
4	14.067	376.0	72.4

The single particle density matrix $n(r)$ is proportional to the spherical Bessel function $j_1(x)$, which oscillates around zero. In the PIMC simulations, $n(r)$ can be obtained in form of a histogram, in which the separations of the open ends weighted with the sign of the permutation are entered. At separations r where it is negative, odd permutations leading negative contributions must outweigh even permutations making positive contributions. $|j_1(x)|$ decays slowly as r^{-2}, which requires macroscopic exchange cycles to occur. Those are solely a consequence of the discontinuity of $n(k)$ at $k = k_F$.

Before we discuss results from PIMC simulation of interacting systems we will examine the scaling behavior of the off-diagonal sampling method. In order to study a certain number of oscillations in $n(r)$, one can make a simple estimation of how many particles are required. For this purpose, we neglect the fact that Eq. 5.11 was derived in thermodynamic limit, $N \to \infty$. In a simulation using a 3D box of size L, one can directly measure $n(r)$ up to $\frac{L}{2}$ and indirectly up to $\frac{L}{2}\sqrt{3}$. This leads to the estimates for the required number of particles given in Tab. 5.1.

From this table, one can quickly realize that the computational demand grows rapidly with the number of zeros i because $N \propto i^3$ and CPU time $\propto N^3 \propto i^6$. Furthermore, it should be noted that one needs to go to sufficiently low temperatures to observe the fermionic effects and that the CPU time scales linearly with the number of time slices. Additionally, positive and negative contributions cancel, which leads to fluctuations in the observables. The fluctuation do not increase as rapidly as for the direct fermion method (see section 2.6.5) since we still use a nodal restriction but one needs converged results from all cycle lengths, which becomes increasingly difficult at low temperature. A detailed analysis of the scaling behavior with temperature remains to be done.

As a first application of the off-diagonal density matrix sampling method, we chose to study the electron gas because of its simplicity. The method can be easily extended to hydrogen or spin-polarized hydrogen. We looked at a system of 33 closed shell spin-parallel electrons at a density of $r_s = 4.0$ ($T_F = 57\,694$K) and selected

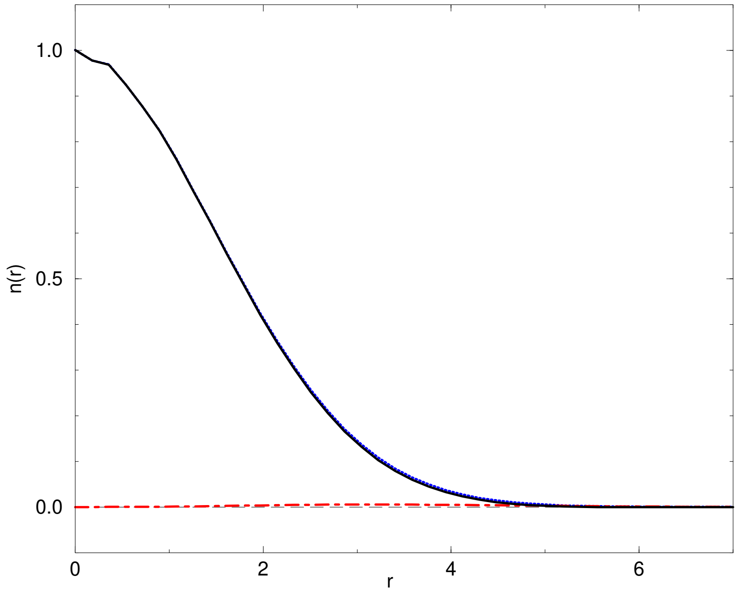

Figure 5.2: $n(r)$ for systems of 33 spin-parallel electrons at $T = 125\,000\,\mathrm{K}$ and $r_s = 4.0$ ($T_F = 57\,694\mathrm{K}$) (solid line). At this temperature, fermionic effects are only a small correction to the classical behavior. Therefore negative contributions (dash-dotted line) are negligible and the sum of the positive contributions (dotted line) are almost identical to the full $n(r)$. We also found that the repulsive interactions do not lead to significant modification to the non-interacting case given by the Gaussian function in Eq. 5.9.

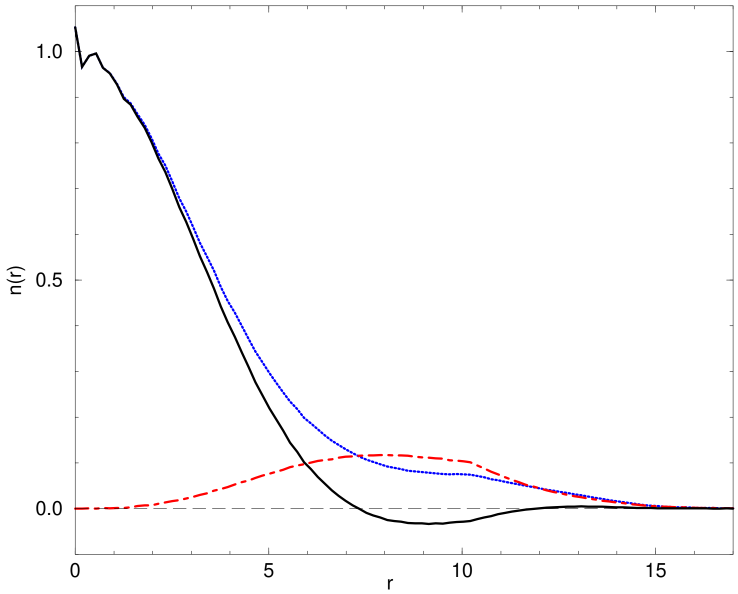

Figure 5.3: $n(r)$ from the system shown in Fig. 5.2 but here for a significantly lower temperature of $T = 15\,625\,\mathrm{K}$, where fermionic effects dominate ($T_F = 57\,694\mathrm{K}$). This leads to negative regions in $n(r)$, as expected from the zero temperature limit given by Eq. 5.11. In these regions, odd permutations from exchange cycles with an even number of particles dominate. The functions decrease rapidly at $r = L/2 = 10.3$ as a result of finite size effects because the minimum image method is applied.

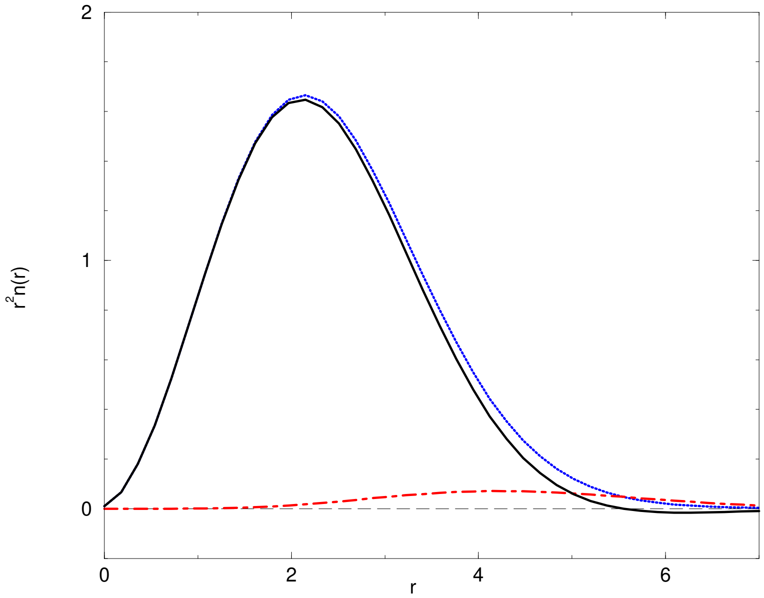

Figure 5.4: $n(r)r^2$ from Fig. 5.2 using the same line styles. The extra r^2 factor emphasizes the small fermionic effects that lead to some negative contributions.

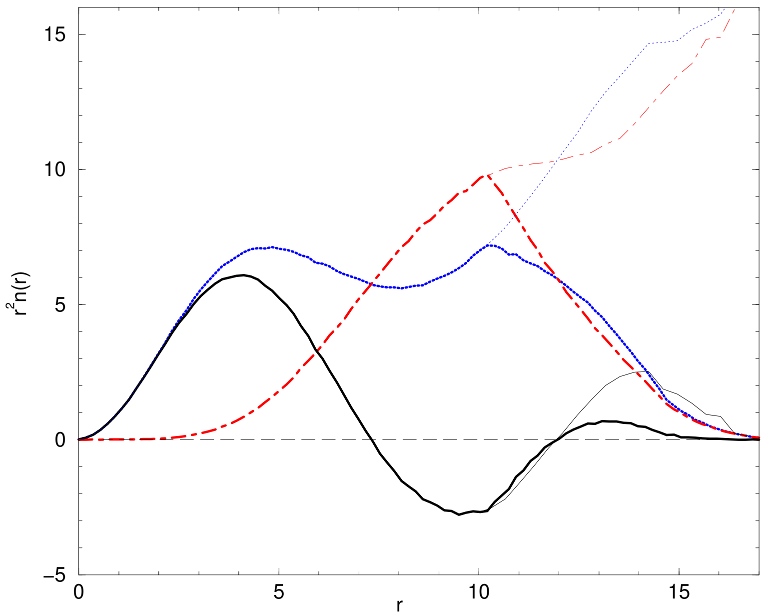

Figure 5.5: $n(r)r^2$ from Fig. 5.3 (thick lines). It shows the oscillating behavior of n=$n(r)$ in fermionic systems (Eq. 5.11). One finds 3 zeros as expected for free particles (see table 5.1). The thin lines show finite size corrections for $r > L/2 = 10.3$.

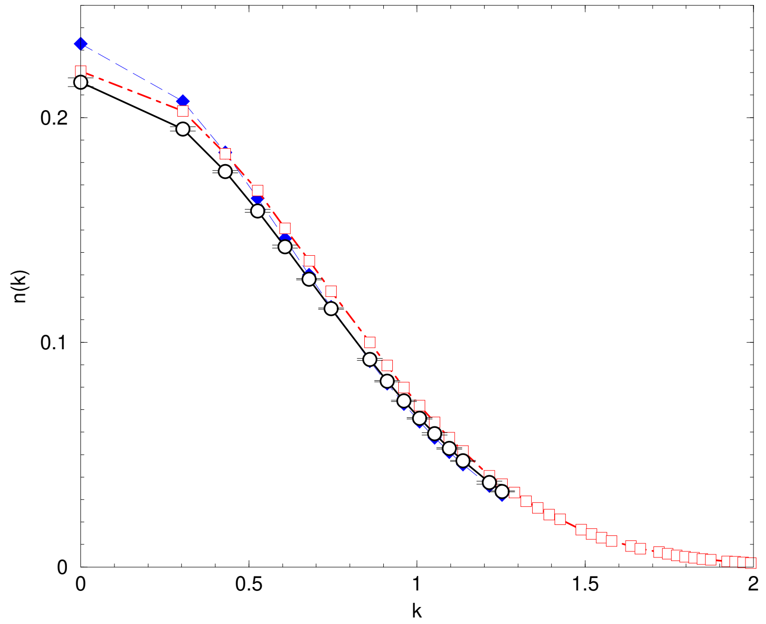

Figure 5.6: Momentum distribution $n(k)$ ($\circ$) for a finite system of 33 spin-parallel electrons at $T = 125\,000\,\mathrm{K}$ and $r_s = 4.0$ ($T_F = 57\,694\mathrm{K}$) also studied in Fig. 5.2. The $\Box$ symbols show the momentum distribution for a finite system of non-interacting fermions under these conditions and the $\Diamond$ display the Maxwell-Boltzmann distribution.

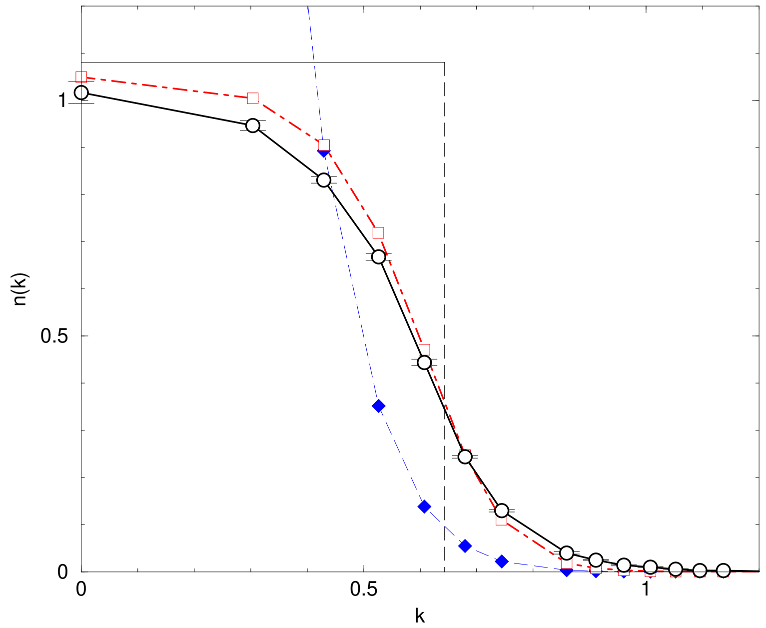

Figure 5.7: Momentum distribution $n(k)$ as in Fig. 5.6 but for a lower temperature of $15\,625\,\mathrm{K}$. This leads to a degenerate Fermi gas described by a Fermi-Dirac distribution, which is also shown for a system of 33 non-interacting fermions at this T ($\Box$) and at zero temperature (solid line). The difference to the Maxwell-Boltzmann distribution ($\Diamond$) is substantial.

the two temperatures 125 000 and 15 625 K that represent the classical case at high temperature and, respectively, the degenerate electron gas at low temperature. For 125 000 K, the observed reduced density matrix $n(r)$ in Fig. 5.2 is in good approximation the classical Gaussian function. Due to the high temperature, permutations are relatively rare. Their contribution can be seen best in Fig. 5.4 where $r^2 n(r)$ is shown. Since we multiplied by the volume element $\propto r^2$, the graph can be interpreted as the probability of finding the two ends of the open path separated by r. The corresponding momentum distribution $n(k)$ in Fig. 5.6 was calculated directly from MC average,

$$n(\mathbf{k}) \propto \left\langle e^{i\mathbf{k}(\mathbf{r}-\mathbf{r}')} \right\rangle \quad , \tag{5.12}$$

rather then using a Fourier transform of $n(\mathbf{r})$, which would have required an extrapolation for large r or to store $n(\mathbf{r})$ on a 3D grid because the spherical symmetry is broken by the cubic simulation box. The observed momentum distribution lies between the Maxwell-Boltzmann distribution and the Fermi distribution for the corresponding non-interacting finite system. All three curves are rather close together because the simulation is performed in a classical regime. The deviations of the PIMC result from the free Fermi distribution show the effect of the repulsive interactions between the electrons, which leads to a depletion of the occupation probability at small k values.

This effect is also present in the low temperature results at 15 625 K where one finds a degenerate electrons gas. The momentum distribution in Fig. 5.7 is a Fermi function rather than a Maxwell-Boltzmann distribution, which can reach arbitrarily higher occupation for $k = 0$ because it is not limited by the Pauli exclusion principle. The solid line denotes the ideal Fermi gas at $T = 0$ given by Eq. 5.10. Thermal excitations as well as the Coulomb interaction lead to the population of momentum states above the ideal Fermi momentum. For interacting systems at $T = 0$, a discontinuity in the momentum distribution is still present but some states are pushed to higher k-values (Ortiz and Ballone, 1994). The comparison with the ideal Fermi gas at $T = 0$ gives an estimate for the thermal excitations at this temperature. The degree of degeneracy is rather high, which has a significant consequence for the reduced density matrix shown in Figs. 5.3 and 5.5. The latter graph shows how positive contributions dominate at small separations r. Then the function goes through zero and even permutations dominate. After that, it becomes positive again and finally approaches zero near $r \approx L/2\sqrt{3}$, which is in good agreement with the estimate given in Tab. 5.1. We corrected for the finite size effects for $r > L/2$ by dividing out the reduction in the volume element. This correction could also have been done by using the Fourier transform of the sampled $n(\mathbf{k})$ but it would have required $n(\mathbf{k})$ a higher number of k-vectors than we kept. The figure also shows that the magnitude of the positive and the negative contributions still grows for $r \gtrsim 10$ but their difference is smaller, which leads to the expected decay of $n(r)$. The reason why the magnitude of the positive and negative contributions still increases can be understood from Fig. 5.8 where the contributions from the individual cycle lengths are shown. Generally, one finds that cycles of an odd (even) number of particles lead mainly to positive (negative) contributions despite the possibility that permutations of nearby closed paths could change the sign since it is the sign of the total permutation that enters in the average. At small separations the positive contributions from open 1-cycles dominate. Two particle permutations give rise to the biggest fraction of negative contributions for $r \lesssim 10$. For $r \gtrsim 10$, the contributions from $\nu = 3$ and longer cycles still increase because the average separation of an open cycle of length ν is given by $\sqrt{4\lambda\beta\nu} = 6.4\sqrt{\nu}$. The cancellation between odd and even cycles makes the $n(r)$ function decay faster than its positive and negative summands.

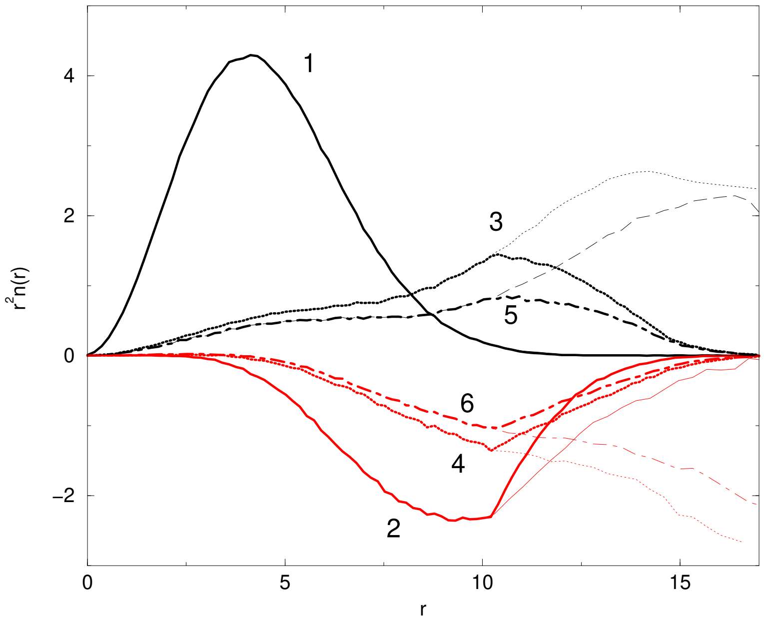

Figure 5.8: Distribution $r^2n(r)$ from Fig. 5.5 split into the different permutation cycles, shown for 1 to 6 particles. Cycles with an odd number of particles mainly lead to positive contributions and those even numbers to negative contributions. The thins lines show the finite size corrections for $r > L/2 = 10.3$. The figure shows how the distribution of the different cycles in the restricted path integral method lead to the oscillations in the $n(r)$ function at sufficiently low T.

5.4 Natural orbitals

5.4.1 Motivation

The two particle density matrix is of particular relevance for the understanding of quantum-mechanical many body systems. It contains more information than can be extracted from diagonal density matrix elements only and can be used to study eigenstates, their energies and the thermal excitations in the system. It is important for the characterization of the electronic excitations in the hydrogen plasma. In principle, one can determine the different electronic states and calculate the occupation probabilities. These are important for the radiative properties of the plasma and allow one to calculate absorption and emission spectra. The purpose of the following calculation is to determine the electronic excitations from a first principles calculation, which can then enter subsequent plasma models as an alternative to results from chemical models, in which the occupation numbers are estimated from the chemical equilibrium of approximately known eigenstates.

Furthermore, one would like to have a way to distinguish between free and bound states. This information can be used to estimate dynamic properties such as the conductivity. However, it has been proven to be a challenging task to give a rigorous and also practical criterion for the definition of free and bound states. In our approach, we followed the ideas of Girardeau (1990), who suggested the use of the two particle density matrix. Its eigenvalues are related to the occupation number and its eigenvector are called *natural orbitals*. They are of particular importance for configuration interaction methods in quantum chemistry because they lead to the fastest convergence (Szabo and Ostlund, 1996).

The two particle density matrix as defined in Eq. 5.2 requires path integral simulations with two open paths, which can be either of the same or of different particle type. One introduces relative and center-of-mass coordinates, $\mathbf{r} = \mathbf{r}_1 - \mathbf{r}_2$ and $\mathbf{r}_{\rm cm} = [m_1\mathbf{r}_1 + m_2\mathbf{r}_2]/(m_1+m_2)$. In a translationally invariant system, the pair matrix depends only on the separation of $\mathbf{r}_{\rm cm} - \mathbf{r}'_{\rm cm}$,

$$\rho^{[2]}(\mathbf{r},\mathbf{r}',\mathbf{r}_{\rm cm},\mathbf{r}'_{\rm cm}) \equiv \rho^{[2]}(\mathbf{r},\mathbf{r}',\mathbf{r}_{\rm cm}-\mathbf{r}'_{\rm cm}) \quad , \tag{5.13}$$

and can be decomposed in its Fourier components (see Lebowitz *et al.* (1992) and Macris and Martin (1994)),

$$\rho^{[2]}_{\mathbf{k}}(\mathbf{r},\mathbf{r}') = \int_{\hat{V}} \mathbf{dr}_{\rm cm}\, e^{-i\mathbf{k}\mathbf{r}_{\rm cm}} \rho^{[2]}(\mathbf{r},\mathbf{r}',\mathbf{r}_{\rm cm}) \quad . \tag{5.14}$$

If one averages over all momentum states one can write,

$$\rho^{[2]}(\mathbf{r}, \mathbf{r}') = \rho^2(r, r', \cos\theta) = \sum_{l=0}^{\infty} \frac{4\pi}{2l+1} \rho_l^{[2]}(r, r') \, \mathrm{P}_1(\cos\theta) \quad , \tag{5.15}$$

where θ is the angle between $\mathbf{r}$ and $\mathbf{r}'$. $\rho_l^{[2]}(r,r')$ is a symmetric matrix with real and positive eigenvalues n_{li}. The eigenvectors $\phi_{li}(r)$ are the natural orbitals corresponding to a pair of particles in the angular momentum state l,

$$\rho_l^{[2]}(r,r') = \sum_i n_{li} \, \phi_{li}(r) \, \phi_{li}^*(r'). \tag{5.16}$$

The eigenvalues n_{li} indicate occupation probability of the ith orbital with angular momentum l and energy E_{li} given by,

$$n_{li} = \frac{1}{Z} e^{-\beta E_{li}} \quad , \tag{5.17}$$

$$Z = \sum_{li} e^{-\beta E_{li}} \quad . \tag{5.18}$$

It should be noted that the orbitals $\phi_{li}(r)$ and the energies E_{li} correspond to many-particle states and are not the same as in single particle theory. However, the terminology used here is very similar.

In this approach, we did not make a distinction between the discrete spectrum of bound states and the continuum of free states. Both are included in the sum of Eq. 5.16. Since we applied this method to PIMC simulations in a finite volume, free states will have a discrete spectrum as well. In the simulation, one calculates the two particle density matrix from the following by average,

$$\rho_l^{[2]}(x, x') = \langle \, \delta(r - x) \, \delta(r' - x') \, \mathrm{P}_1(\cos\theta) \, \rangle \quad . \tag{5.19}$$

In the MC method with open path, one can calculate the relative occupation numbers n_{li}. The Boltzmann factor, $e^{-\beta E_{li}}$, and therefore the orbital energies E_{li} are not directly available because the partition function Z cannot easily be calculated directly in any MC. However, one can, in principle, use the internal energy E from a simulation with closed paths and sets,

$$E = \sum_{li} E_{li} \, n_{li} \quad , \tag{5.20}$$

which is correct in the mean field approximation. From Eq. 5.17, it follows,

$$\ln Z = -\beta E - \sum_{li} n_{li} \ln n_{li} \quad , \tag{5.21}$$

which is equivalent to the expression for the free energy $F = E - TS$. This means Z can be calculated from the occupation numbers n_{li} generated by an off-diagonal simulation and from the single particle energy E taken from diagonal density matrix calculation. Then the energies of the orbital E_{li} follow from Eq. 5.17. The disadvantage of this method is that it requires rather accurate estimates for all occupation numbers including highly excited states. As a consequence, we were not able to determine the absolute occupation numbers and energies even for a simulation of a single hydrogen atom in a periodic box, which will be discussed below.

This off-diagonal sampling method can be applied to different regimes in hydrogen. One can determine the electronic excitations in atoms by opening an electron and a proton path. A pair of open proton paths can be used to study the formation of hydrogen molecules. The eigenvectors then correspond to different rotational and vibrational excitations. In the following sections, we show how this method can be applied in PIMC simulations and show preliminary results for the electronic excitations in hydrogen.

5.4.2 Example: One Hydrogen Atom

The off-diagonal sampling procedure can be simplified for the application to the electronic excitations in hydrogen. For all temperatures under consideration, the thermal de Broglie wave length of the protons is small compared to the inter-particle spacing and also much smaller than that of the electrons. Therefore, one can make the protons classical within a first approximation. In this case, one replaces the proton path by a point particle and needs only one open electron path. The pairs $\mathbf{r}$ and $\mathbf{r}'$ in Eq. 5.15 are then given by the separation of the ends of the electron paths and the proton. This has the advantage that one can average over all protons in a many proton simulation discussed in section 5.4.3.

In the PIMC simulation, one calculates the matrices for a certain number of angular momentum states using the average given by Eq. 5.16. We kept the matrices for $l \leq 5$ and used a uniform grid in real space with 50 points from $r = 0$ to $L/2\sqrt{3}$. This includes an approximation because one does not consider the cubic symmetry of the simulation cell. In the limit of a large cell, this approximation becomes more and more accurate because the majority of the occupied natural orbitals only extends over a fraction of the simulation cell and therefore is not affected by the boundary conditions. The justification for using this basis is that one is generally interested in systems where the natural orbitals are determined by the interactions rather than by boundary effects. However, in systems where those are important, another basis

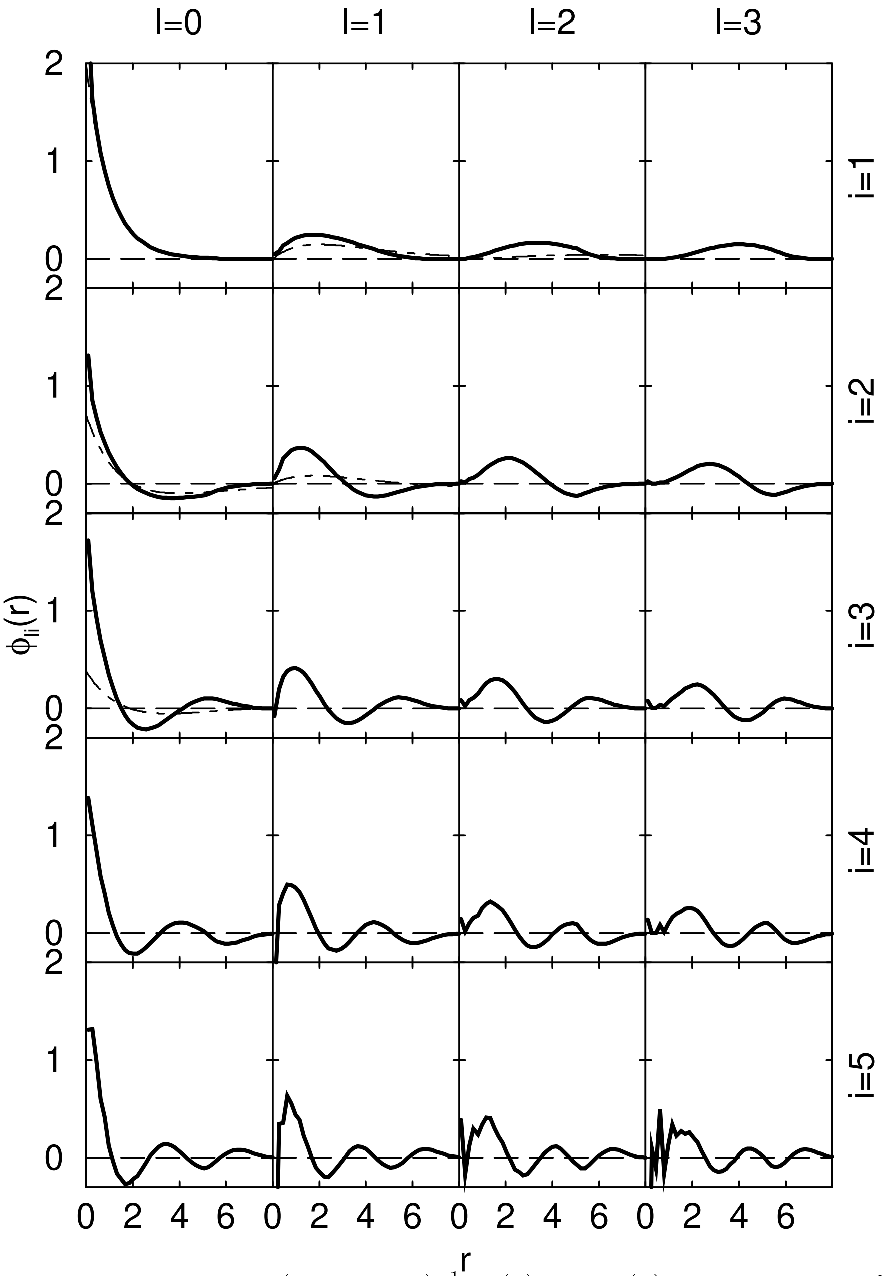

Figure 5.9: Natural orbitals (solid lines) $\frac{1}{r}\phi_{li}(r) \equiv R_{nl}(r)$ with $n = l + i$ for a single hydrogen atom in a periodically repeated box of size $L = 10.2$, which were generated from a simulation at $T = 250\,000\,\mathrm{K}$. The columns correspond to the eigenvectors with angular momentum l calculated by diagonalizing the matrix $\rho_l(r, r')$. The rows show the ith eigenvector beginning with the highest eigenvalue corresponding to lowest energy state. For $n \leq 3$ the eigenstates of the isolated hydrogen atom are shown as dash-dotted lines. The isolated 1s state is almost identical to the corresponding natural orbit and is therefore hidden behind the other line.

that includes the cubic symmetry is more appropriate. Suggestions have been made by Shumway (1999).

The resulting matrices $\rho_l^{[2]}(r, r')$ are then diagonalized, which leads to natural orbitals as eigenvectors and eigenvalues proportional to the occupation numbers. The relative occupation numbers n_{li} are obtained by dividing the eigenvalues by the sum of the traces of all l matrices. We found that the contributions from different matrices decay rapidly with l and that keeping matrices for $l \leq 5$ is more than sufficient.

The resulting natural orbitals for a single hydrogen atom in a periodically repeated box of size $L = 10.2$ are shown in Fig. 5.9. The displayed functions $\frac{1}{r}\phi_{li}(r)$ are expected to approach the radial part $R_{nl}(r)$ with $n = i + l$ of the isolated hydrogen atom in the limit of a large box size. The example reveals a ground state that is identical within statistical and grid errors to the 1s ground state of the isolated hydrogen atom. Studying the eigenvectors at any l with increasing excitations i, one finds that one additional node is introduced at each step i. The states with $n = l + i > 1$ are similar but not identical to those of the isolated hydrogen atom because the finite size of the simulation cell $L/2 = 5.1$ does have an effect, which leads to more localized eigenstates. One also notices that the level of numerical noise in the eigenvectors increases with n. These effects seems to be the strongest near the origin, which suggests that a different basis such as hydrogen orbitals would lead to a lower noise level. Generally, one finds that the noise in the eigenvectors (using the uniform spatial grid) increases for lower temperatures because the occupation number of higher energy states becomes very small. In this case, the eigenvectors are approximately degenerate ($n_{li} = n_{l\,i+1}$) and the noise causes that those states are mixed in the diagonalization procedure. This explains why the noise level in the high eigenvectors increase for lower temperature.

Studying the eigenvalues, one finds that there are a few large positive ones while many others are small and some even negative. The occupation numbers are shown in Fig. 5.10 as a function of temperature. One finds that the occupation probability of the 1s ground state increases with decreasing T. Within the noise level of about 4%, it goes to 1 in the limit of low T. Furthermore, one finds that the occupation of the 2s and 2p are almost the same despite the fact that the 2 eigenvalues come from different matrices. The same argument holds for the 3s, 3p, and 3d level. One can also calculate the differences in energy from the ratio of the occupation numbers. For $E_{2s} - E_{1s}$, one finds 9.2 eV rather than 10.2 eV as expected for the isolated hydrogen atom. These deviations increase if higher levels are studied because higher states are more delocalized and therefore increasingly altered by the boundary effects.

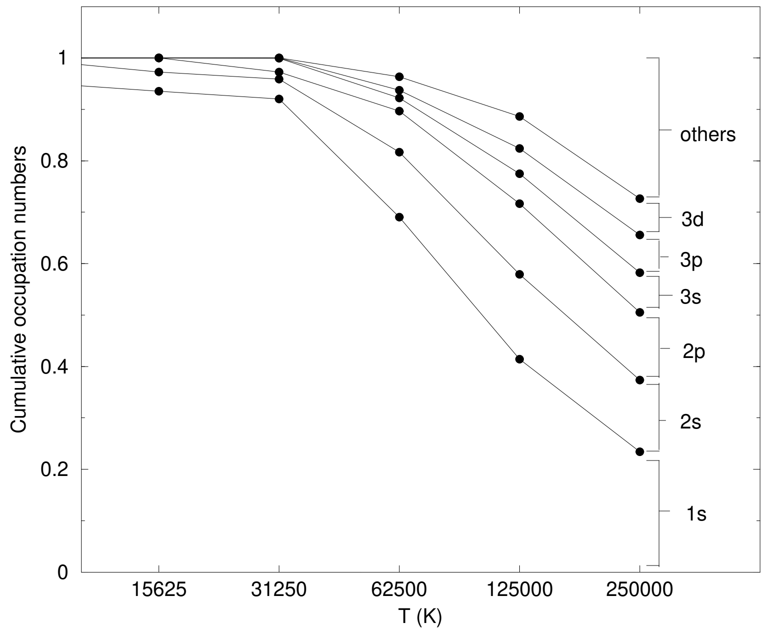

Figure 5.10: Cumulative plot of the occupation numbers for the 6 lowest eigenstates (see Fig. 5.9) of a single hydrogen atom in a periodically repeated box of size $L = 10.2$ shown as a function of temperature.

5.4.3 Many-Particle Systems

The main purpose of the natural orbital analysis is to study many particle systems. There, the situation is significantly more complicated because one has several protons and it turns out to be difficult to generalize the decomposition in Eq. 5.15 to the many-proton case because one has no a priori criterion to which proton a particular open path configuration belongs. The problem exists for classical as well as for quantum mechanical protons. However, there is a method that is conceptually correct but not feasible for real applications. For a fixed configuration of protons, one would store the electron two particle density matrix $(\mathbf{r}_\mathrm{e}, \mathbf{r}'_\mathrm{e})$ as a $N_g^D \times N_g^D$ matrix where N_g is the number of grid points in a spatial direction. After a sufficiently long MC simulation, one finds a converged results for each matrix element and then can diagonalize the matrix. For low temperature and low density the matrix is block diagonal and the eigenvectors correspond to different localized electronic states, each corresponding to a particular proton. This method shows how one would in principle generate the eigenstates for a many particle system. However, it is not practical because it requires the storage of this enormous matrix and extremely good statistics to fill all relevant matrix elements. The following sections discuss how to approximate this result with computationally feasible methods.

Method A

In an off-diagonal PIMC simulation of spin-polarized hydrogen, there are N protons, $N-1$ closed electron paths and one open electron path that can be permuted with the others electrons. The simplest approach to generalize the natural orbital method to systems with several protons would be to loop over all protons $r_{\mathrm{p}i}$ and to add all pairs of $(\mathbf{r}_e - \mathbf{r}_{\mathrm{p}i}, \mathbf{r}'_e - \mathbf{r}_{\mathrm{p}i})$ to the l matrices. Then the analysis proceeds like in the case of the single hydrogen atom. The result for a system of 32 protons and spin-polarized electrons at $T = 10\,000\,\mathrm{K}$ and $r_s = 6$ is shown in Fig. 5.11. We chose to study a system of electrons in the same spin state, which prevents the formation of molecules and simplifies the following analysis. Under this condition, one expects the electrons mainly to be in the 1s ground state at one of the protons because the ideal Saha

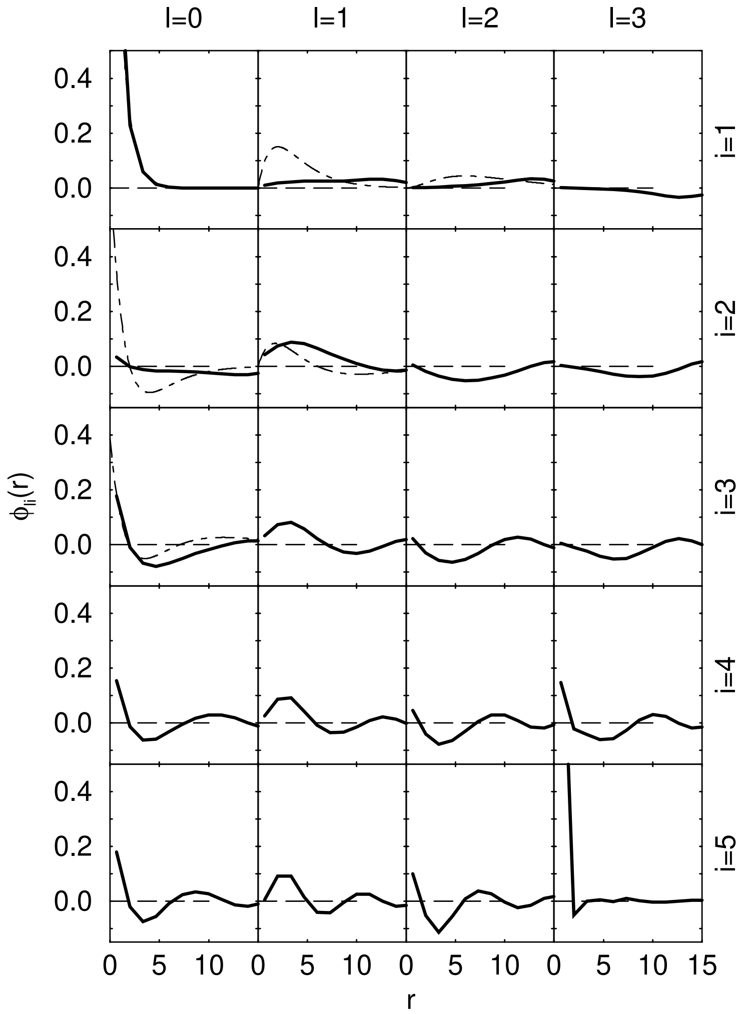

Figure 5.11: Natural orbitals calculated with method A for a system of 32 protons and 32 spin-polarized electrons at $T = 10\,000\,\mathrm{K}$ and $r_s = 6$.

Table 5.2: Occupation numbers for the electron eigenstates in a system of 32 spin-polarized hydrogen atoms at $T = 10\,000\,\mathrm{K}$ and $r_s = 6.0$ estimated by methods A, B, and C.

Method	1s	2s	2p	3s	3p	3d	4s	4p	4d	4f
A	0.535	0.056	0.049	0.042	0.036	0.032	0.027	0.022	0.019	0.017
B	0.973	0.009	0.003	0.002	0.002	0.002	0.000	0.000	0.000	0.007
C	0.919	0.012	0.010	0.006	0.008	0.008	0.003	0.002	0.003	0.006

equation predicts an occupation probability of 0.9998 for the ground state. However, the described analysis procedure (eigenvectors in Fig. 5.11 and occupation numbers in Tab. 5.2) does not reproduce this result. Instead, it leads to a far too low occupation of 0.535 and one finds a significant contribution from higher l components. These contributions can be interpreted as an artifact of this analysis procedure, in which we averaged over all protons, as can be understood from the following argument. If one imagines the electron fixed in the 1s state at proton 1 the pairs of $(\mathbf{r}_e - \mathbf{r}_{\mathrm{p}i}, \mathbf{r}'_e - \mathbf{r}_{\mathrm{p}i})$ from another distant proton always give a small angle θ. The distribution of the angles θ is very non-uniform since it is localized around $\theta = 0$. Therefore those contributions cannot be expressed as an s state.

Method B

In the next approach, we tried to eliminate the contributions from the distant protons by only considering pairs of $(\mathbf{r}_e - \mathbf{r}_{\mathrm{p}i}, \mathbf{r}'_e - \mathbf{r}_{\mathrm{p}i})$ from the two open ends and the nearest proton. If the closest proton for the two ends is not the same then no pair is considered. The results from a simulation with the same parameter are given in Tab. 5.2. They show that the electrons are mainly in 1s ground state as expected. However, the drawback of this method is that it introduces a cut-off for the eigenstates displayed in Fig. 5.12, which is unphysical in the limit of high density, where one expects to find delocalized electronic states that cannot be represented by this approach.

Method C

In the following approach to this problem, we try to eliminate the contribution to the matrices $\rho_l^{[2]}(r, r')$ from distant protons in a more elaborate way. We start from the matrices generated by averaging over all protons but also record distribution of the separation of the open ends $n(r)$ during the PIMC simulation. In the final analysis procedure, we used $n(r)$ to subtract the contribution from a uniform background of $N-1$ protons from the generate matrices $\rho_l(\mathbf{r}, \mathbf{r}')$. The idea behind it is that one

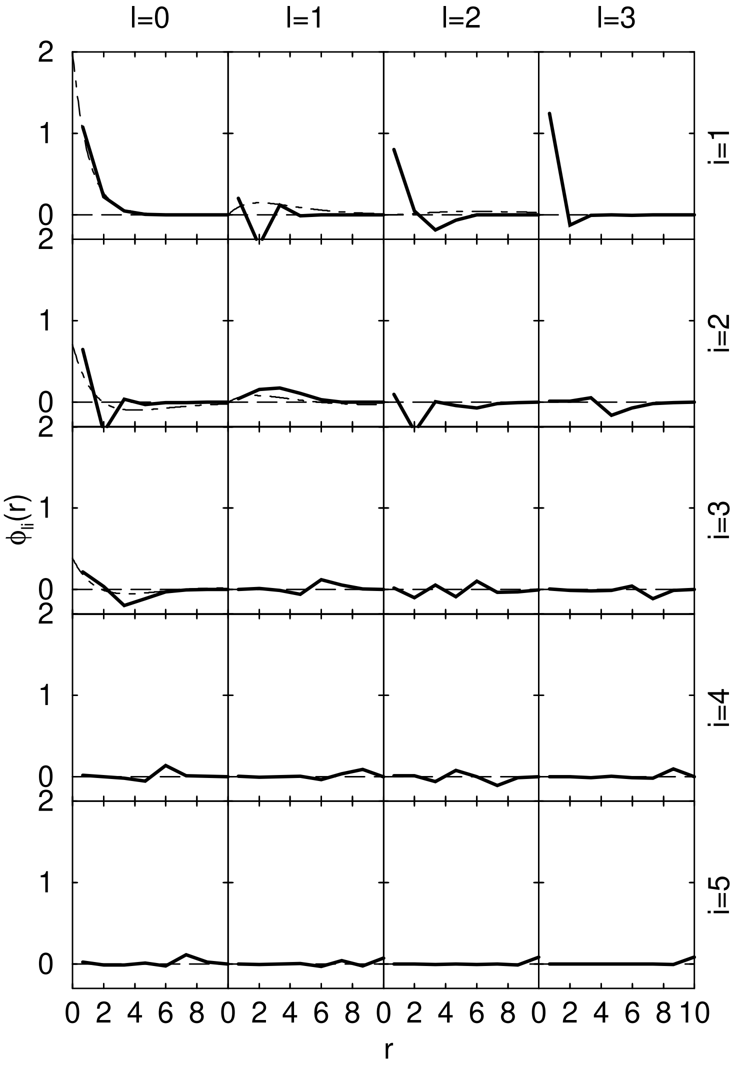

Figure 5.12: Natural orbitals calculated with method B for the system studied in Fig. 5.11.

imagines the electron to be in a certain orbital state at one proton. All other protons lead to additional contributions that need to be subtracted afterwards. Assuming that there is little correlation between the protons, one can model them by a uniform background. The results are shown in Tab. 5.2 and in Fig. 5.13. This method reproduces the high occupation of the 1s state and has also increased the level of the numerical noise. It represents one possible way to deal with problem of multiple pairs $(\mathbf{r}, \mathbf{r}')$ from different protons. However, this idea needs further investigation. One can also imagine other methods that would exclude contributions from distant protons, e.g one can introduce a cut-off or a localization function. The simplest system to test new proposals is composed of one electron and two protons at low temperature. The density matrix is then given by,

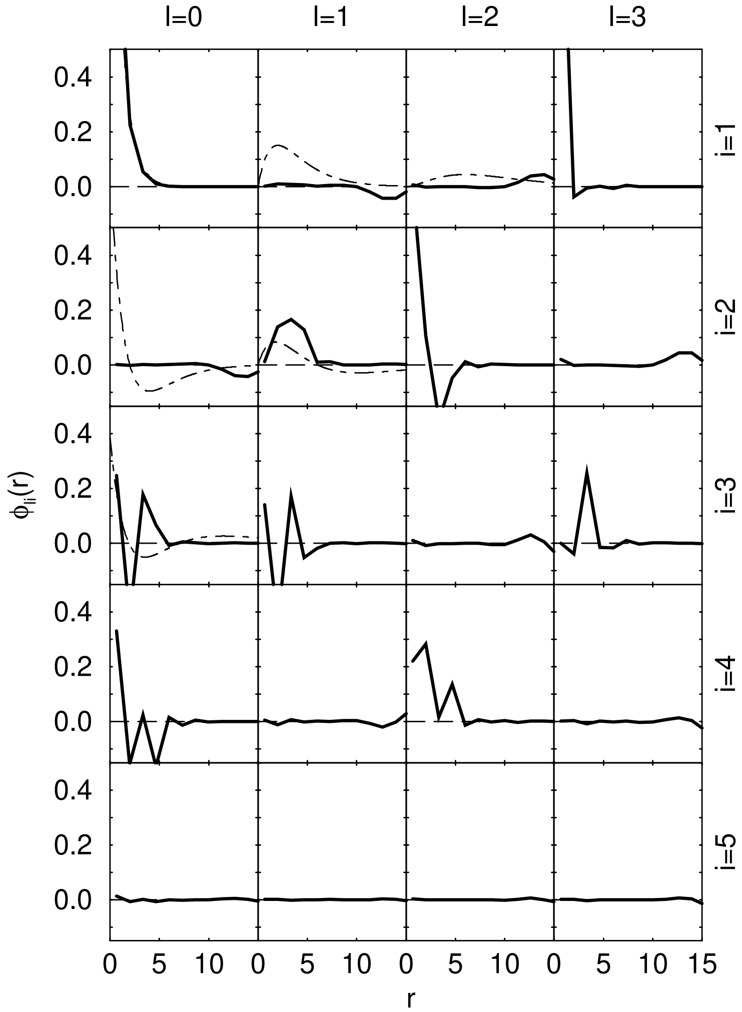

Figure 5.13: Natural orbitals calculated with method C for the system studied in Fig. 5.11.

$$\rho(\mathbf{r},\mathbf{r}') = A\,\phi^*_{1s}(\mathbf{r}-\mathbf{r}_{\mathrm{p}1})\,\phi_{1s}(\mathbf{r}'-\mathbf{r}_{\mathrm{p}1}) + A\,\phi^*_{1s}(\mathbf{r}-\mathbf{r}_{\mathrm{p}2})\,\phi_{1s}(\mathbf{r}'-\mathbf{r}_{\mathrm{p}2}) \quad . \tag{5.22}$$

The next more advanced system would include free states, and one could add a free particle term $B\exp\{-(\mathbf{r}-\mathbf{r}')^2/4\lambda\beta\}$. The coefficients A and B should be reproduced in the analysis procedure. The main question is to find an appropriate basis to decompose the many body density matrix, which can be diagonalized with a reasonable computational demand.

Method D

Another alternative to deal with the contributions from multiple protons can be constructed by using the center of mass of the open polymer in order to select the appropriate proton. We suggest to calculate the center of mass coordinate of the open paths and select the protons, whose center of mass is closest. Then we consider only the separation of the open ends to this proton. This method has the advantage that every open path configuration leads to only one contribution, that it does lead to some localization of the generated pairs without introducing a sharp cut-off, which would be inappropriate for the analysis of delocalized state such as plane waves. We think that this procedure as well as method C should to be pursued further in order to construct the natural orbitals in a dense many-particle system.

Chapter 6

Conclusions

In this work, we have applied path integral Monte Carlo simulations (PIMC) to hot, dense hydrogen and deuterium. Our goal was to determine the equation of state from first principles and to elucidate the high temperature phase diagram. The main focus was on explaining the structural changes that lead to a molecular, an atomic and a plasma regime at low density and exhibit a metallic regime at high density. We determine the equation of state in density and temperature range corresponding to $1 \leq r_s \leq 14$ and $5000 \leq T \leq 10^6\,\mathrm{K}$. The wide range of possible applications include studies of the brown dwarfs and Jovian plants. Furthermore, the data can be used in chemical models in order to fit free parameters, which then allows one to obtain related properties with an improved accuracy.

We developed a variational density matrix (VDM) related to the variational methods at zero temperature. In our approach to dense hydrogen, we derived a VDM that includes interactions and describes bound states, ionization, and dissociation processes. In this approach, we used a single determinant with Gaussian orbitals. Possible extensions include improved single particle orbitals, treating the exchange terms with a higher accuracy and the consideration of correlation effects.

The VDM was developed with the motivation to replace the free particle nodes, used in the PIMC simulations so far, with a more realistic density matrix that already includes the principle physical effects in dense hydrogen. We carefully analyzed what effect the improved nodal surfaces have on the thermodynamics properties derived from PIMC simulations. The most significant changes were found in the regime of the abrupt transition to a metallic state observed using PIMC simulations with free particle nodes. Using VDM nodes, we found no evidence for a phase transition in the parameter range under consideration. It remains to be determined if the improvements in the nodes eliminated the plasma phase transition altogether or if it was shifted to temperatures below 5000 K.

An important part of our research was the comparison with laser shock wave experiments. We performed a detailed analysis in the relevant density range of the various approximations entering into PIMC simulations including different time steps and system sizes as well as the type of nodal surface being employed. None of them had a significant effect on the comparison, which showed that PIMC simulation increased compressibility of 4.3 ± 0.1 on the shock Hugoniot and cannot reproduce the experimental findings of values of about 6 ± 1. Further theoretical and experimental work will be needed to resolve this discrepancy.

Furthermore, we extended the restricted path integral method to the sampling with open path in order to calculate off-diagonal elements of the fermionic many-body density matrix. As a first application to the electron gas, we could show how the momentum distribution of interacting system changes from Maxwell-Boltzmann type at high temperature to a Fermi-Dirac distribution at low temperature. In the path integral formalism, this process is governed by an increasing number of permuting paths, which contribute with different signs to the averages. In the future work, we want to advance the method to lower temperatures, study its scaling behavior and compare with zero temperature calculations.

We also used the off-diagonal sampling technique to determine the natural orbitals of hydrogen at low density. The remaining challenge is how this method can be applied to a many-body system at high density while keeping the computational demand at a reasonable level.

Appendix A

Variational Interaction Terms

The general equations for the variational parameters q in a parameterized density matrix, from Eq. 3.19, are

$$\frac{1}{2}\frac{\partial H}{\partial \vec{q}} + \overleftrightarrow{\mathcal{N}}\ \dot{\vec{q}} = 0 \tag{A.1}$$

where

$$H \equiv \int \rho \mathcal{H} \rho \ \mathbf{dR} = \int \rho \mathcal{H} \rho_I \mathbf{dR} \tag{A.2}$$

and the norm matrix

$$\mathcal{N}_{ji} \equiv \int p_j \ p_i \ \rho^2 \ \mathbf{dR} = \lim_{q' \to q} \frac{\partial^2 N}{\partial q_j \partial q_i'} \tag{A.3}$$

with

$$N \equiv \int \rho(\mathbf{R}, \vec{q}; \beta) \ \rho(\mathbf{R}, \vec{q}\,'; \beta) \ \mathbf{dR} \ . \tag{A.4}$$

The subscript I in Eq. A.2 indicates that only one ρ needs to be antisymmetric and the identity permutation can be used in the other. This appendix contains the detailed formulae for these equations for a parameterized Gaussian density matrix applied to a Coulomb system.

Repeating Eq. 3.56, the parameterized variational density matrix is an anti-symmetrized product of one-particle density matrices,

$$\begin{aligned} \rho(\mathbf{R}, \mathbf{R}', \beta) &= \sum_{\mathcal{P}} \epsilon_{\mathcal{P}} \prod_k \rho_1(\mathbf{r}_k, \mathbf{r}'_{\mathcal{P}_k}, \beta) && \text{(A.5)} \\ &= \sum_{\mathcal{P}} \epsilon_{\mathcal{P}} e^D \prod_k (\pi w_{\mathcal{P}_k})^{-3/2} \exp\left\{ -\frac{1}{w_{\mathcal{P}_k}} (\mathbf{r}_k - \mathbf{m}_{\mathcal{P}_k})^2 \right\} \quad , && \text{(A.6)} \end{aligned}$$

where the amplitude D and the widths w_k and means $\mathbf{m}_k$ are the variational parameters. We also dropped $1/N!$ prefactors which are the same for the norm matrix and thus cancel out. The permutation sum is over all permutations of identical particles (e.g. same spin electrons) and $\epsilon_{\mathcal{P}} = \pm 1$ is the permutation signature. The initial conditions are $w_k = 0$, $\mathbf{m}_k = \mathbf{r}'_k$, and $D = 0$.

For this ansatz the generator of the norm matrix,

$$N = \sum_{\mathcal{P}} \epsilon_{\mathcal{P}} \prod_k [\pi(w_k + w'_{\mathcal{P}_k})]^{-3/2} \exp\left\{-(\mathbf{m}_k - \mathbf{m}'_{\mathcal{P}_k})^2/(w_k + w'_{\mathcal{P}_k})\right\} \exp(D + D')\ .$$

For a periodic system the above equation also is summed over all periodic simulation cell vectors, $\mathbf{L}$, with $\mathbf{m}_k - \mathbf{m}'_{\mathcal{P}_k} \to \mathbf{m}_k - \mathbf{m}'_{\mathcal{P}_k} + \mathbf{L}$. Using this the components of the norm matrix are then:

$$\mathcal{N}_{DD} = \sum_{\mathcal{P}} \epsilon_{\mathcal{P}} N_{\mathcal{P}} \tag{A.7}$$

$$\mathcal{N}_{\mathbf{m}_i D} = \sum_{\mathcal{P}} \epsilon_{\mathcal{P}} \left[\frac{-2(\mathbf{m}_i - \mathbf{m}_{\mathcal{P}_i})}{w_i + w_{\mathcal{P}_i}}\right] N_{\mathcal{P}} \tag{A.8}$$

$$\mathcal{N}_{w_i D} = \sum_{\mathcal{P}} \epsilon_{\mathcal{P}} \left(\frac{-1}{w_i + w_{\mathcal{P}_i}}\right) \left[\frac{3}{2} - \frac{(\mathbf{m}_i - \mathbf{m}_{\mathcal{P}_i})^2}{w_i + w_{\mathcal{P}_i}}\right] N_{\mathcal{P}} \tag{A.9}$$

$$\mathcal{N}_{\mathbf{m}_i \mathbf{m}_j} = \sum_{\mathcal{P}} \epsilon_{\mathcal{P}} \left[\frac{2\delta_{j,\mathcal{P}_i} \overset{\leftrightarrow}{I}}{w_i + w_j} + 4\frac{(\mathbf{m}_i - \mathbf{m}_{\mathcal{P}_i})}{(w_i + w_{\mathcal{P}_i})}\frac{(\mathbf{m}_j - \mathbf{m}_{\mathcal{P}_j^{-1}})}{(w_j + w_{\mathcal{P}_j^{-1}})}\right] N_{\mathcal{P}} \tag{A.10}$$

$$\mathcal{N}_{\mathbf{m}_i w_j} = \sum_{\mathcal{P}} \epsilon_{\mathcal{P}} \left[\frac{\delta_{j,\mathcal{P}_i}}{w_i + w_j} + \frac{1}{w_j + w_{\mathcal{P}_j^{-1}}}\left(\frac{3}{2} - \frac{(\mathbf{m}_j - \mathbf{m}_{\mathcal{P}_j^{-1}})^2}{(w_j + w_{\mathcal{P}_j^{-1}})}\right)\right]\left[\frac{2(\mathbf{m}_i - \mathbf{m}_{\mathcal{P}_i})}{w_i + w_{\mathcal{P}_i}}\right] N_{\mathcal{P}}$$

$$\begin{aligned}\mathcal{N}_{w_i w_j} = \sum_{\mathcal{P}} \epsilon_{\mathcal{P}} \Bigg\{ & \frac{\delta_{j,\mathcal{P}_i}}{(w_i + w_{\mathcal{P}_i})^2}\left[\frac{3}{2} - \frac{2(\mathbf{m}_i - \mathbf{m}_{\mathcal{P}_i})^2}{w_j + w_{\mathcal{P}_j}}\right] + \frac{1}{(w_i + w_{\mathcal{P}_i})(w_j + w_{\mathcal{P}_j^{-1}})} \\ & \left[\frac{3}{2} - \frac{(\mathbf{m}_i - \mathbf{m}_{\mathcal{P}_i})^2}{w_i + w_{\mathcal{P}_i}}\right]\left[\frac{3}{2} - \frac{(\mathbf{m}_j - \mathbf{m}_{\mathcal{P}_j^{-1}})^2}{w_j + w_{\mathcal{P}_j^{-1}}}\right]\Bigg\} N_{\mathcal{P}}\end{aligned} \tag{A.11}$$

where

$$N_{\mathcal{P}} = e^{2D} \prod_j \frac{\exp\left\{-\frac{(\mathbf{m}_j - \mathbf{m}_{\mathcal{P}_j})^2}{(w_j + w_{\mathcal{P}_j})}\right\}}{(\pi(w_j + w_{\mathcal{P}_j}))^{3/2}} = N_{\mathcal{P}^{-1}}\ . \tag{A.12}$$

The Hamiltonian for a periodic system of electrons and ions is given by,

$$\mathcal{H} = -\frac{1}{2}\sum_{i=1}^{N_e} \nabla_i^2 + \sum\sum_{i<j} \psi(\mathbf{r}_{ij}) - \sum_i \sum_I Z_I \psi(\mathbf{r}_{iI}) + \sum_i U_{Mad} + U_{ions} \tag{A.13}$$

where the purely ionic terms are,

$$U_{ions} = \sum\sum_{I<I'} Z_I Z_{I'} \psi(\mathbf{r}_{II'}) + \sum_I Z_I^2 U_{Mad}\ . \tag{A.14}$$

The Ewald potential, $\psi(\mathbf{r})$, which includes interactions with periodic images and incorporates charge neutrality reads,

$$\psi(\mathbf{r}) = \sum_{\mathbf{L}} \frac{\mathrm{erfc}(G|\mathbf{r}+\mathbf{L}|)}{|\mathbf{r}+\mathbf{L}|} + \sum_{\mathbf{k}\neq 0} \frac{4\pi}{\hat{\mathcal{V}} k^2} \exp(-k^2/4G^2) - \frac{\pi}{G^2 \hat{\mathcal{V}}} = \sum_{\mathbf{k}\neq 0} \frac{4\pi}{\hat{\mathcal{V}} k^2} \exp(i\mathbf{k}\cdot\mathbf{r})$$

where $\hat{\mathcal{V}}$ is the periodic cell volume and G an arbitrary constant. The Madelung term in $\mathcal{H}$ is the interaction energy of an electron with it's periodic images and neutralizing background (e.g. $U_{Mad} = -1.41865/L$ for a simple cubic simulation cell, the usual case). To do the integrals, we represent the Gaussians by their Fourier series

$$\left(\frac{2}{\pi w}\right)^{3/2} \sum_{\mathbf{L}} e^{-\frac{2}{w}(\mathbf{r}-\mathbf{m}-\mathbf{L})^2} = \sum_{\mathbf{k}} \frac{1}{\hat{\mathcal{V}}} e^{-k^2 w/8} e^{i\mathbf{k}\cdot(\mathbf{r}-\mathbf{m})} \tag{A.15}$$

and in the interaction terms use the Fourier representation for $\psi(\mathbf{r})$. This finally gives

$$H = \sum_{\mathcal{P}} \epsilon_{\mathcal{P}} \left\{K_{\mathcal{P}} + U_{\mathcal{P}}\right\} N_{\mathcal{P}} \tag{A.16}$$

with

$$K_{\mathcal{P}} = \sum_i \left[\frac{3}{w_i + w_{\mathcal{P}i}} - 2\frac{(\mathbf{m}_i - \mathbf{m}_{\mathcal{P}i})^2}{(w_i + w_{\mathcal{P}i})^2}\right] \tag{A.17}$$

$$U_{\mathcal{P}} = \sum_i \sum_{j>i} W(\tilde{\mathbf{m}}_i - \tilde{\mathbf{m}}_j, \tilde{w}_i + \tilde{w}_j) - \sum_i \sum_I Z_I W(\tilde{\mathbf{m}}_i - \mathbf{R}_I, \tilde{w}_i) + \sum_i U_{\mathrm{Mad}} + U_{\mathrm{ions}}$$

where $\tilde{w}_i \equiv w_i w_{\mathcal{P}i}/(w_i + w_{\mathcal{P}i})$ and $\tilde{\mathbf{m}}_i \equiv (\mathbf{m}_i w_{\mathcal{P}i} + \mathbf{m}_{\mathcal{P}i} w_i)/(w_i + w_{\mathcal{P}i})$. The interaction integral

$$W(\mathbf{r}, w) \equiv \sum_{k\neq 0} \frac{4\pi}{\hat{\mathcal{V}} k^2} e^{-k^2 w/4} e^{i\mathbf{k}\cdot\mathbf{r}} \tag{A.18}$$

is symmetric in $\mathbf{r}$ when the periodic cell has inversion symmetry. Continuing, the left hand side of Eq. A.1 is

$$H_D \equiv \frac{1}{2}\frac{\partial H}{\partial D} = H \tag{A.19}$$

$$H_{w_i} \equiv \frac{1}{2}\frac{\partial H}{\partial w_i} = \frac{1}{2}\sum_{\mathcal{P}} \epsilon_{\mathcal{P}} \left\{\left(\frac{\partial K_{\mathcal{P}}}{\partial w_i} + \frac{\partial U_{\mathcal{P}}}{\partial w_i}\right) N_{\mathcal{P}} + (K_{\mathcal{P}} + U_{\mathcal{P}})\frac{\partial N_{\mathcal{P}}}{\partial w_i}\right\} \tag{A.20}$$

$$H_{\mathbf{m}_i} \equiv \frac{1}{2}\frac{\partial H}{\partial \mathbf{m}_i} = \frac{1}{2}\sum_{\mathcal{P}} \epsilon_{\mathcal{P}} \left\{\left(\frac{\partial K_{\mathcal{P}}}{\partial \mathbf{m}_i} + \frac{\partial U_{\mathcal{P}}}{\partial \mathbf{m}_i}\right) N_{\mathcal{P}} + (K_{\mathcal{P}} + U_{\mathcal{P}})\frac{\partial N_{\mathcal{P}}}{\partial \mathbf{m}_i}\right\} \tag{A.21}$$

with

$$\frac{\partial N_{\mathcal{P}}}{\partial w_i} = \left[-\frac{3}{w_i + w_{\mathcal{P}i}} + 2\frac{(\mathbf{m}_i - \mathbf{m}_{\mathcal{P}i})^2}{(w_i + w_{\mathcal{P}i})^2}\right] N_{\mathcal{P}} \tag{A.22}$$

$$\frac{\partial N_{\mathcal{P}}}{\partial \mathbf{m}_i} = \left[-4\frac{(\mathbf{m}_i - \mathbf{m}_{\mathcal{P}i})}{w_i + w_{\mathcal{P}i}}\right] N_{\mathcal{P}} \tag{A.23}$$

$$\frac{\partial K_{\mathcal{P}}}{\partial w_i} = \left[-\frac{6}{(w_i + w_{\mathcal{P}i})^2} + 8\frac{(\mathbf{m}_i - \mathbf{m}_{\mathcal{P}i})^2}{(w_i + w_{\mathcal{P}i})^3}\right] \tag{A.24}$$

$$\frac{\partial K_{\mathcal{P}}}{\partial \mathbf{m}_i} = \left[-8\frac{\mathbf{m}_i - \mathbf{m}_{\mathcal{P}i}}{(w_i + w_{\mathcal{P}i})^2}\right] . \tag{A.25}$$

where we have used the fact that terms in $\mathcal{P}i$ and $\mathcal{P}^{-1}i$ give the same contribution under the permutation sum and so combined them. The derivatives of the interaction integral are,

$$\frac{\partial U_{\mathcal{P}}}{\partial \mathbf{m}_i} = \frac{2w_{\mathcal{P}i}}{w_i + w_{\mathcal{P}i}}\left[\sum_{j\neq i}\mathbf{W}^{[1]}(\tilde{m}_i - \tilde{m}_j, \tilde{w}_i + \tilde{w}_j) - \sum_I Z_I \mathbf{W}^{[1]}(\tilde{m}_i - \mathbf{R}_I, \tilde{w}_i)\right]$$

$$\begin{aligned}\frac{\partial U_{\mathcal{P}}}{\partial w_i} = \frac{2w_{\mathcal{P}i}}{(w_i + w_{\mathcal{P}i})^2}&\left[w_{\mathcal{P}i}\left(\sum_{j\neq i} W^{[2]}(\tilde{m}_i - \tilde{m}_j, \tilde{w}_i + \tilde{w}_j) - \sum_I Z_I W^{[2]}(\tilde{m}_i - \mathbf{R}_I, \tilde{w}_i)\right)\right.\\ &\left. + (\mathbf{m}_{\mathcal{P}i} - \mathbf{m}_i)\cdot\left(\sum_{j\neq i}\mathbf{W}^{[1]}(\tilde{m}_i - \tilde{m}_j, \tilde{w}_i + \tilde{w}_j) - \sum_I Z_I \mathbf{W}^{[1]}(\tilde{m}_i - \mathbf{R}_I, \tilde{w}_i)\right)\right]\end{aligned}$$

where $\mathbf{W}^{[1]}$ and $W^{[2]}$ denote the derivatives of W with the first and second argument. Comparing equation A.18 and Eq. A.15 the interaction integral may be written as

$$W(\mathbf{r}, w) = \psi(\mathbf{r}) - \sum_{\mathbf{L}} \frac{\operatorname{erfc}\left[\frac{|\mathbf{r}+\mathbf{L}|}{\sqrt{w}}\right]}{|\mathbf{r}+\mathbf{L}|} + \frac{\pi w}{V} \tag{A.26}$$

and its derivatives as:

$$\begin{aligned}\mathbf{W}^{[1]}(\mathbf{r}, w) &= \nabla\psi(\mathbf{r}) + \sum_{\mathbf{L}}\frac{\mathbf{r}+\mathbf{L}}{|\mathbf{r}+\mathbf{L}|^3}\left(\operatorname{erfc}\left[\frac{|\mathbf{r}+\mathbf{L}|}{\sqrt{w}}\right] + \frac{2|\mathbf{r}+\mathbf{L}|}{\sqrt{\pi w}}\exp(-|\mathbf{r}+\mathbf{L}|^2/w)\right)\\ W^{[2]}(\mathbf{r}, w) &= -\sum_{\mathbf{L}}\frac{\exp(-|\mathbf{r}+\mathbf{L}|^2/w)}{w^{3/2}\sqrt{\pi}} + \frac{\pi}{V}\end{aligned} \tag{A.27}$$

For an isolated system ($\mathbf{L}\to\infty$) and these would simplify to,

$$W(\mathbf{r}, w) = \frac{\operatorname{erf}\left[r/\sqrt{w}\,\right]}{r} \tag{A.28}$$

$$\mathbf{W}^{[1]}(\mathbf{r}, w) = -\frac{\mathbf{r}}{r^3}\left(\operatorname{erf}\left[r/\sqrt{w}\,\right] - \frac{2r}{\sqrt{\pi w}}e^{-r^2/w}\right) \tag{A.29}$$

$$W^{[2]}(\mathbf{r}, w) = -\frac{1}{w\sqrt{\pi w}}e^{-r^2/w} \tag{A.30}$$

At $\beta = 0$, the initial derivatives for the variational parameters reduce to

$$\dot{w}_i = 2 \tag{A.31}$$

$$\dot{\mathbf{m}}_i = 0 \tag{A.32}$$

$$\dot{D} = -U_I \tag{A.33}$$

For large numbers of electrons, the computational requirements to treat all exchange terms increase drastically. Here the approximation discussed in section 3.7 is used where the kinetic pair exchange corrections given there are added to the identity permutation term derived here.

Appendix B

Finite Temperature Jastrow Factor

The VDM method can be improved by including correlations that are missed in an Hartree-Fock type ansatz. This is usually done in form of a Jastrow factor f(**R**,**R**') as shown in Eq. 3.79,

$$f(\mathbf{R},\mathbf{R}') = \exp\left\{-\frac{1}{2}\sum_{i<j} u(r_{ij}) + u(r'_{ij})\right\} \quad . \tag{B.1}$$

The Jastrow factor can be calculated at zero temperature using the RPA (see Ceperley and Alder (1981)), then generalized to finite temperature and approximately expressed in the form (Pollock, 2000),

$$u(r) \;=\; \frac{A}{r}\left(1 - e^{-B\,r}\right) \quad , \tag{B.2}$$

where r is the separation of the pair of particles. The coefficients A and B depend on density n, inverse temperature β, and on the type of interacting particles. They are derive that the fulfill the cusp condition at any temperature. The coefficients for a pair of electrons is given by,

$$A_{ee} \;=\; ct \quad , \qquad c = 2\sqrt{r_s^3/3} \quad , \qquad t = \tanh\left(\beta/c\right) \quad , \tag{B.3}$$

$$B_{ee} \;=\; \sqrt{2/A_{ee}} \quad . \tag{B.4}$$

For an electron and an ion of charge Q, they read,

$$A_{ei} \;=\; -\frac{Qc}{t}\left(1 - e^{-\beta t/c}\right) \tag{B.5}$$

$$B_{ei} \;=\; \sqrt{-4Q/A_{ei}} \quad . \tag{B.6}$$

Appendix C

Debye Model

At sufficiently high temperature and low density, the hydrogen plasma behaves like a system of free electrons and protons, which interact via a screened Coulomb potential (Fowler and Guggenheim, 1965; Ebeling *et al.*, 1976). The screening arises from a cloud of opposite charge of the size of the Debye radius r_{D}. Assuming full dissociation, it is given by,

$$r_{\mathrm{D}} = \frac{1}{\kappa} \quad , \quad \kappa^2 = \frac{\beta}{\epsilon_0} \sum_{\text{species } i} n_i Q_i^2 . \tag{C.1}$$

The screening leads to the following corrections u_D and p_D that are added internal energy and pressure of non-interacting Fermi gas,

$$u_{\mathrm{D}} = \frac{\kappa^3}{8\pi\beta n} \quad , \quad p_{\mathrm{D}} = \frac{\kappa^3}{24\pi\beta} \quad . \tag{C.2}$$

If Fermi statistics is not important the Debye corrections can be expressed in the terms of the coupling parameter Γ (Eq. 1.4),

$$\frac{E_{\mathrm{D}}}{E_{\mathrm{id}}} = \frac{\Gamma^{3/2}}{\sqrt{6}} \quad , \quad \frac{p_{\mathrm{D}}}{p_{\mathrm{id}}} = \sqrt{2/3}\,\Gamma^{3/2} \quad , \tag{C.3}$$

where E_{id} and p_{id} are the internal energy and pressure of a ideal gas of distinguishable particles. The Debye screening represents the first correction to the free particle behavior due to interactions in the limit of high temperature and low density. For small values of Γ, the Debye model is a reliable approximation. One finds deviations of less than 20% in pressure and energy for $\Gamma < 0.5$ in discussed density range. However, at sufficiently high Γ, the Debye model overestimates the screening drastically and predicts a too small r_{D}, which leads to unphysically low, even negative pressures.

Appendix D

Equation of State Tables

The following tables contain the equation of state from PIMC simulations of hydrogen and deuterium using different time steps and nodal surfaces. It should be noted that all simulations have been performed using order $n_{\mathrm{A}} = 1$ in the action expansion for the off-diagonal pair density matrix (Eq. 2.38) and order $n_{\mathrm{E}} = 2$ in the energy expansion. As discussed in section 4.1, there are corrections to pressure and energy due to higher orders. They are particularly substantial for the pressure at low temperatures. In the following table, we list the raw simulation data without the corrections.

Table D.1: Equation of state table with pressure and internal energy per atom for hydrogen at the density of $0.000983\,\mathrm{gcm}^{-3}$ ($r_s = 14$) calculated with PIMC simulations of $N_P = 32$ pairs of protons and electrons, using free particle nodes, a time step of $\tau^{-1} = 10^6$K, $n_{\mathrm{A}} = 1$ orders in the action expansion formula 2.38 and $n_{\mathrm{E}} = 2$ orders in the energy expansion.

T (K)	p (GPa)	E (eV)
166 667	2.641 ± 0.001	41.091 ± 0.018
125 000	1.956 ± 0.001	29.979 ± 0.026
62 500	0.902 ± 0.002	11.827 ± 0.042
31 250	0.343 ± 0.001	-2.880 ± 0.046
15 625	0.143 ± 0.001	-11.298 ± 0.064
12 500	0.117 ± 0.001	-11.903 ± 0.032
10 000	0.094 ± 0.001	-12.429 ± 0.027
8929	0.085 ± 0.001	-12.652 ± 0.032
7812	0.076 ± 0.002	-12.971 ± 0.084
6944	0.063 ± 0.001	-13.476 ± 0.053
6250	0.059 ± 0.001	-14.189 ± 0.037
5000	0.053 ± 0.001	-14.708 ± 0.026

Table D.2: EOS table for hydrogen at the density of 0.00270 gcm^{-3} (r_s=10) calculated with PIMC simulations using FP nodes, N_P = 32, τ^{-1} = 10^6K, n_A = 1 and n_E = 2 (see Tab. D.1)

T (K)	p (GPa)	E (eV)
166 667	7.166 ± 0.004	39.979 ± 0.024
125 000	5.264 ± 0.004	28.594 ± 0.027
62 500	2.342 ± 0.005	9.466 ± 0.053
31 250	0.879 ± 0.006	-4.885 ± 0.068
15 625	0.397 ± 0.006	-11.382 ± 0.043
12 500	0.323 ± 0.005	-11.945 ± 0.046
10 000	0.270 ± 0.003	-12.491 ± 0.039
8929	0.234 ± 0.004	-12.903 ± 0.033
7812	0.203 ± 0.004	-13.543 ± 0.028
6944	0.191 ± 0.004	-13.715 ± 0.035
6250	0.168 ± 0.004	-14.282 ± 0.073
5000	0.151 ± 0.004	-14.759 ± 0.018

Table D.3: EOS table for hydrogen at the density of 0.0105 gcm^{-3} (r_s = 8) calculated with PIMC simulations using FP nodes, N_P = 32, τ = 10^6K, n_A = 1 and n_E = 2 (see Tab. D.1)

T (K)	p (GPa)	E (eV)
166 667	13.770 ± 0.010	38.683 ± 0.036
125 000	10.060 ± 0.010	27.120 ± 0.037
625 00	4.337 ± 0.006	7.412 ± 0.034
31 250	1.639 ± 0.009	-5.848 ± 0.041
15 625	0.723 ± 0.012	-11.593 ± 0.037
12 500	0.630 ± 0.008	-12.062 ± 0.037
10 000	0.480 ± 0.006	-12.865 ± 0.028
8929	0.432 ± 0.005	-13.223 ± 0.025
7812	0.371 ± 0.007	-13.881 ± 0.044
6944	0.344 ± 0.006	-14.081 ± 0.050
6250	0.308 ± 0.004	-14.559 ± 0.019
5000	0.297 ± 0.006	-14.797 ± 0.019

Table D.4: EOS table for hydrogen at the density of 0.0125 gcm^{-3} ($r_s = 6$) calculated with PIMC simulations using FP nodes, $N_P = 32$, $\tau = 10^6$K, $n_\mathrm{A} = 1$ and $n_\mathrm{E} = 2$ (see Tab. D.1)

T (K)	p (GPa)	E (eV)
166 667	31.912 ± 0.021	36.602 ± 0.028
125 000	23.036 ± 0.018	24.734 ± 0.032
62 500	9.586 ± 0.020	4.727 ± 0.034
31 250	3.716 ± 0.012	-6.923 ± 0.027
15 625	1.672 ± 0.026	-11.783 ± 0.048
12 500	1.380 ± 0.025	-12.461 ± 0.059
10 000	1.096 ± 0.012	-13.171 ± 0.037
8929	0.992 ± 0.011	-13.472 ± 0.038
7812	0.884 ± 0.011	-13.843 ± 0.030
6944	0.808 ± 0.014	-14.269 ± 0.029
6250	0.769 ± 0.013	-14.368 ± 0.022
5000	0.676 ± 0.016	-14.938 ± 0.019

Table D.5: EOS table for hydrogen at the density of 0.0421 gcm^{-3} ($r_s = 4$) calculated with PIMC simulations using FP nodes, $N_P = 32$, $\tau = 10^6$K, $n_\mathrm{A} = 1$ and $n_\mathrm{E} = 2$ (see Tab. D.1)

T (K)	p (GPa)	E (eV)
166 667	102.747 ± 0.131	32.261 ± 0.050
125 000	73.082 ± 0.111	20.229 ± 0.046
62 500	29.462 ± 0.131	1.051 ± 0.050
31 250	11.863 ± 0.066	-8.144 ± 0.017
25 000	9.075 ± 0.131	-9.809 ± 0.051
20 000	7.320 ± 0.141	-10.985 ± 0.053
15 625	5.530 ± 0.111	-12.057 ± 0.053
12 500	4.325 ± 0.162	-12.982 ± 0.059
10 000	3.700 ± 0.049	-13.543 ± 0.034
8929	3.353 ± 0.069	-13.909 ± 0.035
7812	3.065 ± 0.086	-14.222 ± 0.033
6944	2.893 ± 0.064	-14.382 ± 0.036
6250	2.622 ± 0.075	-14.605 ± 0.035
5000	2.307 ± 0.100	-14.943 ± 0.028

Table D.6: EOS table for hydrogen at the density of 0.0999 gcm^{-3} ($r_s = 3$) calculated with PIMC simulations using FP nodes, $N_P = 32$, $\tau = 10^6$K, $n_\mathrm{A} = 1$ and $n_\mathrm{E} = 2$ (see Tab. D.1). The last column shows the fraction of permuting electrons given by $1 - P_1$ (see section 2.6.8)

T (K)	p (GPa)	E (eV)	$1 - P_1$
166 667	234.381 ± 0.242	28.422 ± 0.042	0.00031 ± 0.00003
125 000	164.852 ± 0.212	16.489 ± 0.027	0.00065 ± 0.00004
62 500	67.526 ± 0.303	-1.166 ± 0.044	0.006 ± 0.001
31 250	27.763 ± 0.192	-8.961 ± 0.030	0.033 ± 0.006
25 000	21.410 ± 0.242	-10.282 ± 0.037	0.039 ± 0.002
20 000	17.428 ± 0.293	-11.297 ± 0.049	0.046 ± 0.004
15 625	13.602 ± 0.343	-12.260 ± 0.050	0.047 ± 0.005
12 500	11.462 ± 0.454	-13.087 ± 0.079	0.036 ± 0.004
10 000	10.600 ± 0.172	-13.593 ± 0.028	0.036 ± 0.003
8929	10.257 ± 0.151	-13.866 ± 0.027	0.022 ± 0.001
7812	9.433 ± 0.131	-14.220 ± 0.032	0.024 ± 0.002
6944	9.055 ± 0.141	-14.438 ± 0.028	0.016 ± 0.001
6250	8.498 ± 0.212	-14.593 ± 0.040	0.025 ± 0.005
5000	7.996 ± 0.212	-14.835 ± 0.018	0.017 ± 0.002

Table D.7: EOS table for *deuterium* at the density of 0.307 gcm^{-3} (r_s=2.6) calculated with PIMC simulations using FP nodes, $N_P = 32$, $\tau = 10^6$K, $n_\mathrm{A} = 1$ and $n_\mathrm{E} = 2$ (see Tab. D.6)

T (K)	p (GPa)	E (eV)	$1 - P_1$
125 000	248.561 ± 0.161	14.675 ± 0.020	0.003 ± 0.001
62 500	103.121 ± 0.344	-2.143 ± 0.038	0.017 ± 0.001
50 000	77.568 ± 0.217	-5.167 ± 0.025	0.030 ± 0.001
31 250	44.905 ± 0.235	-9.160 ± 0.022	0.076 ± 0.002
25 000	35.512 ± 0.366	-10.384 ± 0.029	0.105 ± 0.003
20 000	29.997 ± 0.228	-11.228 ± 0.024	0.129 ± 0.003
15 625	24.503 ± 0.325	-12.211 ± 0.023	0.136 ± 0.006
12 500	21.402 ± 0.399	-12.823 ± 0.030	0.134 ± 0.008
10 000	20.200 ± 0.309	-13.547 ± 0.024	0.092 ± 0.005
8929	19.038 ± 0.402	-13.822 ± 0.051	0.073 ± 0.007
7812	18.311 ± 0.455	-14.167 ± 0.045	0.063 ± 0.002
6944	17.574 ± 0.540	-14.374 ± 0.055	0.065 ± 0.004
6250	17.029 ± 0.413	-14.529 ± 0.042	0.060 ± 0.004
5000	15.817 ± 0.445	-14.736 ± 0.043	0.057 ± 0.003

Table D.8: EOS table for deuterium at the density of $0.390\,\mathrm{gcm}^{-3}$ (r_s=2.4) calculated with PIMC simulations using VDM nodes, $N_P = 32$, $\tau_B^{-1} = 2 \cdot 10^6$K, $\tau_F^{-1} = 8 \cdot 10^6$K, $n_\mathrm{A} = 1$ and $n_\mathrm{E} = 2$ (see Tab. D.6)

T (K)	p (GPa)	E (eV)	$1 - P_1$
125 000	308 ± 5	13.2 ± 0.4	0.002 ± 0.000
62 500	134 ± 1	-2.5 ± 0.1	0.020 ± 0.002
31 250	60 ± 3	-9.4 ± 0.2	0.102 ± 0.004
15 625	34 ± 4	-12.1 ± 0.3	0.204 ± 0.008
10 000	17 ± 5	-14.0 ± 0.4	0.225 ± 0.014

Table D.9: EOS table for deuterium at the density of $0.506\,\mathrm{gcm}^{-3}$ (r_s=2.2) calculated with PIMC simulations using VDM nodes, $N_P = 32$, $\tau_B^{-1} = 2 \cdot 10^6$K, $\tau_F^{-1} = 8 \cdot 10^6$K, $n_\mathrm{A} = 1$ and $n_\mathrm{E} = 2$ (see Tab. D.6)

T (K)	p (GPa)	E (eV)	$1 - P_1$
125 000	411 ± 2	13.3 ± 0.1	0.004 ± 0.000
62 500	183 ± 5	-2.5 ± 0.3	0.032 ± 0.001
31 250	84 ± 3	-9.4 ± 0.2	0.172 ± 0.005
15 625	50 ± 5	-12.0 ± 0.3	0.302 ± 0.005
10 000	36 ± 5	-13.5 ± 0.3	0.320 ± 0.010

Table D.10: EOS table for deuterium at the density of 0.674 gcm^{-3} (r_s=2.0) calculated with PIMC simulations using FP nodes, $N_P = 32$, $\tau_B^{-1} = 2{\cdot}10^6$K, $\tau_F^{-1} = 8{\cdot}10^6$K, $n_\mathrm{A} = 1$ and $n_\mathrm{E} = 2$ (see Tab. D.6)

T (K)	p (GPa)	E (eV)	$1 - P_1$
1 000 000	5433 ± 5	245.7 ± 0.3	0.000 ± 0.000
500 000	2624 ± 4	113.2 ± 0.2	0.000 ± 0.000
250 000	1225 ± 3	45.7 ± 0.1	0.000 ± 0.000
125 000	548 ± 2	12.2 ± 0.1	0.008 ± 0.000
62 500	246 ± 2	-3.1 ± 0.1	0.081 ± 0.001
31 250	125 ± 2	-9.1 ± 0.1	0.365 ± 0.003
15 625	75 ± 3	-11.7 ± 0.1	0.701 ± 0.003
10 000	63 ± 5	-12.5 ± 0.2	0.829 ± 0.004
7812	51 ± 4	-13.5 ± 0.2	0.833 ± 0.010
5000	68 ± 9	-14.4 ± 0.4	0.629 ± 0.007

Table D.11: EOS table for deuterium at the density of 0.674 gcm^{-3} (r_s=2.0) calculated with PIMC simulations using VDM nodes, $N_P = 32$, $\tau_B^{-1} = 2 \cdot 10^6$K, $\tau_F^{-1} = 8 \cdot 10^6$K, $n_\mathrm{A} = 1$ and $n_\mathrm{E} = 2$ (see Tab. D.6)

T (K)	p (GPa)	E (eV)	$1 - P_1$
125 000	540 ± 14	11.7 ± 0.6	0.008 ± 0.001
62 500	236 ± 7	-3.7 ± 0.3	0.071 ± 0.005
31 250	128 ± 5	-9.2 ± 0.2	0.271 ± 0.006
15 625	59 ± 9	-12.8 ± 0.4	0.459 ± 0.009
10 000	48 ± 10	-13.6 ± 0.5	0.534 ± 0.010
7812	53 ± 12	-13.7 ± 0.5	0.557 ± 0.011
5000	26 ± 25	-15.3 ± 1.2	0.666 ± 0.016

Table D.12: EOS table for deuterium at the density of 0.838 gcm^{-3} (r_s=1.86) calculated with PIMC simulations using FP nodes, $N_P = 32$, $\tau_B^{-1} = 2 \cdot 10^6$K, $\tau_F^{-1} = 8 \cdot 10^6$K, $n_\mathrm{A} = 1$ and $n_\mathrm{E} = 2$ (see Tab. D.6)

T (K)	p (GPa)	E (eV)	$1 - P_1$
1 000 000	6752 ± 8	245.3 ± 0.3	0.000 ± 0.000
500 000	3245 ± 5	111.9 ± 0.2	0.000 ± 0.000
250 000	1506 ± 3	44.3 ± 0.1	0.000 ± 0.000
125 000	688 ± 3	11.7 ± 0.1	0.013 ± 0.000
62 500	307 ± 1	-3.6 ± 0.0	0.133 ± 0.001
31 250	166 ± 3	-9.1 ± 0.1	0.488 ± 0.002
15 625	107 ± 7	-11.5 ± 0.3	0.804 ± 0.002
10 000	85 ± 5	-12.4 ± 0.2	0.896 ± 0.001
7812	69 ± 7	-13.0 ± 0.3	0.919 ± 0.001
5000	93 ± 12	-14.4 ± 0.5	0.864 ± 0.005

Table D.13: EOS table for deuterium at the density of 0.838 gcm^{-3} (r_s=1.86) calculated with PIMC simulations using VDM nodes, $N_P = 32$, $\tau_B^{-1} = 2 \cdot 10^6$K, $\tau_F^{-1} = 8 \cdot 10^6$K, $n_\mathrm{A} = 1$ and $n_\mathrm{E} = 2$ (see Tab. D.6)

T (K)	p (GPa)	E (eV)	$1 - P_1$
125 000	654 ± 16	10.3 ± 0.6	0.017 ± 0.002
62 500	322 ± 5	-3.1 ± 0.2	0.122 ± 0.004
31 250	169 ± 6	-9.3 ± 0.2	0.351 ± 0.005
15 625	102 ± 10	-12.2 ± 0.4	0.562 ± 0.010
10 000	97 ± 13	-12.5 ± 0.5	0.674 ± 0.009
7812	69 ± 27	-13.8 ± 1.0	0.689 ± 0.015
5000	49 ± 25	-14.7 ± 1.0	0.777 ± 0.009

Table D.14: EOS table for deuterium at the density of 1.01 gcm^{-3} (r_s=1.75) calculated with PIMC simulations using VDM nodes, $N_P = 32$, $\tau_B^{-1} = 2 \cdot 10^6$K, $\tau_F^{-1} = 4 \cdot 10^6$K, $n_\mathrm{A} = 1$ and $n_\mathrm{E} = 2$ (see Tab. D.6)

T (K)	p (GPa)	E (eV)	$1 - P_1$
125 000	815 ± 6	10.6 ± 0.2	0.023 ± 0.001
62 500	377 ± 9	-4.0 ± 0.3	0.177 ± 0.007
31 250	199 ± 15	-9.9 ± 0.4	0.435 ± 0.009
15 625	162 ± 16	-11.3 ± 0.5	0.675 ± 0.017
10 000	138 ± 37	-12.3 ± 1.1	0.755 ± 0.015

Table D.15: EOS table for deuterium at the density of 1.60 gcm^{-3} (r_s=1.50) calculated with PIMC simulations using VDM nodes, $N_P = 32$, $\tau_B^{-1} = 4 \cdot 10^6$K, $\tau_F^{-1} = 8 \cdot 10^6$K, $n_{\mathrm{A}} = 1$ and $n_{\mathrm{E}} = 2$ (see Tab. D.6)

T (K)	p (GPa)	E (eV)	$1 - P_1$
250 000	2865 ± 12	41.2 ± 0.2	0.006 ± 0.000
125 000	1328 ± 24	9.5 ± 0.5	0.070 ± 0.003
62 500	676 ± 26	-3.9 ± 0.5	0.340 ± 0.005
31 250	409 ± 58	-9.3 ± 1.1	0.650 ± 0.011
15 625	403 ± 104	-9.9 ± 2.0	0.821 ± 0.013

Table D.16: EOS table for deuterium at the density of 2.76 gcm^{-3} (r_s=1.25) calculated with PIMC simulations using VDM nodes, $N_P = 32$, $\tau_B^{-1} = 4 \cdot 10^6$K, $\tau_F^{-1} = 8 \cdot 10^6$K, $n_{\mathrm{A}} = 1$ and $n_{\mathrm{E}} = 2$ (see Tab. D.6)

T (K)	p (GPa)	E (eV)	$1 - P_1$
250 000	5043 ± 37	39.5 ± 0.4	0.024 ± 0.001
125 000	2477 ± 30	9.2 ± 0.3	0.222 ± 0.005
62 500	1509 ± 88	-2.1 ± 1.0	0.568 ± 0.008
31 250	1068 ± 93	-7.3 ± 1.1	0.813 ± 0.008
15 625	960 ± 174	-8.9 ± 2.0	0.911 ± 0.002

Table D.17: EOS table for deuterium at the density of 5.39 gcm^{-3} (r_s=1.0) calculated with PIMC simulations using VDM nodes, $N_P = 32$, $\tau_B^{-1} = 8 \cdot 10^6$K, $\tau_F^{-1} = 16 \cdot 10^6$K, $n_{\mathrm{A}} = 1$ and $n_{\mathrm{E}} = 2$ (see Tab. D.6)

T (K)	p (GPa)	E (eV)	$1 - P_1$
500 000	20814 ± 143	101.5 ± 0.8	0.009 ± 0.000
250 000	10545 ± 153	39.8 ± 0.9	0.122 ± 0.003
125 000	6343 ± 221	14.6 ± 1.3	0.485 ± 0.007
62 500	4877 ± 404	5.9 ± 2.3	0.785 ± 0.003

References

Allen, M. and D. Tildesley, *Computer Simulation of Liquids* (Oxford University Press, New York, 1987).

Beule, D., W. Ebeling and A. Förster, Phys. Rev. B **59**, 14177 (1999).

Bouchard, J. P., A. Goerges and C. Lhuillier, J. Phys. France **49**, 553 (1988).

Bunker, A., S. Nagel, R. Redmer and G. Röpke, Phys. Rev. B **56**, 3094 (1997).

Burrows, A., M. Marley, W. Hubbard, J. Luinine, T. Guillot, D. Saumon, R. Freedman, D. Sudarsky and C. Sharp, Astrophys. J. **491**, 36554 (1997).

Ceperley, D. and B. Alder, Phys. Rev. Lett. **45**, 566 (1980).

Ceperley, D. and B. Alder, Phys. Rev. B **36**, 2092 (1987).

Ceperley, D. M., J. Stat. Phys. **63**, 1237 (1991).

Ceperley, D. M., Rev. Mod. Phys. **67**, 279 (1995).

Ceperley, D. M., "Monte carlo and molecular dynamics of condensed matter systems", (Editrice Compositori, Bologna, Italy, 1996).

Ceperley, D. M. and B. J. Alder, Physica **108B**, 875 (1981).

Ceperley, D. M. and L. Mitas, Adv. Chem. Phys. **93**, 1 (1996).

Collins, G. W., L. B. D. Silva, P. Celliers, D. M. Gold, M. E. Foord, R. J. Wallace, A. Ng, S. V. Weber, K. S. Budil and R. Cauble, Science **281**, 1178 (1998).

Collins, L., I. Kwon, J. Kress, N. Troullier and D. Lynch, Phys. Rev. E **52**, 6202 (1995).

Cui, T., E. Cheng, B. Alder and K. Whaley, Phys. Rev. B **55**, 12253 (1997).

Da Silva, I. B., P. Celliers, G. W. Collins, K. S. Budil, N. C. Holmes, W. J. Barbee, B. A. Hammel, J. D. Kilkenny, R. J. Wallace, M. Ross, R. Cauble, A. Ng and G. Chiu, Phys. Rev. Lett. **78**, 783 (1997).

Ebeling, W., A. Förster, H. Hess and M. Y. Romanovsky, Plasma Phys. Control. Fusion **38**, A31 (1996).

Ebeling, W., W. Kraeft and D. Kremp, *Theory of Bound States and Ionisation Equilibrium in Plasma and Solids*, Ergebnisse der Plasmaphysik und der Gaselektronik, Band 5 (Akademie-Verlag, Berlin, 1976).

Ebeling, W. and B. Militzer, Phys. Lett. A **226**, 298 (1997).

Ebeling, W. and W. Richert, Phys. Lett. A **108**, 85 (1985a).

Ebeling, W. and W. Richert, Phys. Stat. Sol. **128**, 467 (1985b).

Ebeling, W. and R. Sändig, Ann. Phys. **28**, 289 (1973).

Ewald, P., Ann. Phys. **54**, 557 (1917).

Feldmeier, H., Nucl. Phys. A **515**, 147 (1990).

Feynman, R. P., *Statistical Mechanics* (Addison-Wesley, Reading, MS, 1972).

Foulkes, W. M., L. Mitas, R. J. Needs and G. Rajagopal, submitted to Rev. Mod. Phys. (1999).

Fowler, R. and E. Guggenheim, *Statistical Thermodynamics* (Cambridge University Press, Cambrdige, UK, 1965).

Galli, G., R. Hood, A. Hazi and F. Gygi, Phys. Rev. B. **61**, 909 (2000).

Gilgien, L., *Modeling positron-electron correlations in condensed matter systems*, Ph.D. thesis, Université de Genève (1997).

Girardeau, M. D., Phys. Rev. A **41**, 6935 (1990).

Gordillo, C. and D. Ceperley, Phys. Rev. Lett. **79**, 3010 (1997).

Grüter, P., D. Ceperley and F. Laloe, Phys. Rev. Lett. **79**, 3549 (1997).

Hammond, B., W. A. Lester and P. J. Reynolds, *Monte Carlo Methods in Ab Initio Quantum Chemistry* (World Scientific, Singapore, 1994).

Hansen, J., Phys. Rev. A **8**, 3096 (1973).

Heller, E., J. Chem. Phys. **62**, 1544 (1975).

Hohl, D., V. Natoli, D. Ceperley and R. Martin, Phys. Rev. Lett. **71**, 541 (1993).

Holmes, N., M. Ross and W. Nellis, Phys. Rev. B **52**, 15835 (1995).

Jones, M. and D. Ceperley, Phys. Rev. Lett. **76**, 4572 (1996).

Juranek, H. and R. Redmer, J. Chem. Phys. (2000).

Kerley, G. I., "Molecular based study of fluids", p. 107 (ACS, Washington DC, 1983).

Kitamura, H. and S. Ichimaru, J. Phys. Soc. Japan **67 (3)**, 950 (1998).

Kitamura, H., S. Tsuneyuki, T. Ogitsu and T. Miyake, Nature (2000).

Klakow, D., C. Toepffer and P.-G. Reinhard, Phys. Lett. A **192**, 55 (1994a).

Klakow, D., C. Toepffer and P.-G. Reinhard, J. Chem. Phys. **101**, 10766 (1994b).

Kleinert, H., *Path Integrals in Quantum Mechanics and Polymer Physics* (World Scientific, Singapore, 1990).

Knaup, M., P.-G. Reinhard and C. Toepffer, Contrib. Plasma Phys. **39 1-2**, 57 (1999).

Knaup, M., G. Zwicknagel, P.-G. Reinhard and C. Toepffer, "Heavy ion inertial fusion", (2000).

Kohanoff, J. and J.-P. Hansen, Phys. Rev. E **54**, 768 (1995).

Kolos, W. and C. C. J. Roothan, Rev. Mod. Phys. **32**, 219 (1969).

Kolos, W. and L. Wolniewicz, J. Chem. Phys. **41**, 3674 (1964).

Kwon, I., A. Collins, D. Kress, N. Troullier and D. Lynch, Phys. Rev. E **49**, R4771 (1994).

Landau, L. and Y. Zeldovich, Acta Physica-Chem. URSS **18**, 1943 (1943).

Lebowitz, J. L., N. Macris and P. A. Martin, J. Stat. Phys. **67**, 909 (1992).

Lenosky, T. J., S. R. Bickham, J. D. Kress and L. A. Collins, Phys. Rev. B **61**, 1 (2000).

Lenosky, T. J., J. D. Kress and L. A. Collins, Phys. Rev. B **56**, 5164 (1997a).

Lenosky, T. J., J. D. Kress and L. A. Collins, Phys. Rev. B **55**, 11907 (1997b).

Lévy, P., Compositio Math. **7**, 283 (1939).

Macris, N. and P. A. Martin, Operator Theory: Adv. Appl. **70**, 191 (1994).

Magro, W., Ph.D. thesis, University of Illinois at Urbana-Champaign (1996).

Magro, W. R., D. M. Ceperley, C. Pierleoni and B. Bernu, Phys. Rev. Lett. **76**, 1240 (1996).

Mao, H.-K. and R. Hemley, Rev. Mod. Phys. **66**, 671 (1994).

McLachlan, A. D., Mol. Phys. **8**, 39 (1964).

Metropolis, N., A. Rosenbluth, M. Rosenbluth, A. Teller and E. Teller, J. Phys. Chem. **21**, 1087 (1953).

Militzer, B., *Quanten-Molekular-Dynamik von Coulomb-Systemen* (Logos publishing company, Berlin, 1996).

Militzer, B. and D. M. Ceperley, submitted to Phys. Rev. Lett. (2000).

Militzer, B., W. Magro and D. Ceperley, "Strongly coupled coulomb systems", (Plenum Press, New York NY, 1998).

Militzer, B., W. Magro and D. Ceperley, Contr. Plasma Physics **39 1-2**, 152 (1999).

Militzer, B. and E. L. Pollock, Phys. Rev. E **61**, 3470 (2000a).

Militzer, B. and E. L. Pollock, J. Phys. France IV **10**, 315 (2000b).

Nagel, S., R. Redmer, G. Röpke, M. Knaup and C. Toepffer, Phys. Rev. E **57**, 5572 (1998).

Natoli, V. and D. M. Ceperley, J. Comp. Phys. **117**, 171–178 (1995).

Nellis, W., A. Mitchell and *et al.*, J. Chem. Phys. **79**, 1480 (1983).

Norman, G. and A. Starostin, Teplophys. Vys. Temp. **6**, 410 (1968).

Ortiz, G. and P. Ballone, Phys. Rev. B **50**, 1391 (1994).

Pierleoni, C., D. Ceperley, B. Bernu and W. Magro, Phys. Rev. Lett. **73**, 2145 (1994).

Pines, D. and P. Nozieres, *The Theory of Quantum Liquids*, vol. 1 (Addison-Wesley, Redwood City, 1989).

Pollock, E. and D. M. Ceperley, Phys. Rev. B **30**, 2555 (1984).

Pollock, E. and D. M. Ceperley, Phys. Rev. B **36**, 8343 (1987).

Pollock, E. L., Comp. Phys. Comm. **52** , 49 (1988).

Pollock, E. L., private communiation (2000).

Raedt, H. D. and B. D. Raedt, Phys. Rev. A **28 (6)**, 3575 (1983).

Rescigno, T. N., submitted to Phys. Rev. Lett. (1999).

Rogers, F., Astrophys. J. **352**, 689 (1990).

Ross, M., Phys. Rev. B **58**, 669 (1998).

Saumon, D. and G. Chabrier, Phys. Rev. A **46**, 2084 (1992).

Saumon, D., G. Chabrier and H. M. V. Horn, Astrophys. J. **99 2**, 713 (1995).

Schnack, J., *Kurzreichweitige Korrelationen in der Fermionische Molekulardynamik*, Ph.D. thesis, Technische Hochschuile Darmstadt (1996).

Schulman, L., *Techniques and Applications of Path Integrations* (Wiley, New York, 1981).

Shumway, J., Ph.D. thesis, University of Illinois at Urbana-Champaign (1999).

Shumway, J. and D. Ceperley, "Proceedings of international conference on strongly coupled coulomb systems", (St. Malo, France, 1999).

Silvera, I. and M. G. Pravica, Condens. Matter **10**, 11169 (1998).

Singer, K. and W. Smith, Mol. Phys. **57**, 4, 761–775 (1986).

Steiner, E., *The determination and interpretation of molecular wave functions* (Cambdridge University Press, Cambridge, UK, 1976).

Storer, R. G., J. Math. Phys. **9**, 964 (1968).

Surh, M., K. J. Runge, T. Barbee, E. Pollock and C. Mailhiot, Phys. Rev. B **55**, 11330 (1997).

Szabo, A. and N. A. Ostlund, *Modern Quantum Chemistry: Introduction to Advanced Electronic Structure Theory* (Dover Publications Inc., Mineola, NY, 1996).

Theilhaber, J. and B. J. Alder, Phys. Rev. A **43**, 4143 (1991).

Trotter, H. F., Proc. Am. Math. Soc. **10**, 545 (1959).

Wagner, M. and D. M. Ceperley, J. Low Temp. Phys. **102**, 275 (1996).

Weir, S., A. Mitchell and W. Nellis, Phys. Rev. Lett. **76**, 1860 (1996).

Wigner, E. and H. B. Huntington, J. Chem. Phys. **3**, 764 (1935).

Zeldovich, Y. B. and Y. P. Raizer, *Physics of Shock Waves and High-Temperature Hydrodynamic Phenomena* (Academic Press, New York, 1966).

Zhu, X., M. Hybertsen and P. Littlewood, Phys. Rev. B **54**, 13575 (1996).

Zong, F. and D. Ceperley, Phys. Rev. E **58**, 5123 (1998).

Vita

Burkhard Militzer was born on August 19, 1970, in Dresden, Germany. He received a diploma in physics from the Humboldt University at Berlin in 1996. His diploma thesis was titled "Quantum Molecular Dynamics of Coulomb Systems" and his advisor was Prof. W. Ebeling.